AD NUMBER
AD383164
CLASSIFICATION CHANGES
TO: **UNCLASSIFIED**
FROM: **CONFIDENTIAL**
LIMITATION CHANGES
TO: **Approved for public release; distribution is unlimited.**
FROM: **Distribution authorized to U.S. Gov't. agencies and their contractors; Critical Technology; JUL 1967. Other requests shall be referred to Air Force Rocket Propulsion Laboratory, Edwards AFB, CA 93523. This document contains export-controlled technical data.**
AUTHORITY
31 Jul 1979, DoDD 5200.10; AFRPL ltr, 5 Feb 1986

AD 383 164

AUTHORITY: AFRPL
ltr. 5 FEB 86

SECURITY MARKING

The classified or limited status of this report applies to each page, unless otherwise marked.
Separate page printouts MUST be marked accordingly.

THIS DOCUMENT CONTAINS INFORMATION AFFECTING THE NATIONAL DEFENSE OF THE UNITED STATES WITHIN THE MEANING OF THE ESPIONAGE LAWS, TITLE 18, U.S.C., SECTIONS 793 AND 794. THE TRANSMISSION OR THE REVELATION OF ITS CONTENTS IN ANY MANNER TO AN UNAUTHORIZED PERSON IS PROHIBITED BY LAW.

NOTICE: When government or other drawings, specifications or other data are used for any purpose other than in connection with a definitely related government procurement operation, the U. S. Government thereby incurs no responsibility, nor any obligation whatsoever; and the fact that the Government may have formulated, furnished, or in any way supplied the said drawings, specifications, or other data is not to be regarded by implication or otherwise as in any manner licensing the holder or any other person or corporation, or conveying any rights or permission to manufacture, use or sell any patented invention that may in any way be related thereto.

AFRPL-TR-67-214

(Unclassified Title)

ADVANCED THRUST CHAMBER FOR SPACE MANEUVERING PROPULSION

Tasks II and III - Thrust Chamber Segment Evaluations
Final Report

H. G. Diem
R. P. Pauckert

Rocketdyne
A Division of North American Aviation, Inc.
Canoga Park, California

Technical Report AFRPL-TR-67-214

July 1967

Group 4
Downgraded at 3-Year Intervals
Declassified After 12 Years

Air Force Rocket Propulsion Laboratory
Research and Technology Division
Edwards Air Force Base, California
Air Force Systems Command
United States Air Force

AFRPL-TR-67-214

(Unclassified Title)

ADVANCED THRUST CHAMBER FOR SPACE MANEUVERING PROPULSION

Tasks II and III - Thrust Chamber Segment Evaluations
Final Report

H. G. Diem
R. P. Pauckert

Rocketdyne
A Division of North American Aviation, Inc.
Canoga Park, California

Technical Report AFRPL-TR-67-214

July 1967

Group 4
Downgraded at 3-Year Intervals
Declassified After 12 Years

Air Force Rocket Propulsion Laboratory
Research and Technology Division
Edwards Air Force Base, California
Air Force Systems Command
United States Air Force

AFRPL-TR-67-214

(Unclassified Title)

ADVANCED THRUST CHAMBER FOR SPACE MANEUVERING PROPULSION

Tasks II and III - Solid Wall and Tube Wall Segment Evaluations

H. G. Diem
R. P. Pauckert

July 1967

Air Force Rocket Propulsion Laboratory
Research and Technology Division
Edwards Air Force Base, California
Air Force Systems Command
United States Air Force

FOREWORD

(U) This technical report presents the results of the effort under Tasks II and III of the program titled "Advanced Thrust Chamber for Space Maneuvering Propulsion". The Task I studies of the program were conducted during the period 16 May to 15 August 1966 and are reported in AFRPL-TR-66-301. The Task II and III experimental phases of the program were conducted during the period 16 May 1966 to 15 June 1967. The program was authorized by the USAF Rocket Propulsion Laboratory under Contract AF04(611)-11617. The Air Force Program Manager is Mr. W. W. Wells, RPREC.

(U) This publication was prepared by Rocketdyne, a division of North American Aviation, Inc., as Report R-6730-1.

(U) This technical report has been reviewed and is approved.

W. W. Wells, AFRPL Program Manager

ABSTRACT

(C) An analytical and experimental study was conducted to evaluate the most critical design aspects of the advanced LF_2/LH_2 propulsion system concept selected under previous contract AF04(611)-10745. These design aspects were associated with the toroidal thrust chamber of the aerospike engine which produced 30,000 pounds of thrust. Combustion chamber performance, heat transfer characteristics, regenerative cooling capability, and structural integrity were investigated and demonstrated by testing segments of the complete chamber.

(C) The experimental efforts were first conducted with water-cooled segments and resulted in the selection of a near-optimum injector/combustion chamber configuration. An injector having an impinging fan orifice pattern together with a combustion chamber which converged continuously from the injector to the throat was found to give high C* efficiency while maintaining heat transfer rates within the capability of a two-pass regenerative cooling system design. It was also demonstrated that gases for turbine operation could be withdrawn from the combustion chamber through the injector without seriously degrading injector performance. The properties of these tapoff gases were found to be relatively independent of chamber pressure.

(C) Two tube-wall segments were designed for two-pass cooling on the basis of the solid-wall segment results. These segments demonstrated regenerative cooling over the 9:1 throttling range. Chamber performance in excess of 99 percent C* efficiency over the throttle range was achieved. Three dynamic throttling tests demonstrated injector stability over the critical low-to-middle thrust range.

(C) Two structural segments were fabricated using lightweight rib and honeycomb support structure. These segments were cycled from 0 to 650 psig more than 15 times using hydraulic pressure to simulate chamber pressure. Analytical and experimental data agreed closely and indicated that throat area variations over the throttling range would be less than 3 percent for chambers using either the rib or honeycomb designs.

CONTENTS

Foreword ii
Abstract iii
Section I 1
Introduction and Summary 1
1. General 1
2. Concept 2
3. Program Objectives 3
4. Program Approach 4
5. Summary of Results 4
Section II 7
Task II: Solid-Wall Segment Evaluation 7
1. General 7
2. Design Description 8
3. Solid-Wall Segment Design Analysis 37
4. Experimental Procedures 45
5. Solid-Wall Segment Testing 48
6. Performance Data Analysis 53
7. Heat Transfer Analysis 76
Section III 111
Task III: Tube-Wall Segment Evaluation 111
1. General 111
2. Tube-Wall Throat Inserts 111
3. Tube-Wall Segments 125
4. Lightweight Support Structure Segments 152
Section IV 221
Conclusions and Recommendations 221
References 223
Appendix A
Temperature Distribution and Resulting Strains in Throat Region of Water Cooled Copper Segment A-1
Appendix B
Solid Wall Segment Base Pressure Measurements B-1
Appendix C
Structural Weight Equations C-1
Appendix D
Structural Analysis Method D-1

ILLUSTRATIONS

1. Engine System Configuration 1
1a. Toroidal Aerospike Thrust Chamber 2
2. Segment Test Configurations 5
3. Test Hardware Interchangeability 9
4. Solid Wall Segment Assembly 10
5. Water-Cooled Solid-Wall Segment 11
6. Exploded View of Solid-Wall Segment 12
7. Basic Injector Configurations 14
8. Bottom View of Injector 16
9. Top View of Injector 17
10. Two-Row Triplet Injector 18
11. Spray Pattern of Two-Row Triplet Injector 19
12. Impinging Fan Concept 21
13. Single Row Impinging Fan Injector 22
14. Spray Pattern for Impinging Fan Injector 23
15. Injector Design Variations 24
16. Injector for Mixture Ratio Bias 25
17. Adapter for Mixture Ratio Bias 26
18. Injector Tapoff Configuration 27
19. Molecular Weight and Combustion Temperature for LF_2/GH_2 29
20. Chamber "A" Cross Section 30
21. Solid Wall Segment Contours 31
22. Contours B and C Chamber and Nozzle Cross-Section 33
23. Solid Wall Segment Throat Section 34
24. Water-Cooled Contour E 35
25. Additional Chamber Contour 36
26. Experimental Throat Discharge Coefficients 41
27. Calculated Nozzle Efficiencies 43
28. Throat Shrinkage Resulting From Thermal Loads 44
29. Schematic Flow Diagram of Test Stand Victor 46
30. Test Instrumentation Schematic 47
31. CRT Plot of Chamber Pressure vs Time 54
32. CRT Plot of Thrust vs Time 55
33. Effect of Chamber Pressure of C* Performance of Contours A Through E 61
34. Comparison of Performance of Contours A Through E 62
35. Variation of C* Efficiency with Chamber Contour Parameter . . 63
36. Variation of C* Efficiency with GH_2 Injection Mach Number 65
37. Variation of C* Efficiency With Atomization Parameter, Triplet Injector 67
38. Approximate Fan Perimeters - 10 Element Impinging Fan Pattern 68
39. Tapoff System Instrumentation Schematic 71
40. Molecular Weight and Combustion Temperature for LH_2/GH_2 . . 72
41. Ratio of F_2 Injector Pressure Drop/Chamber Pressure vs % Maximum P_c 75
42. Typical Plot of $N_{ST} \times (N_{PR})^{2/3}$ vs Area Ratio 81
43. Effect of Convergence Angle on Nozzle Heat Transfer for 3.5 Inch Chamber Length Segment 82

44. Comparison of 15- and 30-Degree Throat Convergence Angle Heat Transfer Rates - Effect of Length Along Contour From Start of Convergence 83
45. Effect of Combustion Chamber Contour on 30-Degree Nozzle Heat Transfer Rates 85
46. Variation in Heat Transfer Parameter With Axial Distance for Contour A 86
47. Effect of Combustion Chamber Length on Nozzle Heat Transfer Parameter for 15-Degree Convergence Angle Segment . . 87
48. Effect of Injector Type on Heat Transfer Parameter Profile in Contour C 88
49. Triplet and Impinging Fan Injectors Comparison of Heat Transfer Parameter Profiles in Contour E Chamber 90
50. Effect of GH_2 Injection Velocity on Combustion Zone Heat Transfer Parameter, Contour C 91
51. Effect of GH_2 Injection Velocity on Nozzle Region Region Heat Transfer Parameter, Contour C 92
52. Effect of GH_2 Injection Velocity on Nozzle Heat Transfer Parameter - Contour E 93
53. Effect of Mixture Ratio Bias on Nozzle Heat Transfer Parameter - Contour E 94
54. Effect of Mixture Ratio Bias on Nozzle Heat Transfer Parameter, Contour C 95
55. Effect of Tapoff on Heat Transfer Contour E 97
56. Effect of Nickel Plating on Nozzle Heat Transfer Parameter, Contour E 98
57. Effect of Gaseous Fluorine on the Distribution of Heat Transfer Parameter Along Contour E 100
58. Distribution of Heat Transfer Parameter for Contour F . . 101
59. Distribution of Heat Transfer Parameter for Contour G . . 102
60. Heat Flux Distribution for Contour G 104
61. Variation in Heat Transfer Parameter With Chamber Pressure - Contour G 105
62. Throat Heat Flux Versus Chamber Pressure - Contour G . . . 106
63. Distribution of Exponent $n(Q/A \propto P_c^n)$ Along Contour G . . . 107
64. Comparison of Peak Gas Side Film Coefficients for Water-Cooled Contours 109
65. Comparison of Total Heat Input to Various Contours . . . 110
66. Regenerative Nozzle Wafer 113
67. Cross-Sectional Temperature Distribution in Nickel Tube . . 115
68. Tube Wall Throat Insert Components 116
69. Assembled Tube Wall Throat Core 117
70. Nickel Tube-Wall Throat Insert 118
71. Tube-Wall Insert and Water-Cooled Chamber 119
72. Facility Schematic Showing Regenerative Cooling Lines . . 120
73. Estimated and Measured Pressure Drops for Water-Flow Calibration of the CRES Tube Throat Insert 122
74. Tensile Strength of 347 CRES 124
75. Tube-Wall Segment 126
76. Tube-Wall Segment 127
77. Sample EB-Welded Tube Blankets Before and After Forming . . 128
78. Completed Tube-Wall Segment 130

79. Pressure Drop vs Water Flowrate for Nickel Tube-Wall Segments 131
80. Tube-Wall Segment LH_2 Coolant Circuit 134
81. Chamber Pressure vs Time for Dynamic Throttling Test . . . 135
82. C* Efficiencies In Contour G Chambers 139
83. Effect of GH_2 Injection Velocity on Performance 140
84. Injector Fluorine Pressure Drop vs Flowrate for Impinging Fan Injector 142
85. Measured Heat Input for Tube-Wall Segment No. 1 145
86. Comparison of Measured and Design Flowrates for Tube-Wall Segment No. 2 146
87. Cooling Margin for Tube-Wall Segment No. 2 147
88. Estimated Peak Tube Wall Temperatures for Tube-Wall Segment No. 2 149
89. Coolant Tube Isotherm Profile 150
90. Measured Heat Input for Tube-Wall Segment No. 2 151
91. Toroidal Chamber Structures 154
92. Two Rings With Pressure Between Them - With Intermediate Baffle Ties 157
93. Fixed-Fixed Beam 158
94. Ring Interaction Analysis - Subsonic Baffle 160
95. Subsonic Bolt Analysis Model 162
96. Thrust Chamber Cross-Section Showing Deflection Continuity Lines 166
97. Spring Analog of Bolt-Baffle Combination 167
98. Spring Analog of Combustion Chamber-Baffle Combination . . . 168
99. Schematic of Core Loading 172
100. Cantilever Loading of Baffle Bolts 172
101. Rib Structure Segment 173
102. Structural Test Segment - Rib Supports 174
103. Required Fillet Size vs Alloy Strength 176
104. Cross-Section of Honeycomb Segment 177
105. Composite Rib/Honeycomb Structural Segment 181
106. Sample of Electron-Beam Welded Rib Channels 182
107. Closeup of Electron-Beam Weld in Rib Channels 183
108. Honeycomb Edge Plating Sample 186
109. Nickel Plating and Weld Sample 187
110. Plated Edge Weld Joint Sample 189
111. Subscale Honeycomb Braze Sample 190
112. Shear Strength of Candidate Braze Alloys 192
113. Face Sheet to Honeycomb Braze 193
114. Honeycomb Panels and Masks Prior to Plating 194
115. Plated and Brazed Honeycomb Panel 195
116. Partial Assembly of Rib Panel 197
117. Rib Panel Before Welding 198
118. Rib Panel After EB Welding 199
119. Rib Panel EB Welds 200
120. Partially Assembled Rib Structural Segment 201
121. Rib Structural Segment After Heat Treat 203
122. Plated Honeycomb Cores and Closeouts in Formblock 204
123. Honeycomb Panel with Rib Aft Structure 205
124. Partially Assembled Honeycomb Structural Segment 206
125. Honeycomb Panels and Baffles Assembled in Weld Fixture . . 207
126. Analytical Model of Segment Outerbody 212

127. Calculated Deflections at Midspan of Segments 213
128. Structural Loads With and Without Throat Plugs 214
129. Instrumentation for Rib Structure Segment 216
130. Test Setup for Structural Segments 217
131. Measured Bolt Load vs Pressure for Rib Segment 218
132. Measured Strain vs Pressure for Rib Segment 219
133. Rib Structural Segment Throat Deflection at 650 psig . . . 220

TABLES

1. Thrust Chamber Contour Characteristics 32
2. Solid-Wall Segment Test Summary 49
3. Performance Data Summary 50
4. Mixture Ratio Bias Results 70
5. Tapoff Test Results 73
6. Summary of Experimental Parameter Variations 77
7. CRES Tube Throat Insert Test Summary 123
8. Tube-Wall Segment Test Summary 132
9. Summary of Tube-Wall Segment Performance 136
10. Summary of Throttling Test 103 137
11. Summary of Throttling Test 105 137
12. Tube-Wall Segment Cooling Test Summary 143
13. Structural Support Concept Comparison 163
14. Properties of Inconel-718 185
15. Structural Segment Weight Comparison 208
16. Summary of Potential Weight Reductions 210
17. Maximum Throat Deflection at 650 psig 211

SECTION I

INTRODUCTION AND SUMMARY

1. GENERAL

(C) A study was conducted under sponsorship of AFRPL during the 1965 calendar year to define an advanced optimized LF_2/LH_2 space maneuvering propulsion system (Contract AF04(611)-10745). The mission of primary interest, which defined the propulsion system requirements, was that of intercept and rendezvous with passive and evasive target satellites. The system gross weight was selected as 20,000 pounds to be adaptable to the present Titan IIIC launch vehicle.

(C) The study defined an optimum engine configuration that utilized concentric thrust chambers. The outer primary thrust chamber of 30,000 pounds thrust incorporated the toroidal-aerodynamic spike design concept. The inner secondary thrust chamber of 3300 pounds thrust was of a bell design. The thrust chambers were fed from independent turbopumps which were driven by tapoff gases from each of the thrust chambers. Each of the thrust chambers were throttled over a 9:1 thrust range which gave the engine system an overall throttle ratio of 81:1. The configuration is illustrated in Fig. 1.

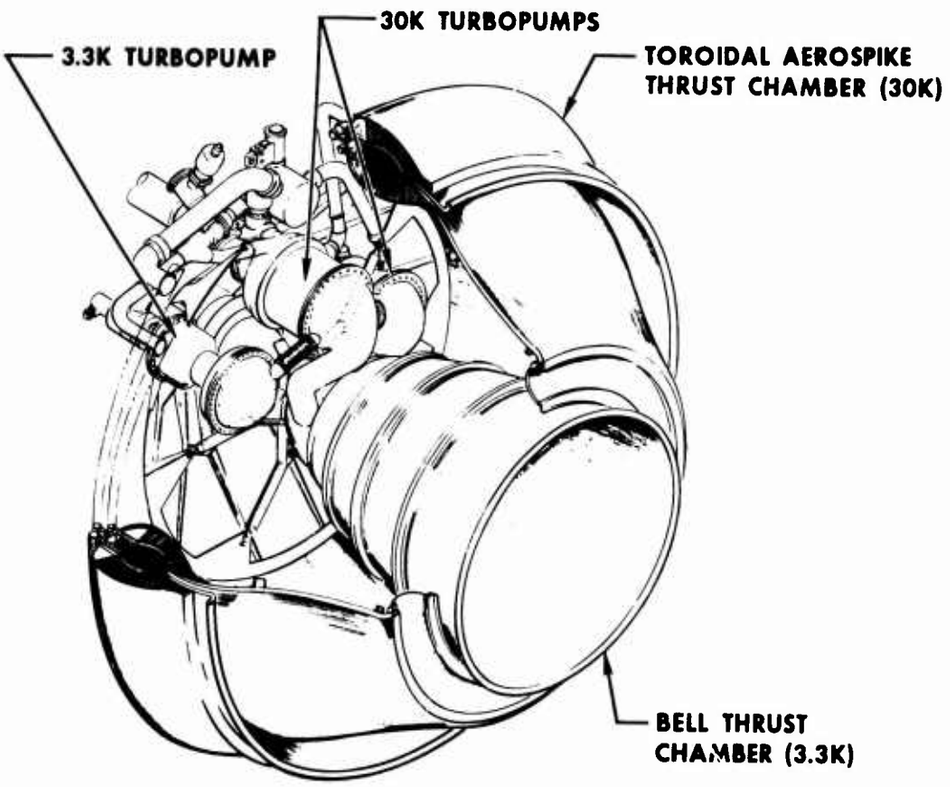

Figure 1. Engine System Configuration

(U) Since the potential mission performance capability gains of this propulsion system concept were very attractive, a demonstration of critical design features was considered desirable. Because the toroidal-aerospike thrust chamber was the single most unique concept and was the primary basis for the engine design, demonstration effort was concentrated in this area.

2. CONCEPT

(C) The thrust chamber concept consists of a toroidal combustion chamber with inner and outer regeneratively cooled walls. These are joined together by an annular injector. The outer wall extends past the throat region to form an expansion shroud. The tubes forming the inner wall are extended past the throat and are contoured to form the primary nozzle expansion surface. The configuration is illustrated in Fig. 1a.

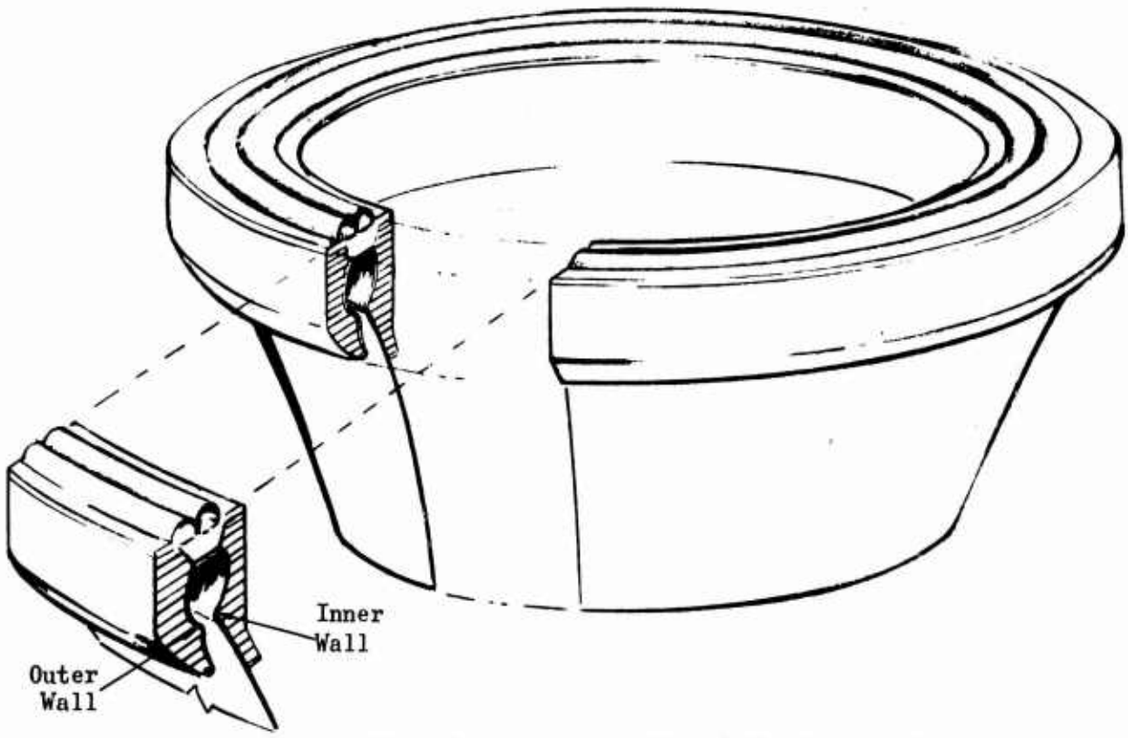

Figure 1a. Toroidal Aerospike Thrust Chamber Configuration

(C) The integrity of the combustion chamber is achieved by a lightweight structural arrangement where the separating loads due to the chamber pressure are resisted by inner and outer body structures which are supported intermittently around the chamber by combustion chamber baffles. The baffles, in addition to providing a structural support, serve as compartmentation devices to assure combustion stability.

(C) The basic design parameters of the 30K toroidal-aerospike thrust chamber are listed below. These parameters provided the baseline for all hardware design and test evaluations of this program.

Propellants	-	LF_2/LH_2
Thrust (max)	-	30,000 lbs
Chamber Pressure	-	650 psia to 70 psia
Mixture Ratio	-	13:1

(U) The toroidal chamber evaluation approach was to test a segment of the complete chamber as illustrated in Fig. 1a. The segment represents approximately 1/47 of the complete toroid circumference. Combustion performance, heat transfer, and structural evaluations was accomplished on the segment. Previous testing at Rocketdyne has shown that results from segments duplicate those obtained with the complete 360-degree toroid. Segment testing permitted the desired test data to be obtained at reduced hardware costs and with relative experimental ease.

3. PROGRAM OBJECTIVES

(C) The program was divided into three primary tasks. Task I extended the studies of Contract AF04(611)-10745 to determine the mission performance capabilities of heavier and larger gross weight space maneuvering vehicles that can be adapted to Saturn IB and growth versions of the Titan IIIC launch vehicles. Also, for the 20,000-pound gross weight vehicles defined previously in Contract AF04(611)-10745, the orbital life capabilities beyond the previously established requirement of 14 days were determined. The results of these studies were reported separately as report AFRPL-TR-66-301 and are therefore not included in this report.

(C) The basic goal of Tasks II and III was the demonstration of the critical features of the toroidal thrust chamber, while delivering high performance at the operating parameters defined above. The specific objectives of the Tasks II and III were as follows:

1. Demonstrate high combustion efficiency (97 percent of theoretical shifting c* over the design throttling range of 9:1
2. Determine the effect of chamber contour and injector characteristics on performance and heat flux distribution
3. Demonstrate the feasibility of supplying temperature-controlled chamber tapoff gas (simulating turbopump requirements) by regulating the injector mixture ratio distribution
4. Demonstrate the ability to regeneratively cool the chamber
5. (C) Demonstrate that the lightweight support structure can maintain the nozzle throat size within an acceptable tolerance

(U) Task II, called Solid Wall Segment Evaluation, included objectives 1, 2 and 3 above. Task III, called Tube Wall Segment Evaluation, included objectives 1, 4 and 5.

4. PROGRAM APPROACH

(U) The approach for conducting Tasks II and III is illustrated in Fig. 2. The objectives of Task II were accomplished using solid wall, water cooled hardware. Injector performance, heat transfer, and hot gas tapoff evaluations were conducted over the throttle range using these relatively inexpensive components. These results provided for selection of the best combustion chamber geometry and injector configuration for the tube wall evaluations of Task III.

(U) Task III had three parts consisting of tube wall throat insert evaluation, complete tube wall segment evaluation, and structural segment evaluation (Fig. 2). The tube wall throat inserts provided verification of the heat transfer results of the solid wall tests in the critical throat region and defined initial test conditions for the cooled segments. The tubes of the inserts were hydrogen cooled while the opposite side was water cooled to obtain additional heat transfer data.

(U) Following the throat insert testing, regeneratively cooled thrust chamber segments were tested using the best injector from the previous segment tests.

(U) Two lightweight structural segments were fabricated and pressure tested. These segments differed from each other in that a rib-type backup structure was used on one segment while honeycomb was used in the structure of the other segment.

5. SUMMARY OF RESULTS

(C) During the 12 month program period, 153 hot firings of solid wall and tube wall segments were conducted. In addition, mechanical structural testing of two segments with lightweight support structures was accomplished. All program objectives were successfully accomplished as a result of this testing.

(C) Under Task II, 128 water-cooled solid-wall segment firings were made in which numerous variations of combustion chamber geometry and injector pattern were evaluated. This testing, supplemented by company sponsored effort, evolved a chamber configuration which had a throat heat flux approximately 30 percent below that of earlier configurations while still maintaining relatively high performance. The configuration, called "contour G", had a continously converging chamber wall from injector to throat which promoted maximum boundary layer growth in a very short chamber length. The distance from injector to throat was 3 1/2 inches. The maximum values of throat heat flux were 22.2 Btu/sec.-in.^{2} at 650 psi chamber pressure.

SOLID WALL SEGMENT

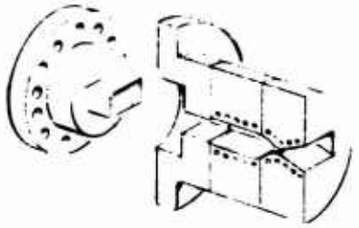

TUBE WALL THROAT INSERT

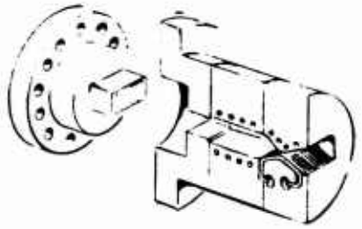

STRUCTURAL SEGMENT

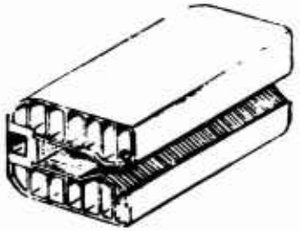

COMPLETE TUBE-WALL SEGMENT

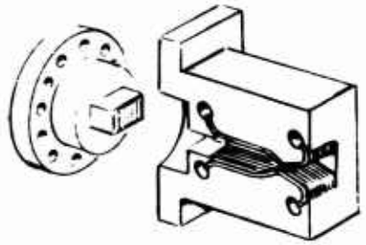

Figure 2. Segment Test Configurations

(C) All solid wall segment tests were conducted with ambient hydrogen for the injector. Relatively high C* efficiency (96.5 percent of shifting) was achieved with the contour G chamber and an impinging fan injector pattern. Analytical predictions indicated this performance would be increased several percent when heated hydrogen from the cooling jacket (~ 650F) was used instead of ambient hydrogen. (This was subsequently verified in Task III).

(C) Also as part of Task II, the feasibility of supplying temperature controlled chamber tapoff gas (simulating turbopump power requirements) was demonstrated. Nine tests were conducted. In seven of these tests, temperatures were varied over a range of 1600 F to 150 F by adjustment of a tapoff probe through the injector face. For a given adjustment setting of the probe, the tapoff gas temperature was shown to be relatively insensitive to variation of chamber pressure over a range of 290 to 485 psia. At temperatures near the design point (1500 F), the effect of tapoff on performance was shown to be negligible.

(C) Under Task III, 20 firings were conducted with full tube wall segments of the contour G configuration and the impinging fan injector. C* efficiencies in excess of 99 percent were achieved with stable combustion over the complete throttle range (650 psia to 70 psia) when the segment was operated regeneratively. The hydrogen temperature entering the injector manifold on these tests was approximately 650 F. The higher fuel injection temperature improved the injector performance significantly over that achieved with ambient hydrogen.

(C) Results of the Task III cooling evaluation demonstrated the feasibility of regeneratively cooling the 30K toroidal combustion chamber with a two-pass cooling circuit. Successful cooling was achieved at full chamber pressure (650 psia) using essentially rated flow (3% over cooling) and at full throttled conditions (70 psia) using less than rated flow. These are the two most critical operating conditions. The heat input to the chamber dropped off almost linearly with chamber pressure when heated hydrogen was injected in place of ambient hydrogen at throttled conditions. This was due to reduced wall heat input near the injector end resulting from increased combustion efficiency.

(C) Also as part of Task III, two lightweight toroidal chamber support structure designs were evaluated. One design utilized a rib type support structure while the second utilized honeycomb. Segments approximately 21 inches in length comprising 3 baffle compartments were fabricated and tested by hydraulically applying simulated chamber pressure. Pressure loadings were applied over the complete range of chamber pressure (650 psia to 70 psia) in numerous cycles on each segment. The measured deflections agreed closely with analytical predictions which correspond to calculated throat area variations of approximately 2.6 and 2.9 percent for the rib and honeycomb designs respectively. These variations are well within the original targeted design value of 10 percent.

SECTION II

TASK II: SOLID-WALL SEGMENT EVALUATION

1. GENERAL

(C) The solid-wall segment evaluation phase of the program was directed to take maximum advantage of the simplicity and reliability of water-cooled segments to determine performance and heat transfer characteristics of various injector and combustion chamber geometries. Previous experience with chambers having circular cross-sections was extended on this program to include new chamber contours and injector orifice patterns. Injector mixture ratio bias for heat flux control and turbine tapoff gas provision was also investigated during this phase of the program. The goal of the solid-wall segment evaluation was to demonstrate an injector/combustion chamber configuration which will provide high (97 percent or greater) c* efficiency over a throttling range of 9:1 while maintaining heat fluxes within the limits of the regenerative-cooling capability of an engine system.

(C) The general approach to the evaluation included the following steps:

1. Chamber Geometry Characterization
2. Basic Injector Characterization
3. Injector Mixture Ratio Bias and Hot Gas Tapoff Evaluation

The chamber geometry characterization was initiated by conducting tests with the circular chamber to verify previous data obtained with this chamber. Slight modifications were made to the injector orifice pattern to eliminate fan impingement on the narrow walls of subsequent chambers. Alternate chamber configurations selected on the basis of previous and current results were then tested to determine the optimum chamber geometry from the standpoints of performance (c*) and heat transfer.

(C) The basic injector characterization testing included evaluation of variations in the orifice pattern of the basic triplet injector and evaluation of an alternate injector pattern. The alternate pattern was selected on the basis of comparative, single-element, water/helium spray tests and test experience from other programs. The injector tests aided in the selection of the best injector/chamber combination for the subsequent tube-wall segment evaluations of Task III.

(U) Injector mixture ratio bias testing included determination of the effect of fuel injection at the periphery of the injector on the heat flux and performance in the chamber. The tapoff gas evaluation included extraction of hot gas, suitable for engine turbine power, from the combustion chamber.

2. DESIGN DESCRIPTION

(U) The philosophy upon which the design of the solid-wall segment hardware was based involved: (1) maximum use of existing hardware, (2) maximum interchangeability of hardware during the solid wall segment testing and in the subsequent tube evaluation phase of the program. This approach is illustrated in Fig. 3. The new injector design (1) was readily adaptable to either the existing circular chamber, the alternate solid-wall chambers (6 and 3), or the tube-wall segment (10). The alternate injector differed from injector (1) only in the orifice configuration and both were, therefore, interchangeable. The adapters (2 and 5) were simple, uncooled sections to position the injector face exactly at the chamber entrance. The water-cooled throat section (4) could be used with any of the alternate chamber sections. The circular chamber included a throat and short diverging nozzle. The tube-wall throat sections (8 and 9) of Task III were designed to be compatible with the alternate chamber sections.

a. Segment Assembly

(C) The solid-wall segment assembly (shown in Fig. 4) consisted of the injector, adapter, chamber, and nozzle subassemblies, together with closure rings and mounting hardware. The width of the segment was 3 inches, and was representative of approximately 1/47 of the total circumference of the toroidal engine. The double-bolted configuration permitted removal of the injector without disturbing the chamber and nozzle, or removal of the nozzle or chamber without disconnecting the propellant feed system from the injector. A coverplate was bolted to the aft closure ring to seal the assembly for pressure checking purposes. A photograph of the assembly is shown in Fig. 5 and an exploded view of the components is presented in Fig. 6.

b. Injectors

(U) Concept description. The successful design of a predictably performing rocket engine injector requires a thorough understanding of the fluid dynamic and chemical kinetic processes which govern the combustion process. Minor variations in injector design or operation can result in large changes in the thrust chamber performance, stability, and heat transfer environment. The infinite number of possible variations in injector design makes direct correlation between the mechanical features of the injector and its resultant behavior a difficult task. The problem, however, may be simplified by recognizing that the process of propellant injection takes place in the form of a spray which may be described in terms of fundamental physical parameters. The spray characteristics, defined in terms of the degree of propellant atomization and distribution, provide the basis for establishing design criteria for injectors, and are the foundation from which specific application to any design requirement is established. The basic characteristics which describe the quality of the injector spray and the many design factors which influence this figure-of-merit permit the establishment of the injector design approach.

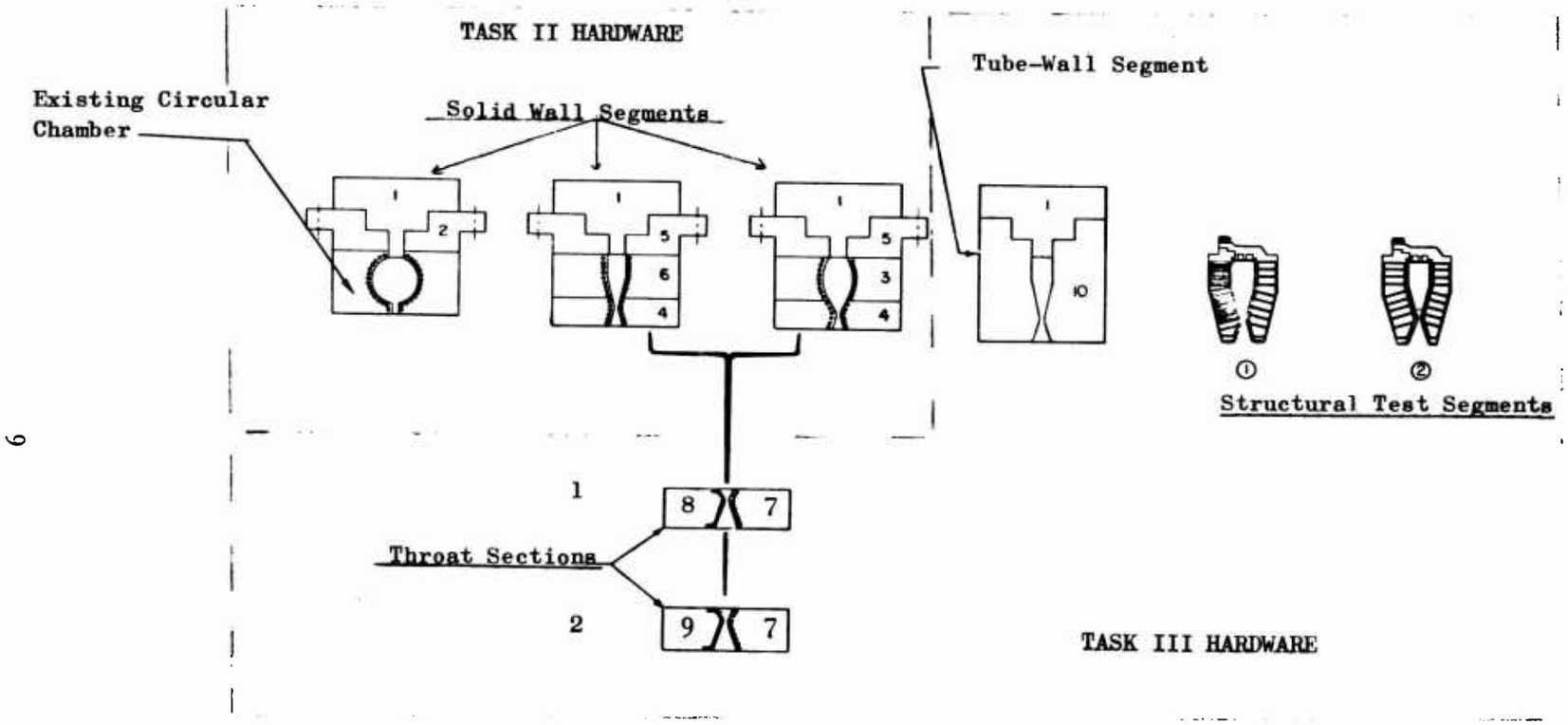

Figure 3. Test Hardware Interchangeability

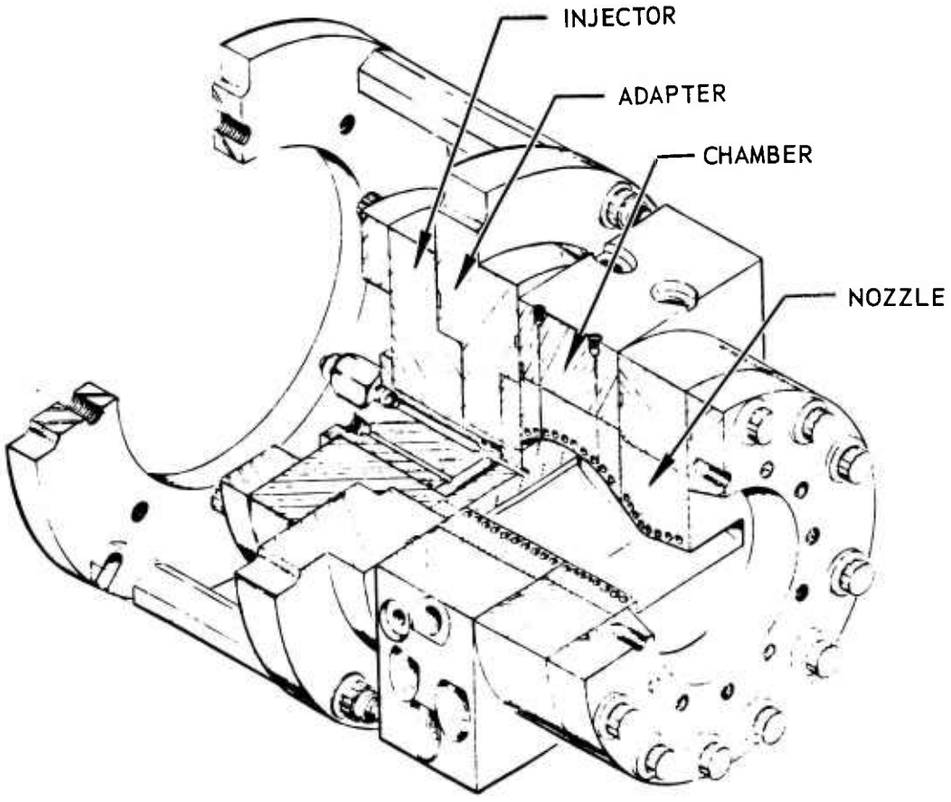

Figure 4. Solid-Wall Segment Assembly

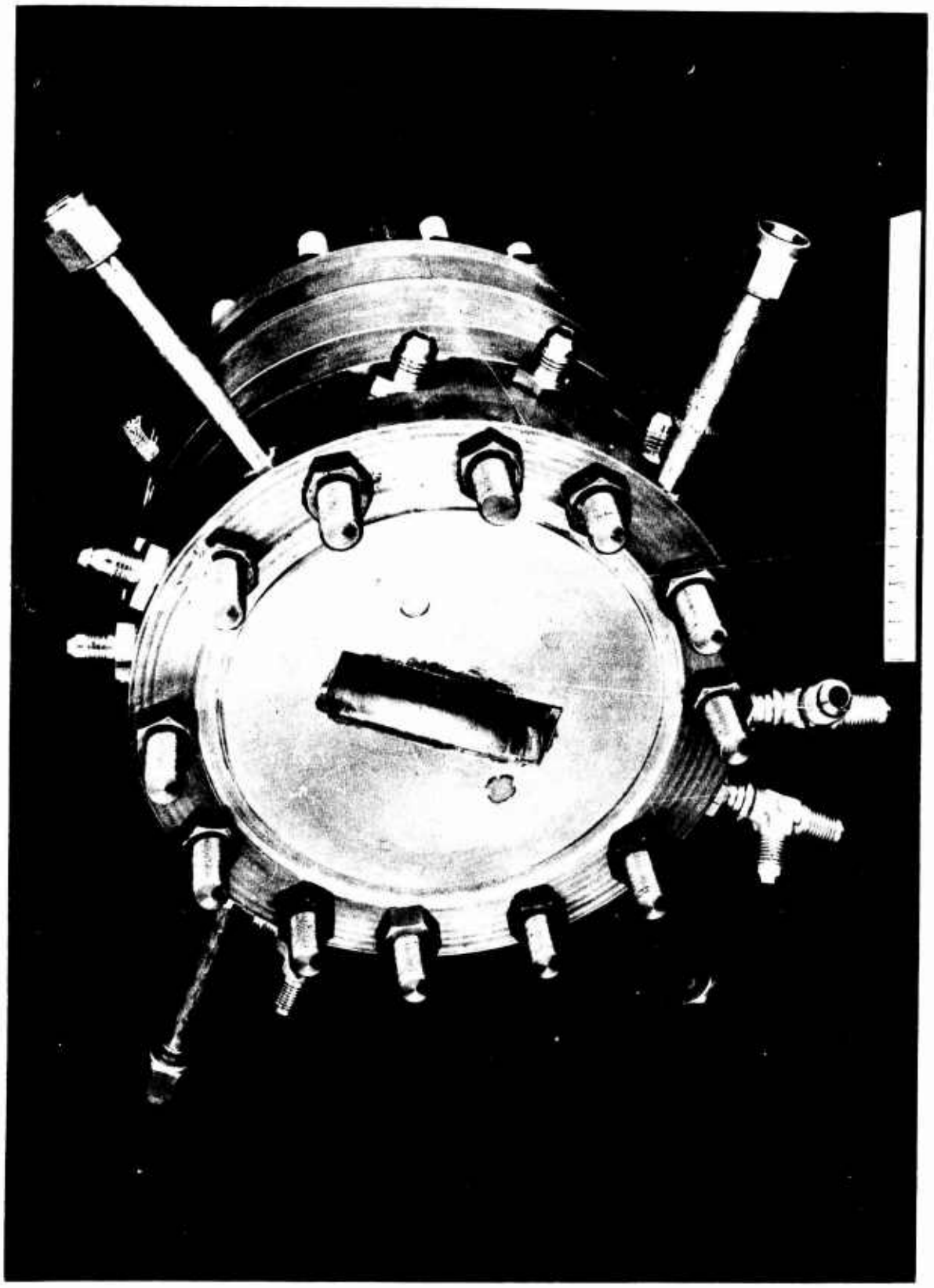

Figure 5. Water Cooled Solid-Wall Segment

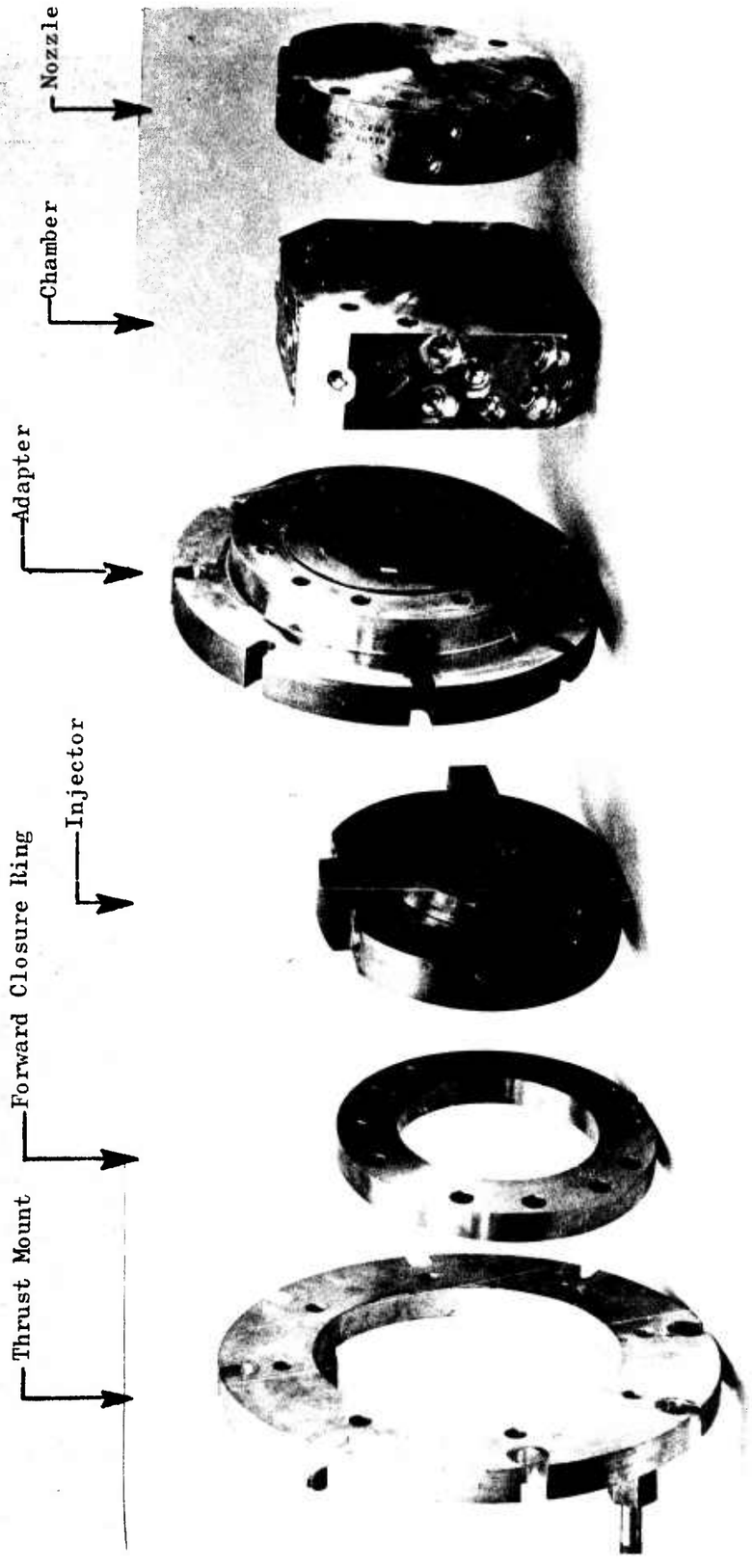

Figure 6. Exploded View of Solid-Wall Segment

(C) The specific injector designs for this program were controlled primarily by the following basic requirements:

1. The injector must be capable of at least a 9:1 throttling ratio.
2. The injector must be capable of high performance over the entire operating range.
3. The injector should feature simplicity and reliability, particularly from an overall propulsion system standpoint.

(C) Two basic injector concepts were selected for evaluation in the program. The two designs incorporated the following basic element arrangements: (1) triplets (two liquid streams impinging on a central GH_2 stream); and (2) impinging fans (two liquid fans impinging on a central GH_2 stream). Typical elements for the two injector types are shown schematically in Fig. 7.

(U) Triplet Injector Pattern. The triplet injector pattern was the concept previously selected for the Maneuvering Satellite engine defined in Contract AF04(611)-10745. This basic pattern, which has previously undergone LF_2/GH_2 segment testing under company sponsorship with promising results, was the basic pattern used in the Task II test program. It was used in the thrust chamber contour (geometry) characterization testing and was also used to initiate the injector characterization testing.

(U) The previous investigations indicated that the atomization characteristics are a function of the relative gas-to-liquid velocity and the quantity of gas available to atomize a given mass of liquid. Thus:

$$\text{Drop Size} = f\left(V_{gas}, \dot{W}_{gas}, V_{liq}, \dot{W}_{liq}\right)$$

(U) From this criteria, a basic gas-liquid triplet element evolved. A basic doublet self-impinging stream element was known to produce a spray field of liquid drops and ligaments of a given size depending upon the jet velocity and jet diameter. Previous investigations showed that by superimposing a high velocity gas flow upon this spray field, the resulting drop size could be substantially reduced. Thus, cold-flow studies were conducted at Rocketdyne to determine the level of velocity required to significantly alter the degree of atomization if the gas flow originated from a point source centrally located between the doublet streams. In addition, the gas-jet spreading characteristics and, therefore, the impingement point, the impingement angle, and orifice diameters were studied.

(U) Cold-flow results for the triplet pattern indicated that a triplet element could be used to atomize liquid propellants effectively. In addition, the results indicated that the spray-field was completely enveloped by the gas and that, at the high gas momentums, good gas-liquid distribution resulted.

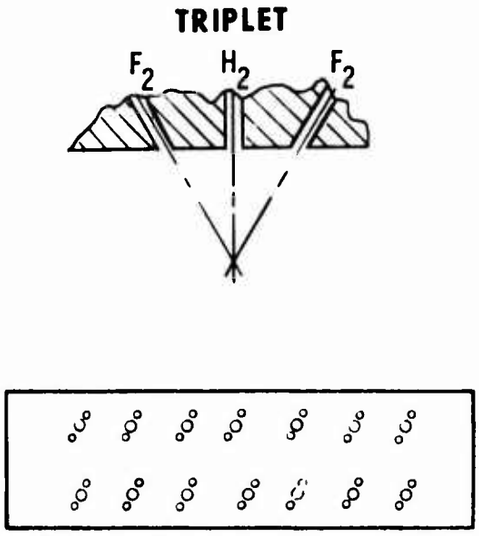

Figure 7. Basic Injector Configurations

(C) Impinging-Fan Pattern. The cold-flow analysis data obtained prior to the program for the triplet (gas/liquid) injector pattern suggested that the liquid condition was important to the efficient utilization of the gas to produce liquid atomization. The triplet results indicated that a significant portion of the initial injectant gas momentum was not being effectively used. Schlieren photographs showed that, at lower gas momentum, the liquid at the point of impingement resembles an impenetrable body. Therefore, from an aerodynamic standpoint, the most optimum design would be one that results in a liquid-spray field which allows gas penetration at the impingement point. The spray field which is most susceptable to gas penetration is one which is in the form of a thin, unstable liquid fan. Thin fans are desirable because they: (1) result in maximum liquid shear forces per unit surface area, (2) are dynamically unstable due to surface tension forces, and (3) have nonaxial components of velocity which will promote the disintegration of the fan into ligaments and drops.

(C) Cold-flow models employing several differing injection techniques for producing thin liquid fans were evaluated (prior to this program). One technique which was evaluated was the fan-impinging pattern. This pattern produced excellent liquid-fans which were very uniform in mass distribution and could be controlled directionally. Each injector element contained two sets of opposing doublets and a centrally located gas orifice. The doublets were employed to produce liquid fans whose flat side faced the central gas orifice or orifices. The liquid fans and the gas stream in turn impinged at a central common location. Comparison of impinging-fan injector cold-flow photographs with the triplet photographs showed that the impinging-fan design produced a higher degree of liquid atomization at significantly lower gas momentums than that of the triplet.

(C) Injector Design. The injector subassembly is shown in Fig. 8 and 9. Liquid fluorine enters the injector through two parallel inlets and is manifolded through the injector body to the injector face. The injector body and face were made of copper. Gaseous hydrogen enters the steel core through a single inlet; the other inlet shown is an instrumentation tap. The hydrogen manifold is formed by the gap between the core and the injector body.

(C) The injector basic triplet orifice pattern, which is an O-F-O arrangement, is shown in Fig. 10. Fourteen elements are staggered on the 1 x 3-inch face of the injector. The oxidizer orifices are arranged so that the resulting fans are canted to avoid impingement on the walls of the narrow chambers. The spray pattern of this injector is shown in Fig. 11, in which the fine atomization and uniform distribution characteristics of this injector pattern are indicated. An important parameter related to injector performance is the quantity $\dot{W}_O/\dot{W}_F V_F$ where $\dot{W}_O$ and $\dot{W}_F$ are the oxidizer and fuel flowrates, respectively, and V_F is the fuel injection velocity. A graph of C* efficiency vs this parameter will generally indicate a maximum value of efficiency; i.e., an optimum value for the parameter. The method

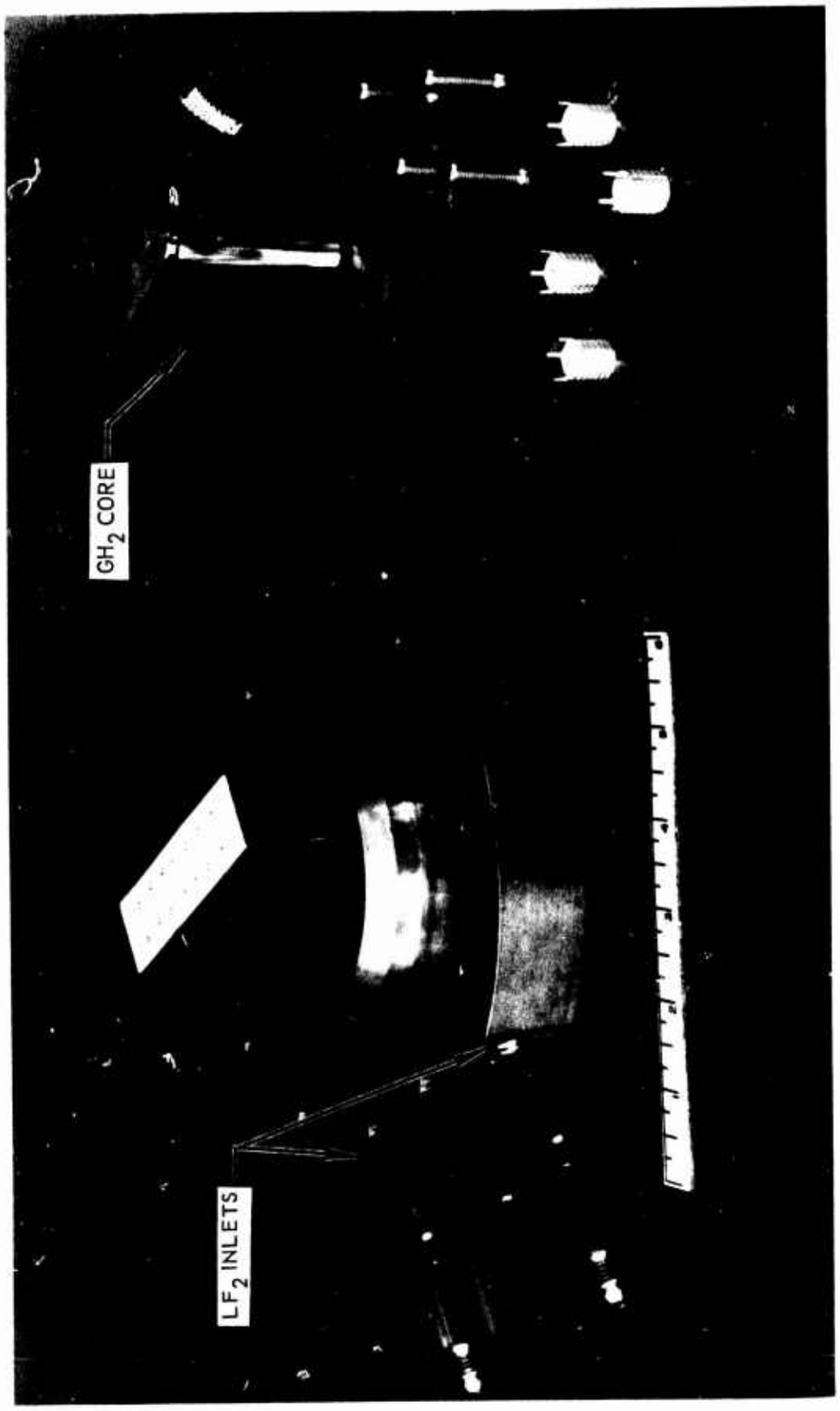

Figure 8. Bottom View of Injector

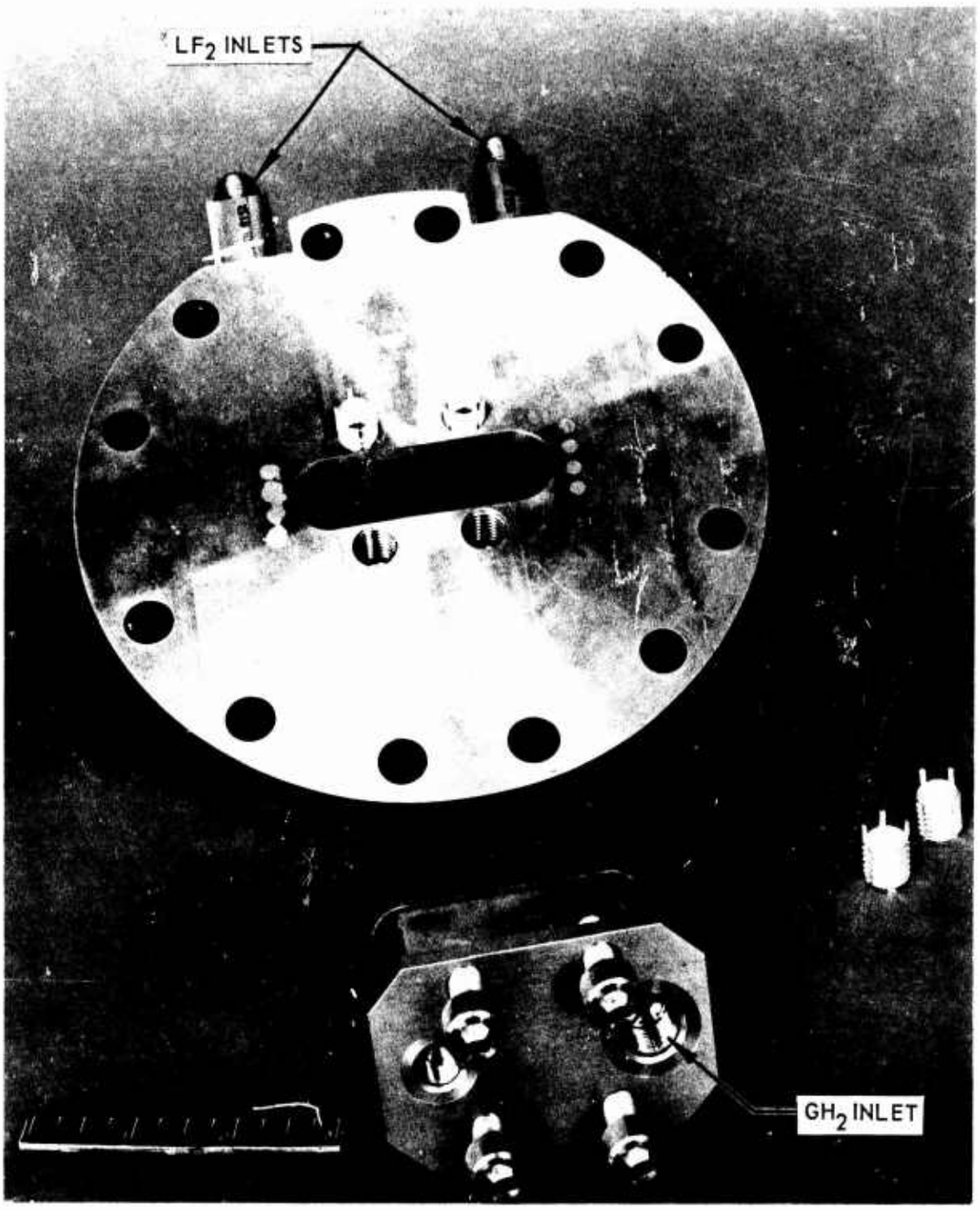

Figure 9. Top View of Injector

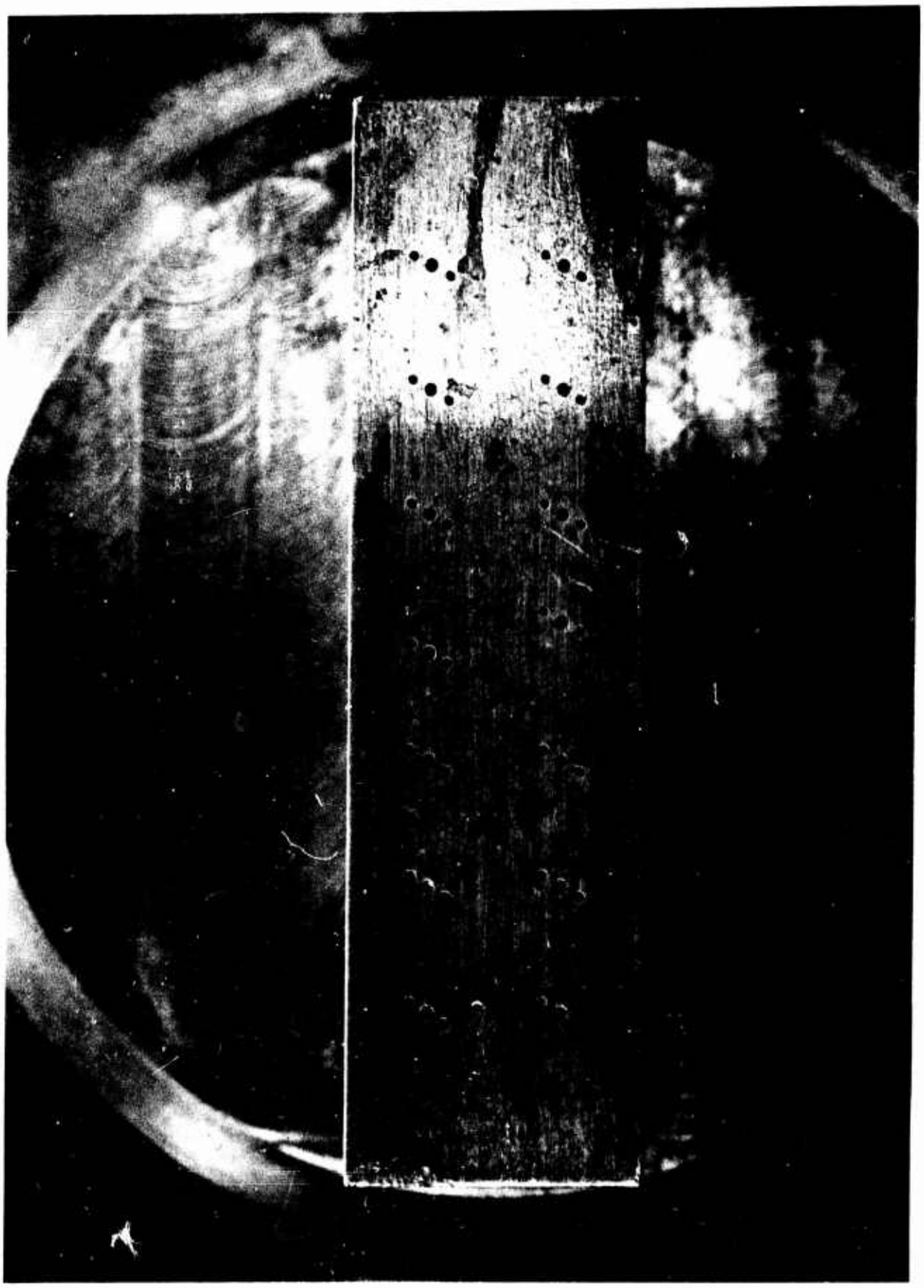

Figure 10. Two Row Triplet Injector

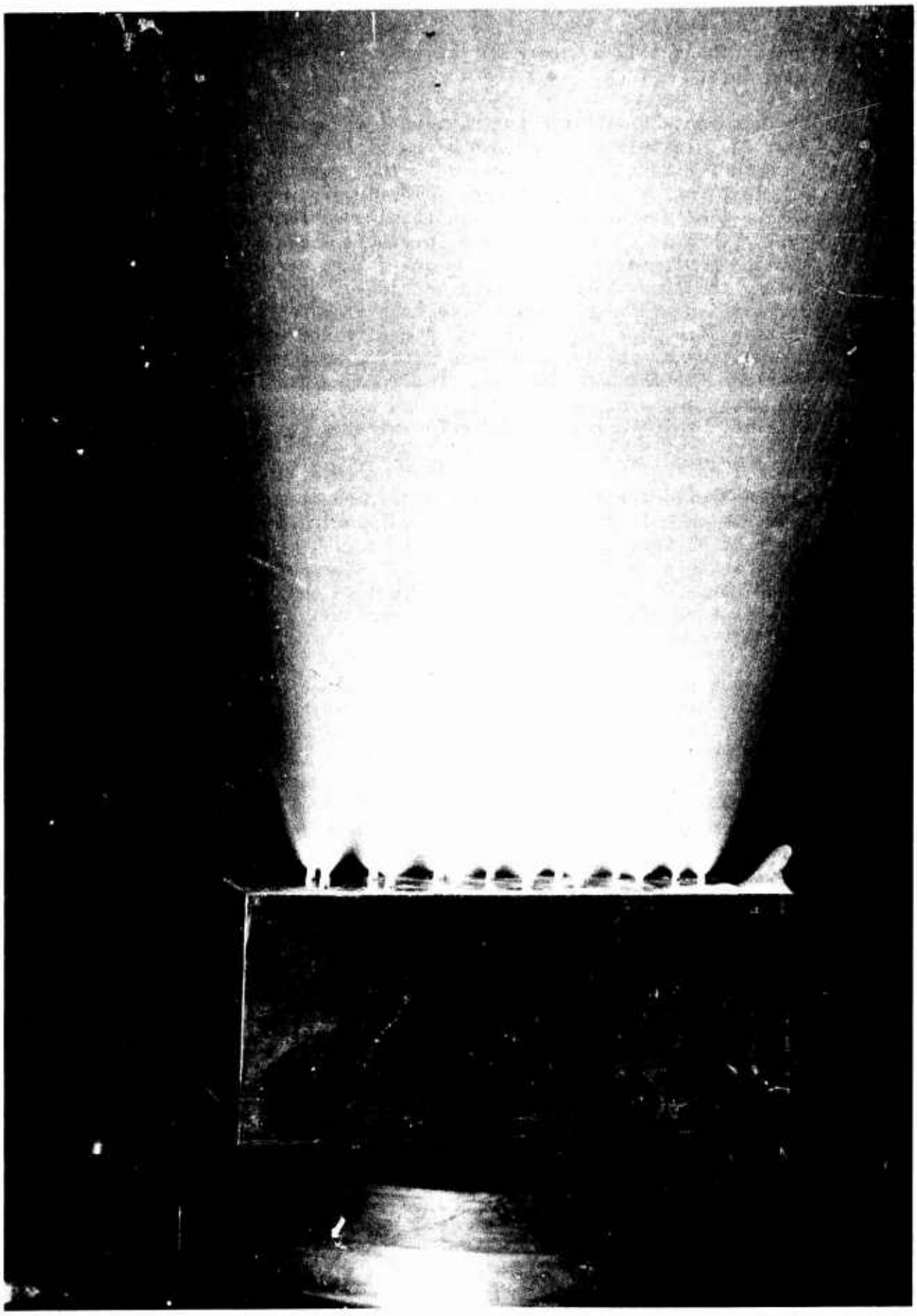

Figure 11. Spray Pattern - Two Row Triplet Injector

of varying the parameter in this program was to enlarge the size of the GH_2 orifices. The initial diameter of the orifices was 0.037 inch. The orifices were enlarged in two steps to 0.043 inch and then to 0.055 inch.

(C) The alternate basic injector pattern (impinging fan) is shown in Fig. 12. In this pattern, two pairs of LF_2 orifices each formed fans on either side of the GH_2 orifice. The result of this double impingment was that less hydrogen velocity was required to atomize the LF_2 to the same degree as in the triplet so that the injector operated well with a lower pressure drop through the GH_2 orifices. Also, since the LF_2 impingement over the GH_2 orifice occurred over a length (normal to the line through the LF_2 orifices), it was expected that better atomization and mixing could be obtained by replacing the single GH_2 orifice with 2 or more orifices of equivalent area. Single element evaluations of the impinging fan pattern were made using water to simulate the LF_2 and gaseous helium to simulate the GH_2. The resulting spray patterns indicated improved atomization, compared with the triplet, at low simulated GH_2 velocities.

(C) Several designs for basic impinging fan injectors were made. The design selected for its simplicity consisted of a single row of 10 elements on a flat face. Each element included a single GH_2 orifice. The face of this injector is shown in Fig. 13. The resulting water spray pattern is depicted in Fig. 14. Atomization was further enhanced when a gas was injected to simulate the hydrogen flow. The method of feeding the pattern was essentially the same as for the triplet injector.

(C) The above basic injector patterns were both of 1 inch width by 3 inch length. Additional variations of these basic patterns were designed and fabricated during the program period under company sponsorship. Two of these designs shown in Fig. 15, were the 14 element triplet and the 14 element impinging fan. Both of these designs were of 2" width and required special adapter rings for installation into the wider combustion chambers. In other design details, the two injectors were similar to the 1" width designs described above.

(U) Provision for Mixture Ratio Bias. An investigation of heat transfer rate control by biasing the mixture ratio of the injector such that the edges of the injector operated at a lower mixture ratio than the core was conducted. Two design concepts were devised to accomplish this: (1) modifying the nominal injector design; (2) modifying the injector-to-chamber adapter design.

(U) The modification of the injector was made so that the method of injection would most nearly simulate engine operation. One injector was successfully modified in accordance with this philosophy. However, since the initial injector design did not provide for this type of injection, the clearance between propellant manifolds were small. The primary features of this design are shown in Fig. 16. Gaseous hydrogen bias manifolds were drilled in the injector face parallel to the LF_2 manifolds. The GH_2 bias manifolds were connected

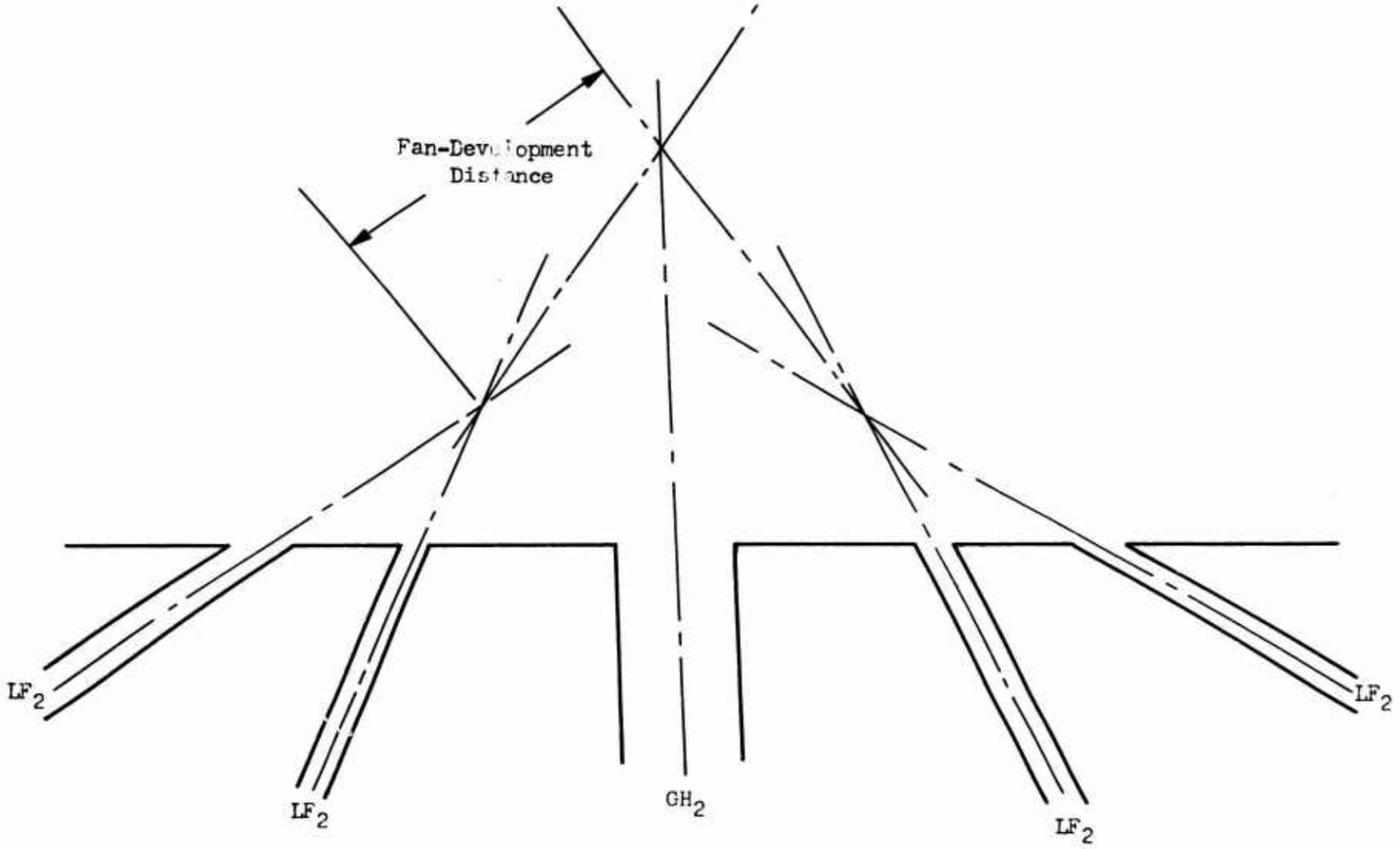

Figure 12. Impinging Fan Concept

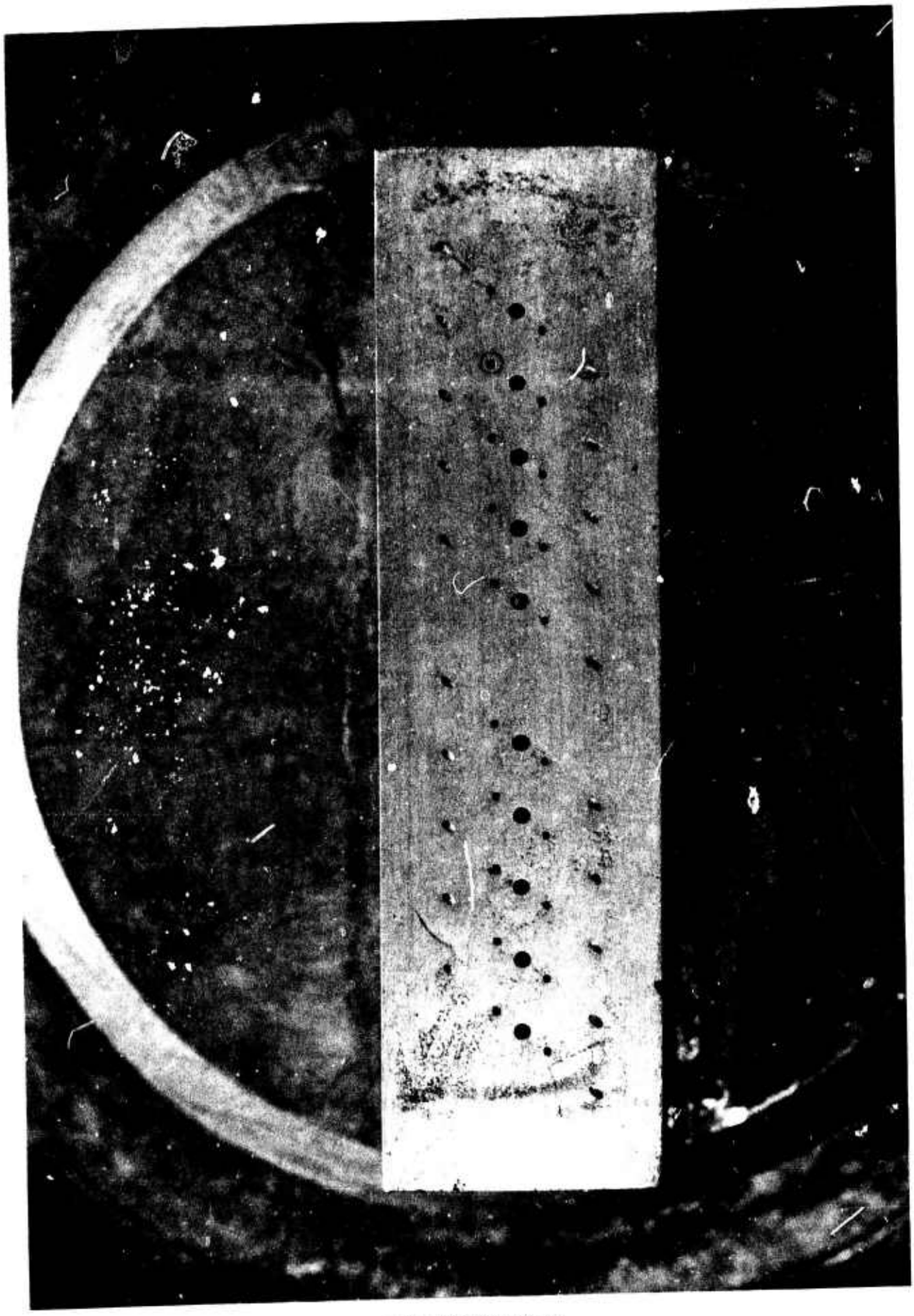

Figure 13. Single Row Impinging Fan Injector

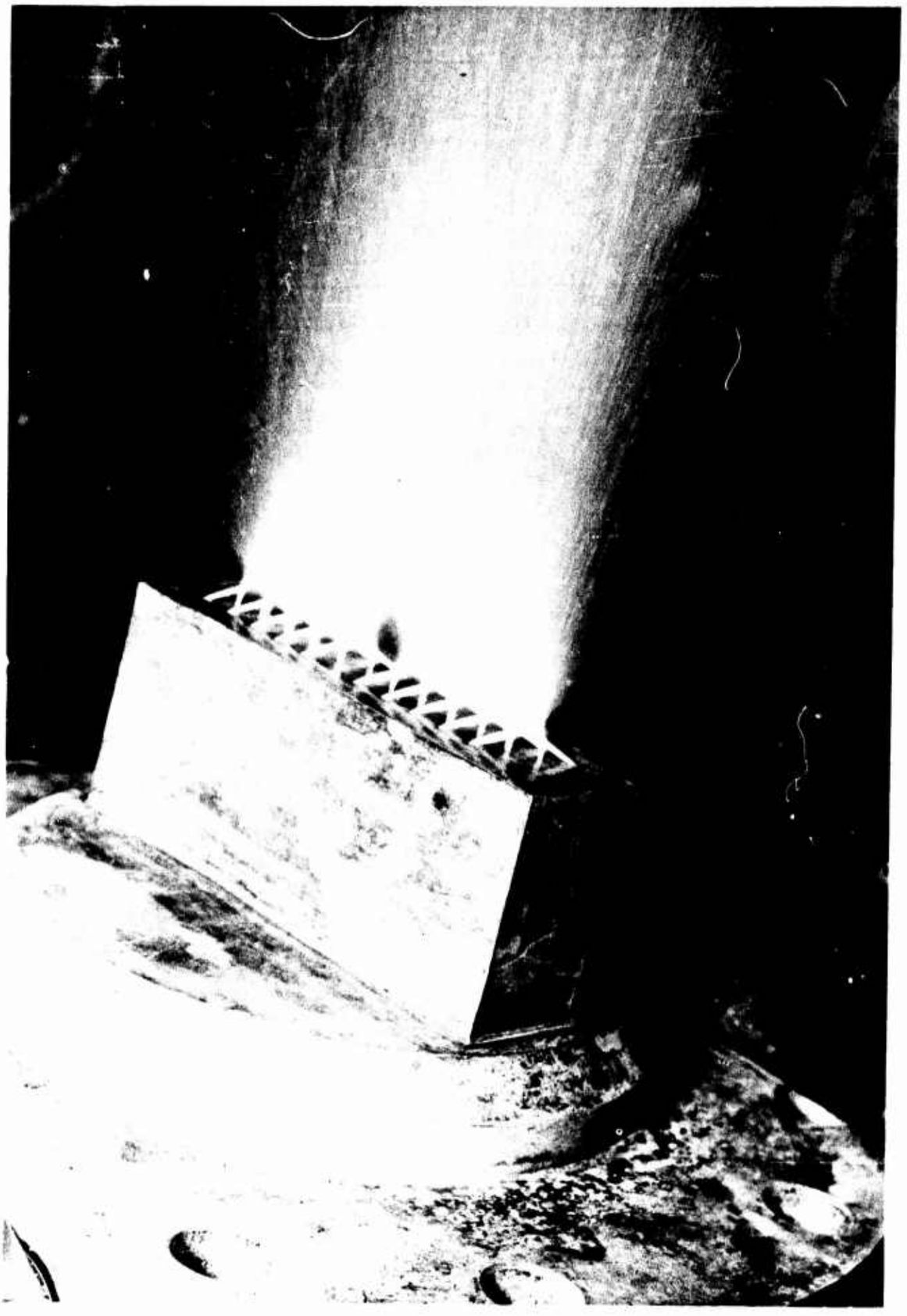

Figure 14 . Spray Pattern for Impinging Fan Injector

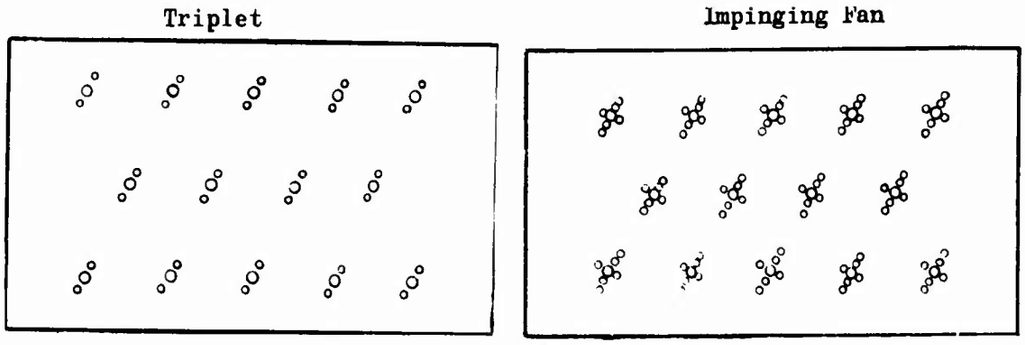

Figure 15. Injector Design Variations

to the primary GH_2 manifold by relatively large drilled passages. From the GH_2 bias manifolds, the hydrogen flowed through small axial-metering holes near the edge of the injector. Mixture ratio bias control was obtained by varying the number and size of the metering holes. Hole sizes were varied to provide bias flows to 12 to 30 percent of the total H_2 flow.

(U) The design shown in Fig. 17 provided for mixture ratio bias injection through the modified injector/chamber adapter. Advantage was taken of the fact that the adapter extended slightly into the combustion chamber. This extension was converted into GH_2 manifolds on both contour sides of the injector. Gaseous hydrogen entered the manifolds through external fittings on the adapter. The adapter flow was, therefore, independent of the injector flow which permitted considerable flexibility in the test program.

(C) Injector Provision for Hot Gas Tapoff. Engine fabrication and operation can be simplified by eliminating the conventional gas generator and using hot gases tapped from the combustion chamber as the turbine driving fluid. These gases may be tapped from the vicinity of the combustion chamber wall or from the injector. The construction of the injector was such that obtaining tapoff gases from this source appeared the most feasible. Thrust chamber gas tapoff was considered as an alternate, but this concept was not investigated because of the highly successful results obtained with the injector tapoff configuration.

(C) The purposes of the tapoff tests were to demonstrate (1) structural integrity of the injector while withdrawing hot gases through the injector face; (2) that combustion chamber performance was not strongly affected by this method of obtaining tapoff gas, and (3) that the tapoff gas properties were reasonably constant at all chamber pressures.

(C) In this configuration shown in Fig. 18, the combustion chamber hot gases were mixed with the GH_2 flowing through the annular gap between the tapoff tube and injector body. The combined gases then exited through the tapoff tube. The temperature of the tapoff gas depended

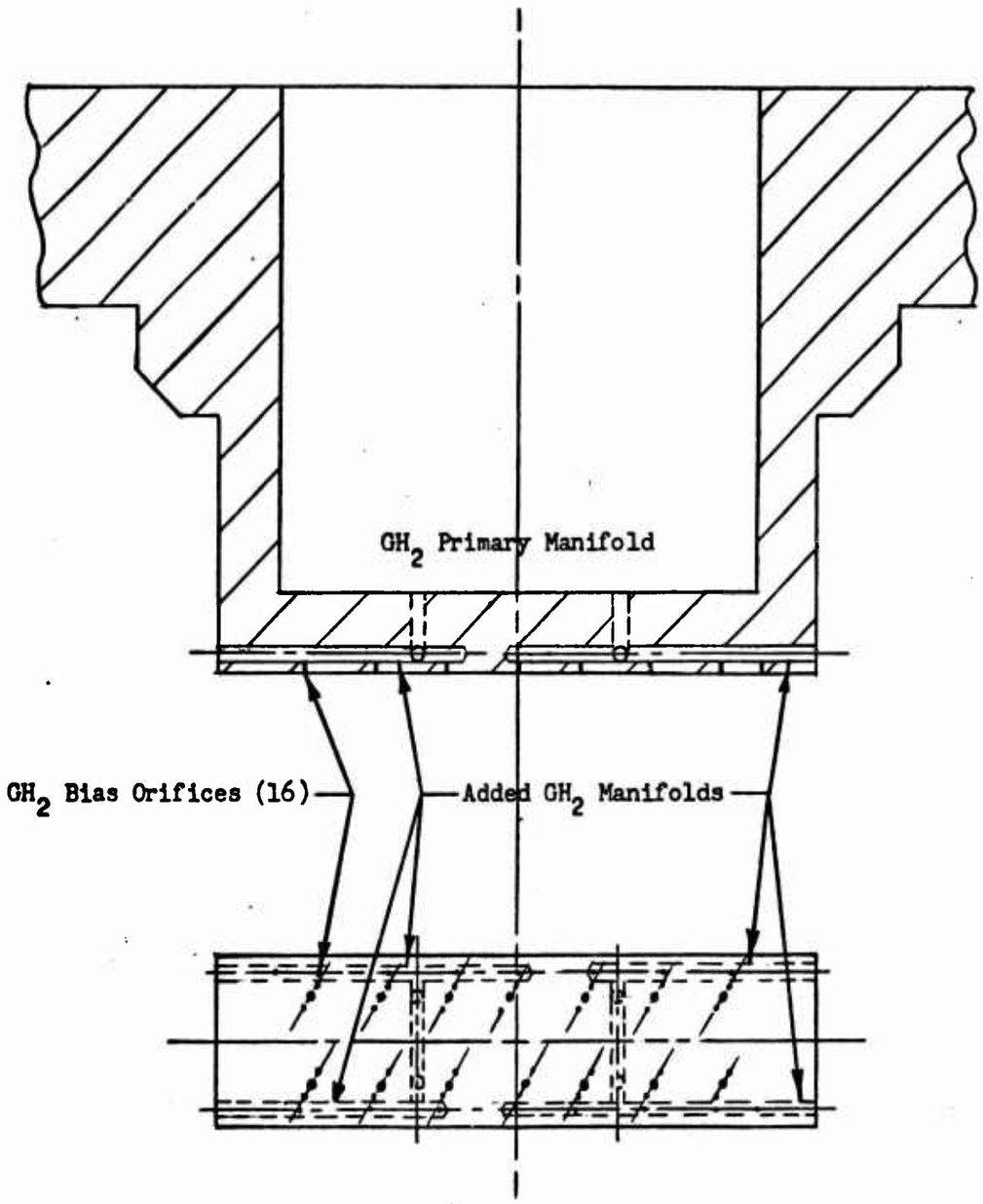

Figure 16 . Injector for Mixture Ratio Bias

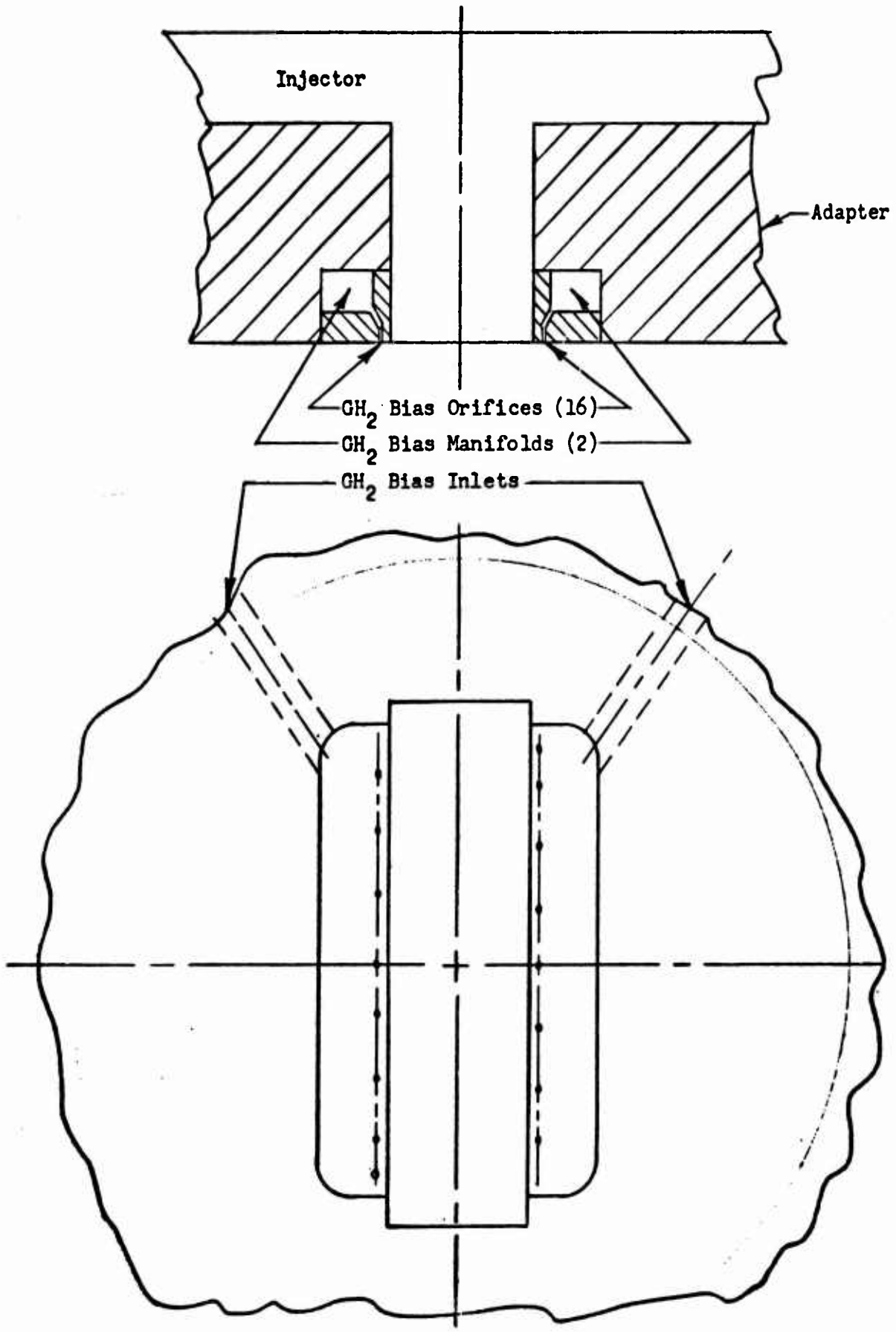

Figure 17. Adapter for Mixture Ratio Bias

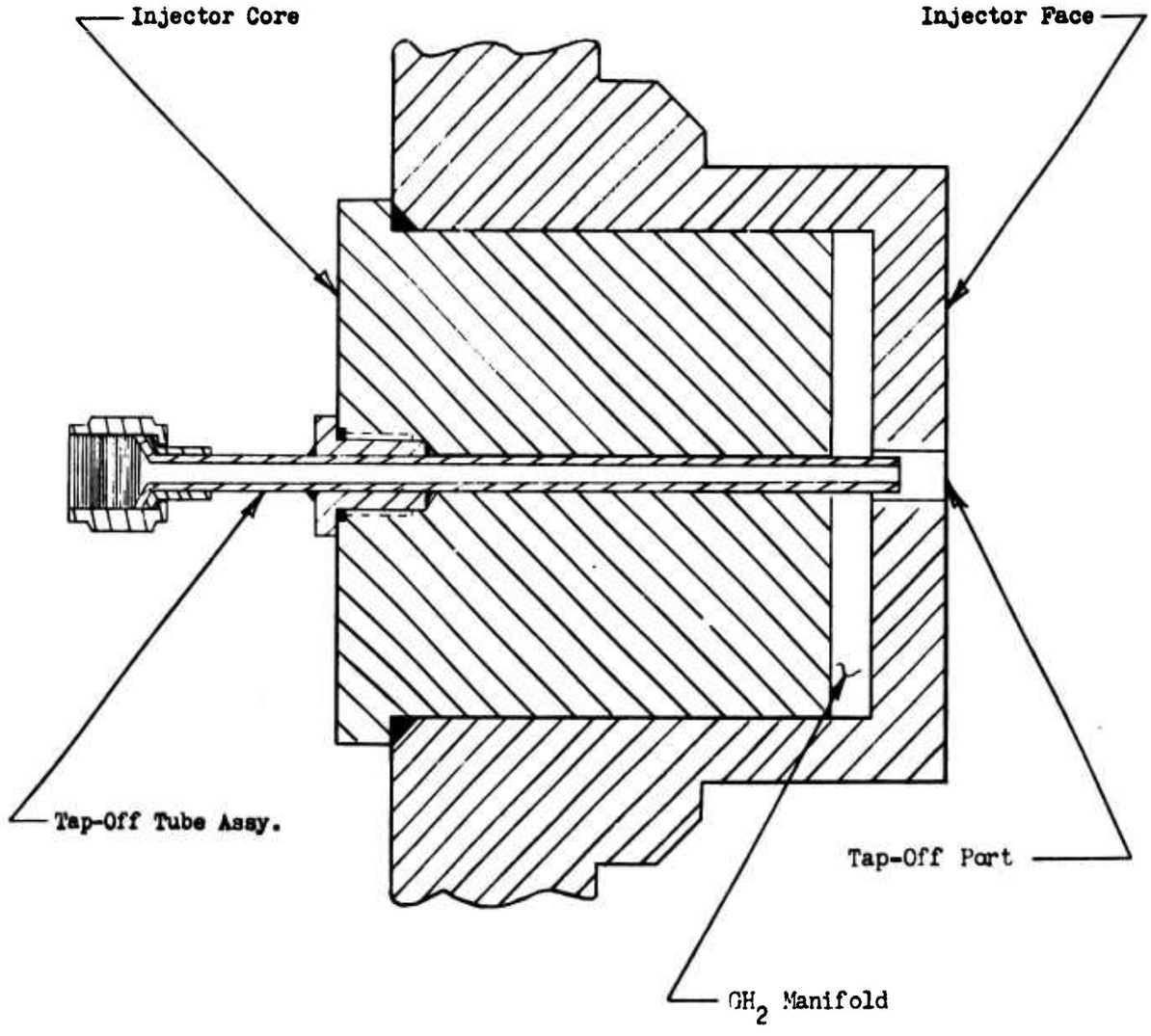

Figure 18. Injector Tapoff Configuration

upon the width of the annular gap and the position of the end of the tapoff tube with respect to the injector face. As the tapoff tube was retracted behind the injector face, a greater percentage of hydrogen from the manifold entered the tapoff tube and the tapoff gas mixture ratio and final temperature was reduced. Increasing the annular gas gap also resulted in more GH_2 entering the tapoff tube relative to the amount of combustion chamber gas entering. However, as the gap was increased, more hydrogen flowed into the combustion chamber through the gap, thus affecting the injector mixture ratio distribution and possibly affecting performance.

(U) This injector tapoff configuration resulted in substantially constant tapoff gas mixture ratio because the hydrogen manifold pressure was almost directly proportional to chamber pressure. The variation of tapoff gas temperature and molecular weight with mixture ratio is shown in Fig. 19.

(U) The results of the tapoff test series are discussed on page 70.

c. Combustor Body and Nozzle

(C) The effect of combustor body geometry on performance and heat transfer rates was evaluated in the solid-wall segment configuration. The high specific impulse of the F_2/H_2 propellant combination, together with the attendant high combustion temperature and gas specific heat product, results in high heat flux conditions imposed on the wall surface compared to propellants such as N_2O_4/N_2H_4 + UDMH: and O_2/RP-1. Control of boundary layer growth and alteration of combustion chamber size was required to achieve an optimum balance between coolant bulk temperature rise, reduced throat and nozzle peak heat flux, and performance.

(C) Five contours or geometries were selected for evaluation based on previous program results. These contours, shown on Fig. 21, had a common injector-to-throat distance of 3 1/2 inches, except for contour D which had a 5 inch distance. All utilized the 1 inch wide injector configurations. The chamber contour characteristics are summarized in Table 1.' All chambers were fabricated from solid copper material.

(U) The circular wall contour A chamber (shown in schematic cross section in Fig. 20) was divided into six axial heat transfer measurement regions. Of these locations, three (I through III) were considered as nozzle regions and three (IV through VI) as chamber regions. Each location in the nozzle consisted of a single independent coolant passage (0.201 inch diameter), whereas in the chamber, each location consisted of five passages (0.125 inch diameter) fed in parallel. The coolant passages were designed to receive the heat transferred from the curved wall side of the chamber; the end plates were cooled separately. This chamber configuration was available at the start of the program.

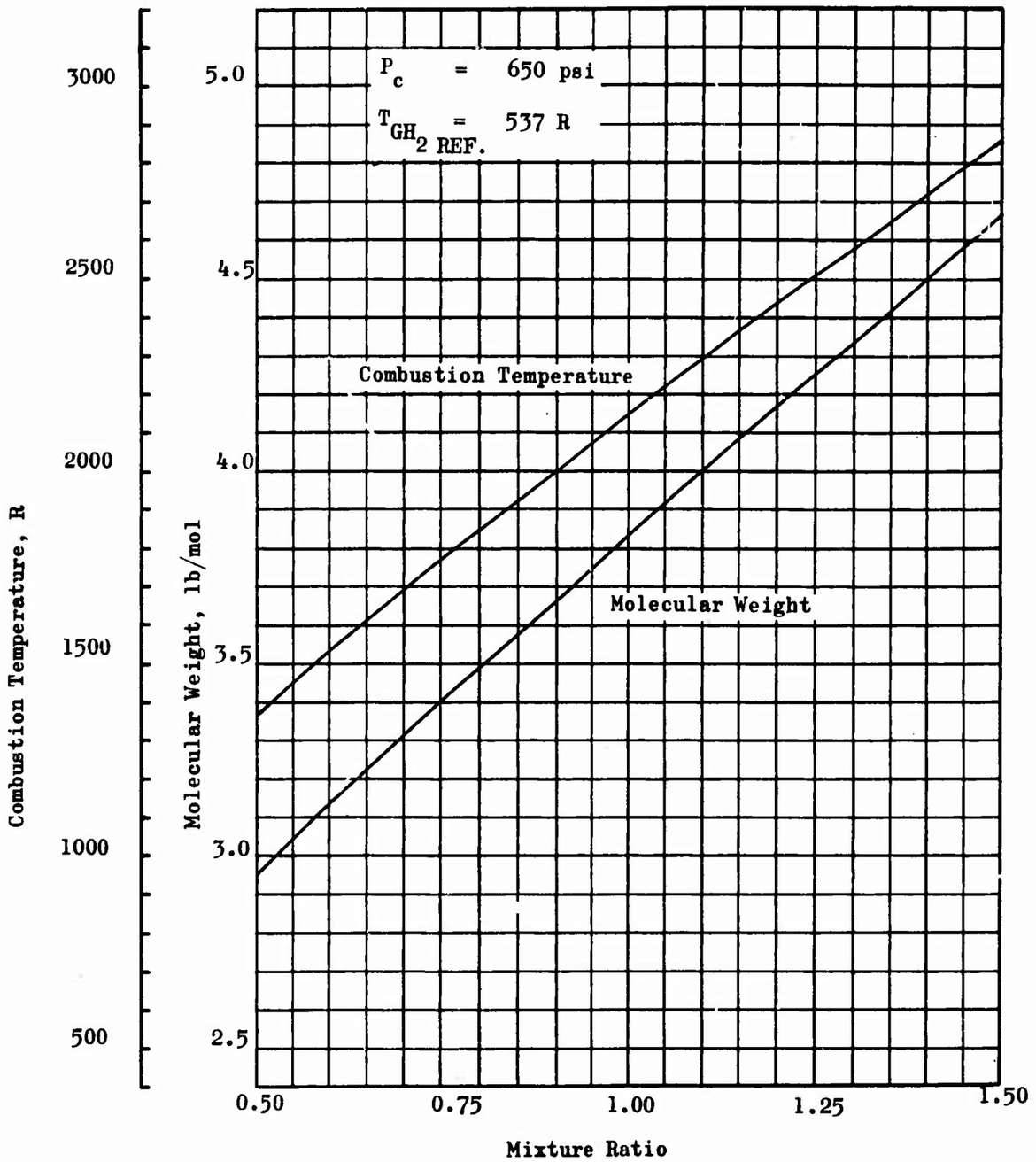

Figure 19. Predicted Molecular Weight and Combustion Temperature for LF_2/GH_2

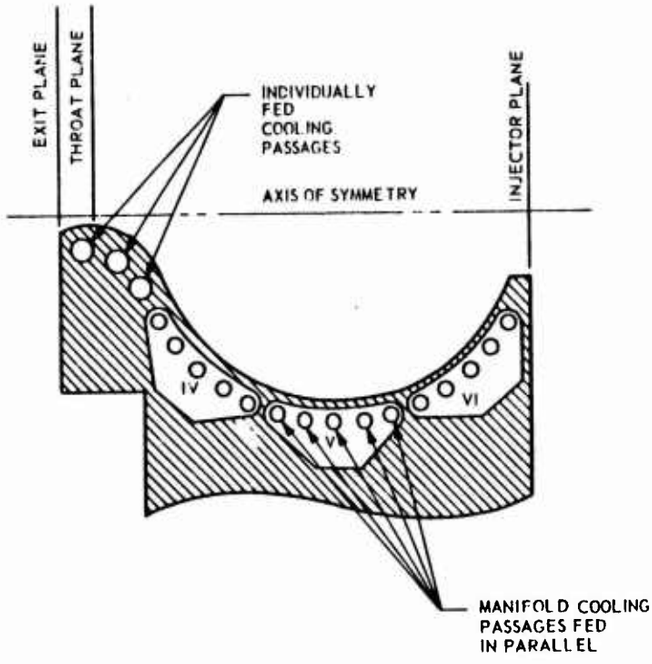

Figure 20. Chamber "A" Cross Section Showing Passage Geometry

(U) The contour B and C chambers, which were newly designed for this program, are shown in schematic cross section in Fig. 22. Each chamber, and nozzle was divided into 18 axial heat transfer measurement regions, as shown. Of these locations, 10 passages (1 through 10) were located in the chamber section. Each location consisted of a single water inlet passage which divided into two smaller passages to provide coolant along the contour and side walls of the chamber. The diameter of the coolant passages which extract heat from the chamber walls was 0.166 inch. Near the throat (passages 11 through 15), the diameter of the passages was reduced to 0.136 inch.

(C) The copper nozzle was designed to fit both the contour B and contour C combustion chambers. The nozzle entrance half-angle was 30 degrees and the exit half-angle was 15 degrees. The expansion area ratio was 4:1. A photo viewing the nozzle entrance is shown in Fig. 23.

(C) Contours D and E were designed to investigate the effects of nozzle length and convergence angle on performance and heat transfer rates. Contour E, as shown in Fig. 24, consisted of two sections to facilitate fabrication. The basic nozzle used with Contours B and C had a 30-degree entrance angle and a 15-degree divergence angle. Contour E was designed to accommodate the basic nozzle with the converging and diverging sides reversed.

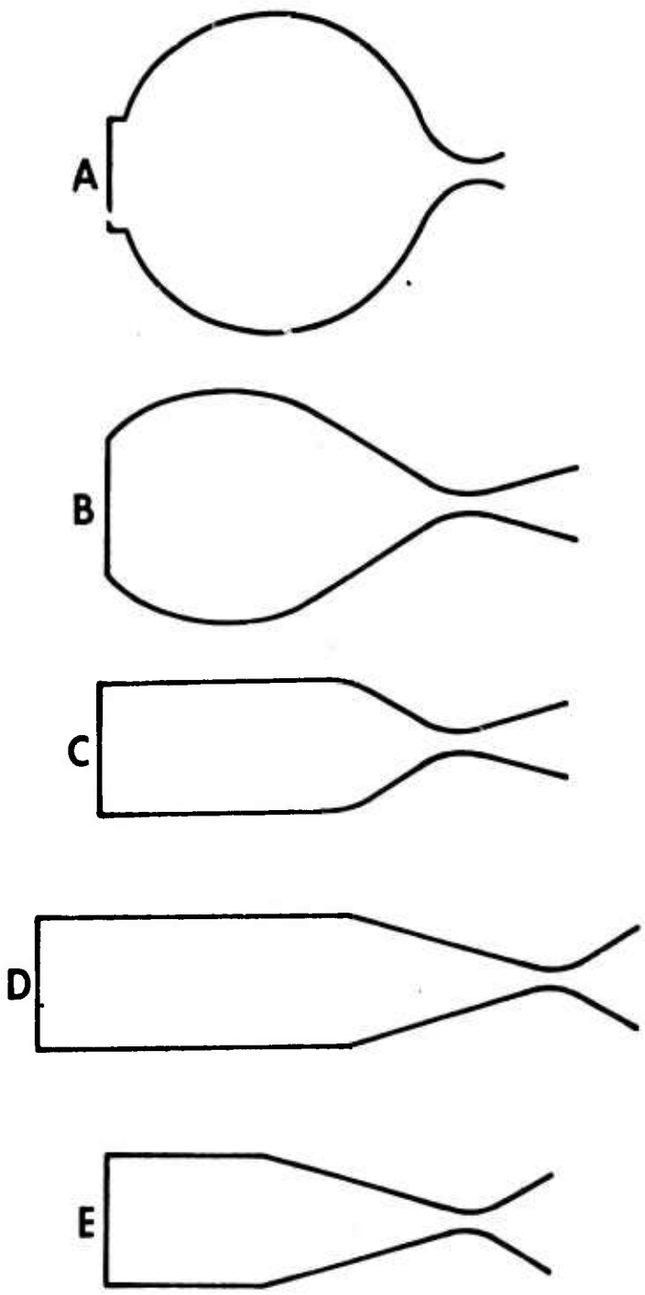

Figure 21. Solid-Wall-Segment Contours

TABLE 1

THRUST CHAMBER CONTOUR CHARACTERISTICS

Contour	Injector-Throat Distance, inches	Nominal Convergence Angle, degrees	Maximum Contraction Area Ratio	Expansion Nozzle Area Ratio	Contour Wall Shape
A	3.5	60	18		Circular
B	3.5	30	12	4	Curved
C	3.5	30	7	4	Straight
D	5.0	15	7	5.45	Straight
E	3.5	15	7	5.45	Straight

CONFIDENTIAL

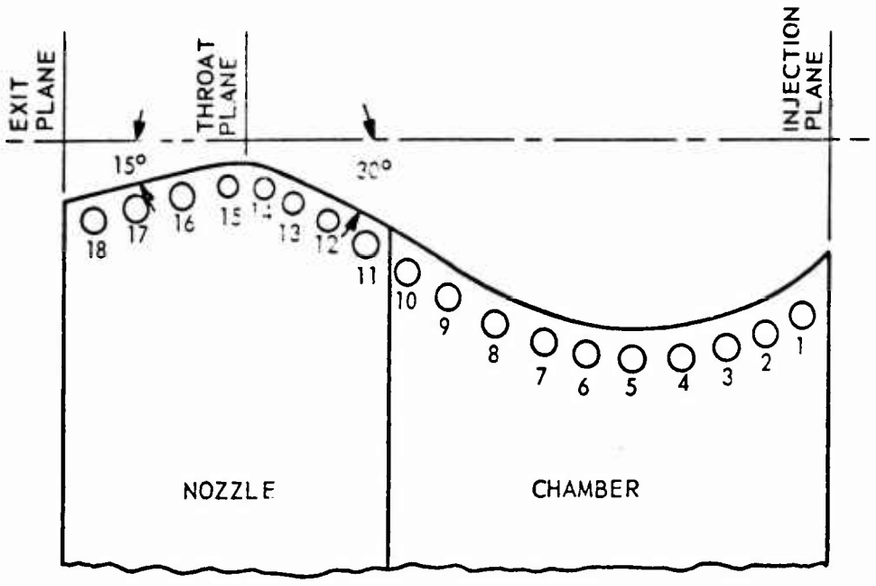

Figure 22a. 30-Degree Chamber and Nozzle Cross Section (Contour B)

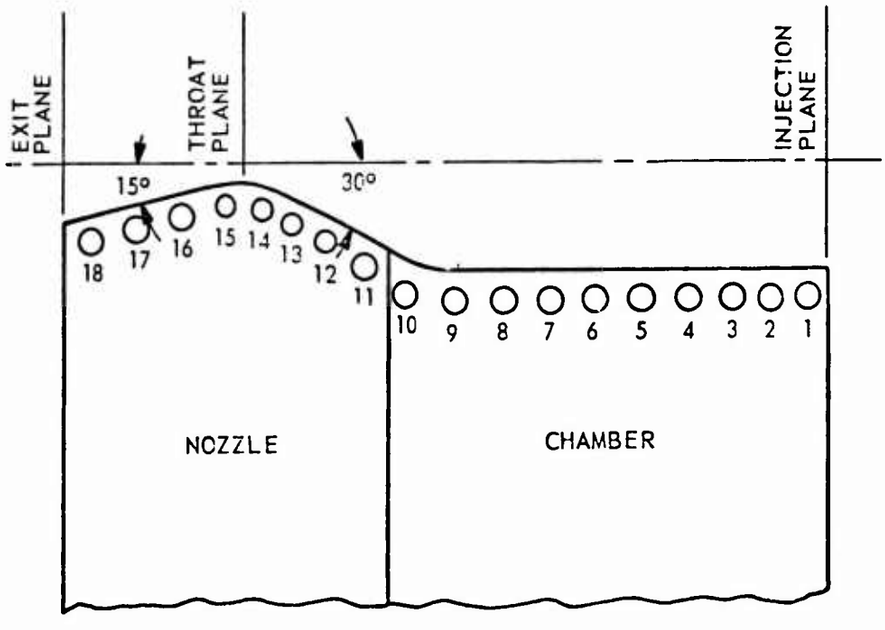

Figure 22b. Parallel-Wall Chamber and Nozzle Cross Section (Contour C)

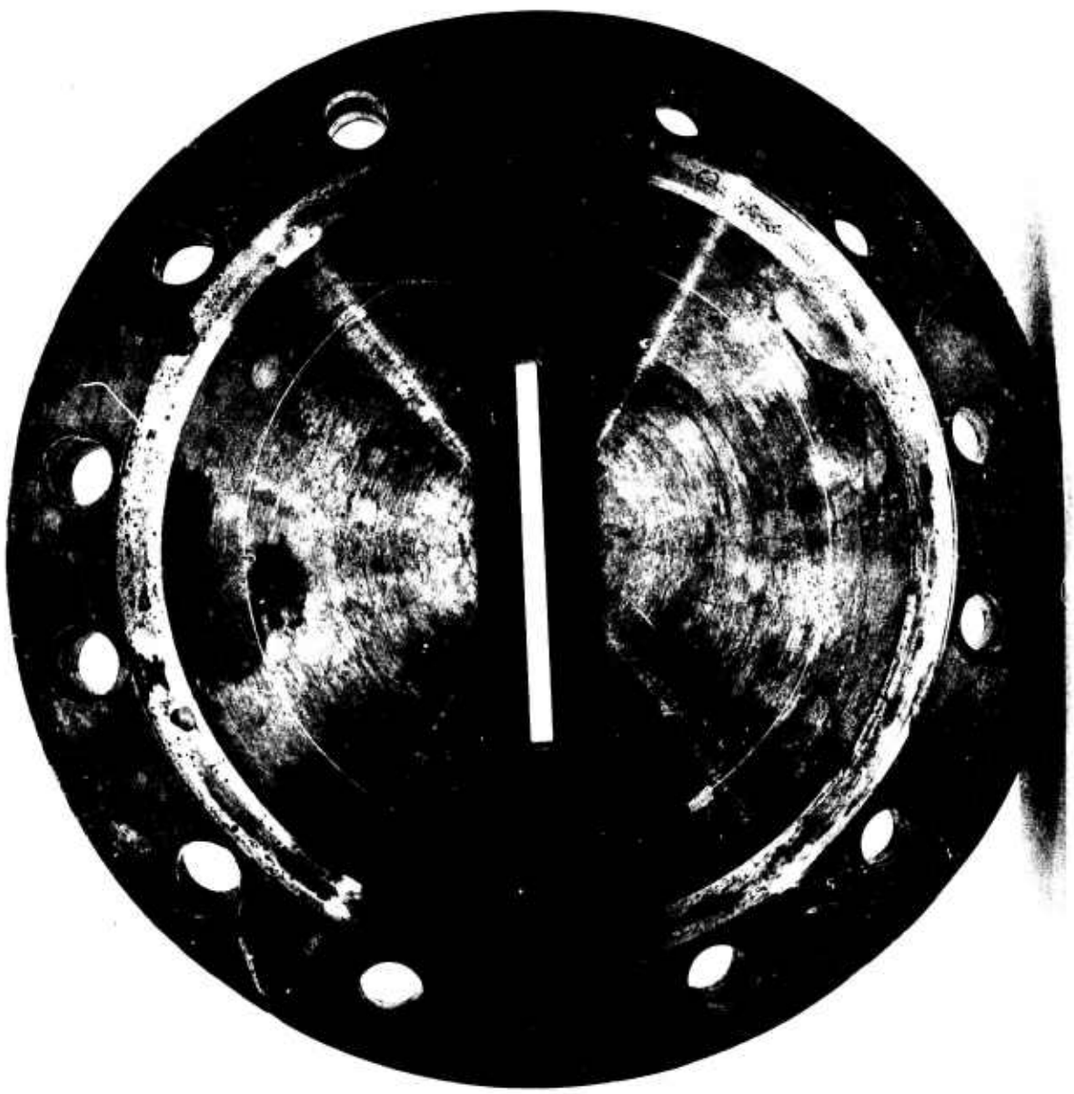

Figure 23. Solid Wall Segment Throat Section

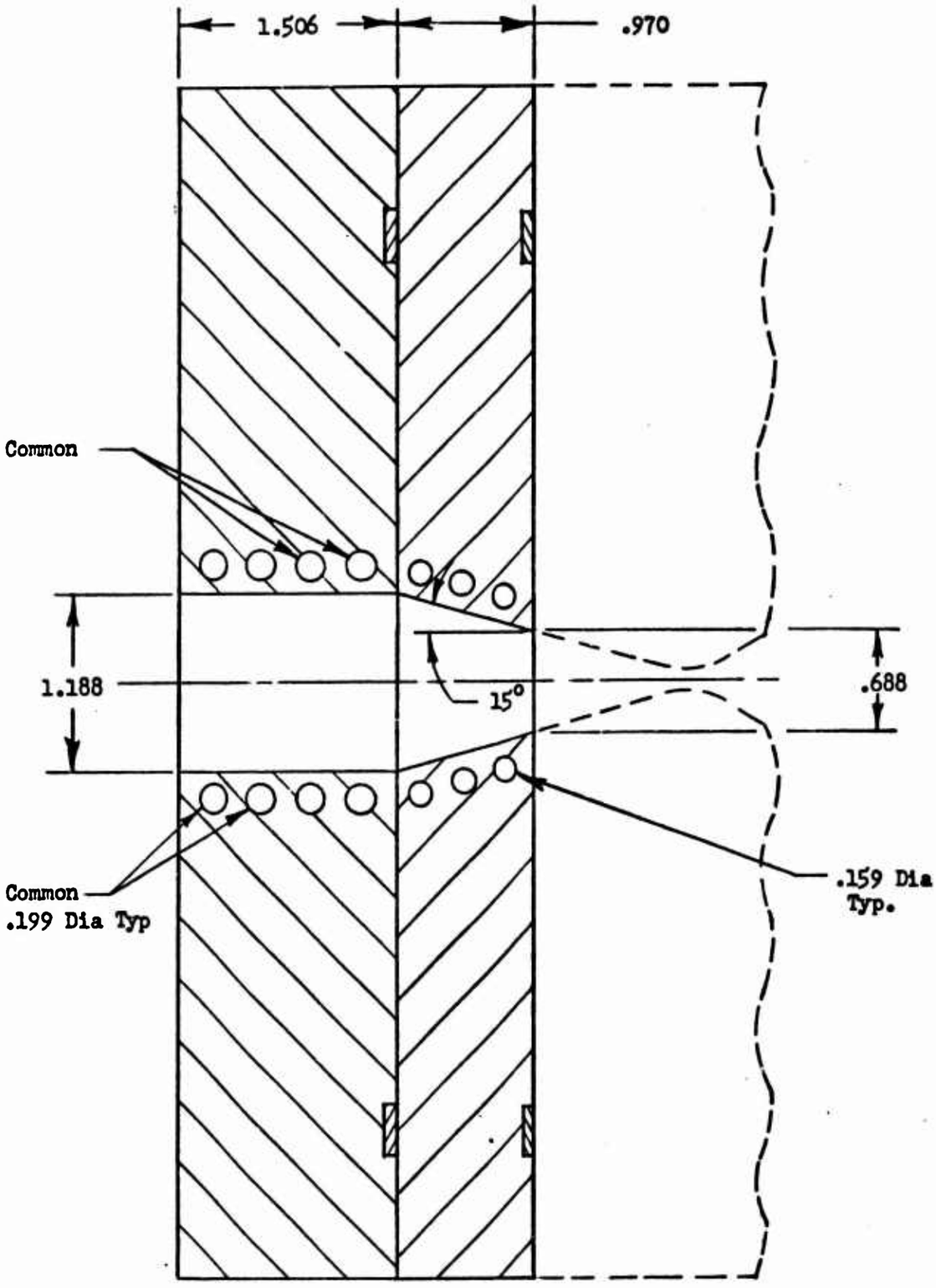

Figure 24. Water Cooled Contour E

(U) On the basis of the heat transfer data obtained with the Contour C chamber, it was determined that adequate cooling in the combustion chamber could be obtained with fewer water-coolant holes which were recessed further from the hot-gas chamber wall than in the contour C chamber. This design permitted simpler and more rapid fabrication techniques to be employed. Because of the increased water coolant hole spacing, it was possible to deep drill the holes and thus avoid the core-and-collar fabrication technique required for previous chambers. The chamber section (straight wall) had four water cooling passages which were individually supplied. Contour D differed from contour E only in length. Contour E was converted to contour D by adding another 1.5-inch long straight-walled section to the chamber.

(U) The copper surface of the nozzles generally experienced progressive roughening, particularly after the first few tests. To determine whether the nozzle surface material or roughness influences the heat transfer rates, nozzles were plated with 0.3 mils of chromium and 1.0 mils of nickel. The results of the tests are discussed in Section II, 7.f.

(C) In addition to the combustion chamber contours described above, two additional geometries were designed under company sponsorship to further evaluate the effects of chamber convergence angles. These contours, shown on Fig. 25, each had a 3 1/2 inch distance from injector to throat. Contour F utilized the 1-inch injector configurations and has a continuous 6 degree convergence from injector to the nozzle approach section which had a 15 degree convergence. Contour G utilized the 2 in. wide injector configurations and had a continuous 15-degree convergence from the injector to the throat. Both contours utilized the same nozzle configuration which had been previously designed for contours B through E. Wall coolant passage design was the same as for contour E described above.

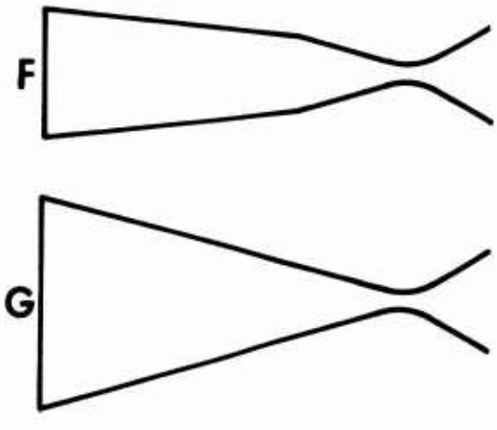

Figure 25. Additional Chamber Contours

3. SOLID WALL SEGMENT DESIGN ANALYSIS

(U) Heat transfer and performance analyses were conducted for the solid-wall segment model. These analyses were accomplished to ensure compatibility of the model with the thermal environment and to provide the theoretical data required for the reduction and analysis of the test data.

a. Thermal Analysis

(U) Injector Face. The heat transfer analysis of an injector can be divided into several broad primary categories: (1) heat load imposed by the combustion process, (2) cooling capabilities of the propellants, (3) the physical and thermal characteristics of the injector material, and (4) geometry considerations. This separation is primarily for convenience of discussion since the various aspects of the problem are actually closely interrelated. The last three items can be grouped under the general heading of injector-cooling capability.

(U) The determination of the local heat flux at the injector face is the most difficult portion of an injector heat transfer analysis. The difficulty arises in attempting to predict both the flow field near the injector face and the properties of the recirculating gases since these factors are greatly affected by the injector orifice geometry. Although analytical prediction of the heat load to the injector is not yet possible, there are existing experimental data for use in estimating reasonable values. Hot-firing experience at Rocketdyne tends to indicate that the injector heat fluxes are approximately equal to the local chamber wall values.

(C) Using the aforementioned criterion combined with the thrust chamber heat transfer analyses, an injector face heat flux of about 2 to 4 Btu/in.^{2}-sec at 650-psia chamber pressure was estimated. A nominal value of 3 Btu/in.^{2}-sec was utilized in the subsequent analysis. If it is further assumed that the average injector heat flux level equals the local chamber wall value throughout the throttling range, a heat flux of about 0.5 Btu/in.^{2}-sec at 70-psia chamber pressure (9:1 throttling) will result.

(U) Previous copper-faced injectors tested to date have shown endurance over the range of required thrust chamber conditions using ambient temperature gaseous hydrogen ($\sim$ 60 F) and liquid fluorine. The only question remaining was whether sufficient cooling could be achieved using heated hydrogen such as would occur during regenerative operation with the tube wall segments of Task III.

(U) An analysis was conducted using a digital computer program to ascertain material temperature profiles in the region of the hydrogen orifices. A single orifice was elected for study, and the convective cooling capability of the hydrogen in the orifice was calculated from the relation (Ref. 1):

$$N_{Nu} = 0.024\, N_{Re}^{0.8}\, N_{Pr}^{0.4} \left(\frac{T_B}{T_W}\right)^{0.55} \varphi_E$$

where

N_{Nu} = Nusselt Number
N_{Re} = Reynolds Number
N_{Pr} = Prandtl Number
T_B = Hydrogen bulk temperature
T_W = Orifice wall temperature
φ_E = Entrance correction factor

$$\varphi_E = 1.8 \left(\frac{L}{D}\right)^{-0.15} \quad \text{for } \frac{L}{D} < 27$$

(U) This latter factor is important for the small L/D values encountered in injector orifices.

(C) The results of the analysis for full-thrust conditions indicated that the maximum face temperature was about 1100 F, which was well below the melting point of copper ($\sim$ 1980 F).

(U) The hydrogen temperature, as it enters the injector, may increase as throttling occurs so that the injector face will tend to operate at a higher temperature than the full-thrust case. A preliminary analysis indicated that the maximum face temperature under these conditions could be marginal; however, previous test results to date at these conditions have not indicated any overheating.

(U) Combustion Chamber and Nozzle. There were three primary thermal considerations in the design of the water-cooled copper chambers and nozzles: (1) to ensure that adequate water velocity was obtained to prevent wall burnout; (2) the coolant passages must be close enough to the combustion surface to prevent large temperature differentials and excessive wall surface temperatures, and (3) the water bulk temperature rise must be sufficiently high to ensure accuracy in the temperature rise measurements. The above three criteria were utilized in the design under previous test programs. The present solid-wall segment designs are capable of handling a throat heat flux of 56 Btu/in.^{2}-sec based on copper-wall temperature limitations. The nozzle and combustion zone can handle about 44 Btu/in.^{2}-sec because of the slightly larger spacing between holes and the combustion surface.

(U) A detailed heat transfer analysis was also conducted to determine the temperature distribution in the throat region of the water-cooled segments. The temperature distributions were determined for a range of gas-side film coefficients and were used in obtaining the change

(U) in the throat area from thermal conditions during firing. This area change is used in the data analysis and its determination is presented in detail in Appendix A.

b. Performance Analysis

(U) Analyses were conducted to determine the throat discharge coefficient and the nozzle thrust coefficient for the solid-wall segment. These quantities were used to obtain experimental values of c* from measured chamber pressure, thrust, and flow rate. Chemical reaction kinetics and boundary-layer theoretical results were combined with the potential flow analysis for the nozzle.

(C) The flow field for the segment nozzle was first computed to obtain the potential flow discharge coefficient and inviscid thrust coefficient for equilibrium flow of fluorine/hydrogen combustion products with the design mixture ratio and a chamber pressure of 650 psia. A transonic solution was first generated.

(C) The supersonic flow field was computed using the right characteristic from the throat flow solution as a starting line for a plane flow method of characteristics solution using a digital computer program. The flow field was computed using a variable properties solution for equilibrium flow of F_2/H_2 (nozzle mixture ratio = 14 and Pc = 650 psia). The nozzle was a plane flow, 15 degree, straight-wall nozzle with an area ratio of 4. (The 30 degree nozzle was also subsequently analyzed). The impulse function across the input line and wall pressures were integrated to obtain the nozzle thrust coefficient based on geometric throat area. Flow properties along the nozzle wall were computed for calculation of viscous wall drag and boundary layer displacement thickness.

(C) The following is a summary of the results of the inviscid performance calculations (for the 15 degree nozzle).

Ideal thrust coefficient (C_F ideal)	1.616
Computed thrust coefficient (C_F computed)	1.596
Geometric efficiency ($\eta C_F = \frac{C_{F_{\text{computed}}}}{C_{F_{\text{ideal}}}}$)	0.988
Potential discharge coefficient, C_w, $\frac{\text{computed mass flow}}{\text{ideal mass flow}}$	0.997

(C) Application of the boundary layer equations was made to predict the skin friction drag, the boundary layer thickness at the throat, and nozzle discharge coefficient in the plane-flow models. The boundary layer approach utilized the integral momentum and energy equations to form an analytical model. The considerations included the incorporation of a pressure gradient term in the momentum equation, a nonadiabatic wall condition, compressible flow conditions, and a variable boundary layer velocity profile. The handling of the

integral energy and momentum forms was accomplished with a finite difference solution. This approach has been formulated into an IBM digital computer pro[illegible]

(C) Experimental discharge coefficients (Ref. 2) are illustrated in Fig. 26 as a function of the nondimensional quantity, $L/D\ [A_5(A_4-A_5)]$. If it is assumed that the experimental discharge coefficients are also valid for plane-flow models where the end affects are negligible and that the axisymmetric "B" term can be replaced by the throat gap for a plane-flow case, the solid-wall segments discharge coefficients can be compared to the predicted experimental values. For the parallel-wall (contour C) chamber, the $L/D\ [A_5/(A_4-A_5)] = 1.2$; thus, the corresponding experimental discharge coefficient is 0.998. The theoretical value is also approximately 0.998 at a chamber pressure of 650 psia.

(U) The frictional drag along the chamber and nozzle walls can be related to a thrust coefficient decrement as follows:

$$\Delta C_{F_{B.L.}} = \frac{F_D}{P_c A_t}$$

where

ΔC_F = decrement of thrust coefficient

F_D = frictional drag, pounds

P_c = chamber pressure, psia

A_t = geometric throat area, $in.^2$

(U) The frictional thrust coefficient efficiency is defined as:

$$\eta_{C_{F_{(Drag)}}} = \frac{\Delta C_{F_{B.L.}}}{C_{Fi}}$$

where

C_{Fi} = ideal thrust coefficient based on chemical equilibrium composition

(C) The thrust coefficient efficiency based on frictional considerations $\left(\eta_{C_{F_{(Drag)}}}\right)$ for the nominal (650 psia) chamber pressure was 98.1 percent.

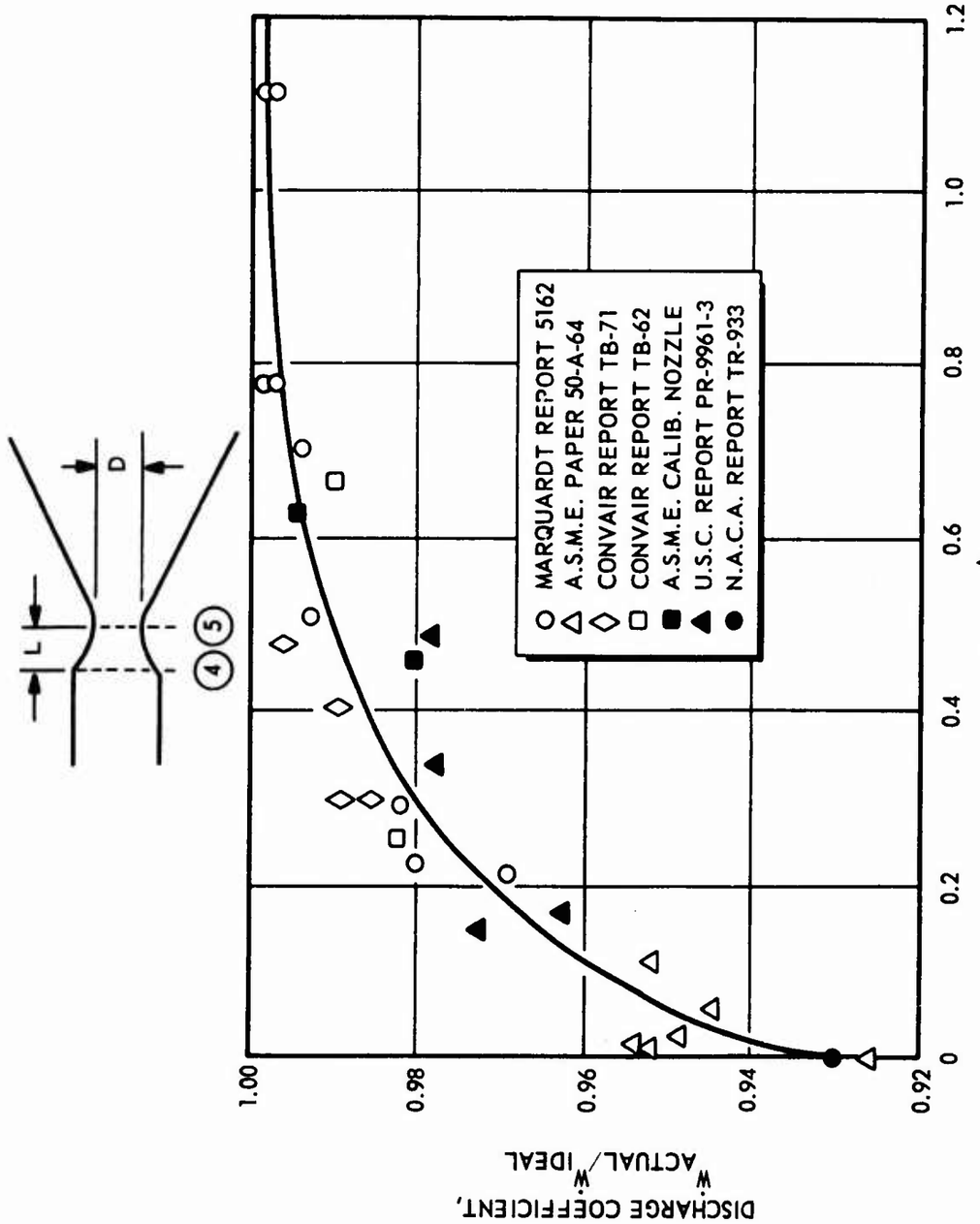

Figure 26. Experimental Throat Discharge Coefficients

(U) Finally, an analysis of the solid-wall test segment was made to determine the performance loss due to a lack of chemical equilibrium in the nozzle flow field. The approximated reaction kinetic (ARK) technique was used to determine the performance losses. For this analysis, the gases were assumed to remain in complete chemical equilibrium until the expansion rate becomes too great for the maintenance of chemical equilibrium and "freezing" occurs. After freezing occurs, the composition was assumed to remain fixed throughout the rest of the nozzle. The freezing point was determined using the Bray freezing criterion. In using the Bray criterion, the expansion rate at each point in the nozzle was compared with the expansion rate required to maintain chemical equilibrium.

(U) To determine the expansion rate at each point in the nozzle, the results of the method of characteristics solution of the flow field was used to break the flow field up into streamtubes. A computer program was used to conduct an ARK analysis on each of these streamtubes, determine the freezing point, and then determine the final exit conditions for each streamtube. An integration across the exit area of the momentum and pressure of each streamtube was then performed to determine the performance of the nozzle.

(C) The results of the two-dimensional analysis indicate kinetic efficiencies ranging from 100 percent at full thrust to 94 percent for fully throttled operation. The expansion rate results in a significant performance loss at low chamber pressures, even though the final area ratio is only 4.0. At higher chamber pressures the freezing area ratio approaches the final area ratio of 4.0 and the losses become insignificant. In a nozzle designed for high performance, the kinetic loss can be reduced significantly by proper design of the initial diverging section of the nozzle. This was not attempted for the test nozzle.

(C) Similar analyses to the above were conducted on the plane flow, 30 degree, straight-wall nozzle with an area ratio of 5.45. The discharge coefficient, drag efficiency, and geometric efficiency are shown for the range of chamber pressures in Fig. 27. The kinetic efficiencies ranged from .995 at 650 psia chamber pressure to .962 at 70 psia chamber pressure.

(U) A detailed stress analysis was conducted to determine the effects of thermal and pressure induced forces on the throat gap during segment operation. The analysis is described in Appendix A. The conclusions drawn from the analysis were: 1) the throat gap deflections resulting from pressure forces and from thermal growth of the entire nozzle block were negligible, 2) significant throat gap variations do result from the steep thermal gradients at the nozzle surface as shown in Fig. 28.

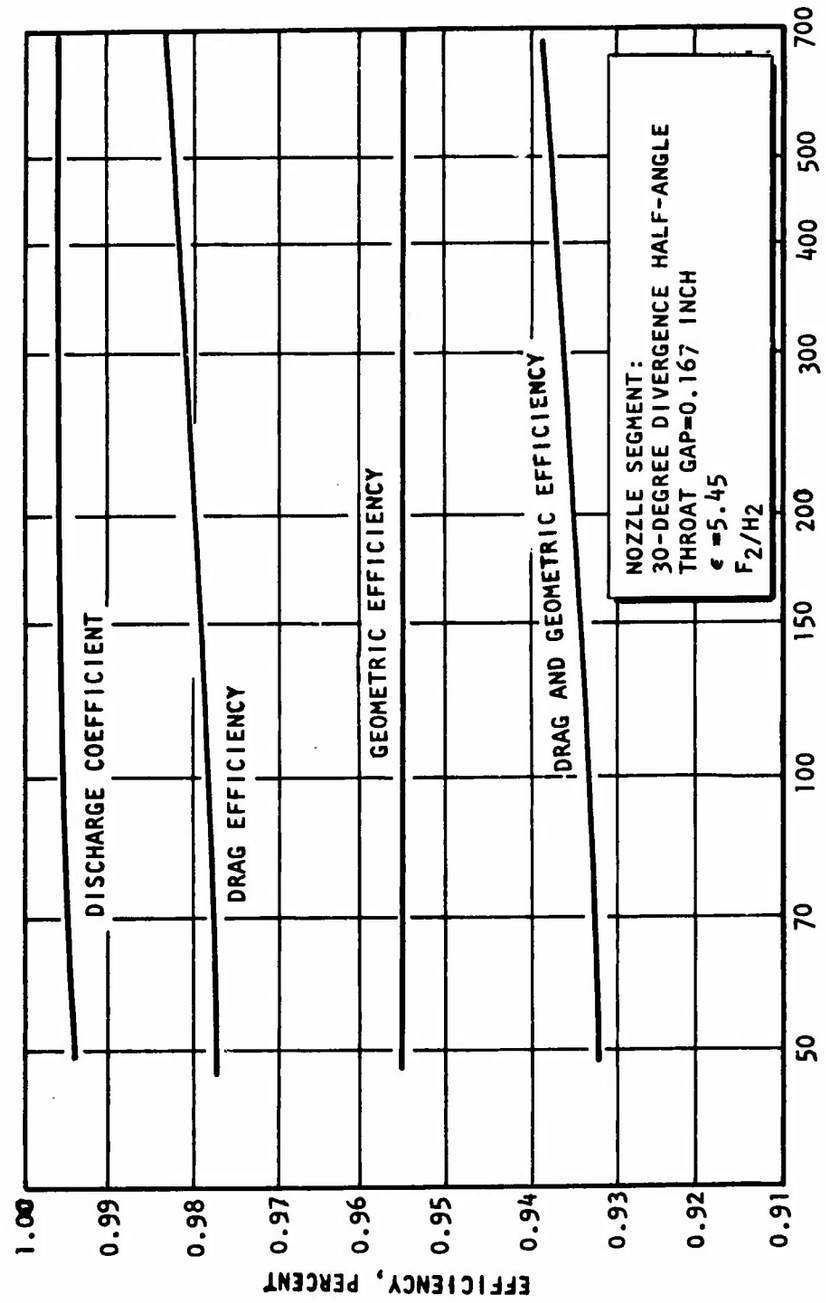

Figure 27. Calculated Nozzle Efficiencies

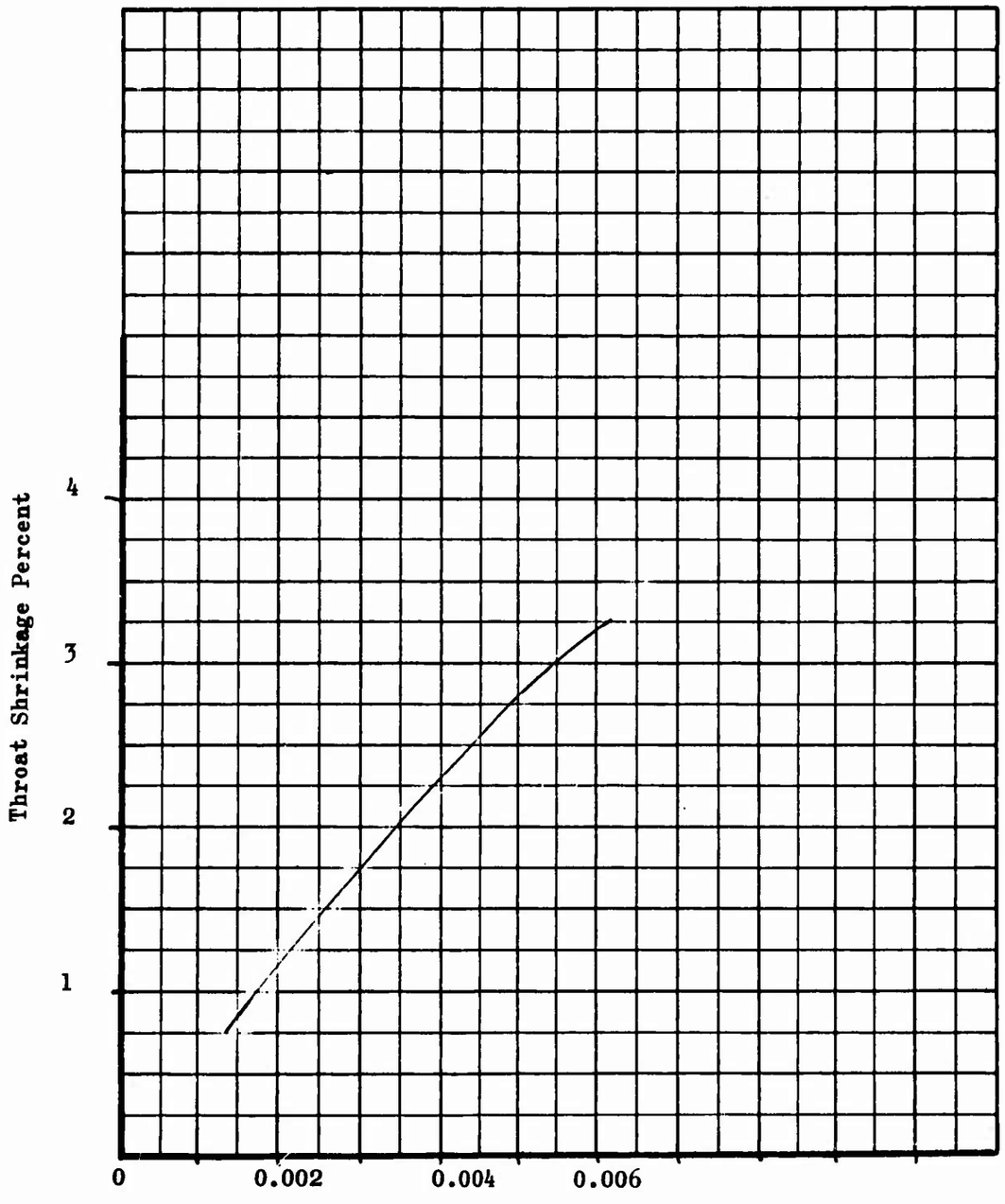

Figure 28. Throat Shrinkage Resulting from Thermal Loads

4. EXPERIMENTAL PROCEDURES

a. Test Stand Description

(U) Experimental firings were conducted on test stand Victor in the Propulsion Research Area fluorine facility. A schematic flow diagram is shown in Fig. 29. Liquid fluorine was obtained by condensation of GF_2 (supplied from manifolded 400-psi shipping cylinders) in a liquid nitrogen heat exchanger and was stored in a prechilled, 43-gallon, LN_2-jacketed run tank. Fluorine condensation and transfer procedures, developed over several years, were carried out routinely and without difficulty. Following completion of a set of firings, LF_2 remaining in the tank was allowed to gasify back into the supply bottles.

(U) The fluorine flow system was chilled with jacketed LN_2 from the condenser to within a few inches of the injector, including all valves and flowmeters. Filtered helium was used for fluorine tank pressurization.

(C) The schematic line between the 43-gallon LF_2 tank and the main oxidizer valve shown in Fig. 29 represents two identical supply lines, differing only in the sizes of the installed flowmeters; one line served for flowrates corresponding to chamber pressures of 70 to 300 psia and the other for flowrates corresponding to pressures of 300 to 650 psia.

(U) Gaseous hydrogen was supplied from the area tank farm through a suitable pressure-regulating system. Gaseous nitrogen purges were used on both the oxidizer and fuel sides.

b. Instrumentation

(U) A schematic diagram indicating instrument locations is shown in Fig. 30. Redundant measurements were made of most of the important experimental parameters to increase data reliability. The particular transducers used are described below.

(U) (1) Thrust. The thrust chamber mount was supported on flexures which allow free movement parallel to the engine axis, restrained in the thrust direction by a Baldwin-Lima-Hamilton double-bridge load cell (Model U-382).

(U) (2) Pressure. All pressures were measured with bonded strain gage transducers (Taber "Teledyne" Series 206).

(U) (3) Flowrate. Hydrogen flowrate was measured by a sonic venturi meter. Fluorine flowrate was measured by two turbine flowmeters in series (Fischer-Porter Models 1/2-2 and 1/2-9) in each of the oxidizer supply lines.

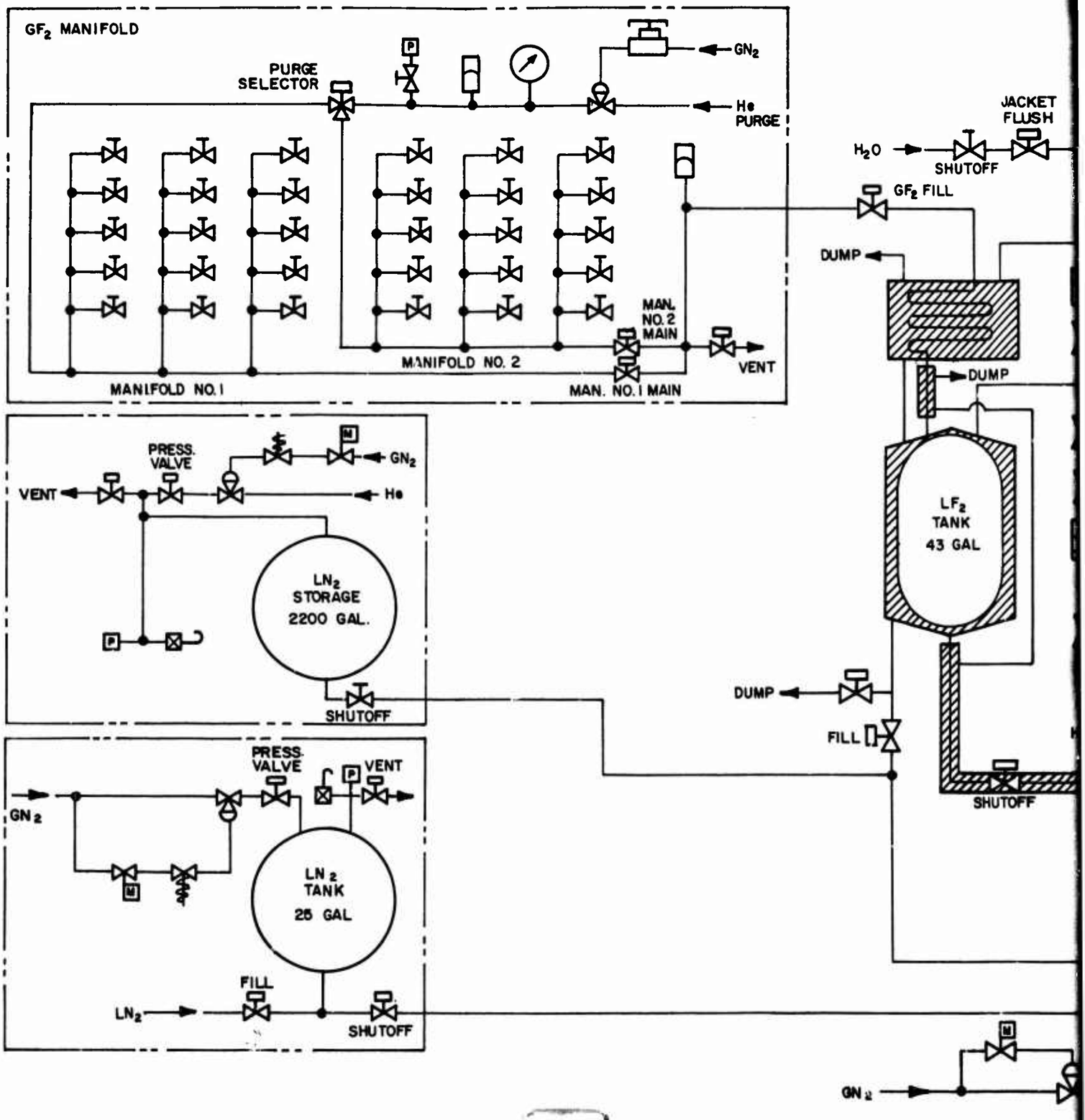
GF2 MANIFOLD
PURGE SELECTOR
GN2
He PURGE
MANIFOLD NO. 1
MANIFOLD NO. 2
MAN. NO. 1 MAIN
MAN. NO. 2 MAIN
VENT
H2O
JACKET FLUSH
SHUTOFF
GF2 FILL
DUMP
LF2 TANK 43 GAL
PRESS. VALVE
VENT
He
LN2 STORAGE 2200 GAL.
SHUTOFF
FILL
LN2 TANK 25 GAL
LN2

1

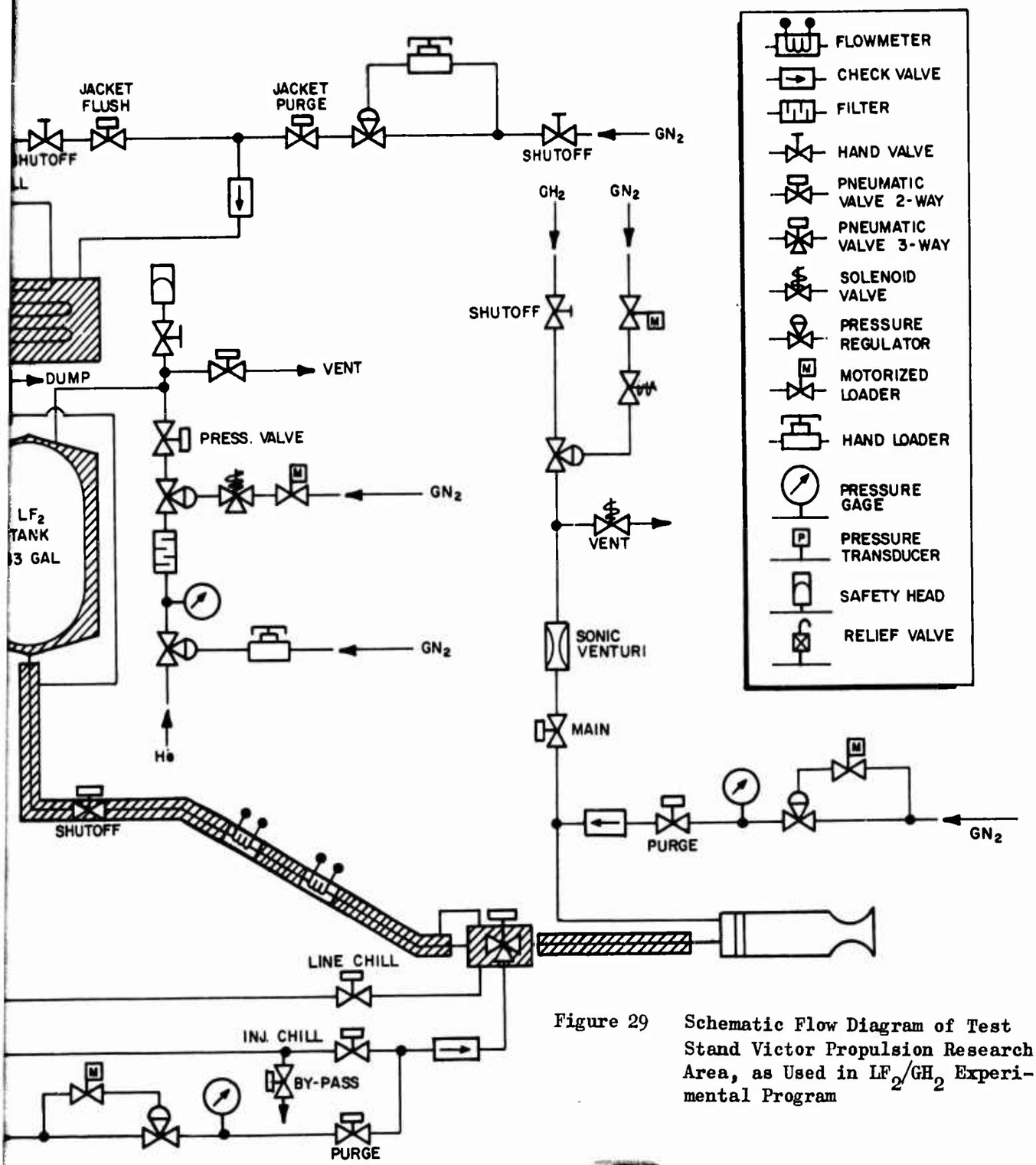

Figure 29 Schematic Flow Diagram of Test Stand Victor Propulsion Research Area, as Used in LF_2/GH_2 Experimental Program

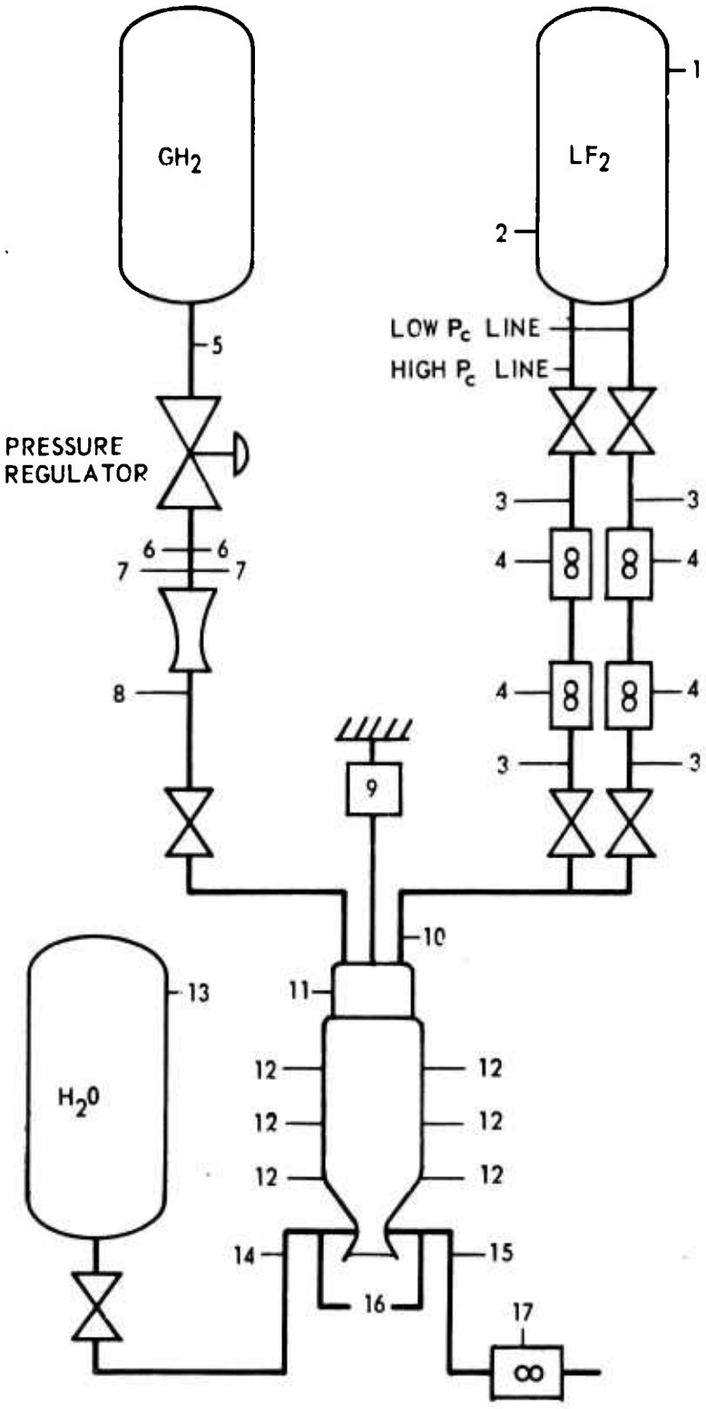

INSTRUMENTATION

1 FLUORINE TANK PRESSURE
2 FLUORINE TANK TEMPERATURE
3 FLUORINE SUPPLY TEMPERATURE
4 FLUORINE FLOWRATE
5 HYDROGEN SUPPLY PRESSURE
6 VENTURI PLENUM TEMPERATURE
7 VENTURI PLENUM PRESSURE
8 VENTURI EXIT PRESSURE
9 THRUST
10 FLUORINE INJECTION PRESSURE
11 HYDROGEN INJECTION PRESSURE
12 CHAMBER PRESSURES
13 WATER TANK PRESSURE
14 WATER INLET PRESSURE
15 WATER OUTLET PRESSURE
16 WATER TEMPERATURE DIFFERENTIAL
17 WATER FLOWRATE

Figure 30. Test Instrumentation Schematic

(U) (4) Temperature. Liquid fluorine temperatures were measured with two shielded platinum resistance bulbs in each line (Rosemount Model 176), immersed in the liquid stream, one upstream of the first flowmeter and the other downstream of the second. Hydrogen temperatures in the venturi plenum were measured with iron-constantan thermocouples. Differential inlet-outlet temperatures of the water coolant were measured with three-element, chromel-alumel thermopiles.

c. Data Recording

(U) All pressure, temperature, and flow measurements were recorded on tape during each firing by means of a Beckman Model 210 Data Acquisition and Recording System. This system acquires analog data from the transducers, which it converts to digital form in binary-coded decimal format. The latter were recorded on tapes which were then used for computer processing.

(U) The Beckman Data Acquisition Unit sequentially samples the input channels at a rate of 5625 samples per second. Programmed computer output consists of tables of time vs parameter value, printed out as the instantaneous values at approximately 10-millisecond intervals during the firing or, for extended firings, as the instantaneous values at preselected intervals (or "slices") throughout the firing, together with calibration factors, zero readings, and related data. The same computed results are machine plotted and displayed as CRT outputs on appropriately scaled and labeled grids.

(U) Primary data recording was on the Beckman 210 System. In addition, the following auxiliary recording systems were employed:

1. An eight-channel Brush Mark 200 recorder was used in conjunction with the Beckman unit primarily to establish time intervals for computer data reduction and, additionally, for "quick-look" information on important parameters.
2. Two CEC, 36-channel, direct-reading oscillographs were used as backup for the Beckman 210 System and for recording of coolant water flowrates (which were not recorded on the Beckman).
3. Direct-inking graphic recorders, either Dynalog rotary chart or Esterline-Angus strip chart, were used to set prerun propellant supply pressures to monitor chilldown time, to provide "quick-look" information, and as secondary backup to the Beckman and oscillograph recorders.

5. SOLID WALL SEGMENT TESTING

(U) During the Solid Wall Segment Evaluation, a total of 128 tests were conducted under the contract. These tests were performed to investigate the effects of combustion chamber and injector variations on the heat transfer and performance characteristics of the segment and to demonstrate the feasibility of tapping hot combustion chamber gases

through the injector for use as a turbine drive fluid. A breakdown of the number and purpose of these tests, together with the range of chamber pressure investigated, is presented in Table 2.

TABLE 2

SOLID WALL SEGMENT TEST SUMMARY (C)

	No. Tests	P_c Range, psia
Contour Characterization	87	48-666
Injector Characterization	27	119-550
Hot Gas Tapoff	9	268-483
Mixture Ratio Bias Effects	5	435-518

(U) Some overlapping of the various areas existed; for example, the contour characterization tests provided baseline reference point data for the other areas of investigation.

(C) Table 3 is a summary of the operating conditions and performance results for the data producing tests conducted for the solid wall segment evaluation. The column headings refer to the following parameters:

Purpose: Primary test objective. C - contour evaluation, I - injector characterization, B - mixture ratio bias, T - tapoff

Chamber: one of the five chamber contours described in Fig. 21.

Injector: 1, 4 Triplet injectors with 0.037 in.dia.GH_2 orifices
1-A Triplet injector with 0.043 in. dia. GH_2 orifices
1-B Triplet injector with 0.55 in.dia.GH_2 orifices
1-B-1 Triplet injector 1-B with tapoff port
3 Impinging Fan Injector (single row)

Duration: time from attainment to 90 percent of chamber pressure to decay to 90 percent of chamber pressure

P_c stagnation chamber pressure

$\dot{W}_T$ total propellant flowrate (excluding tapoff gas)

MR mixture ratio, oxidizer/fuel (excluding tapoff gas)

F measured thrust

A_t geometric area of throat

C^*_{theo} theoretical value of C* at listed P_c and MR

$(\eta_{C^*})_p$ ratio of experimental C* based on P_c to C^*_{theo}

$(\eta_{C^*})_F$ ratio of experimental C* based on F to C^*_{theo}

TABLE 3

PERFORMANCE DATA SUMMARY

Test No.	Purpose	Chamber	Injector	Duration, seconds	F lb	Pc psia	$\dot{W}_T$, lb/sec	MR	A_t in^2	C^*_{theo} ft/sec	$(\eta C^*)_p$ %	$(\eta C^*)_F$ %	$h_{g_{throat}}$ Btu / in^2-sec-F x10^{-4}
5	C	A	0	1.3	-	616	1.092	11.4	0.437	8255	94.0	-	57
6	C	A	0	2.3	-	569	1.268	13.4	0.535	8145	93.0	-	66
7	C	A	1	2.2	-	241	0.534	13.4	0.541	8050	97.0	-	-
8	C	A	1	2.2	-	580	1.269	11.8	0.541	8225	94.6	-	-
11	C	A	1	5.0	229	305	0.677	13.2	0.505	8085	89.6	91.1	-
12	C	A	1	10.0	224	297	0.667	12.8	0.505	8100	88.4	88.9	-
13	C	A	1	5.0	-	504	1.057	12.5	0.505	8175	92.9	-	-
18	C	B	1	7.0	210	326	0.684	13.4	0.497	8082	93.2	94.5	45
19	C	B	1	7.6	307	469	0.956	12.9	0.496	8151	94.7	94.7	56
20	C	B	1	6.5	302	461	0.919	13.7	0.496	8108	97.5	97.0	54
21	C	B	1	7.7	370	566	1.069	12.4	0.496	8193	100.9	99.7	-
22	C	B	1	7.8	362	556	1.069	12.9	0.496	8169	99.6	98.8	69
25	C	B	1	19.0	104	180	0.383	16.1	0.498	7870	95.6	95.2	-
29	C	B	1	24.0	98	168	0.362	14.9	0.498	7925	94.2	95.4	-
31	C	C	1	18.0	221	341	0.686	13.7	0.499	8080	98.0	97.8	41
32	C	C	1	10.1	134	219	0.445	14.3	0.499	7995	98.8	99.3	-
33	C	C	1	20.2	-	159	0.326	13.6	0.499	7990	98.8	-	-
34	C	C	1	18.5	125	206	0.419	13.3	0.500	8040	98.8	99.3	-
35	C	C	1	9.5	161	257	0.520	13.5	0.500	8055	98.5	98.2	-
36	C	C	1	23.0	247	378	0.754	12.2	0.500	8160	97.9	97.8	56
37	C	C	1	22.0	205	319	0.652	13.9	0.500	8055	97.0	96.3	45
38	C	C	1	19.1	338	511	1.031	14.8	0.500	8070	97.3	95.9	71
39	C	C	1	23.2	-	115	0.243	15.1	0.500	7860	98.4	-	-
43	C	C	1	14.0	-	97	0.211	12.8	0.503	7917	98.0	-	-
44	C	C	1	15.0	-	86	0.188	14.1	0.503	7885	98.1	-	-
45	C	C	1	15.0	-	65	0.142	12.9	0.503	7915	97.7	-	-
49	C	C	1	13.2	311	464	0.919	14.5	0.492	8070	97.4	98.9	45

CONFIDENTIAL

TABLE 3 (Continued)

Test No.	Purpose	Chamber	Injector	Duration, seconds	F lb	Pc psia	$\dot{W}_T$ lb/sec	MR	A_t in^2	C^*_{theo} ft/sec	$(\eta C^*)_p$ %	$(\eta C^*)_F$ %	$h_{g_{throat}}$ $\frac{Btu}{in^2\text{-sec-F}} \times 10^{-4}$
50	C	C	1	13.2	266	402	0.806	16.8	0.492	7935	98.7	99.3	35
55	C	D	1	2.3	255	403	0.831	13.7	0.497	8095	95.0	95.5	27
56	C	D	1	2.0	314	492	0.994	13.0	0.497	8150	97.6	95.4	39
58	C	D	1	1.9	347	555	1.100	13.2	0.497	8155	97.0	94.5	49
59	C	D	1	1.9	323	511	1.019	12.1	0.497	8195	96.4	95.0	48
60	C	D	1	1.9	182	303	0.614	13.2	0.497	8085	97.6	98.2	26
61	C	D	1	1.9	279	446	0.892	13.2	0.497	8130	97.2	96.2	40
62	C	D	1	1.8	352	559	1.111	13.4	0.497	8150	97.1	94.7	50
63	C	E	1	1.9	250	414	0.832	13.5	0.494	8110	95.7	93.7	35
64	C	E	1	1.9	307	495	0.986	13.0	0.494	8152	95.8	94.0	40
65	C	E	1	1.9	372	595	1.165	13.0	0.494	8172	97.0	94.5	48
66	C	E	1	1.9	192	316	0.645	13.8	0.494	8060	95.3	97.0	32
67	C	E	1	1.9	384	604	1.173	13.3	0.494	8160	97.9	97.3	58
78	I	C	1-A	3.7	251	434	0.928	13.3	0.508	8120	93.5	92.4	62
79	I	C	1-A	3.7	194	299	0.656	15.4	0.508	7970	93.7	92.0	46
80	I	C	1-A	3.7	253	381	0.813	13.9	0.508	8080	94.2	93.0	56
81	I	C	1-A	3.7	284	425	0.894	13.3	0.507	8120	94.6	93.5	59
82	I	C	1-A	3.7	320	480	1.015	14.7	0.506	8065	94.2	92.2	60
86	I	C	1-A	4.0	147	238	0.485	10.6	0.506	8175	98.6	96.2	—
87	I	C	1-A	4.0	164	262	0.552	13.6	0.506	8050	96.2	94.1	—
88	I	C	1-A	4.4	157	252	0.562	17.1	0.506	7850	93.6	91.3	—
90	I	C	1-A	29.0	—	119	0.258	11.9	0.506	8035	95.8	—	—
91	I	C	1-B	3.5	291	445	0.933	12.6	0.506	8160	93.9	91.0	52
93	C	E	4	3.8	234	399	0.753	10.6	0.480	8235	97.6	96.3	32
94	C	E	4	3.8	218	375	0.725	12.5	0.474	8140	95.7	95.1	30
95	C	E	4	3.8	223	382	0.751	13.0	0.472	8120	93.6	93.9	31
96	C	E	4	3.8	190	331	0.647	13.4	0.471	8080	95.1	96.0	24
97	C	E	4	3.8	247	425	0.810	12.9	0.470	8140	95.8	94.3	34
98	C	E	4	3.8	244	421	0.812	13.0	0.470	8132	94.7	93.2	34
99	C	E	4	3.8	236	409	0.799	12.7	0.469	8145	93.2	92.2	35

CONFIDENTIAL

TABLE 3 (Continued)

Test No.	Purpose	Chamber	Injector	Duration, seconds	F lb	Pc psia	$\dot{W}_T$ lb/sec	MR	A_t in^2	C^*_{theo} ft/sec	$(\eta C^*)_p$ %	$(\eta C^*)_F$ %	$h_{g_{throat}}$ $\frac{Btu}{in^2\text{-sec-F}} \times 10^{-4}$
100	I	E	3	3.4	166	299	0.633	14.2	0.468	8035	87.2	89.7	33
101	I	E	3	3.2	228	345	0.816	14.0	0.470	8077	89.0	89.6	40
102	I	E	3	3.2	252	431	0.829	13.2	0.470	8125	89.4	89.6	43
103	I	E	3	3.5	250	428	0.933	18.6	0.470	7817	87.0	86.3	42
104	I	E	3	3.7	249	428	0.897	16.1	0.470	7170	88.8	87.9	41
105	I	E	3	3.6	253	437	0.879	13.0	0.470	8136	90.7	90.3	42
106	I	E	3	3.8	166	301	0.629	13.9	0.470	8053	88.6	90.2	32
107	I	E	3	3.7	227	397	0.809	13.5	0.470	8103	90.0	90.0	40
108	I	E	1-B	3.2	185	319	0.621	13.4	0.470	8080	96.0	97.9	28
109	I	E	1-B	3.5	252	426	0.812	13.3	0.470	8118	96.8	96.3	41
110	I	E	1-B	3.5	286	480	0.910	13.3	0.470	8133	96.8	95.8	47
111	I	E	1-B	3.5	319	531	1.005	13.2	0.470	8150	96.4	95.3	51
112	T	E	1-B-1	3.6	*	411	0.792	14.1	0.468	8075	95.8	-	-
113	T	E	1-B-1	1.6	*	423	0.798	14.3	0.463	8070	98.0	-	37
114	T	E	1-B-1	3.5	*	425	0.807	13.4	0.468	8115	96.7	-	39
116	T	E	1-B-1	5.8	*	282	0.600	17.3	0.468	7860	90.3	-	34
117	T	E	1-B-1	5.8	*	274	0.593	15.7	0.468	7955	90.5	-	28
118	T	E	1-B-1	5.9	*	468	0.971	17.3	0.468	7930	91.5	-	56
129	T	E	1-B-1	5.8	*	353	0.703	13.3	0.468	8100	92.9	-	41
130	T	E	1-B-1	5.7	*	290	0.580	13.5	0.468	8065	93.5	-	33
131	T	E	1-B-1	5.7	*	483	0.971	14.7	0.468	8040	91.8	-	61

*Tapoff thrust effect not measured

CONFIDENTIAL

(U) The measured values (averaged where multiple instrumentation is used) of chamber pressure, propellant mixture ratio (O/F), total propellant flowrate, segment throat area, and thrust level are presented. The theoretical C* efficiency based on chamber pressure and mixture ratio is tabulated together with the calculated values of C* based on both chamber pressure and thrust measurements. The experimental gas film throat heat transfer coefficients are also tabulated for each test.

(U) Reproductions of typical CRT (Cathode Ray Tube) plots of chamber pressure and thrust are shown in Fig. 31 and 32. The cutoff characteristic was peculiar to the facility LF_2 valve used. For performance calculations, more precise values of these parameters were obtained from the on-line printout values of the Beckman data which provided finely incremented point-to-point data as well as time-averaged data over any specified time increment.

6. PERFORMANCE DATA ANALYSIS

(C) Analysis of the performance data was directed toward determining the effects of thrust level, chamber contour, and injector pattern on the characteristic velocity efficiency, η_{C^*}, of the segment. The goal of this effort was to obtain an injector/chamber combination having a C* efficiency in excess of 97 percent over the entire throttling range. The methods of analysis of the test data included application of factors to account for heat losses, throat discharge coefficient, drag, reaction kinetics, nozzle flow divergence, nozzle throat shrinkage, segment base pressure, and static-to-stagnation chamber pressure conversions.

a. Analysis Method

(U) The basis of comparison of combustion performance is characteristic velocity (C*) efficiency (percent of theoretical shifting equilibrium characteristic velocity). Characteristic velocity was calculated by two independent methods, one based on measured chamber pressure and the other on measured thrust. Standard equations were used, with corrections applied for energy losses and for departures from ideal, one-dimensional flow which were calculated by the methods described in Ref. 3.

(U) Calculations Based on Chamber Pressure. Characteristic velocity efficiency based on chamber pressure is defined by the following equation:

$$\eta_{C^*} = \frac{(P_c)_o \ (A_t)_{eff}{}^g}{(\dot{W}_T) \ (C^*)_{theo}} \qquad (1)$$

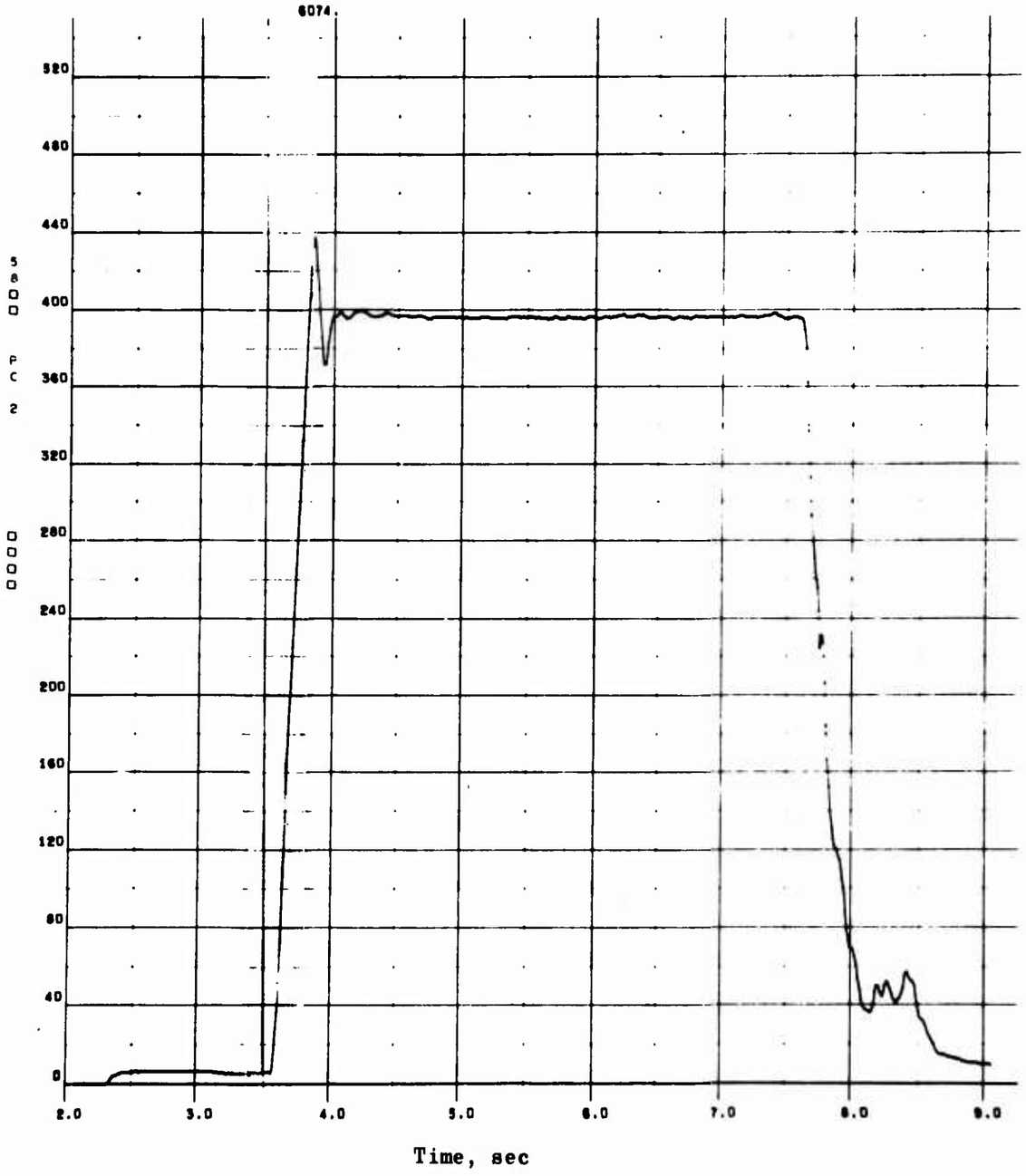

Figure 31. CRT Plot of Chamber Pressure vs Time

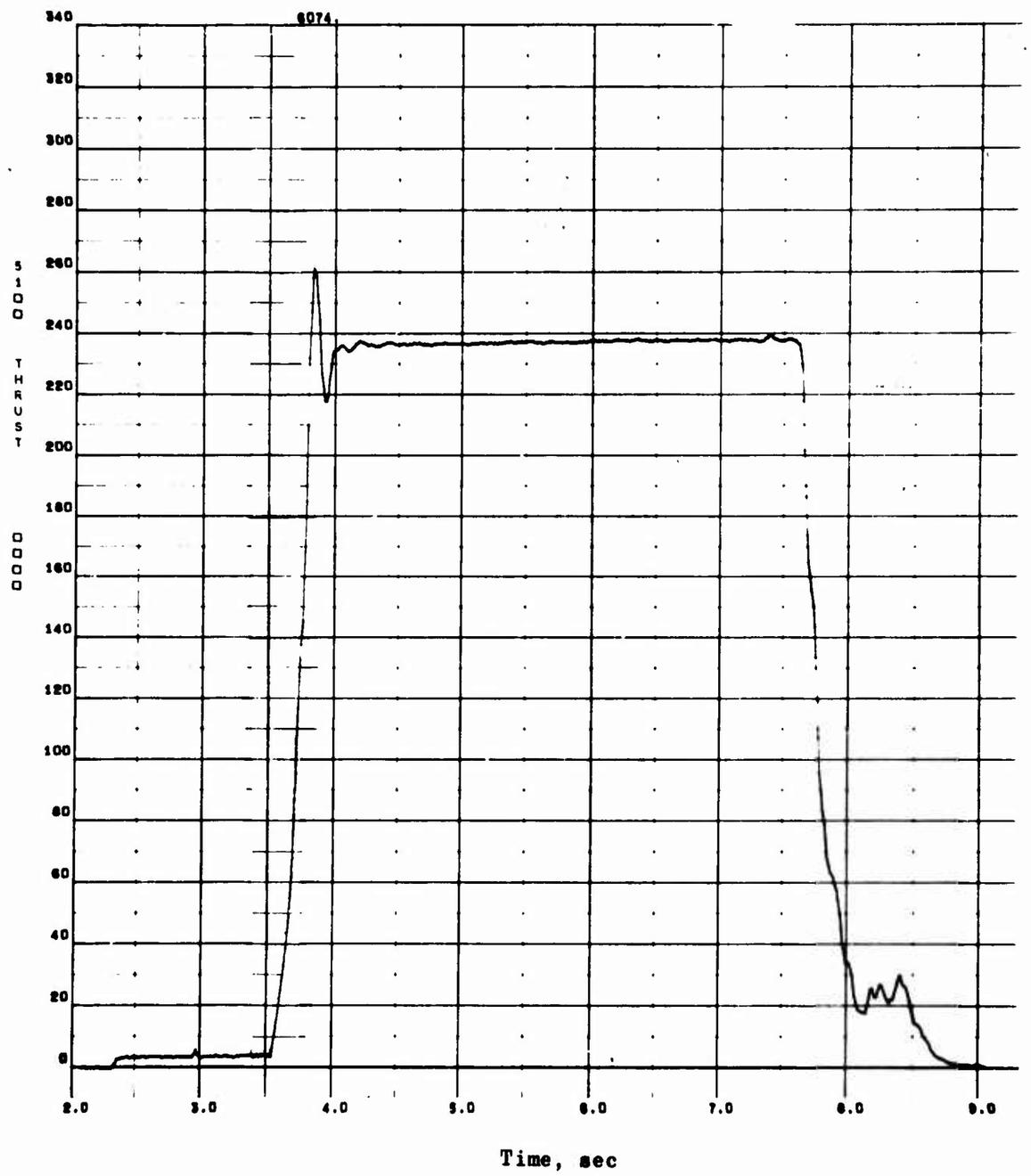

Figure 32. CRT Plot of Thrust vs Time

(U) where

$(P_c)_o$ = stagnation pressure at the throat, psia

$(A_t)_{eff}$ = effective thermodynamic throat area, $in.^2$

g = gravitational acceleration, ft/sec^2

$\dot{W}_T$ = total propellant weight flowrate, lb/sec

$(C^*)_{theo}$ = theoretical characteristic velocity based on shifting equilibrium

(U) Values calculted from Eq. 1 incorporate the corrections required because all the factors involved are not measured directly, but are obtained by application of suitable corrections to measured parameters. Equation 1 may therefore be written as follows:

$$\eta_{C^*} = \frac{P_c \, A_t \, g \, f_p \, f_{dis} \, f_{FR} \, f_{HL} \, f_{TE}}{(\dot{W}_o + \dot{W}_F) \quad (C^*)_{theo}} \qquad (2)$$

where

P_c = measured static pressure at start of nozzle convergence, psia

A_t = measured geometric throat area, $in.^2$

g = 32.174 ft/sec^2

$\dot{W}_o$ = oxidizer weight flowrate, lb/sec

$\dot{W}_F$ = fuel weight flowrate, lb/sec

$(C^*)_{theo}$ = theoretical C* based on shifting equilibrium, ft/sec

f_p = factor correcting observed static pressure to throat stagnation pressure

f_{dis} = factor correcting throat area for effective discharge coefficient

f_{TE} = factor correcting throat area for thermal expansion effects

f_{FR} = factor correcting measured chamber pressure for frictional drag of combustion gases at chamber wall

f_{HL} = factor correcting measured chamber pressure for heat losses from combustion gases to chamber wall

(U) For C* based on chamber pressure, the applicable corrections are as follows:

1. <u>Correction for measured static chamber pressure to stagnation pressure.</u> Measured static pressure at start of nozzle convergence is normally corrected to throat stagnation pressure by assumption of no combustion in the nozzle and application of the isentropic flow equations. At high

(U) contraction ratios, however, such as those in the present chambers (ranging from 8 to 18), the static/stagnation pressure ratio is very nearly unity, so that no specific correction is necessary.

2. Correction for heat loss to chamber walls. The applicable correction is obtained from measured heat flux to the coolant water by use of the following expression (Ref. 3):

$$f_{HL} = \left\{1 + \left[\frac{1}{\eta C^{*2}}\right]\left[\frac{Q}{\dot{W}_T}\right]\left[\frac{1}{C_p T_c}\right]\right\}^{1/2} \qquad (3)$$

where

f_{HL} = heat loss correction factor

Q = measured total heat flowrate (Btu/sec) to chamber walls and coolant, from injector face to plane of the throat

$\dot{W}_T$ = measured total propellant flowrate (lb/sec)

C_p = specific heat of combustion gas, frozen equilibrium (Btu/lb/R)

T_c = theoretical chamber temperature at test condition, R

3. Correction for drag loss. In high contraction ratio chambers, gas velocity in the combustion chamber is very low, hence this loss is negligibly small and no specific correction was used.

4. Correction for throat discharge coefficient. Application of the theoretical and empirical correlations for throat discharge coefficient described in the previous subsection 3 to the throat of the present thrust chambers resulted in a discharge coefficient of 0.998.

5. Correction of throat area for thermal expansion effects. The magnitude of this correction is a function of the gas side film heat transfer coefficient and, therefore, depends on the injector/chamber geometry and the chamber pressure. The value of the correction therefore was necessarily determined for each configuration and test condition. The calculation method is described in Appendix A.

(U) Calculations Based on Thrust. The alternate determination of C* efficiency is based on the following defining equation:

$$\eta_{C^*} = \frac{F_{vac}\, g}{(C_F)_{vac}\, \dot{W}_T\, C^*_{theo}} \qquad (4)$$

(U) where

F_{vac} = vacuum thrust, corrected, lb

g = gravitational acceleration, ft/sec^2

$(C_F)_{vac}$ = theoretical shifting thrust coefficient (vacuum)

$\dot{W}_T$ = total propellant weight flowrate, lb/sec

C^*_{theo} = theoretical shifting-equilibrium characteristic velocity, ft/sec

(U) By application of suitable corrections to measurements of thrust made at sea level, corrected values of vacuum thrust may be obtained. With these values, which include allowances for all important departures from ideality, theoretical thrust coefficients may be used for calculation of C*, i.e., C_F efficiency is 100 percent if there is no combustion in the nozzle, if chemical equilibrium is maintained in the nozzle expansion process, and if energy losses from the combustion gases are accounted for.

(U) Applicable corrections to measured thrust are specified in the following equation:

$$\eta_{C^*} = \frac{(F + P_a A_e)\, g\, \varphi_{FR} \varphi_{DIV} \varphi_{HL} \varphi_k}{(C_F)_{theo}\, (\dot{W}_O + \dot{W}_F)(C^*)_{theo}} \qquad (5)$$

where

F = measured thrust, pounds

P_a = ambient pressure, psia

A_e = area of nozzle exit, $in.^2$

g = 32.17 ft/sec^2

$(C_F)_{theo}$ = theoretical shifting thrust coefficient (vacuum)

$\dot{W}_O$ = measured oxidizer weight flowrate, lb/sec

$\dot{W}_F$ = measured fuel weight flowrate, lb/sec

$(C^*)_{theo}$ = theoretical shifting equilibrium characteristic velocity, ft/sec

φ_{FR} = correction for frictional losses

φ_{DIV} = correction for nozzle divergence

φ_{HL} = correction for heat losses to chamber and nozzle walls

φ_k = correction for chemical kinetic losses

(U) For C* based on measurement of thrust, the applicable corrections are as follows:

(U) Correction for Frictional Drag. This factor corrects for the energy losses due to drag forces resulting from the viscous action of the combustion gases on the thrust chamber walls. Its magnitude, which is the integral of the local friction forces over the chamber and nozzle inside wall, was determined by means of a boundary-layer analysis utilizing the integral momentum equation for turbulent flow. This analysis accounts for boundary-layer effects from the injector to the nozzle exit by suitable description of the boundary layer profile and local skin friction coefficient. This analysis was conducted as described in the previous subsection 3.

(U) Correction for Nozzle Divergence. The one-dimensional theoretical performance calculations assume that flow at the nozzle exit is uniform and parallel to the nozzle axis. The correction factor, φ_{DIV}, allows for nozzle divergence, i.e., for nonaxial flow and for nonuniformity across the nozzle exit plane. It was calculated by means of a computer program which utilized the axisymmetric method of characteristics for a variable property gas. Computation begins with a transonic analysis using series expansions of the differential equations of motion near Mach 1 to calculate the irrotational flow field. This provides a characteristic line for use in the analysis of the supersonic portion of the nozzle. The resulting pressures are integrated over the given geometry. This analysis was conducted as described in the previous subsection 3.

(U) Correction for Chemical Kinetic Losses (φ_k). These losses account for energy which is not recovered by recombination of disassociated species in the combustion products. The losses were calculated according to the method described in the previous subsection 3.

(U) Correction for Heat Losses (φ_{HL}). The correction for heat losses was based on the method of Ref. 3.

$$\varphi_{HL} = \left\{ +1 \left[\frac{1}{I_s^2} \right] \left[\frac{Q}{\dot{W}_T} \right] \left[\frac{2U\zeta}{g} \right] \right\}^{1/2} \qquad (6)$$

where

φ_{HL} = heat loss correction factor

I_s = measured specific impulse, seconds

Q = measured heat loss (Btu/sec) between injector face and nozzle exit

$\dot{W}_T$ = measured total propellant flowrate, lb/sec

ζ = $1 - (T_e/T_c)$

T_e = gas temperature at nozzle exit, R

T_c = gas temperature in combustion chamber, R

(C) Correction for Base Pressure. Pressure measurements at various locations on the base of the water-cooled segments indicated that for the higher values of chamber pressure (i.e., 300 psia) an aspiration of the base was occurring which required a thrust correction of approximately 0.7 percent. These measurements and data are described in Appendix B.

b. Analysis Results - Contour Effects

(U) Five combustion chamber contours (A through E) were evaluated during the contract effort. The performance, based on chamber pressure measurements, of each of the contours when tested with the same triplet injector configuration is shown in Fig. 33. While only performance values based on chamber pressure were plotted, values for both chamber pressure and thrust measurement methods are shown in Table 3. Generally good agreement was obtained between the values obtained with the two methods. Comparison of the performance of the five contours is shown on Fig. 34.

(C) The efficiency curves of the "rounded" chambers (contours A and B) exhibit a minimum point at approximately 350 psia which is not evident with contour C. In the latter, there is no significant variation in C* efficiency over the entire pressure range tested from its average value of 98 percent.

(U) To explain these results, a conv ent parameter for indicating variation in chamber contour i sed which shows the fraction of "excess" width:

$$\frac{W_2 - W_1}{W_1}$$

where

W_1 = width of injector (1 inch in all cases)

W_2 = maximum width of combustion chamber

W_2 = 3 inches in Contour A

W_2 = 2 inches in Contour B

W_2 = 1 inch in Contour C

(U) Variation in C* efficiency with this parameter is shown in Fig. 35 for three levels of chamber pressure. Atomization of LF_2 in a triplet gas-liquid element occurs in two stages, (1) primary atomization at the point of gas-liquid impingement where atomization results from LF_2 impingement and gas impingement, and (2) secondary atomization after the gas-liquid impingement; the rate of further atomization being a function of many variables including the available time for gas-liquid interaction.

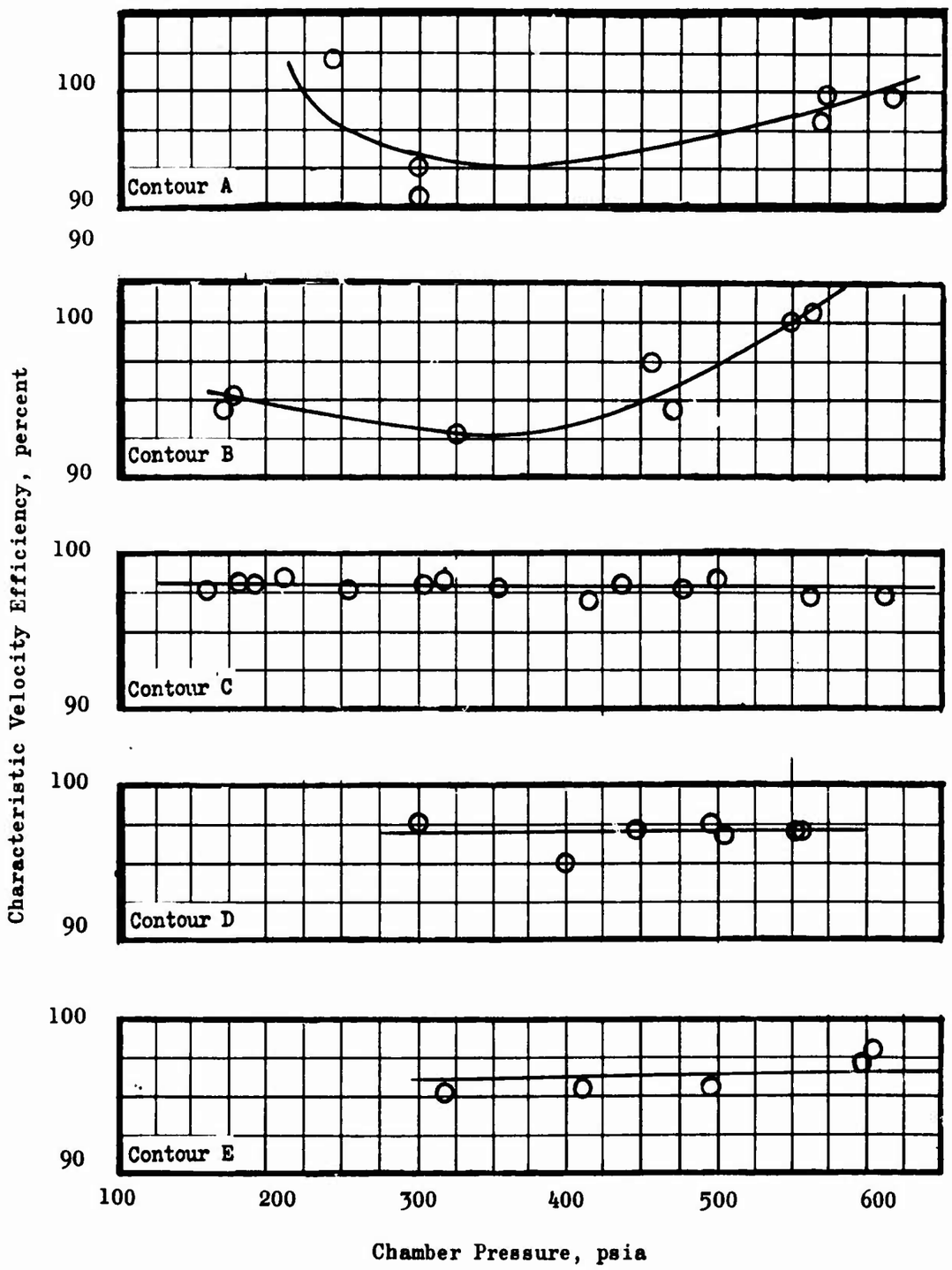

Figure 33. Effect of Chamber Pressure on C* Performance on Contours A through E.

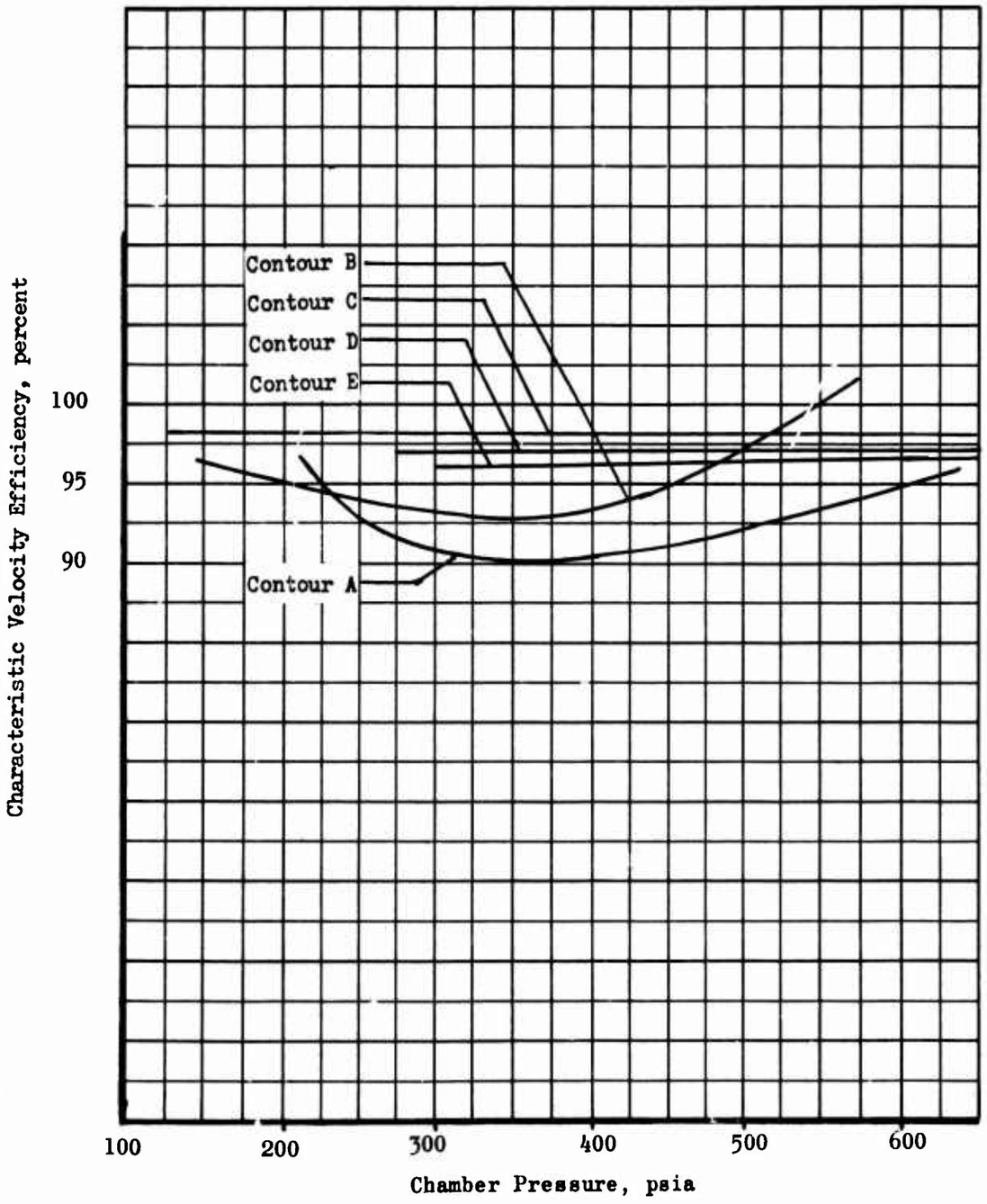

Figure 34. Comparison of C* Performance for Contours A through E.

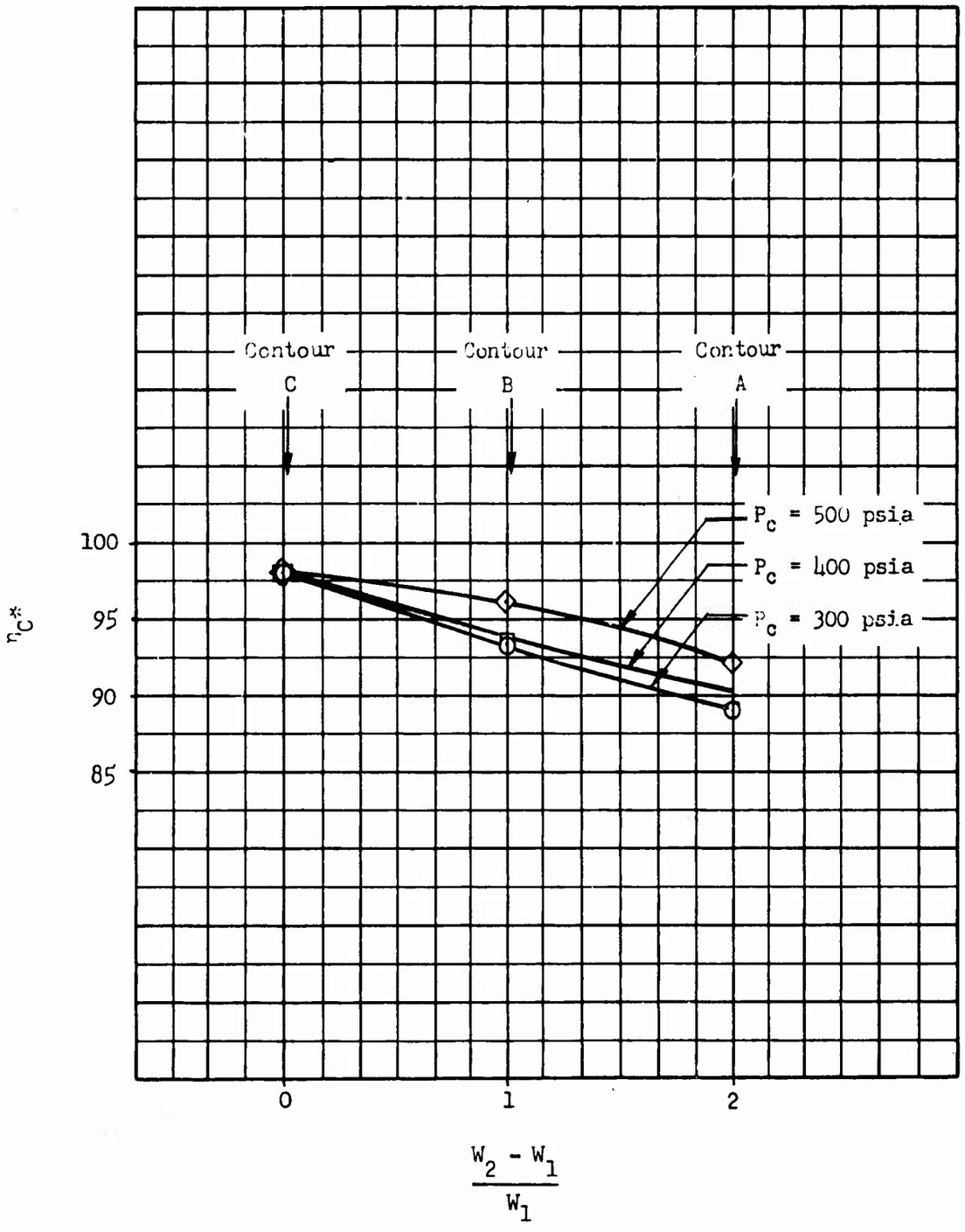

Figure 35. Variation of C* Efficiency With Chamber Contour Parameter

(C) In contours A and B, the diverging chamber allows the GH_2 to expand around the fluorine so that secondary atomization is restricted. As chamber pressure (LF_2 flowrate) is reduced, the primary atomization becomes less effective because of the reduced LF_2 injection velocity. However, below a certain chamber pressure the amount of fluorine vaporized in the injector becomes significant so that the fluorine injection velocity actually increases with reduction of chamber pressure. The result is that primary atomization is improved and performance increases as chamber pressure is reduced. Improved primary atomization would also result from the introduction of heated GH_2 into the injector as in the actual operating condition for the tube-wall thrust chamber (note this effect was subsequently demonstrated in the tube-wall segments tests of Task III).

(C) Bringing the chamber walls progressively closer to the injector spray (contours A, B, and C) increased the effectiveness of secondary atomization and subsequent spray distribution by restricting the lighter GH_2 from expanding around and away from the impinging LF_2 streams. However, as the chamber wall was contoured to further intersect the elements of the spray (i.e., contour E) secondary atomization was impaired and large droplets tended to accumulate on the chamber wall. A progressive lowering in performance can be expected in modifying the chamber contour such that increased interaction occurs. Conversely, the slight improvement of performance in contour D compared to contour E is attributable to the reduction in interaction obtained by lengthening the chamber.

(C) As will be discussed in the heat transfer analysis section, the conditions which promote interaction also tend to result in initiation of boundary layer growth close to the injector, a condition desirable for reduction of chamber heat flux. To test these effects, a contour was fabricated and tested under company sponsorship which converged continuously from the one inch wide injector to the nozzle inlet section (contour F). As anticipated, the increased interaction in this segment configuration resulted in a reduction of performance below the contour E value. The C* efficiency of this modified contour was approximately 95 percent.

c. Effect of Hydrogen Injection Velocity

(C) The degree of liquid atomization produced by the triplet injector configuration is a function of the hydrogen injection momentum which, at a given flowrate, is directly dependent upon injection velocity. An optimum hydrogen injection velocity is one which results in the best degree of LF_2 atomization. The hydrogen orifices of the triplet injector (D = 0.0372 inch) result in an injection Mach number of 0.9 using ambient temperature GH_2. Two enlargements of the orifices, to give successive injection Mach number of 0.65 and 0.4, were evaluated. Performance results in contour C are shown in Fig. 36, in which C* efficiencies of each of the injector configurations are plotted. Decrease in hydrogen injection Mach number from 0.9 to 0.65 resulted in a 3-percent performance degradation (98 to 95 percent); the single firing at Mach number 0.4 indicated no significant further performance decrease.

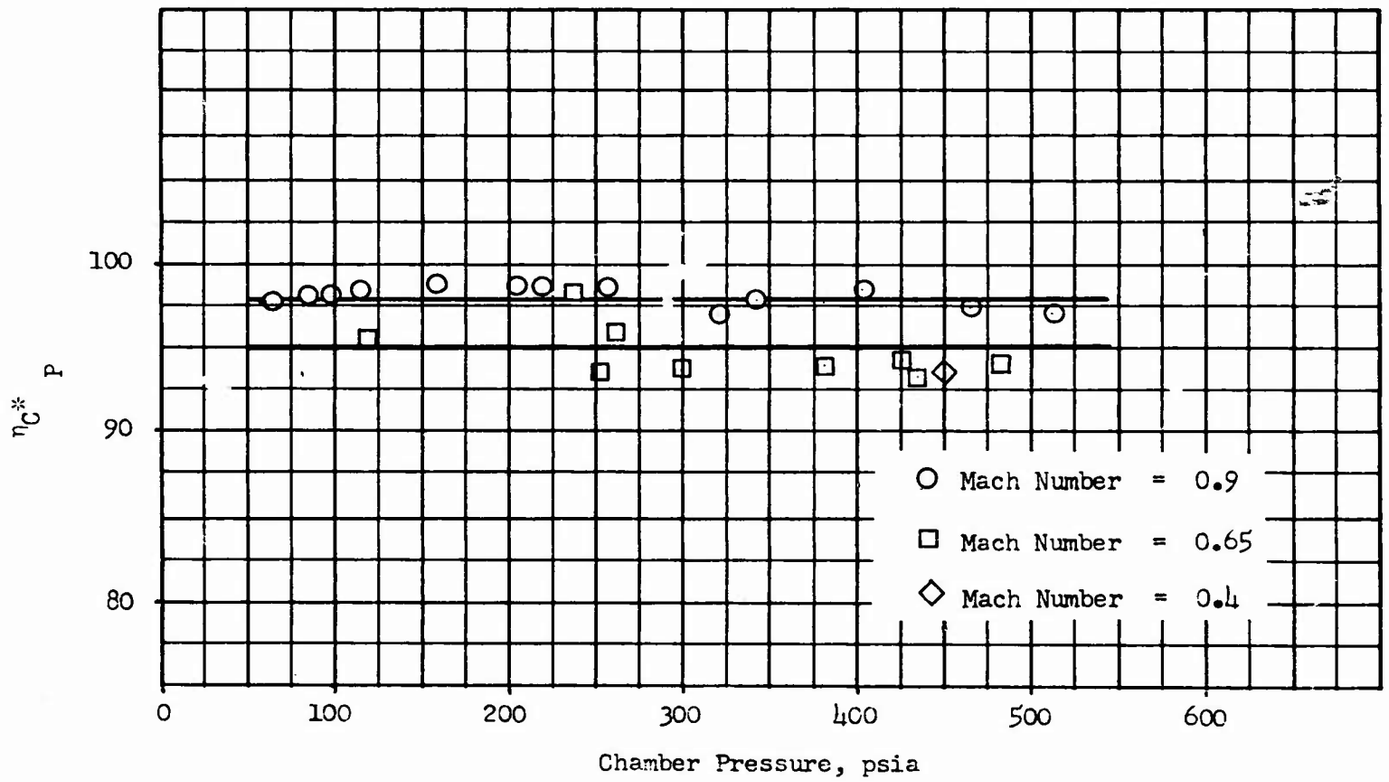

Figure 36 . Variation of C^* Efficiency With GH_2 Injection Mach Number, Triplet Injector, Chamber Contour C.

(C) Correlation of performance results exhibited by liquid-gas-liquid triplet injectors was made in terms of the ratio of liquid mass to be atomized to the energy available for atomization (the gas momentum):

$$\frac{\dot{W}_O}{\dot{W}_F V_F}$$

(C) At constant mixture ratio, $\dot{W}_O/\dot{W}_F$, only the hydrogen gas velocity, V_F, influence this parameter. The triplet injector results are summarized in Fig. 37 showing C* efficiency as a function of the parameter. The general shape of the curve shown agrees with LO_2/GH_2 data obtained in other programs using triplet injector designs. In these related programs, maximum efficiencies with this injector type occurred when the parameter, $\dot{W}_O/\dot{W}_F V_F$, was in the 1.5×10^{-3} to 2.5×10^{-3} range. The data in Fig. 37 suggest that, at a value of approximately 2.5×10^{-3}, the injector would deliver near-theoretical C* levels (approximately 99 percent) over the entire chamber pressure range, using a chamber contour of the C type.

(C) The test conditions for the solid wall segment, employing ambient temperature hydrogen gas (approximately 540 R), prevented actual experimentation at a value of $\dot{W}_O/\dot{W}_F V_F = 2.5 \times 10^{-3}$ because the injection Mach number limited the injection velocity obtainable. Under actual engine operating conditions, however, a value of 2.5×10^{-3} could readily be achieved since, for H_2 injection temperatures on the order of 1000 R, the required injection Mach number would be approximately 0.89. The performance levels (approximately 98 percent) obtained experimentally with ambient temperature GH_2 simulate the approximate condition of heated hydrogen injection Mach number of 0.66. It will be noted later that when heated hydrogen was used in the tube-wall segment tests (Task III) performance in excess of 99 percent η_{C^*} actually was achieved over the entire chamber pressure range.

d. Alternate Injector Type

(C) As an alternate to the basic triplet injector pattern, a second injection element concept called the "impinging fan" was evaluated. This configuration, shown schematically in Fig. 12, involved the formation of two spray fans by self-impingement of two pairs of fluorine streams followed by intersection of the fans over a central, high-velocity gaseous hydrogen jet.

(C) The first impinging fan injector that was designed and fabricated consisted of 10 elements uniformly spaced along the center of the injector. A sketch of the estimated approximate fan perimeter in the plane approximately 1 inch from the injector face is shown in Fig. 38.

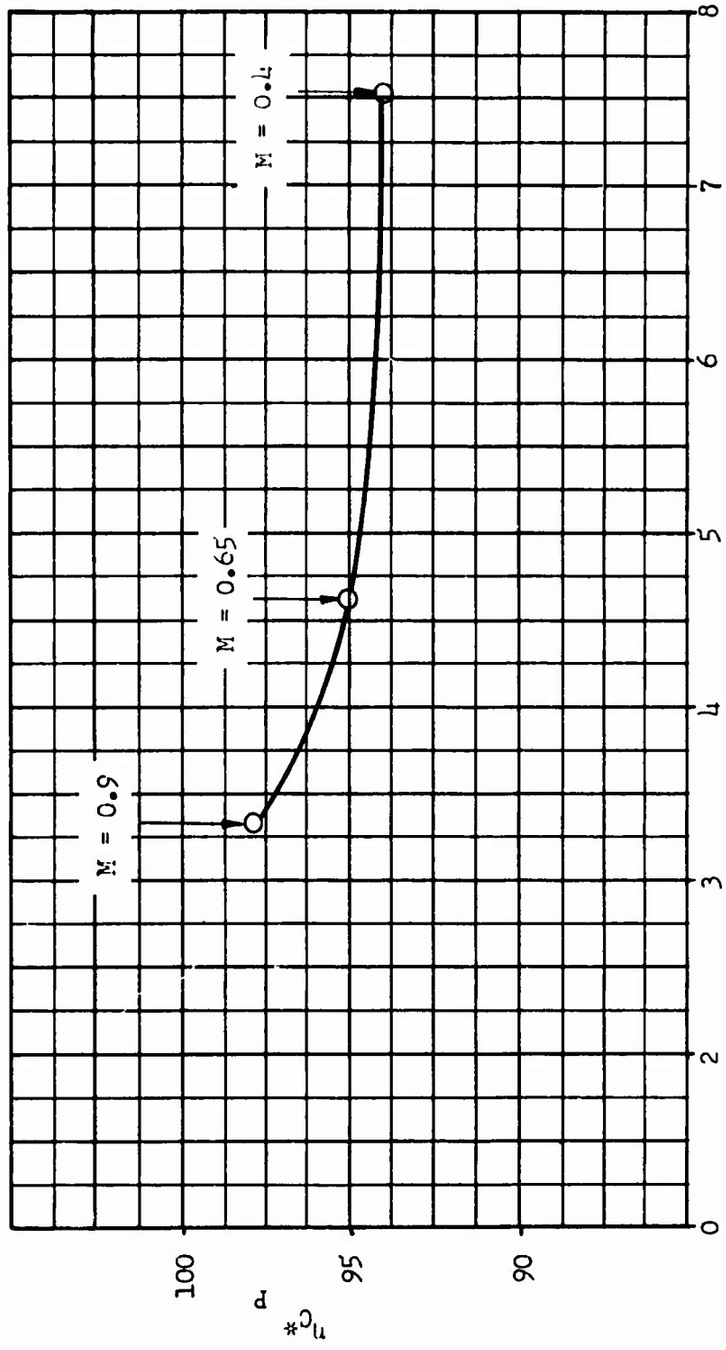

Figure 37 • Variation of C* Efficiency With Atomization Parameter, Triplet Injector

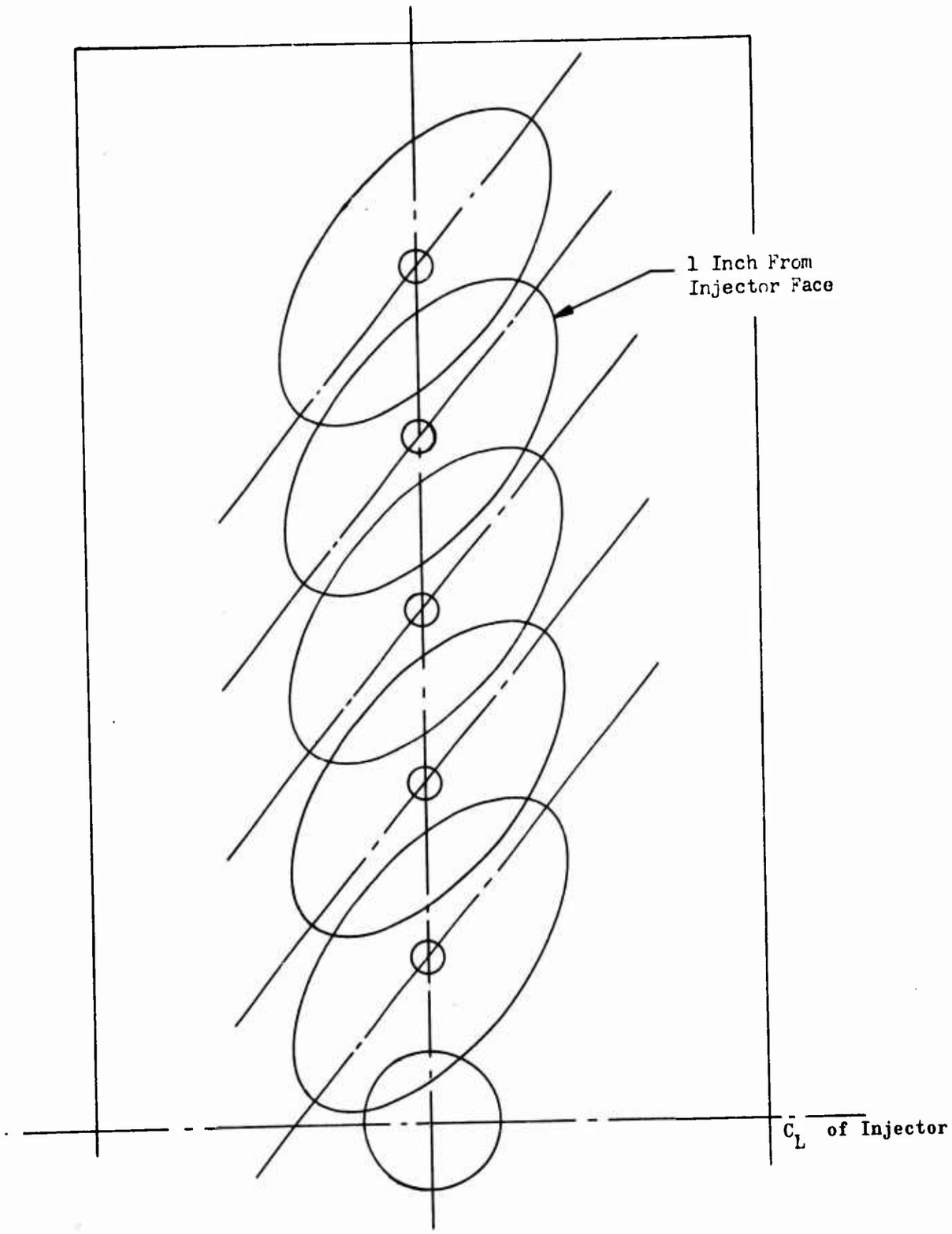

Figure 38. Approximate Fan Perimeters - 10 Element Impinging Fan Pattern

(C) It is evident that the concentration of the liquid mass at the center of the injector has the same effect as that obtained by increasing the chamber wall separation (as in contours A and B). The lessened C* efficiency of these two contours in comparision to that of contour C indicates that this impinging fan injector design might also show performance degradation. Analysis of data from tests of this injector in contour E resulted in performance approximately 3 percent lower than that of the triplet injector. This single row impinging fan injector was designed for ease of fabrication. It provided a data point for the tradeoff between performance and simplicity.

(C) Based on this experience, a second impinging fan injector was designed to provide improved propellant distribution. It contained a total of 14 elements, arranged in three rows on a two inch wide injector face. In addition, the 14-element injector had three axial GH_2 orifices per element. The diameters of these orifices were matched to the LF_2 mass distribution in the impinging fan. This injector was described earlier and is illustrated in Fig. 15.

(C) To accommodate three rows of elements, a 2-inch injector and corresponding combustion chamber were designed. The new chamber had a contour that converged continuously at a 15 degree angle from the injector to the throat. This contour was chosen for heat transfer reasons and was called contour G. Performance of the contour G/ impinging fan injector combination was approximately 96.5 percent of theoretical C*. Historically, this was the point at which a good correlation of the data in terms of the wall interaction model was obtained. Subsequent redesign of the injector to eliminate the interaction resulted in C* efficiency performance in excess of 99 percent. The first three row impinging fan injector achieved similar performance subsequently when tested with heated hydrogen in the Task III tube-wall segments by virtue of its increased hydrogen injection velocity and its ability to atomize and vaporize the LF_2 to the extent that the interaction influences were greatly reduced.

e. Mixture Ratio Bias

(U) The purpose of these tests was to determine the effects of wall film coolant on heat transfer rates and performance. Two performance data producing tests were conducted in a contour E chamber using the mixture ratio bias adapter described on Page 31. This adapter permitted independent control of the GH_2 flowrates to the injector (core) and to the bias orifices. The results of these tests are presented in Table 4.

(C) TABLE 4

MIXTURE RATIO BIAS RESULTS

Chamber Pressure psia	GH_2 Bias, percent	Mixture Ratio, O/F		C* Reduction, percent
		Overall	Core	
435	12	13.5	15.3	8
501	30	14.4	20.6	9

(C) The large reduction in C* efficiency (from a nominal reference value of 96.5 percent) is partially attributable to off-design operation of the injector core mixture ratio. Additional testing with redesigned injectors would be required to separate this effect from the actual film cooling effect on performance although it is expected that significant performance recovery could be achieved by redesign. The data from these two tests also indicated that the relationship between performance and amount of film cooling was highly nonlinear in the region investigated.

f. Injector Tapoff

(C) Nine tests were conducted using the tapoff injector configuration described on Page 33 to demonstrate injector structural integrity, degree of injector performance degradation, and tapoff gas properties over the throttling range.

(U) The facility and instrumentation setup used for the tapoff test series are shown schematically in Fig. 39. The tapoff gas flowed into an enlarged tube which served as a plenum chamber for the sonic orifice located at the exit. The sonic orifice simulated the turbine nozzles and therefore was the flow-regulating device for the system. The mixture ratio of the tapoff gases was controlled by the annular gap between the injector and the tapoff tube and by the depth of insertion of the tapoff tube as described earlier. A series of thermocouples was installed along the length of the tube to verify that combustion had been completed prior to flowing through the sonic orifice. The measured temperature, T, of the tapoff gas was used to determine the mixture ratio and molecular weight, M, of the gas (based upon the gas properties shown in Fig. 40). For the relatively low temperatures and mixture ratios associated with tapoff gases, the molecular weight is nearly independent of pressure. The pressure measurement, P, was used in the following equation primarily to determine the flowrate, W.

$$\dot{W} = KC_D AP(M/29T)^{1/2}$$

where K depends upon the specific heat ratio for the gas but is approximately 0.53 for the conditions tested. The discharge coefficient is C_D and the area of the sonic orifice is represented by A.

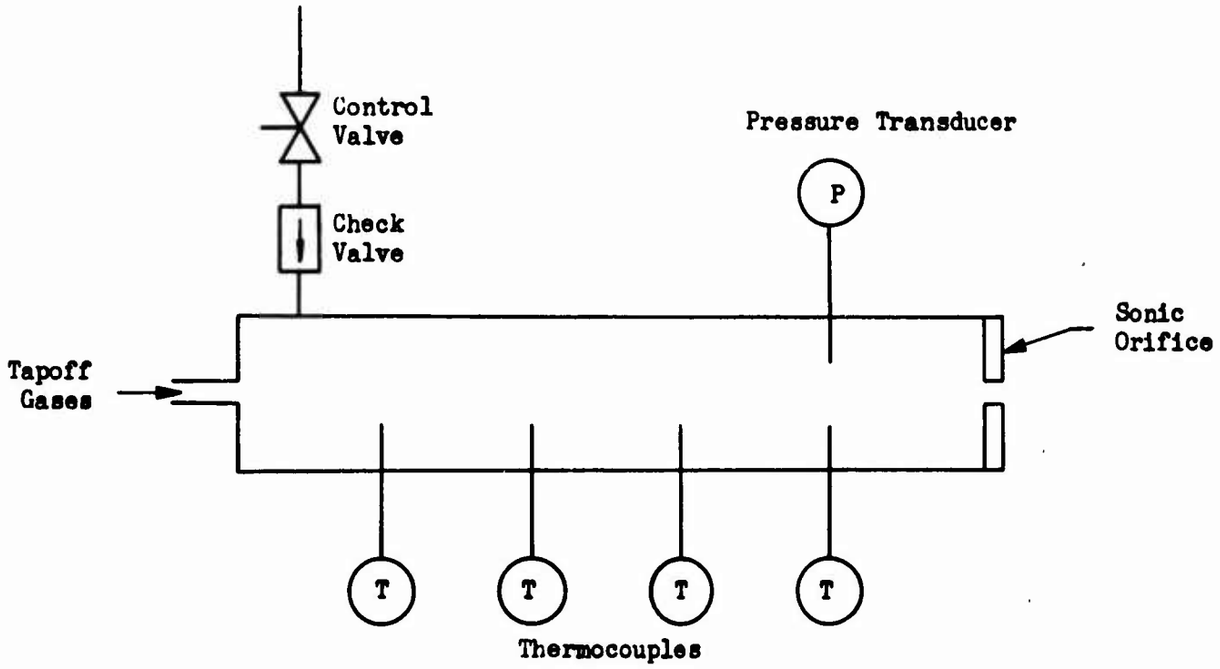

Figure 39 . Tapoff System Instrumentation Schematic

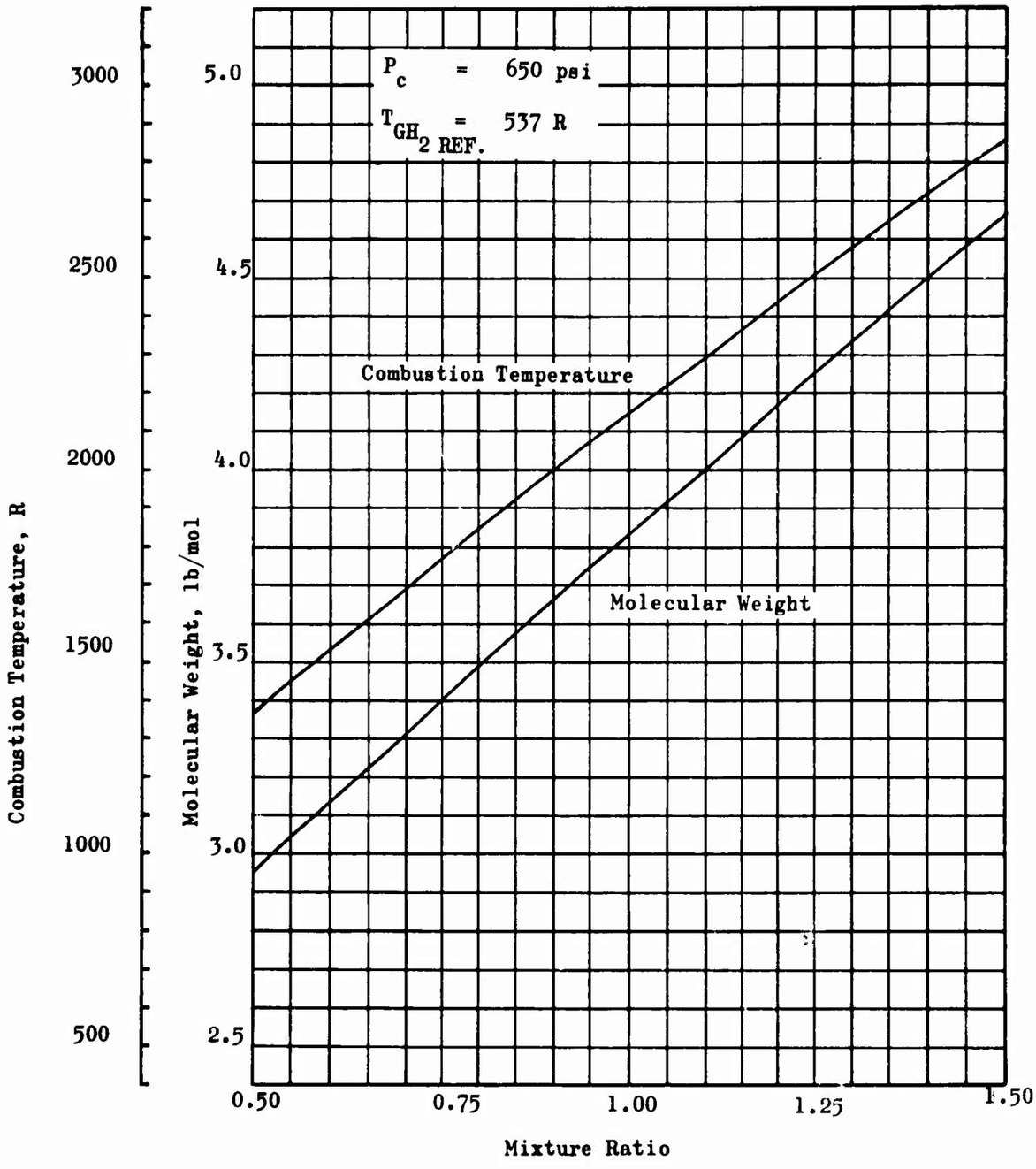

Figure 40. Molecular Weight and Combustion Temperature for LF_2/GH_2

(U) The tests were to investigate only steady-state operation because the actual transient will depend upon the configurations of several components not included in the test hardware; e.g., control valves and turbopump. A GN_2 purge was introduced into the plenum chamber and injector to eliminate transient off-mixture-ratio conditions at start. The purge was improperly sequenced during the first three tests of this series which resulted in some damage to the tapoff tubes.

(C) One of these tests was successful (no tapoff tube overheating) and resulted in a tapoff gas temperature of approximately 1600 F. This was achieved with an annular gap of 0.006 inch and with the tapoff tube receased 0.30 inch behind the injector face. On the two remaining tests, the tapoff tube burned. On the two unsuccessful tests, the GN_2 purge has been terminated prematurely during the start transient. The purge termination was subsequently delayed until completion of start transition. No further difficulties were encountered thereafter and the injector, and tapoff tubes were in good condition after the subsequent test series.

(C) Because the temperature of the tapoff gases during the first test was based upon extrapolating transient data (a shielded thermocouple was used) it was decided to enlarge the annular gap to 0.012 inch. Three tests conducted with this gap size resulted in relatively low temperatures. The gap was then reduced to 0.009 inch, and tests were conducted at chamber pressures ranging from 290 to 483 psia. The tapoff gas temperature varied from 940 to 1030 F over this range of pressures. Test conditions and results are summarized in Table 5.

(C) TABLE 5

TAPOFF TEST RESULTS

Test Number	Gap, inches	Recess, inches	Chamber Pressure, psia	Gas Temperature, F	Tapoff Flow, percent	C* percent
113	0.006	0.20	423	-	-	98
112	0.006	0.30	411	1600*	1.1	96
130	0.009	0.30	290	1020	1.2	93.5
129	0.009	0.30	353	940	1.1	92.9
131	0.009	0.30	483	1030	1.4	91.8
117	0.012	0.30	274	335	1.4	90.5
118	0.012	0.30	468	400	1.5	91.5
116	0.012	0.37	282	150	1.4	90.3

*Extrapolated

(C) Data from the first two tests with relatively high tapoff gas temperature indicate that high injector performance can be maintained by the proper combination of annular gap and tapoff tube insertion depth. It should be noted that the design gas temperature for the engine is in this range (1500 F).

g. Feed System Stability

(C) Feed system stability is related to the injector pressure drops. Because the gaseous hydrogen pressure drop varies almost linearly with flowrate, a relatively high GH_2 injection pressure drop is maintained over the entire throttle range. The pressure drop on the fluorine side of the injector would vary with the square of the flowrate if the fluorine were liquid throughout the throttle range. This would result in a variation of 81:1 in ΔP over the throttling range of 9:1. For a design pressure drop of 160 psi at full thrust this would result in an LF_2 pressure drop of only 2 psi when throttled to the lowest thrust level.

(U) Fortunately, as the chamber is throttled the heat input to the fluorine (Btu/lb) from the combustion gases and (in the regeneratively cooled chamber) from the heated GH_2 increases and results in partial gasification of the LF_2. Only a small amount of vaporization is necessary to significantly increase the pressure drop and stabilize the oxidizer injection system. If this vaporization begins to occur at a sufficiently high thrust level such that the LF_2 pressure drop is adequate for stability, the system will be stable over the entire throttling range.

(C) Solid wall segment tests conducted early in the program with ambient temperature GH_2 experienced feed-system-coupled instabilities on tests attempted below approximately 170 psia. The magnitude of these oscillations was reduced by orificing the facility so that operation at chamber pressures as low as 65 psia was possible although oscillations were intermittently present on some of the tests. Under a company sponsored effort, the three-row triplet injector was operated at thrust levels down to less than 8 percent of rated thrust. The resulting variation of pressure drop and chamber pressure is shown in Fig. 41. Almost all of the LF_2 was vaporized at the lowest chamber pressure (the percent vaporization increases rapidly for throttling ratios greater than approximately 8:1) with resulting stable operation. It will be shown in Section IV that stable operation over the throttling range resulted when an injector with an even lower nominal value of $\Delta P_{inj}/P_c$ was used in a tube wall segment with the heated hydrogen fed into the injector.

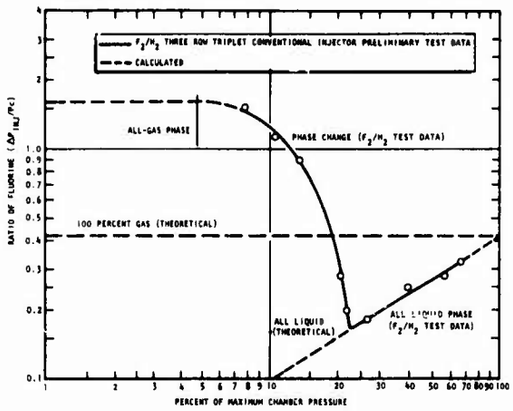

Figure 41. Ratio of F_2 Injector Pressure Drop/Chamber Pressure vs % Maximum P_c

h. Significant Performance Results

(C) The results of the solid wall segment test evaluation program have demonstrated important trends in the effects of contour shape on the C* efficiency and that high efficiencies can be obtained by taking advantage of these effects. The importance of GH2 injection velocity was also shown to be significant, and the magnitude of the C* efficiency attainable (99 percent) with heated hydrogen was accurately predicted. Mixture ratio bias tests, while of a preliminary nature, did indicate that significant performance losses could result from application of this method of heat transfer rate control. The injector tapoff test results indicated that, by proper selection of geometric parameters, high performance and constant tapoff gas properties could be maintained over the chamber pressure range tested (290 to 483 psia).

7. HEAT TRANSFER ANALYSIS

(U) Analysis of the test data was directed towards determining the effect of various parameters on the heat transfer rates throughout the thrust chamber and, particularly, at the throat of the nozzle. The effects of chamber geometry, injector pattern, propellant injection velocities, mixture ratio bias, hot gas tapoff, and surface effects were evaluated. A summary of experimental parameter variations is shown in Table 6.

The method of analyzing the heat transfer data is first discussed followed by presentation of the results for each of the above effects.

a. Method of Analysis

(U) The heat transfer test data included the coolant water flowrate and overall bulk temperature rise for each transverse water coolant passage in the chamber nozzle. The water flowrates were measured with turbine flowmeters, and the bulk temperature rises were determined with chromel-alumel thermopiles installed to measure directly the difference between the inlet and outlet temperatures at each passage.

(U) The heat transfer rate into each water passage is given, in terms of the water flowrate $(\dot{m})$ the water specific heat (C_p), and the water bulk temperature rise (ΔT_b) by:

$$Q = \dot{m} \; C_p \; \Delta T_B \tag{7}$$

(U) The average chamber heat flux in the region of each coolant passage is obtained by associating a one-dimensional gas-side heat transfer area with the passage and dividing the heat transfer rate into the passage by the appropriate area:

$$Q/A = \frac{\dot{m} \; C_p \; \Delta T_B}{A} \tag{8}$$

(U) The coolant-side film coefficient is computed using the ralation:

$$h_c = 0.023 \; \frac{k}{D} \; \left(\frac{VD\rho}{\mu}\right)^{0.8} \; \frac{C_p}{k}^{0.4} \tag{9}$$

where k, ρ, μ, and V are the thermal conductivity, density, viscosity and velocity respectively of the coolant water.

TABLE 6

SUMMARY OF EXPERIMENTAL PARAMETER VARIATIONS

(Mixture Ratio (NOM) = 13:1)

Variation	P_c Range (psia)	Number of Tests
Throat Convergence Angle		
15 degree - Contour E	316-604	5
30 degree - Contour C	65-511	15
Combustion Chamber Contour		
Round - Contour A	305-616	12
Curved - Contour B	106-566	18
Straight - Contour C, D, and E	65-604	28
Converging - Contour F and G	63-666	80
Combustion Chamber Length		
3.5 in. - Contour E	316-604	5
5.0 in. - Contour D	303-559	8
Injector Pattern (Basic)		
Triplet		
Contour C	65-511	15
Contour E	316-604	5
Impinging Fan		
Contour C	550	1
Contour E	229-518	9
Hydrogen Injection Velocity		
M_{GH_2} = 9	65-511	15
M_{GH_2} = 0.65	119-480	13
M_{GH_2} = 0.4	319-534	5
Injector Mixture Ratio Bias		
Contour C - Triplet	448	1
Contour E - Triplet	435-501	3
Hot Gas Tapoff		
Contour E - Triplet	274-483	9
Chamber Wall Surface Condition		
Nickel Plating	331-425	7
Chrome Plating	402-464	2
GF_2 vs LF_2 Injection		
Contour E - Triplet	20-49	4

(U) A coolant -side wall temperature, T_{WC}, assuming forced convection with no nucleate boiling is then computed from the bulk temperature, T_B, as:

$$T_{WC} = T_B + \frac{q/A}{h_c} \tag{10}$$

(U) If this value exceeds the coolant saturation temperature, T_{sat}, the coolant-side is assumed to be in a nucleate boiling regime and the coolant-side wall temperature is found by the relation:

$$T_{WC} = T_{SAT} + 50 \tag{11}$$

(U) Otherwise, the value for forced convection given by Eq. 10 is used. An average gas-side film coefficient is then obtained for each passage using the one-dimensional equation:

$$h_g = \frac{q/A}{(T_{AW} - T_{WC}) - \sum \frac{X}{k_W} q/A} \tag{12}$$

(U) X and k_W are the effective thickness and thermal conductivity, respectively, of the wall between the chamber and the cooling passage. The adiabatic wall temperature, T_{AW} is obtained from the actual combustion temperature by the relation:

$$T_{AW} = T_C \frac{1 + \sqrt[3]{N_{PR}} \frac{\gamma-1}{2} M_\infty^2}{1 + \frac{\gamma-1}{2} M_\infty^2} \tag{13}$$

(U) N_{PR} is the Prandtl number, γ is the specific heat ratio, and M_∞ is the free-stream gas Mach number.

The actual combustion temperature, T_c, is given in terms of the ideal combustion temperature corresponding to 100 percent combustion efficiency by:

$$T_C = T_{C_{ideal}} \eta C^{*2} \tag{14}$$

(U) Although the coolant passage geometry is highly two-dimensional, a one-dimensional relation such as Eq. 12 will yield correct heat transfer coefficients if the proper value of the wall thickness is used. Use of the arithmetic average between the maximum and minimum "reaches" for each passage is substantiated by the conduction analysis of the segment chamber (Appendix A).

(U) During short duration tests (2-5 seconds), the high heat-sink capacity of the copper block in the region behind the coolant passages prevents the chamber from entirely reaching steady-state operation. As a result, a slight amount of heat leaks past the coolant passage into the copper backup structure. The amount of leakage depends upon the coolant spacing and the local heat flux. For the small spacings and heat-transfer-rates characteristic of the test segments, the results of a two-dimensional transient conduction analysis indicate that the amount of heat leakage should be less than 0.5 percent in the throat region and less than 2 percent in the lower heat flux regions of the combustion zone.

(U) Heat-transfer data correlations using either the locat heat flux or gas-side flow coefficient have two distinct disadvantages: (1) these parameters are functions of chamber pressure, propellant combustion, mixture ratio, and characteristic velocity efficiency; and (2) these parameters vary strongly with the local mass velocity (area ratio) and therefore increase at a rapid rate in the throat region. A more general correlating parameter can be obtained by non-dimensionalizing the heat transfer coefficient by dividing it by $\rho V C_p$ to form the Stanton number and multiplying by $(C_p \mu)^{2/3}/k$, thereby forming the Stanton-Prandtl parameter which is related to Reynolds number based upon the momentum boundary layer thickness through the modified Reynolds' analogy

$$N_{ST} \times N_{PR}^{2/3} \propto \left(\frac{\rho V \theta}{\mu}\right)^{-0.25} \qquad (15)$$

where θ is the momentum boundary layer thickness.

(U) This relation indicates that the Stanton-Prandtl parameter is a weak function of local mass velocity and hence chamber pressure, area ratio, and characteristic velocity efficiency, and also a weak function of combustion product properties. It can be used to provide a direct indication of the local boundary layer development. The distribution of this parameter along a thrust chamber wall surface indicates which regions of the chamber contour are effective in promoting boundary layer growth.

(U) In addition, using turbulent flow analogies between energy and momentum transfer, the Stanton-Prandtl parameter can be closely related to the skin friction coefficient. For flow over a flat plate

$$N_{ST} \times N_{PR}^{2/3} = \frac{C_F}{2} \qquad (16)$$

(U) This relationship is affected by the presence of free-stream turbulence, pressure gradients, and surface roughness. However, based upon this simplified relationship of Eq. 16, typical experimental values of skin friction coefficient vs length Reynolds number can be used to indicate approximate values of $N_{ST} \times N_{PR}^{2/3}$.

(U) Since none of the coolant passages are located exactly at the nozzle throat, several methods were considered for extrapolating measured average heat transfer rates to obtain throat peak values. The method adopted involves plotting the average values of $N_{ST} \times N_{PR}^{2/3}$ vs area ratio on both the upstream and downstream sides in the throat region. A typical plot is shown in Fig. 42. Local average values of the Stanton-Prandtl parameter are plotted over the area ratio region associated with each passage. A predicted continuous distribution is obtained by a graphic integration, and the throat peak value is determined. A throat peak gas-side film coefficient adjusted to a mixture ratio of 13.0 is obtained from the relation:

$$h_{g)_{peak}} = (N_{ST} \times N_{PR}^{2/3})_{peak} \quad N_{PR}^{-2/3} \quad \left(\frac{m_{total}}{A_{throat}}\right)(C_p) \tag{17}$$

(U) The throat peak heat flux for a wall temperature of 1600 F is computed by:

$$q/A)_{peak} = h_{g)_{peak}} \quad (T_{AW} - 1600) \tag{18}$$

b. Contour Variations

(U) The contour variables investigated were the convergence angle, the contour curvature, and the distance from the injector to the throat. The influence of convergence angle is seen by comparing contour C and E data. Data from contours A, B, and C provide information to compare combustion chamber curvature effects. The results of the tests of contour D and E indicate the effects of chamber length. For each of these comparisons, a common injector was used (basic triplet) so that this influence would not be present. (For contour geometries, refer to Figures 20, 21, 22, 24, and 25).

(C) Throat Convergence Angle (15 degree vs 30 degree). A comparison of the data from contours C and E presented in Fig. 43 show a substantial reduction in the local heat transfer rates in the convergence section, throat, and low-area-ratio diverging region of the nozzle for the 15-degree converging angle nozzle over the 30-degree converging angle values. However, it appears that this reduction should not be attributed to the reduced convergence angle, but rather to the accompanying increase in convergence section length. The length from the start of convergence to the throat is approximately 2.1 inches for contour E and only 1.3 inches for contour C. The local heat transfer rate distribution is plotted as a function of length along the contour from the start of convergence for the 30-degree and 15-degree chambers in Fig. 44. This shows that, at the same convergence length from the start of convergence, the 15-degree chamber rates are similar to the 30-degree rates. The gas-dynamic start of convergence does not correspond exactly to the geometric point (plotted) and may explain the displacement between the curves in Fig. 44.

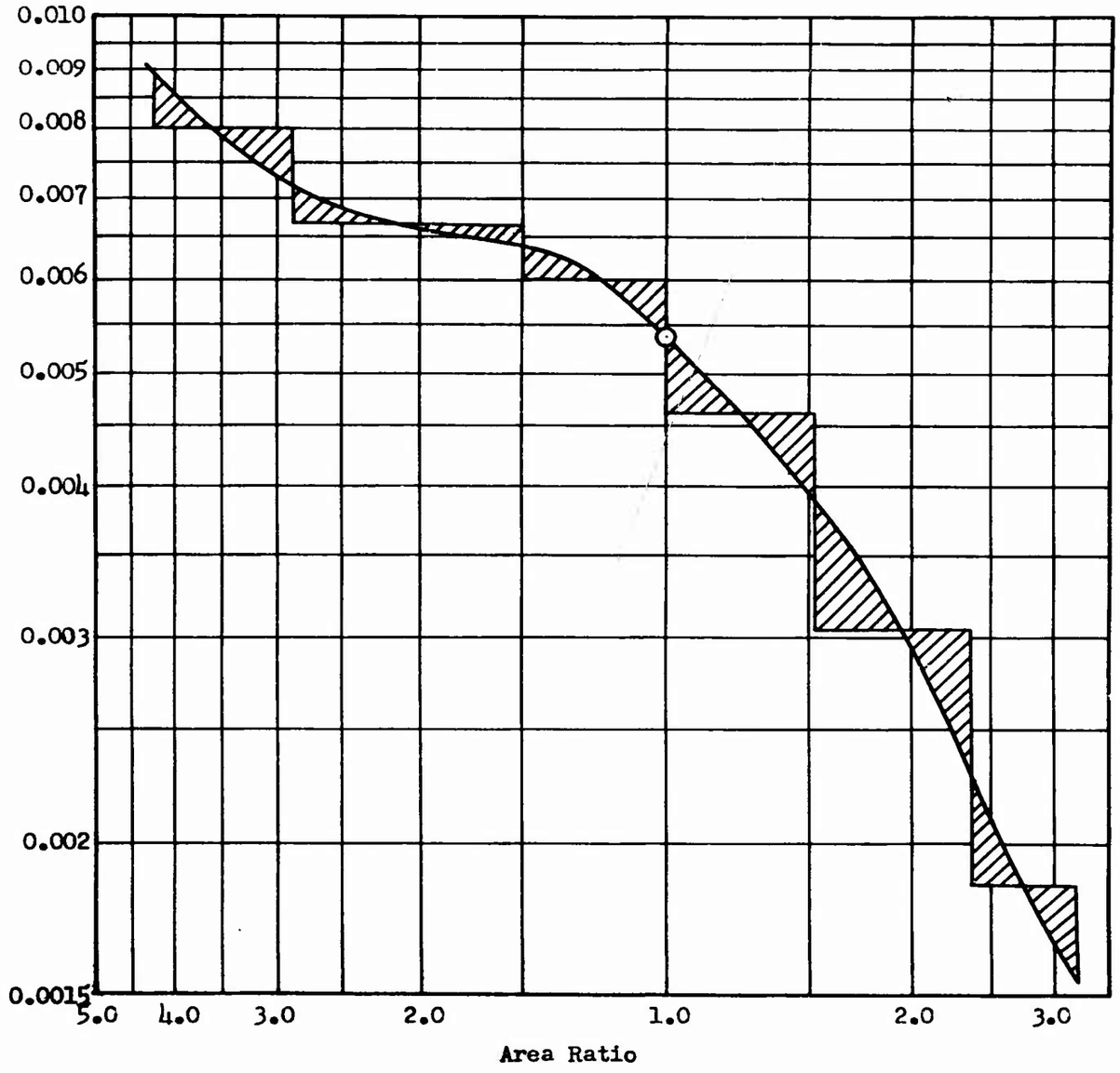

Figure 42. Typical Plot of $N_{ST} \times (N_{PR})^{2/3}$ vs Area Ratio

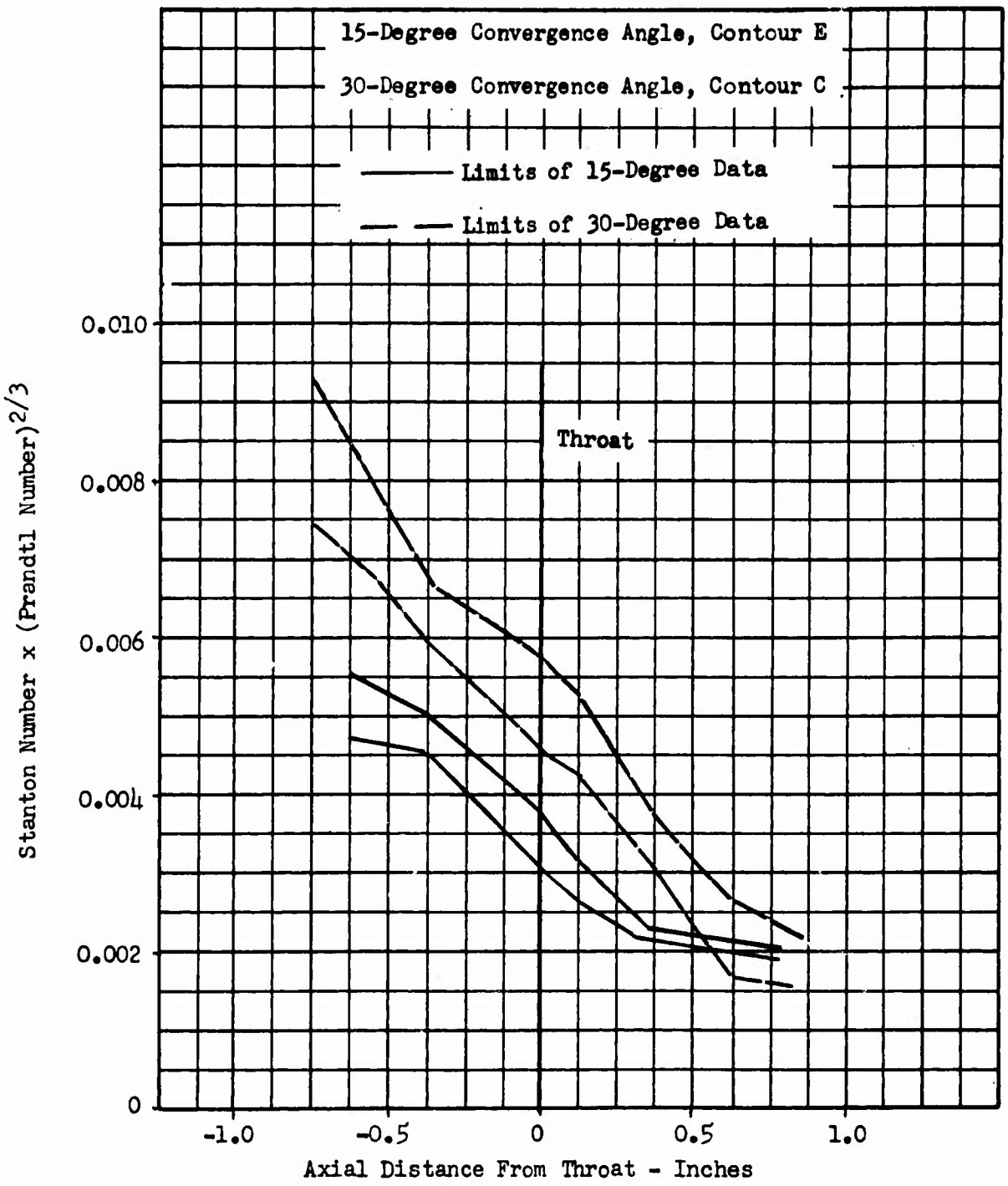

Figure 43 . Effect of Convergence Angle on Nozzle Heat Transfer for 3.5 Inch Chamber Length Segment

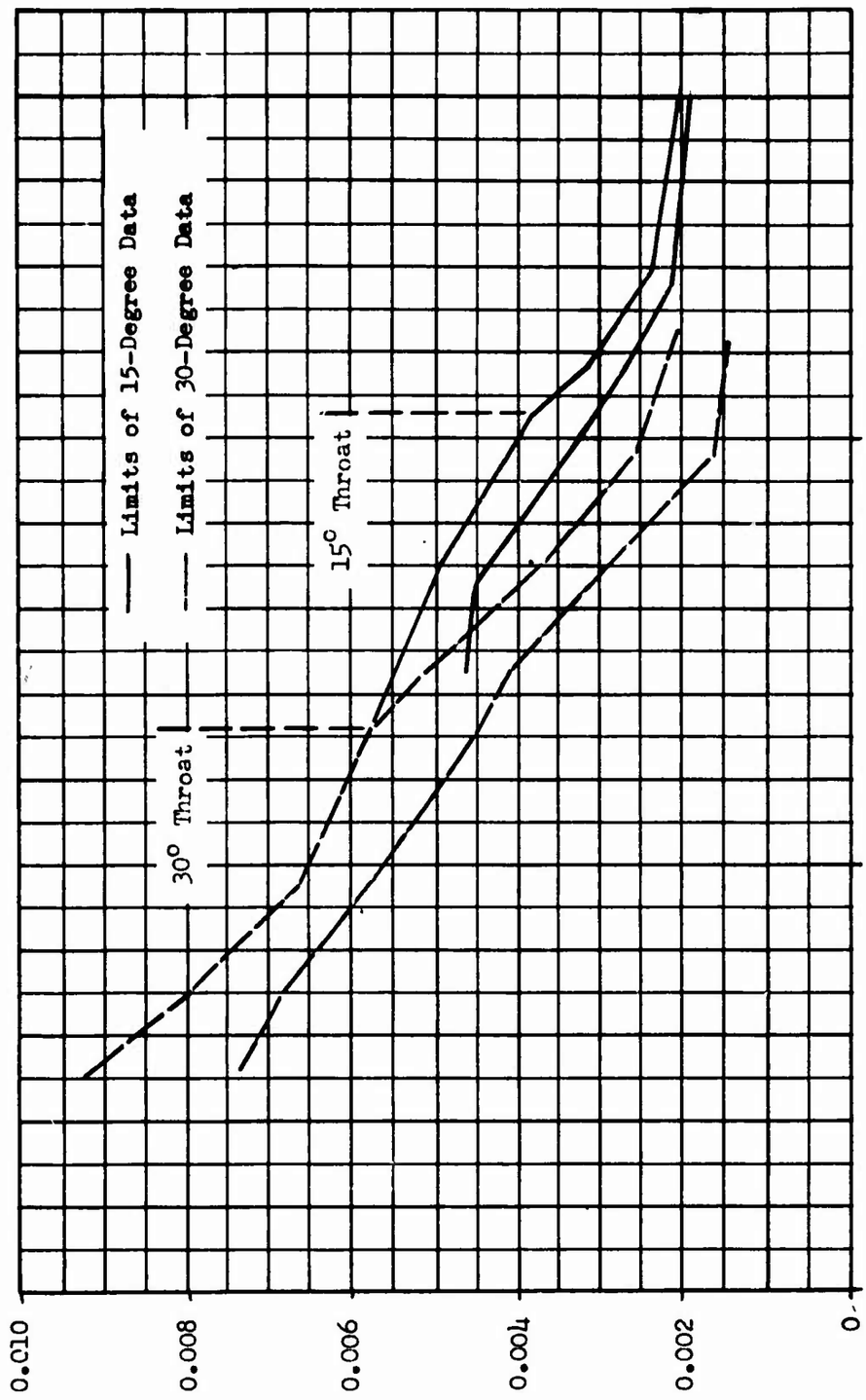

Figure 44. Comparison of 15- and 30- Degree Throat Convergence Angle Heat Transfer Rates - Effect of Length Along Contour From Start of Convergence

(U) Since the heat transfer rate distributions for both configurations show rapid reduction in the local Stanton-Prandtl number beginning at the start of convergence and continuing into the nozzle, it is probable that the lower throat region heat transfer rates of the 15-degree chamber resulted from the additional convergent length. The fact that the local heat transfer rates fall off rapidly in the convergence section indicates that the favorable pressure gradient plays an important part in stabilizing the boundary layer and in promoting its growth.

(C) Combustion Chamber Contour. The $N_{ST} \times N_{PR}^{2/3}$ profiles for the identical nozzle portions of contours B and C were found to be essentially the same (Fig. 45) indicating that there were no lasting effects resulting from the differing upstream combustion-zone geometries. Contour A did not have a separate nozzle section nor did the expansion region continue much beyond the throat. The basic flow convergence appears to start approximately one inch upstream of the throat where it is seen (Fig. 46) that the data tend to coalesce markedly. The $N_{ST} \times N_{PR}^{2/3}$ parameter then decreases rapidly as the throat is approached, and the flow is rapidly accelerated. The resulting throat heat transfer rates for contour A are slightly higher than the values for the 15-degree convergence half-angle nozzle geometry of contour E.

(C) Combustion Chamber Length. Combustion chamber lengths of 3.5 and 5.0 inches (axial distance from injector to throat) were tested with the 15-degree convergence-angle throat section. Heat transfer measurements were obtained for these two configurations (contour D and E) in the throat region only, since the combustion zone sections used with these configurations were uncooled in the initial test configurations. The throat-region heat transfer rates for the two combustor lengths tested are compared in Fig. 47 and no significant difference was observed for these two particular geometries.

c. Injector Types and Variations

(U) The effects of two injector characteristics (the injector face pattern and the GH_2 injection velocity) were investigated.

(C) Injector Pattern (Triplet vs Fan) One test was conducted with the impinging fan injector in contour C (the straight wall chamber with a 30-degree converging angle nozzle). Seven tests were conducted with this injector in the contour E (straight wall chamber with a 15-degree converging angle nozzle).

(C) Heat transfer data for the entire combustion zone and nozzle were obtained for the contour C firing. The heat transfer rates are compared to those obtained with the triplet injector in the same contour in Fig. 48. The variation with length was very similar for both injector types, although the magnitudes differ, indicating that the tests were a valid comparison of injector effects. The combustion-zone heat transfer rates with the impinging fan injector were reduced 50 to 60 percent from those obtained with the triplet injector. At the throat, the impinging

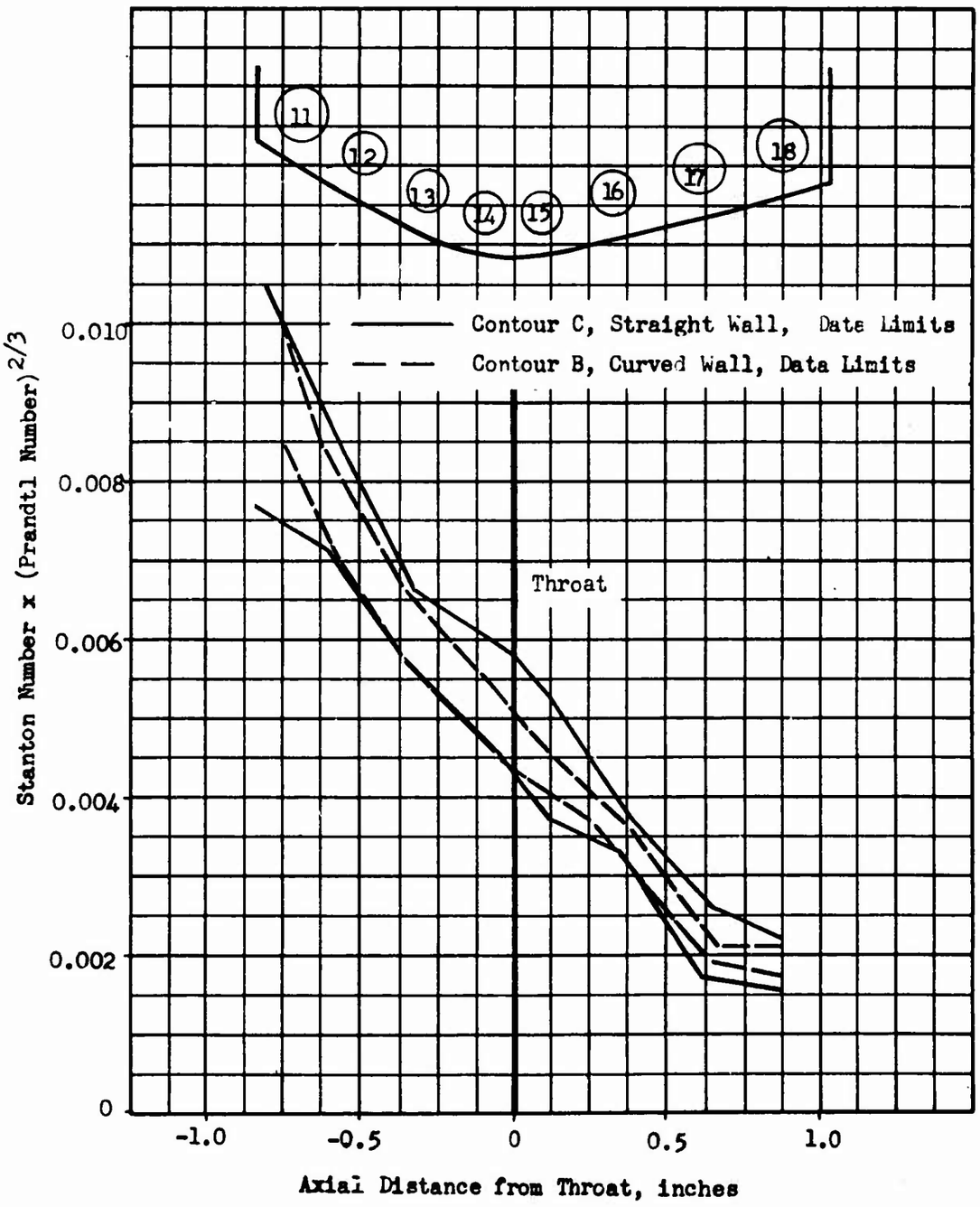

Figure 45. Effect of Combustion Chamber Contour on 30-Degree Nozzle Heat Transfer Rates

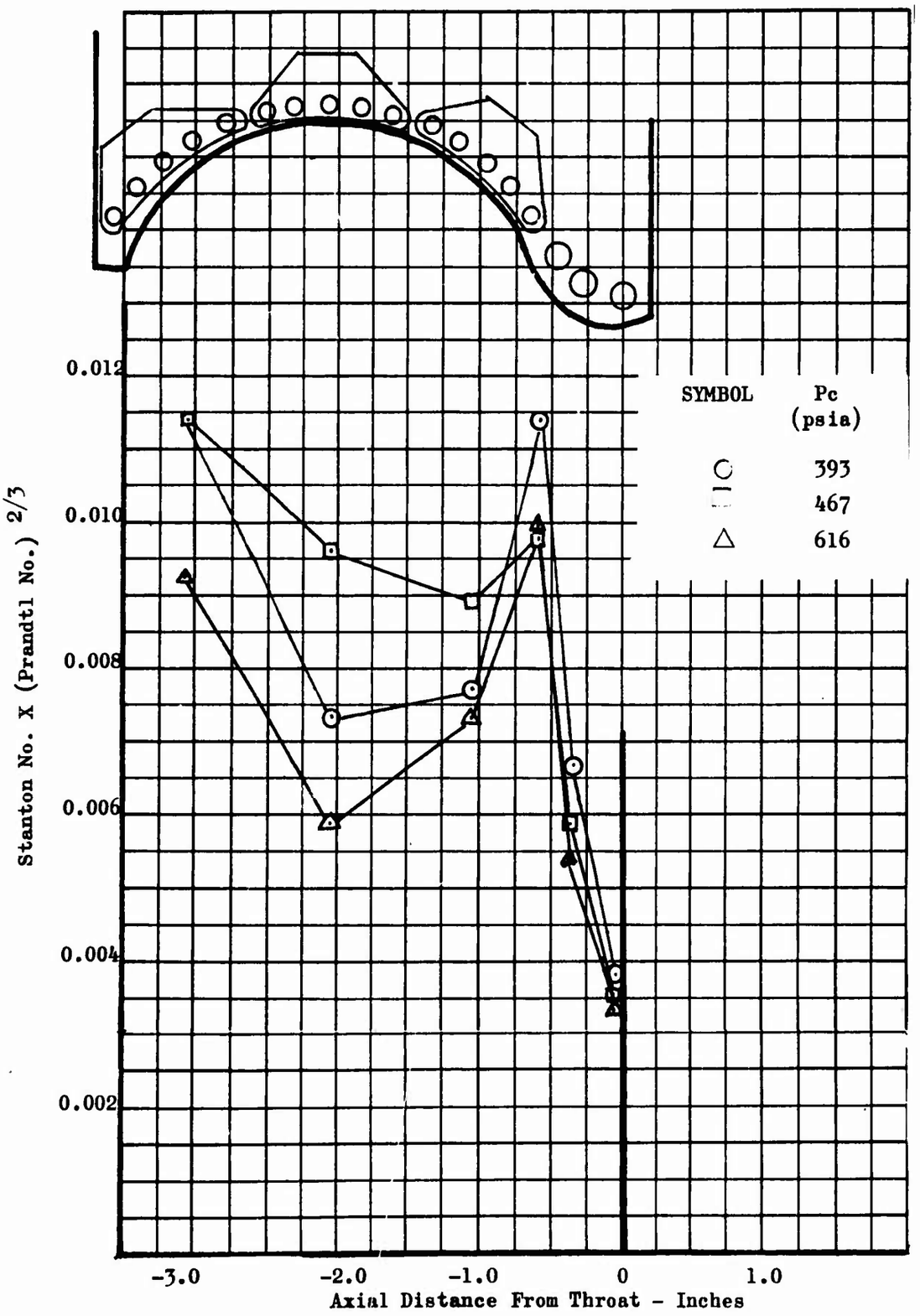

Figure 46 . Variation in Heat Transfer Parameter with Axial Distance for Contour A

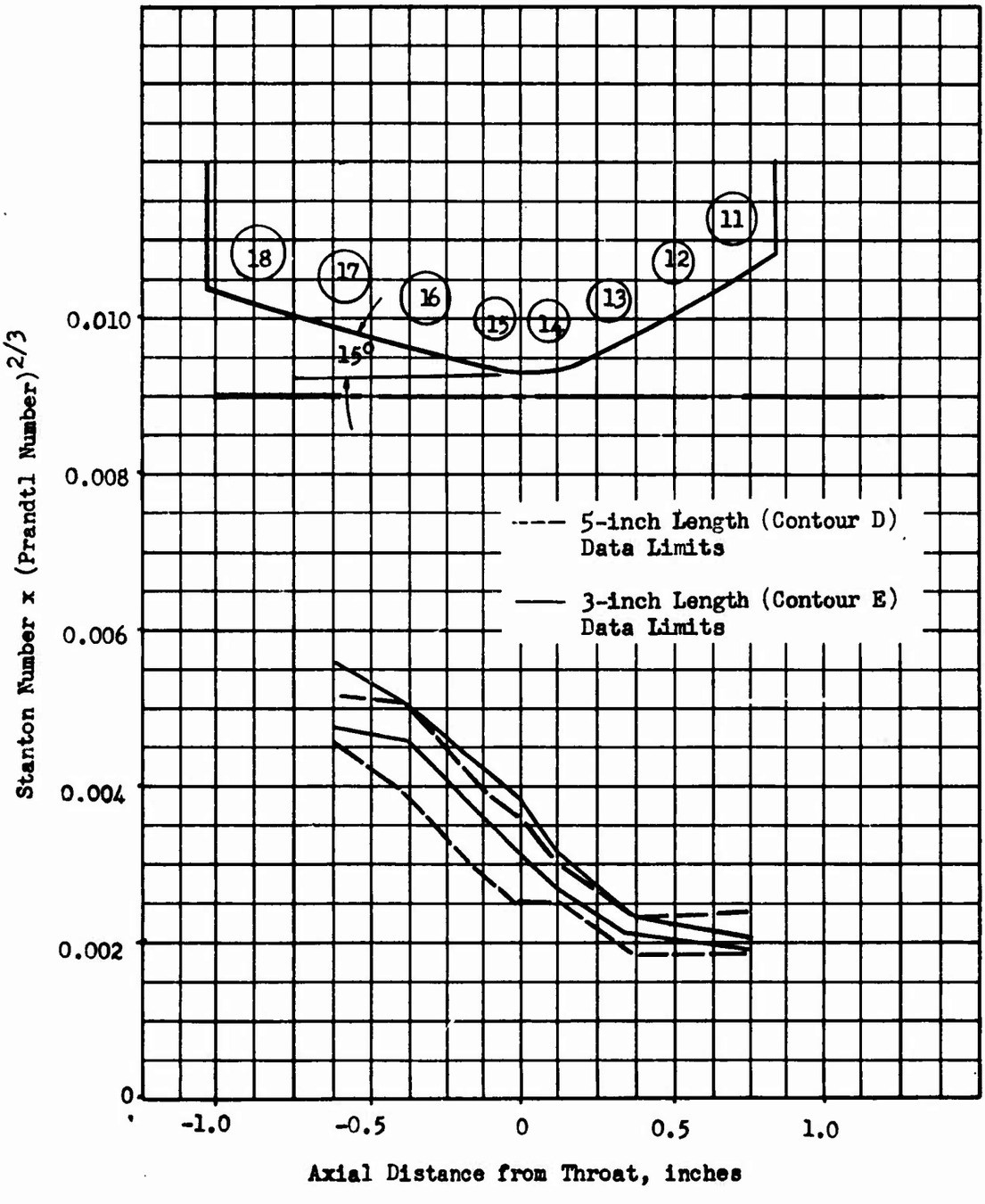

Figure 47 . Effect of Combustion Chamber Length on Nozzle Heat Transfer Parameter for 15-Degree Convergence Angle Segment

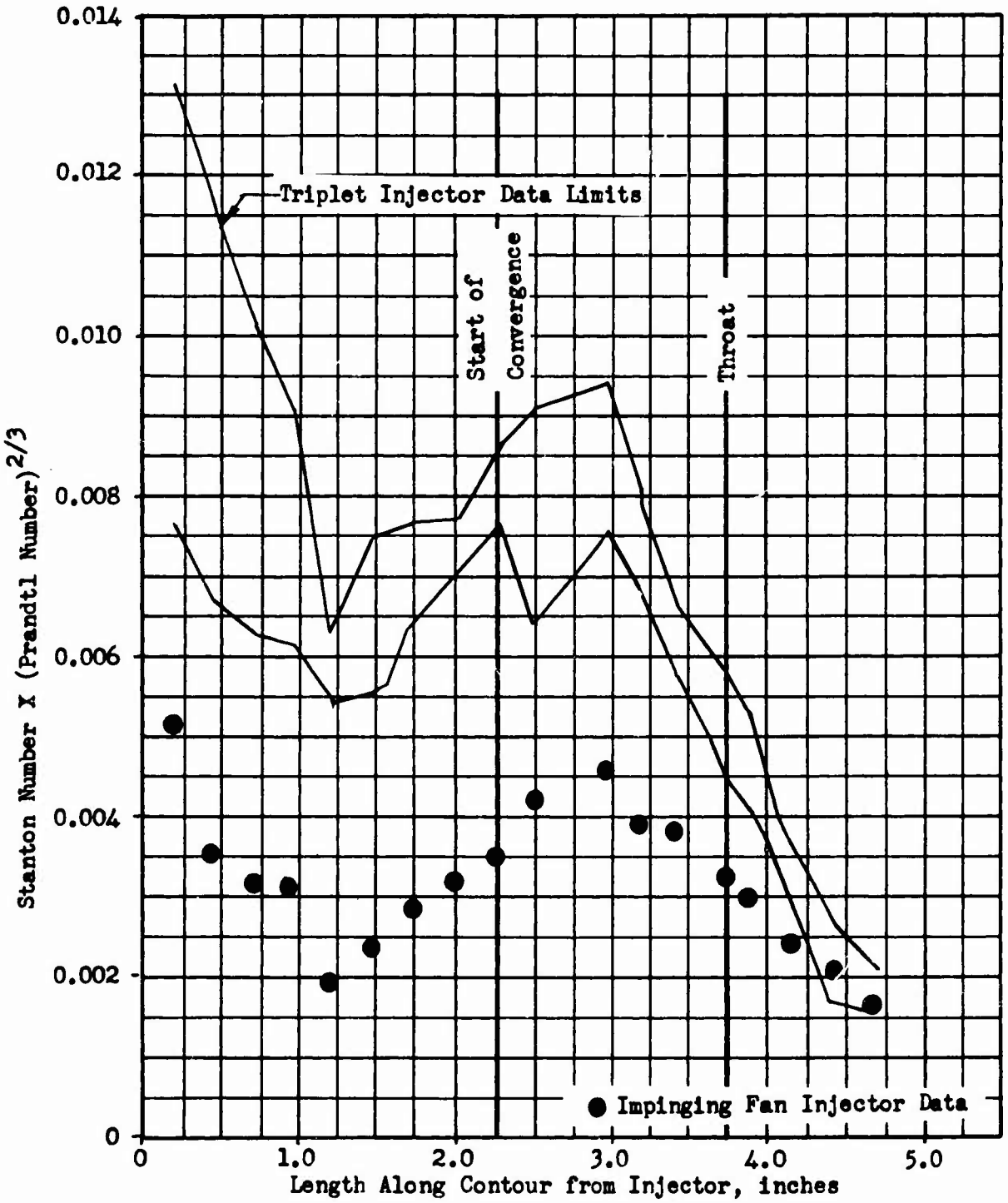

Figure 48 . Effect of Injector Type on Heat Transfer Parameter Profile in Contour C

(C) fan injector exhibited a heat transfer rate 37 percent lower than the triplet. Near the nozzle exit, the values for the two injectors were similar.

(C) The data obtained from the contour E firings with the triplet were limited to the nozzle region only, since the combustion zone was uncooled. As shown in Fig. 49 the first, or furthest upstream impinging fan data point was appreciably below the data band for the triplet injector. However, the impinging fan data agreed with the triplet injector data in the vicinity of the throat. Except for locations close to the injector and close to the nozzle exit, the heat transfer parameter profiles with the impinging fan injector were comparable for both contours C and E.

(C) Hydrogen Injection Velocity. The effect of hydrogen injection velocity on heat transfer rates was investigated by enlarging the hydrogen orifices of the triplet injector. The nominal GH_2 injection Mach number, under segment test conditions with ambient GH_2, was approximately 0.9. The orifices were enlarged in two steps: first to provide a GH_2 injection Mach number of approximately 0.65 and again later to provide an injection Mach number of 0.40. All three injection conditions were tested in contour C and the 0.9 and 0.4 Mach numbers were also tested in contour E.

(U) The resultant combustion-zone heat transfer data for contour C is presented in Fig. 50. The combustion-zone rates exhibited the same characteristic with no apparent effect of the reduced injection velocity afforded by the larger hydrogen injection orifices.

(C) The effect of GH_2 injection velocity on the nozzle heat transfer rates in contour C is shown in Fig. 51. Assuming that the data for $M_{GH_2} = 0.4$ represent the midlocus of the corresponding data band, it may be concluded that, within the range of velocities and chamber pressures investigated, reducing the velocity had a moderate effect on the heat transfer rates in the nozzle converging section, but only a very slight effect in the throat and diverging sections. Similar trends may be seen in Fig. 52 in which the Mach 0.9 and 0.4 data are compared for the contour E configurations.

d. Mixture Ratio Bias

(U) As part of the heat transfer investigation under Task II of the program, experimental evaluations were conducted to establish the effect of injector mixture ratio bias on the combustion zone and nozzle-region heat transfer rates. Four hot firings were conducted, one in the chamber contour C and three in contour E.

(C) Combustion zone rates were only available for the firing in contour C. These rates were in general the same as those without mixture ratio bias except for a rise in the local rates near the injector. The nozzle region heat transfer parameters for the mixture ratio bias evaluations are presented in Fig. 53 and 54. The nozzle region values for 12, 21,

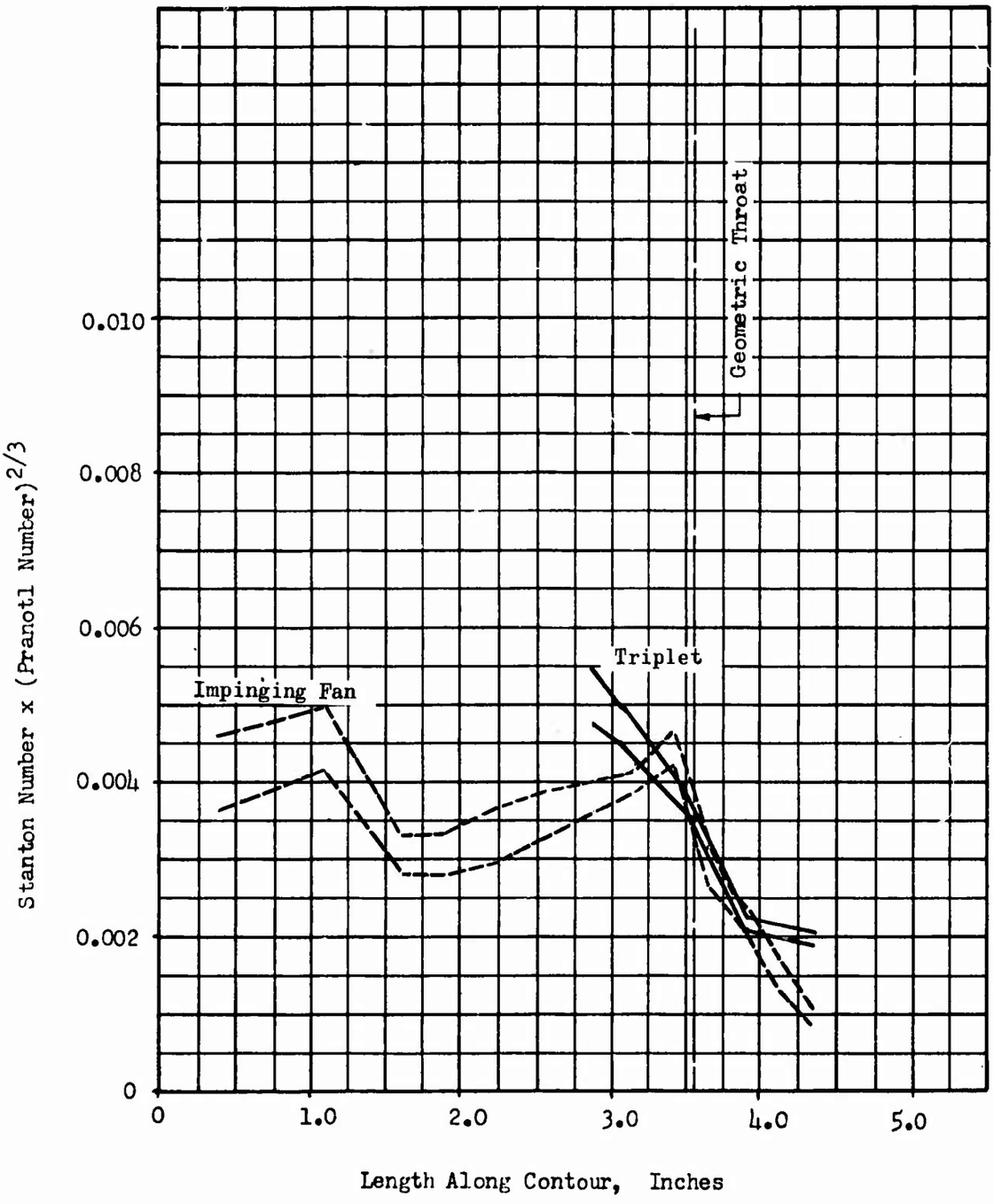

Figure 49 . Triplet and Impinging Fan Injectors Comparison of Heat Transfer Parameter Profiles in Contour E Chamber

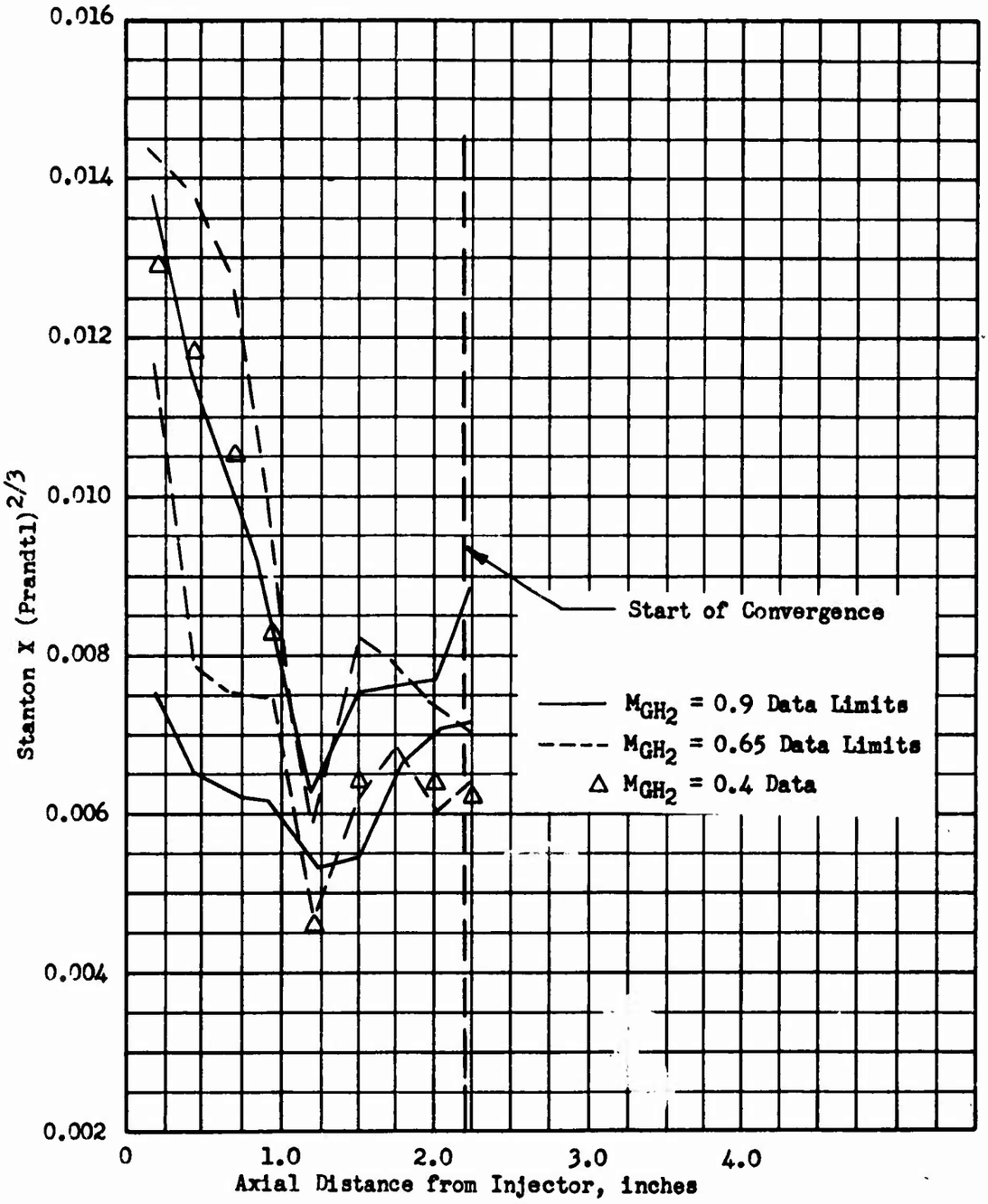

Figure 50 . Effect of GH_2 Injection Velocity on Combustion Zone Heat Transfer Parameter, Contour C

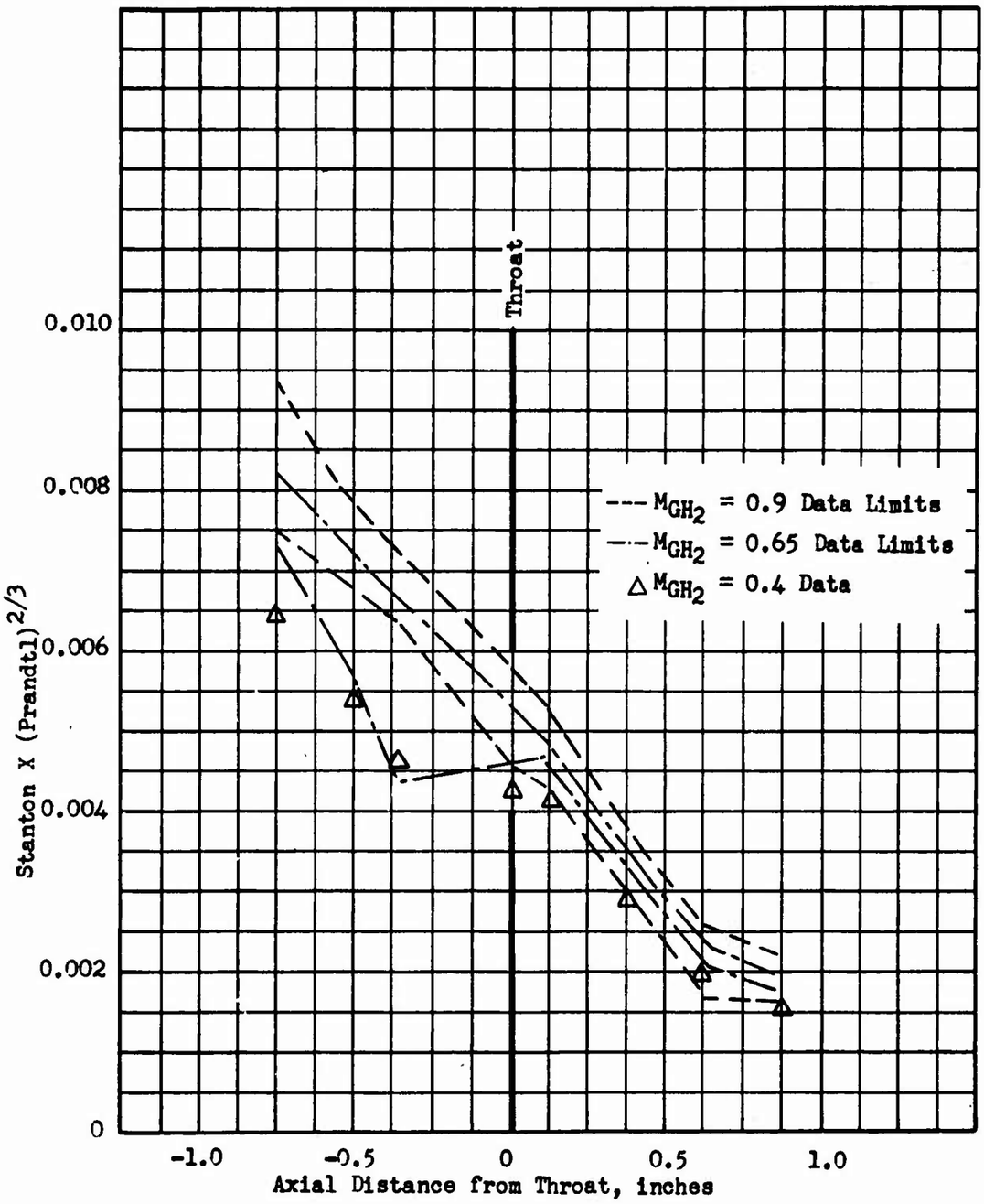

Figure 51 Effect of GH_2 Injection Velocity on Nozzle Region Heat Transfer Parameter, Contour C

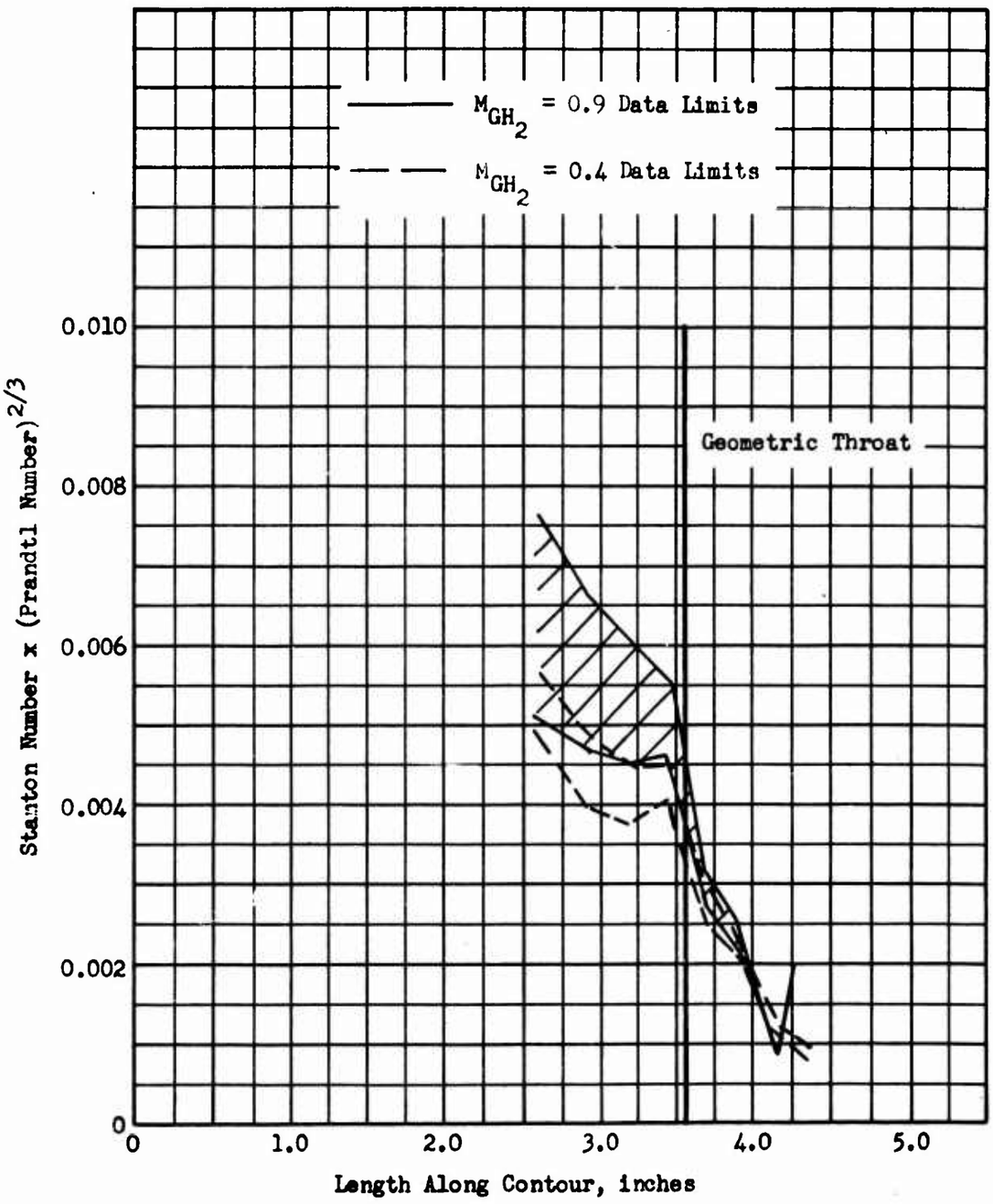

Figure 52 Effect of GH_2 Injection Velocity on Nozzle Heat Transfer Parameter - Contour E

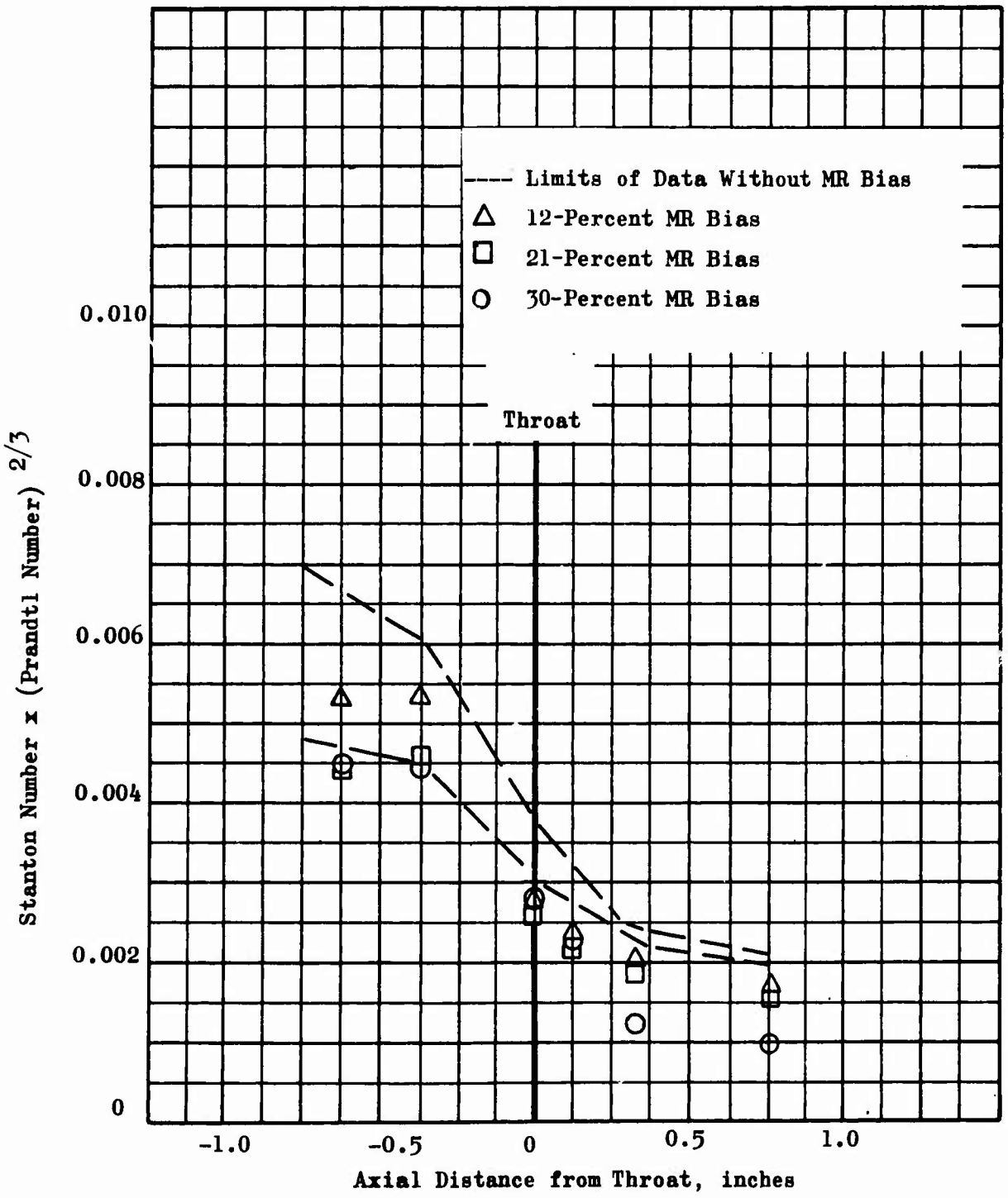

Figure 53. Effect of Mixture Ratio Bias on Nozzle Heat Transfer Parameter - Contour E.

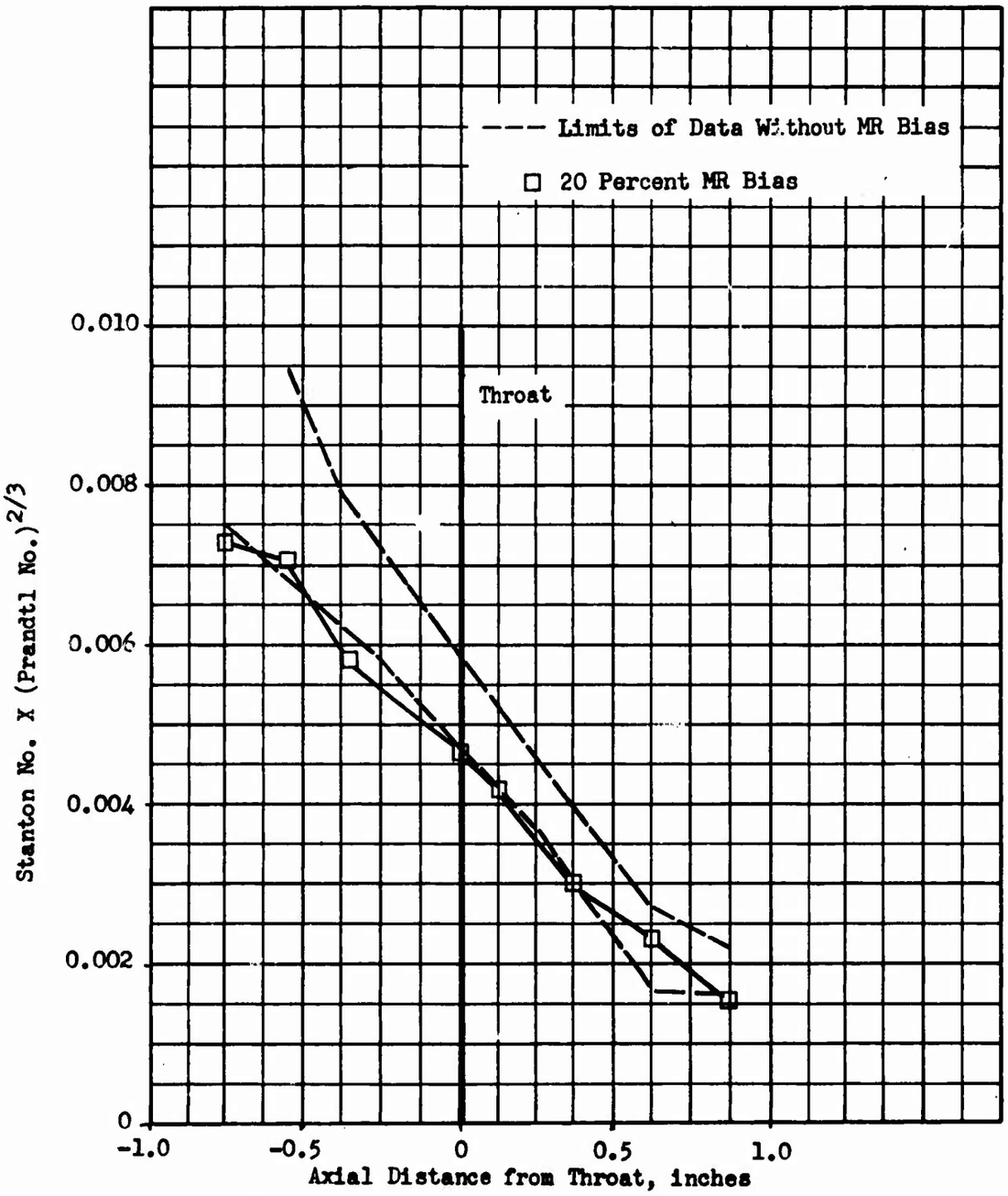

Figure 54 . Effect of Mixture Ratio Bias on Nozzle Heat Transfer Parameter, Contour C

(C) and 30 percent fuel diverted along the walls in contour E are shown in Fig. 53. For these runs, there was an indicated reduction of approximately 20 percent in throat and overall nozzle rates. Similarly, for contour C, a 12-percent reduction is indicated in Fig. 54. These values of heat transfer rate reduction are referred to the average data without mixture ratio bias. The reduction does not appear to be proportional to the bias flowrate; the reduction with 30-percent bias flow appears to be similar to that with the 12-percent flow on the contour E tests. The throat data values probably represent nearly the same actual value within the limits of repeatability.

e. Hot Gas Tapoff

(C) As discussed in detail in the previous section on Performance Data Analysis, 9 tests were conducted for evaluation of hot gas tapoff using a contour E chamber and a triplet injector. Tapoff flows of 1.1 to 1.5 percent with tapoff temperatures of 1600 to 335 F were achieved.

(C) The tapoff flows resulted in no apparent change in heat transfer. The results of the tests all fell within the previous data band for contour E. Figure 55 shows the results of two tapoff tests plotted on the previous data band. The no-tapoff data points are for a test with the particular injector used for the tapoff tests series but without tapoff flow and further substantiate the results obtained.

f. Surface Plating

(C) Two nozzle sections were chrome and nickel plated respectively to determine the effect of the surface conditions on the heat transfer rates. Previous periodic measurements of the copper surface roughness in the nozzle portion of the chamber indicated a roughness range of approximately 60 to 250 microinches (r.m.s.). This could account for a convective film coefficient increase of approximately 20 percent. Two tests were conducted with the chrome plated nozzle in the contour C configuration. Most of the chrome in the converging portion of the nozzle was depleted during these tests, and no valid comparative data were obtained.

(C) Seven tests were conducted with a nickel-plated nozzle in a contour E configuration. All seven tests were conducted at similar chamber pressures (approximately 400 psia) with very good reproducibility of the data as shown in Fig. 56. There was no apparent trend of heat transfer rates increasing with time. Post test inspection of the nickel nozzle, furthermore, indicated that essentially none of the nickel plating was lost although the surface roughness had increased slightly.

(U) The heat transfer rates measured with the nickel nozzle were found to lie on the lower edge of the band of all other contour E data; i.e., there was no significant reduction in the heat transfer rates resulting from use of the nickel-plated nozzle.

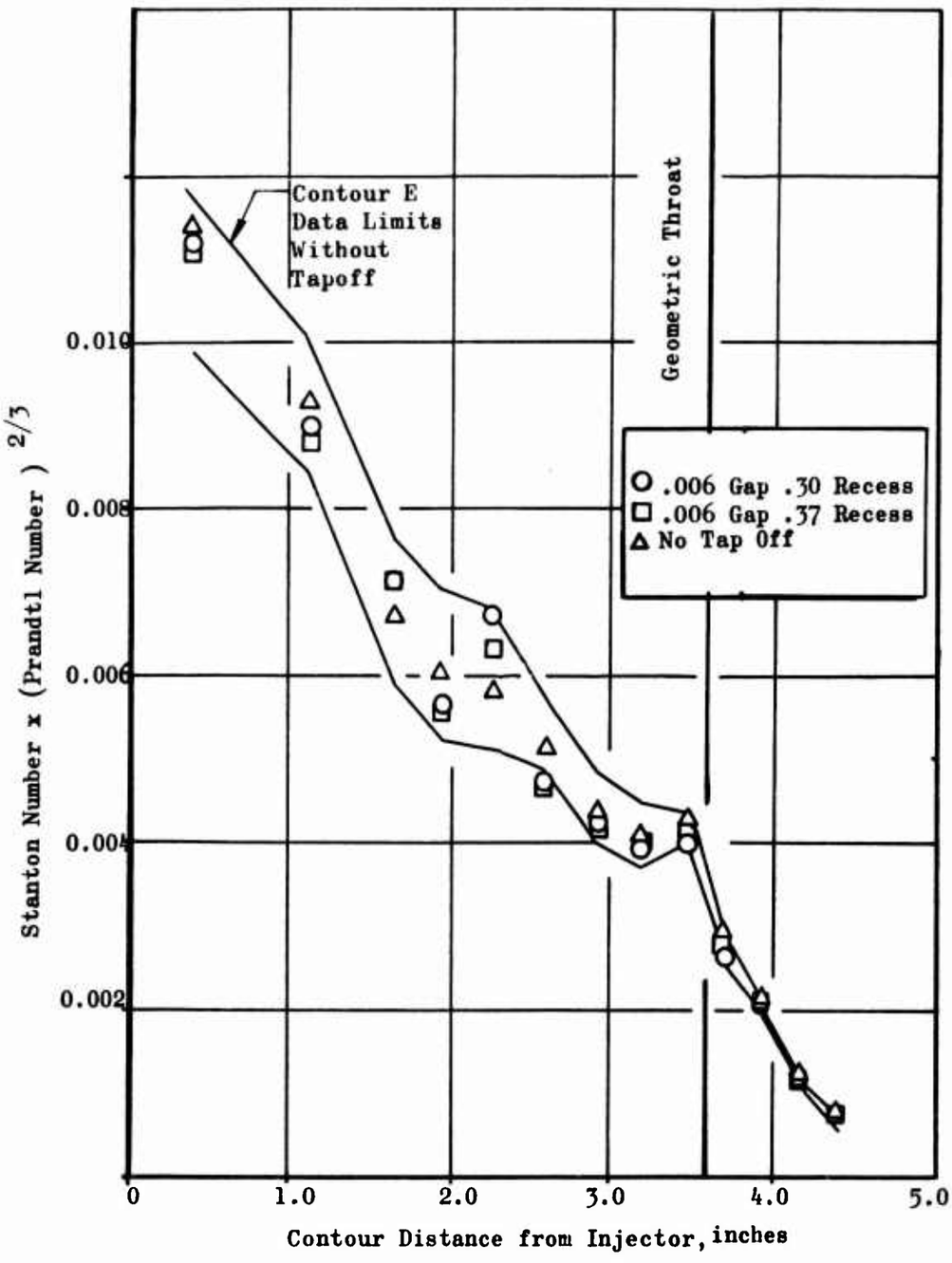

Figure 55. Effect of Tapoff on Heat Transfer
Contour E

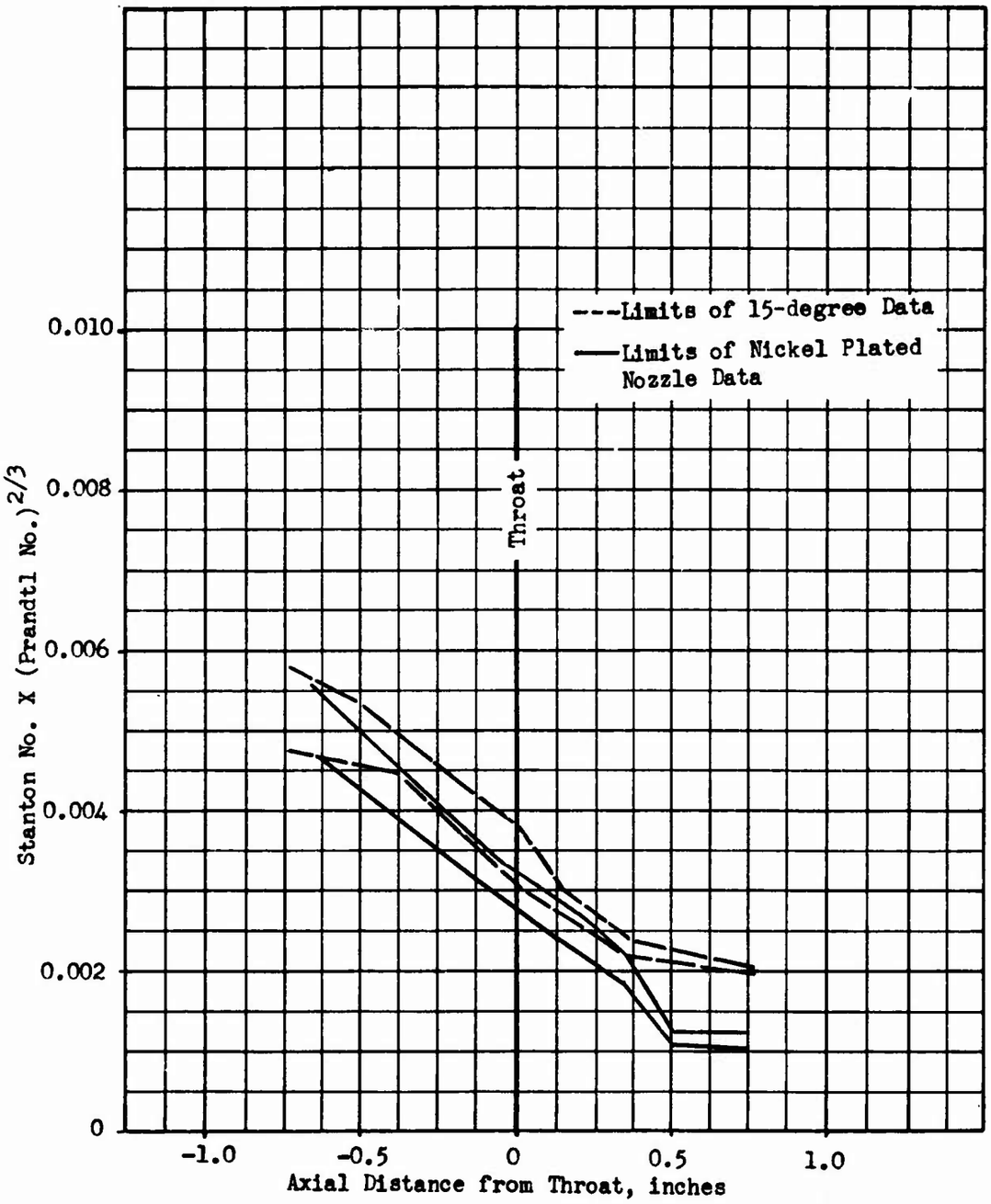

Figure 56 . Effect of Nickel Plating on Nozzle Heat Transfer Parameter, Contour E

g. Gaseous F_2 vs Liquid F_2 Injection.

(C) To evaluate the effect on heat transfer of gaseous fluorine injection as compared to the usual cryogenic injection of fluorine, a 1 inch basic triplet injector was modified and tested. The modification consisted of enlarging the fluorine orifices which resulted in the injector momentum ratio of oxidizer to fuel injection streams being non-optimum for high performance. The results of the tests nevertheless provided an approximate indication of the effect on heat transfer and are compared to a similar test of liquid fluorine injection in Fig. 57. The data indicated higher rates near the injector for gaseous fluorine but no significant difference between gaseous and liquid fluorine over the remainder of the contour.

h. Additional Chamber/Injector Variations

(U) The results from the evaluation of contours A, B, C, D, and E indicated the importance of increase in chamber convergence length for effective boundary layer growth and reduction of heat transfer rates in the throat region. To further investigate this effect, two additional chamber contours or geometries were evaluated under company sponsorship. These contours were designated F and G and are illustrated in Fig. 25.

(C) Contour F. The three tests of contour F with a triplet injector yielded the $N_{ST} \times N_{PR}^{2/3}$ distribution shown in Fig. 58. The flow attached to the wall near the third passage of the straight convergence. The abrupt change in convergence angle from the chamber to the nozzle section apparently disrupted the flow and sharply increased the local heat transfer rates at the entrance to the nozzle section. Throat heat transfer rates were at most 5 percent higher than contour E rates with the same nozzle section. These results showed the importance of a smooth continuous convergence to the throat.

(C) Contour G. In order to increase the chamber length used for boundary layer growth over that of previously tested contours and, hence, reduce throat region heat transfer rates, contour G, which converged continuously from a two inch injector width at an angle of 15 degrees, was fabricated. To achieve the required full injection, a two-inch wide three row impinging fan injector was also fabricated (Fig. 15). It was anticipated that this combined injector-combustion chamber configuration would give the maximum boundary layer growth achievable within the 3.5 inch length combustion chamber.

(C) A series of tests ranging in chamber pressure up to 645 psia was conducted with contour G. The distribution of the Stanton-Prandtl parameter along the chamber for this test series is shown in Fig. 59. This is compared with the throat region distribution of contour B obtained during earlier testing. Examination of Fig. 59 indicates that the impingement and flow attachment point as indicated by the peak value of the Stanton number has been moved substantially upstream with contour G. Because of this and although contours B and G have similar Stanton number profiles downstream of this point, the throat value for

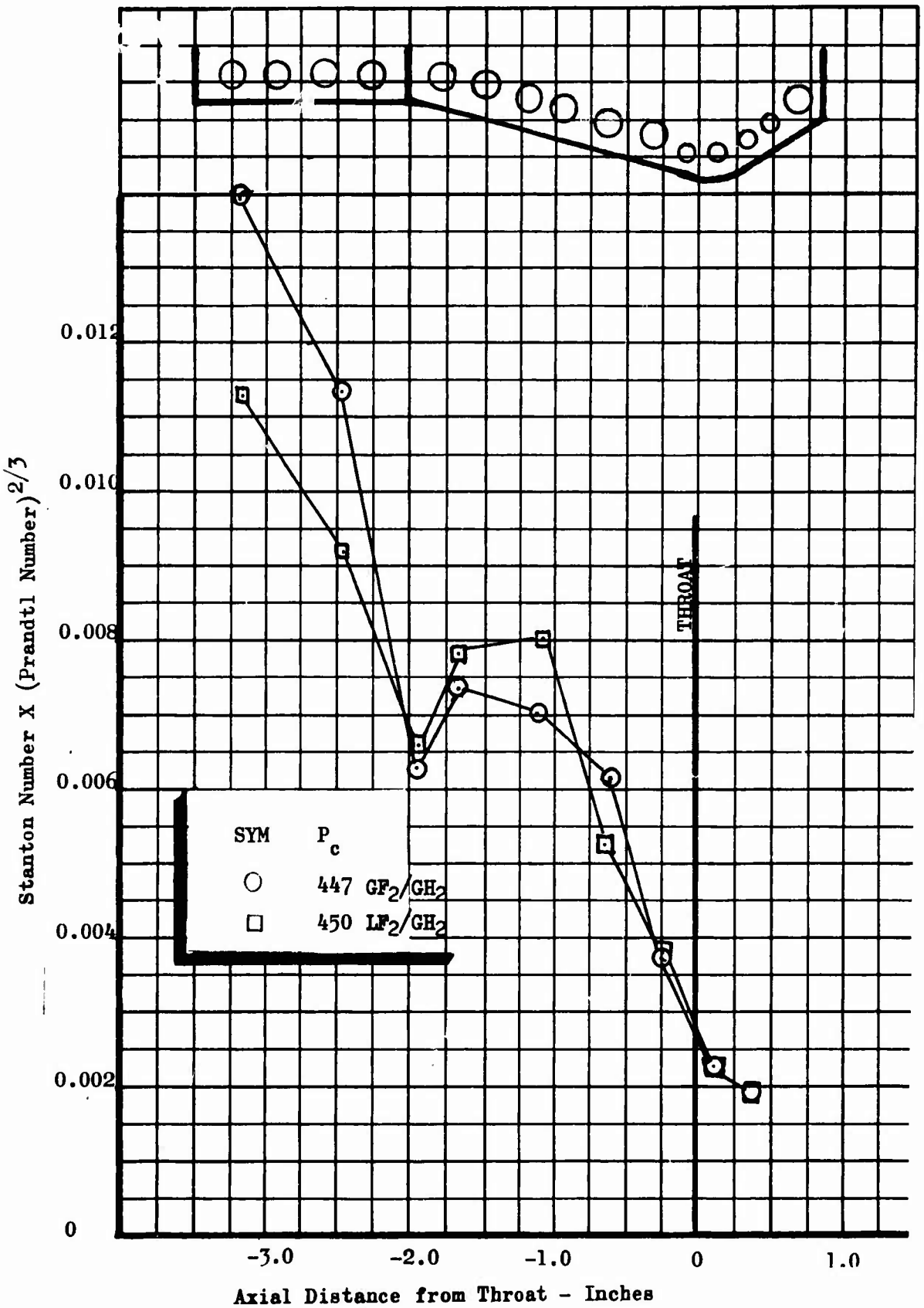

Figure 57 . Effect of Gaseous Fluorine on the Distribution of Heat Transfer Parameter Along Contour E

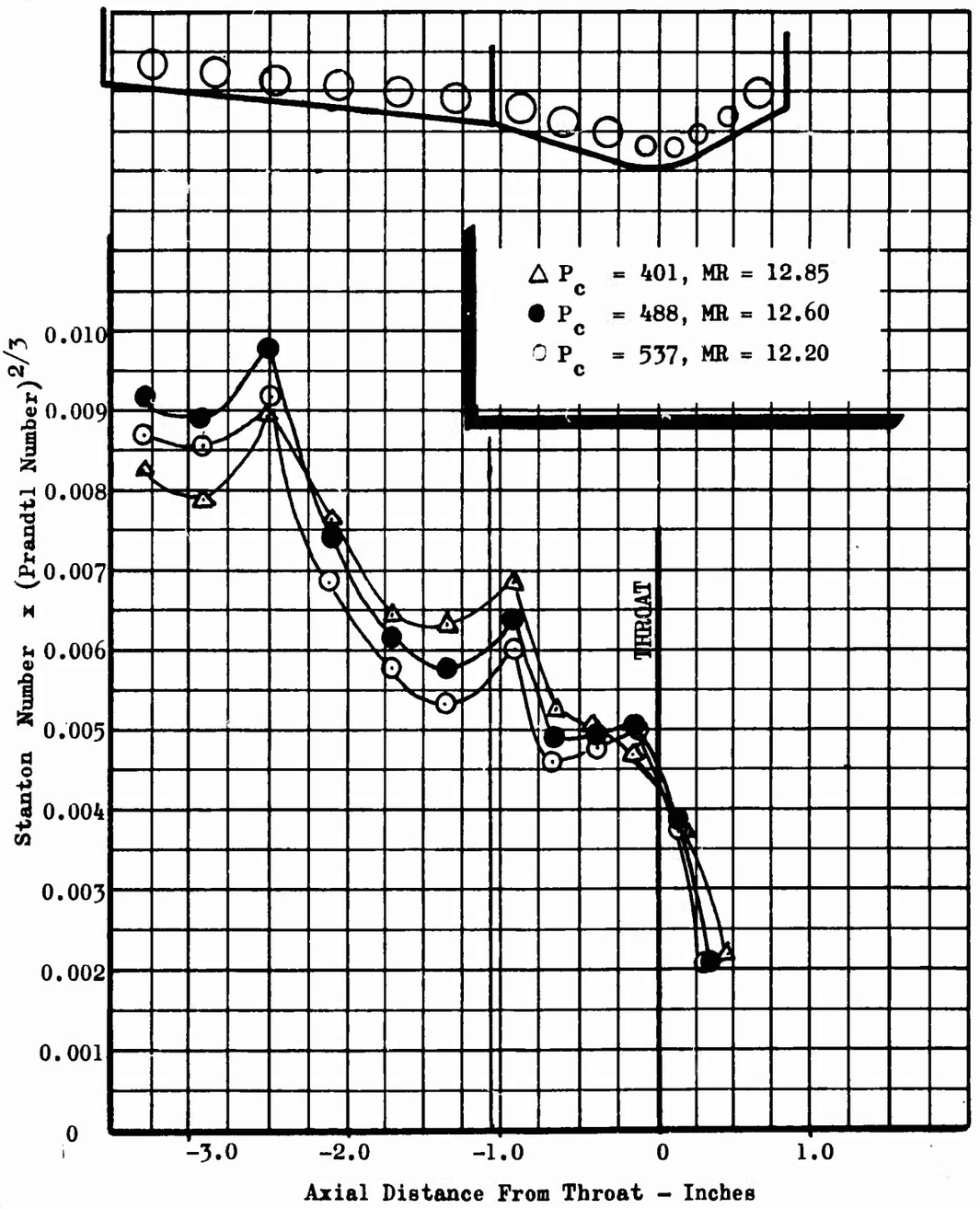

Figure 58 . Distribution of Heat Transfer Parameter for Contour F

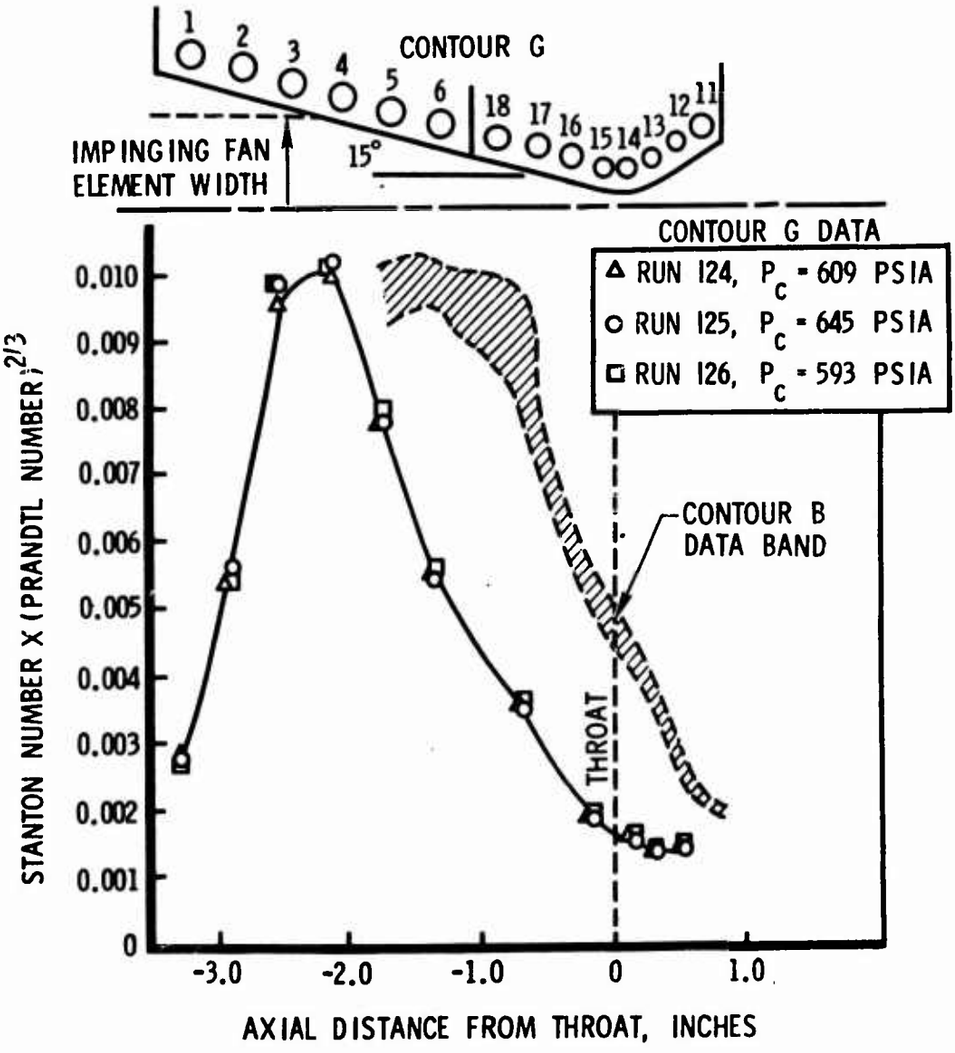

Figure 59 . Distribution of Heat Transfer Parameter for Contour G

(C) contour G is substantially lower. The contour G throat value of 0.002 is less than half of the value of 0.0046 obtained for contour B at the same operating conditions. The measured heat flux distributions for several contour G tests are shown in Fig. 60.

(C) The variation in the throat Stanton-Prandtl parameter with chamber pressure is shown in Fig. 61. The slope of -0.35 indicates a variation in the local heat flux with chamber pressure of $q/A \propto P_c^{0.65}$ as shown in Fig. 62. Since this exponent is 0.8 - 1.0 for turbulent flow, it is apparent that the boundary layer in the throat is not turbulent. The local heat flux was plotted vs chamber pressure for each Stanton-Prandtl number along the chamber and the exponent in $(q/A \propto P_c^n)$ was determined. The distribution of these exponents is shown in Fig. 63. The high values near the injector are indicative of a detached or poorly attached flow. Downstream of the impingement and attachment point where the exponent is approximately 0.8, the flow is turbulent. In the throat region, due to the large favorable pressure gradient and high degree of wall cooling, the boundary layer is stabilized and driven into a laminar regime. This phenomenon of "reverse transition" has been observed recently by several investigators and reported in the open literature. Since the pressure gradient is highest in the throat region, the laminarization of the boundary layer is likely to be localized in that region. However, several observers have found that the laminar boundary layer persists well into the supersonic region of the nozzle. For the subject contour, the high expansion rate downstream of the throat (30 degree expansion angle) results in a final transition to a turbulent boundary layer.

(C) The Stanton numbers from Fig. 61 were used to compute throat heat fluxes over the 9:1 throttling range. The heat flux varies from 22.2 Btu/in^2-sec at the nominal operating point to 5.3 Btu/in^2-sec at the 9:1 throttling point (Fig. 62).

i. Summary of Significant Results

(C) The 15-degree nozzle convergence angle chambers resulted in significantly lower throat region heat transfer rates as compared to the 30-degree chambers. This effect was believed due to the increased length from the start of convergence to the throat rather than the reduced angle.

(C) Data from all configurations showed that the high local combustion chamber Stanton numbers decrease rapidly from the start of the convergence section, apparently due to the stabilizing influence of the favorable pressure gradient on the boundary layer. In order to provide a longer convergent ramp for boundary layer growth, the contour G chamber was fabricated and tested. This configuration resulted in the lowest measured throat heat flux of 22.2 Btu/in.^{2}-sec at the P_c = 650 psia design point (mixture ratio = 13.0, η_{c^*} = 98 percent, T_{WG} = 1600 F). A comparison of the throat gas side film coefficients for each of the contours tested is shown in Fig. 64. These results were of primary importance in the tube wall segment design for Task III since the throat (peak) heat flux level determines the required coolant tube size and/or number of coolant passes.

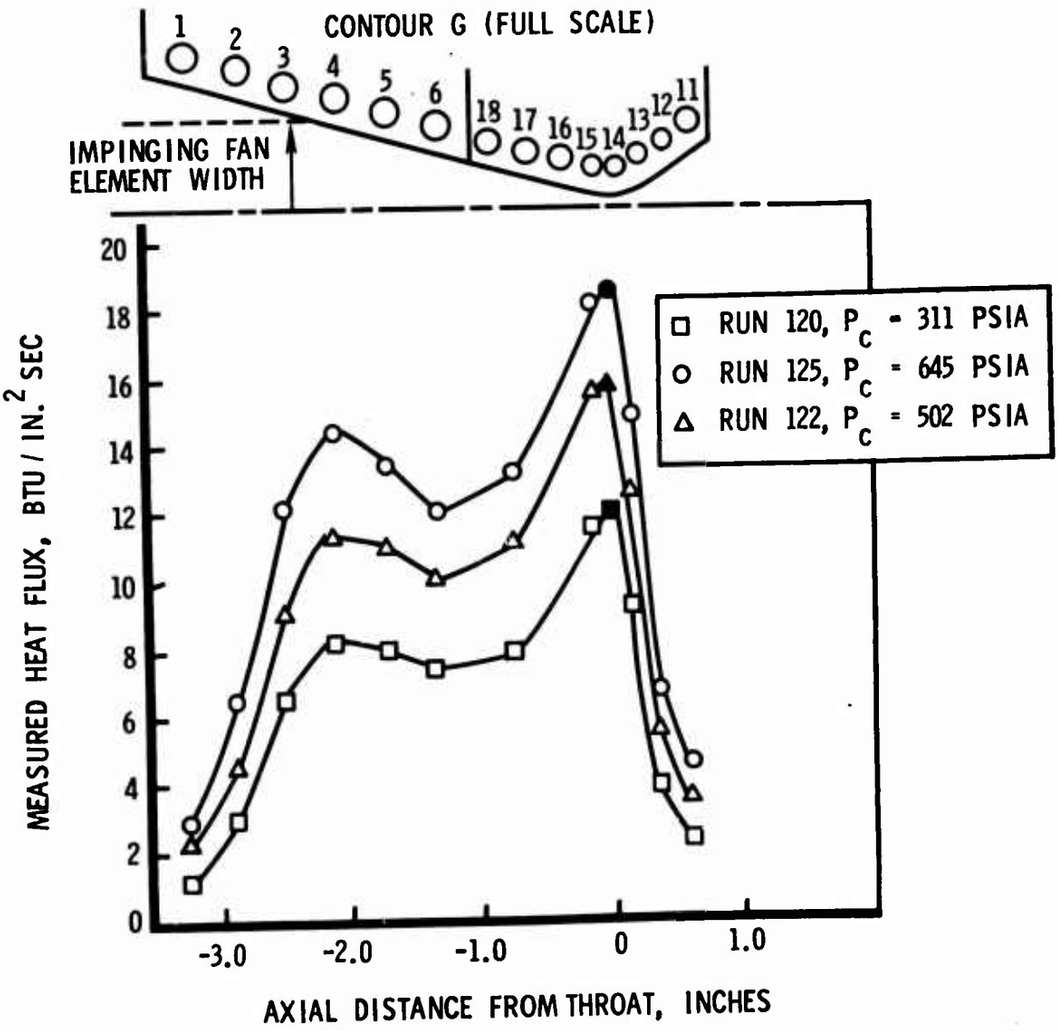

Figure 60 . Heat Flux Distribution for Contour G

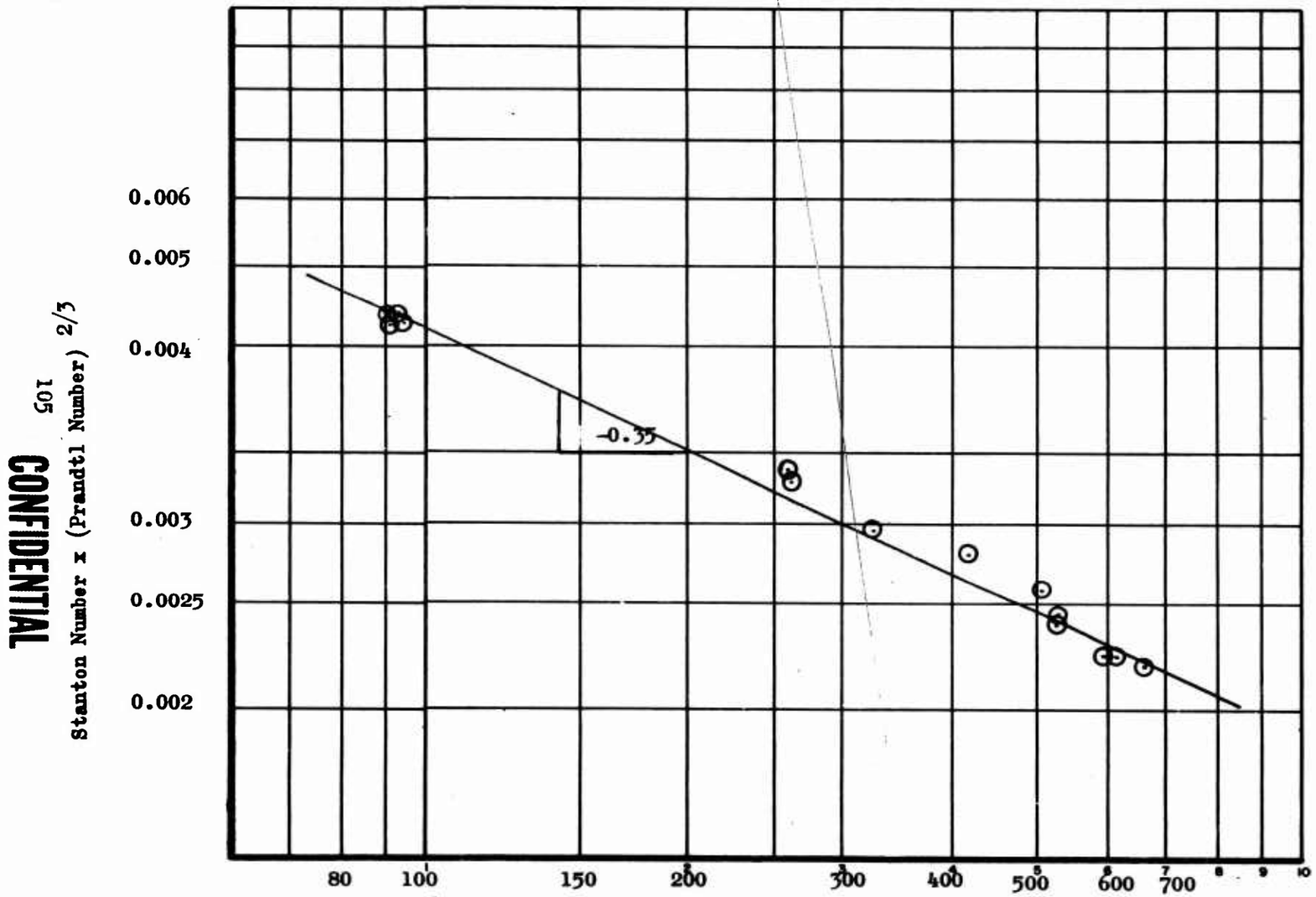

Figure 61 . Variation in Heat Transfer Parameter with Chamber Pressure - Contour G

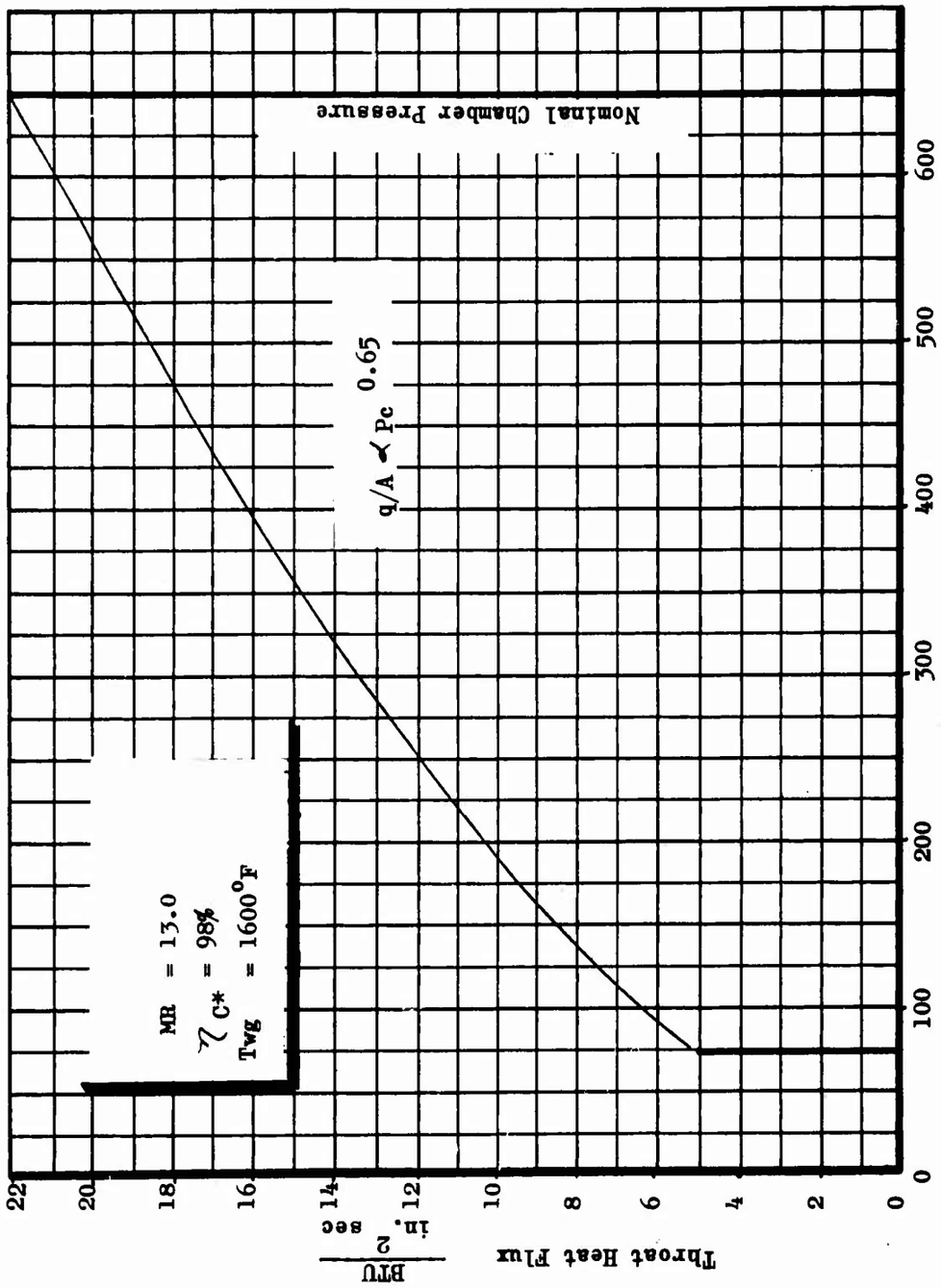

Figure 62 . Throat Heat Flux Versus Chamber Pressure - Contour G

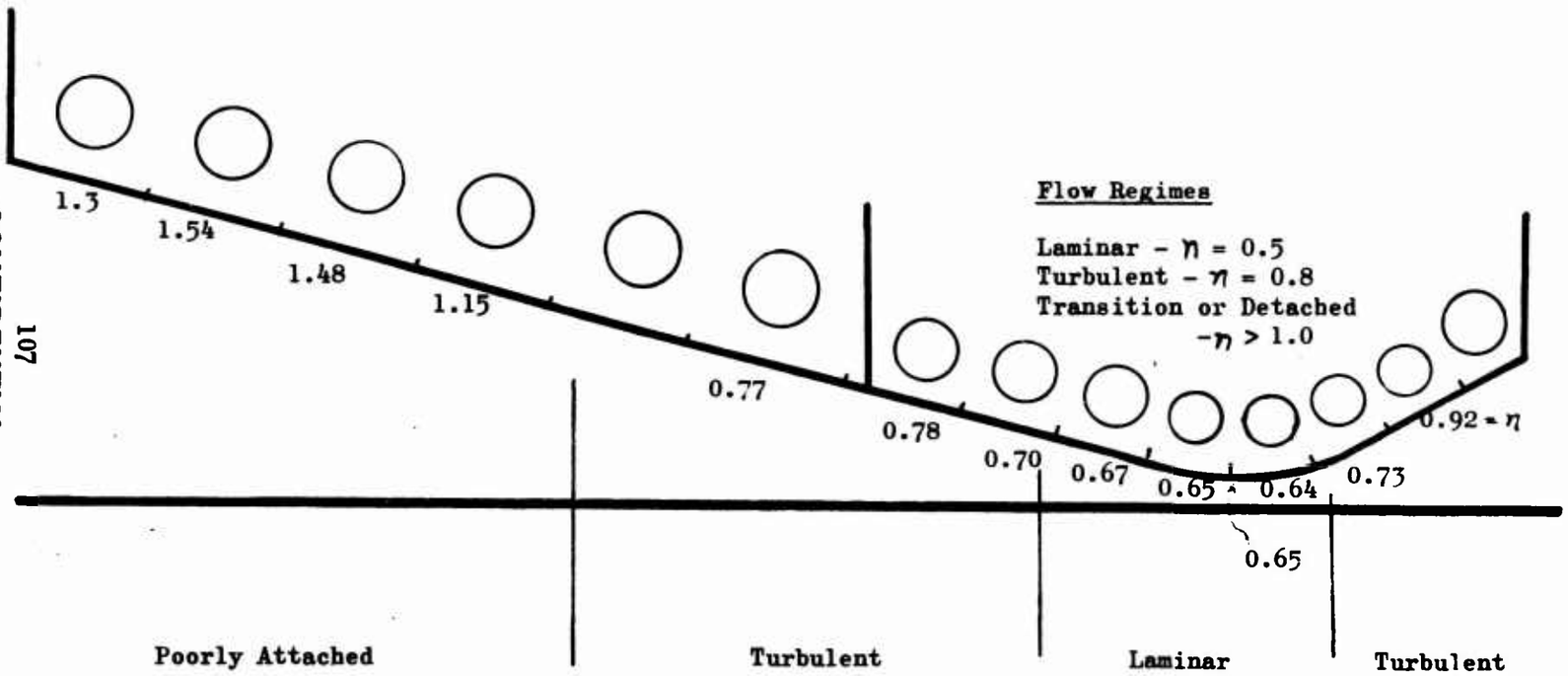

Figure 63. Distribution of Exponent n ($Q/A \propto P_c^{\,n}$) Along Contour G

(P_c Range 300 - 650 psia)

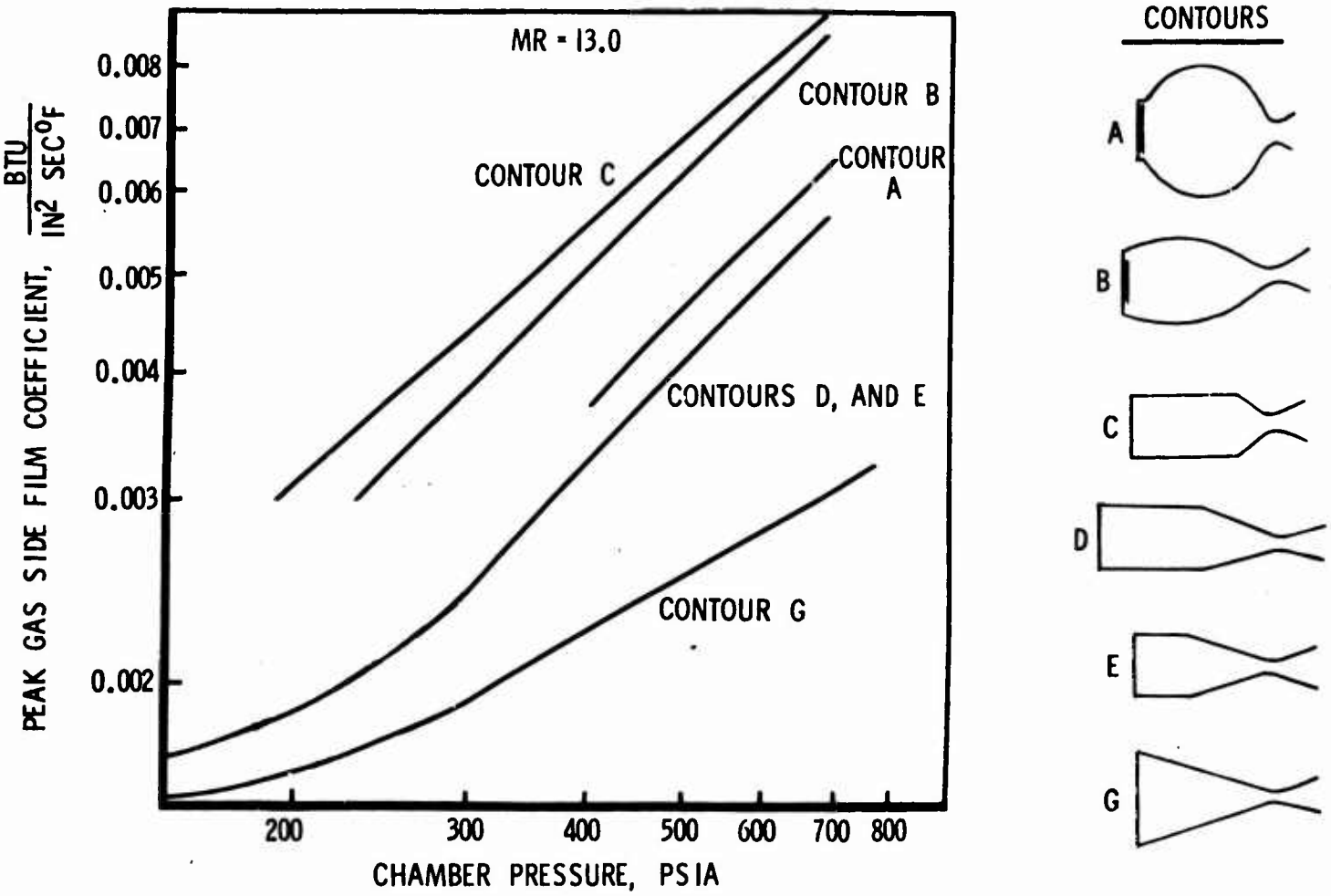

Figure 64 . Comparison of Peak Gas Side Film Coefficients for Water-Cooled Contours

(C) No effect on throat region heat transfer rates was observed when the constant area combustion zone length was increased by 1.5 inches (contour D vs contour E). This result most likely occurred because there was no change in the nozzle convergence angle or length between the two compared contours. Increase of combustion chamber length by increase of the convergence section, however, would likely result in further reduction in throat region heat transfer. This was subsequently verified on other tests with variations of contour G.

(C) Tests of the impinging fan injector in contour C yielded combustion zone heat transfer rates significantly lower than for the triplet injector. As a result, the throat peak value was reduced by 37 percent. However, when tested with the 15 degree convergence nozzle, the impinging fan and triplet injector showed comparable throat heat transfer rates. The same result was observed for the two injector types with contour G.

(C) On contour E tests with mixture ratio bias, in which a significant percent of hydrogen flow was introduced along the chamber walls from the injector face, no reduction in combustion zone heat transfer rates was observed. However, some reduction was noted in the throat region. Because of the increased stabilized boundary layer with contour G, it is anticipated that injector mixture ratio bias would be more effective in reducing local combustion zone heat transfer rates with this geometry.

(C) The total heat inputs for contours B, C. E, and G are shown in Fig. 65 over the design throttle range of 9:1. The heating rates did not fall off linearly over the whole chamber pressure range (650 to 70 psia) because of the proportionally larger heating rates near the injector at the lower chamber pressures. These data, together with those of Fig. 64, were used in the tube wall segment design for Task III. Measured bulk temperature rises, or total heat inputs, during the subsequent tube wall segment testing were compared with the predicted values of Fig. 65 to provide for final design verification (discussed on Page 144).

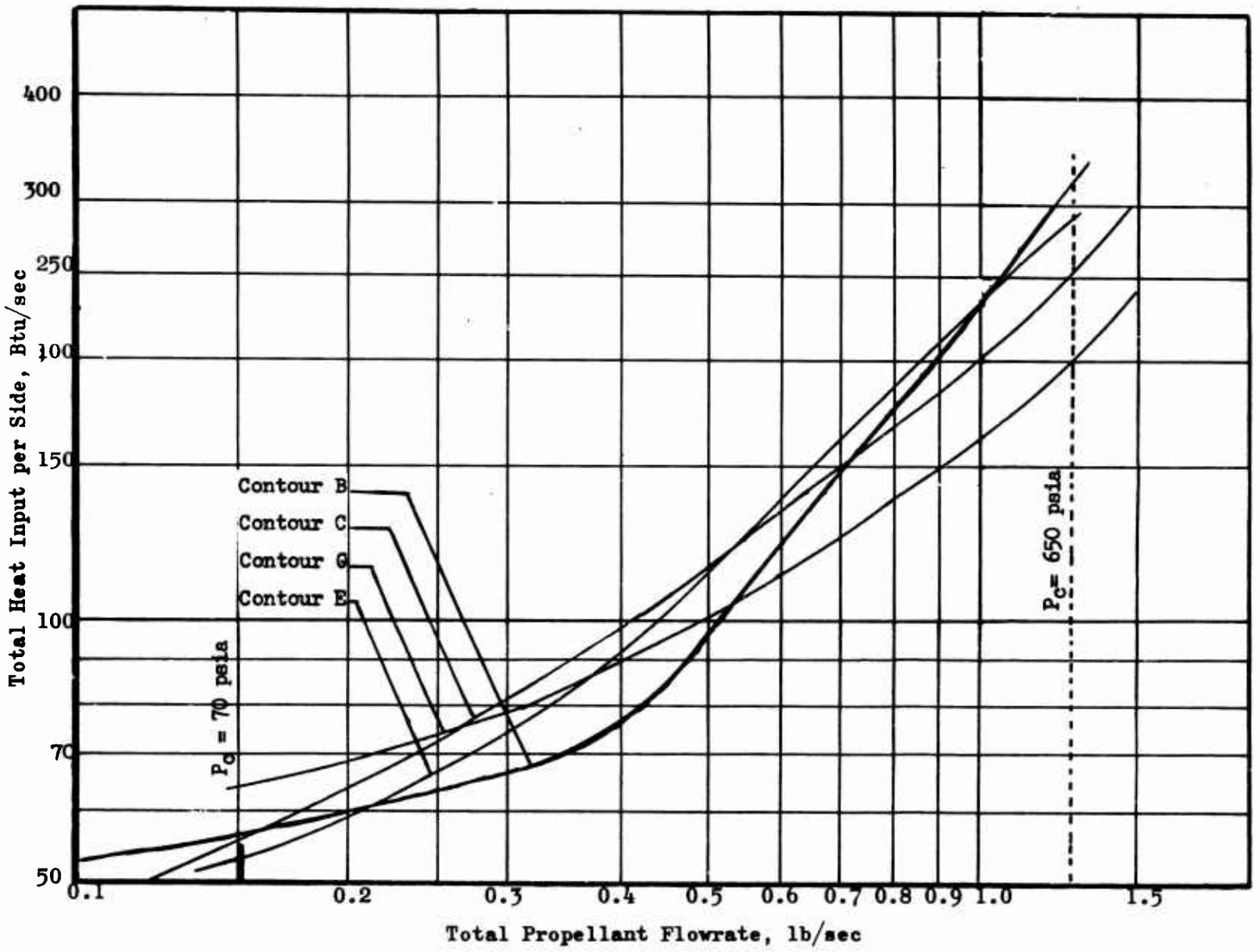

Figure 65. Comparison of Total Heat Input to Various Contours

SECTION 1.1

TASK III: TUBE-WALL SEGMENT EVALUATION

1. GENERAL

(U) This task utilized the information and data obtained in Task II to design and demonstrate the capabilities of the tube-wall toroidal segment. Specific objectives of Task III tube-wall testing were:

1. Demonstrate the performance, durability, and regenerative-cooling capability of the tube-wall thrust chamber segments
2. Demonstrate by structural testing that the deflection of segment lightweight support structure as a function of operating loads can be maintained within design limits

(C) To accomplish these objectives, Task III tube-wall segment testing was conducted in three phases:

1. Tube-wall throat section segment firings to demonstrate the regenerative-coolant tube design in the region of maximum heat flux (throat region) prior to testing the complete tube-wall segment
2. Tube-wall segment firings to demonstrate regenerative-cooling capability and performance over the 9:1 throttling range
3. Support structure mechanical loading tests to determine the structural characteristics of lightweight structural support specimens. Two types of structure were evaluated, honeycomb and rib structure.

(U) The contour-evaluation data of Task II were used to specify the internal dimensions of the Task III hardware. The best injector configuration, determined from the solid-wall tests, was used with the tube-wall throat inserts and the tube-wall segments. The heat transfer data obtained with the solid wall hardware specified the coolant velocities and number of passes required for the tube-wall configurations.

2. TUBE-WALL THROAT INSERTS

(U) The tube-wall throat insert represented an intermediate step between the solid-wall and tube-wall segments. The purpose of the inserts was to provide a relatively inexpensive means of verifying the tube-wall design in the most critical area, the throat region.

a. Design Description

(C) Hardware for the tube-wall throat section evaluation testing was assembled by using injectors, injector adapters, and combustion chamber sections from the Task II firing program. To these components, a tube-wall throat test section was attached (Fig. 66). The tube-wall throat test section was similar to the all-water-cooled throat section used in Task II, with the exception that one-half of the double expansion contour was replaced by a separate block of material assembled with longitudinally oriented, constant-diameter tubes defining that contour and simulating the prototype, regenerative-cooling circuit. The other contour wall and side walls were of solid-wall construction with water-coolant passages entering through the side of the insert. From the side of the insert, the water-cooled passages run parallel to the side wall, across the nozzle, parallel to the opposite side wall, and out the opposite side of the throat insert. Each of the eight passages was a separate circuit to isolate different heat fluxes within the throat section.

(C) The regenerative tubes on the nozzle contour wall were hydrogen cooled. They were located over a support body and brazed in place. Each end of the tubes was fed from separate manifolds which ran out the side of the insert section. Pressure and temperature instrumentation ports were provided in each manifold. Coolant within the throat tubes could be flowed in either direction.

(C) Two throat insert configurations were designed corresponding to tubes of different materials and sizes:

Nickel	0.093 OD by 0.024 wall (32 required)
Stainless Steel	0.062 OD by 0.012 wall (48 required)

(C) The tubes were of constant cross section which duplicated the full-tube design configuration at the throat.

(C) The stainless-steel tube design was a conventional approach which required the fabrication processes of tapering, forming to contour, flattening, and brazing into an assembly. The tube size was basically for a two-pass design, but coolant flow rate on the throat insert tests could be varied to simulate any number of passes.

(C) The nickel-tube design utilized a relatively thick wall of high conductivity material to distribute heat around the tube. The design was analyzed using a thermal analyzer type computer program to determine the temperature distribution around the tube. The tubes were analyzed for the maximum heat flux condition at the throat. It was found that for the expected heat flux level, the tube outer diameter should be about twice the tube inner diameter or less if any heat distribution benefit was to be obtained. If the outer tube diameter was very much

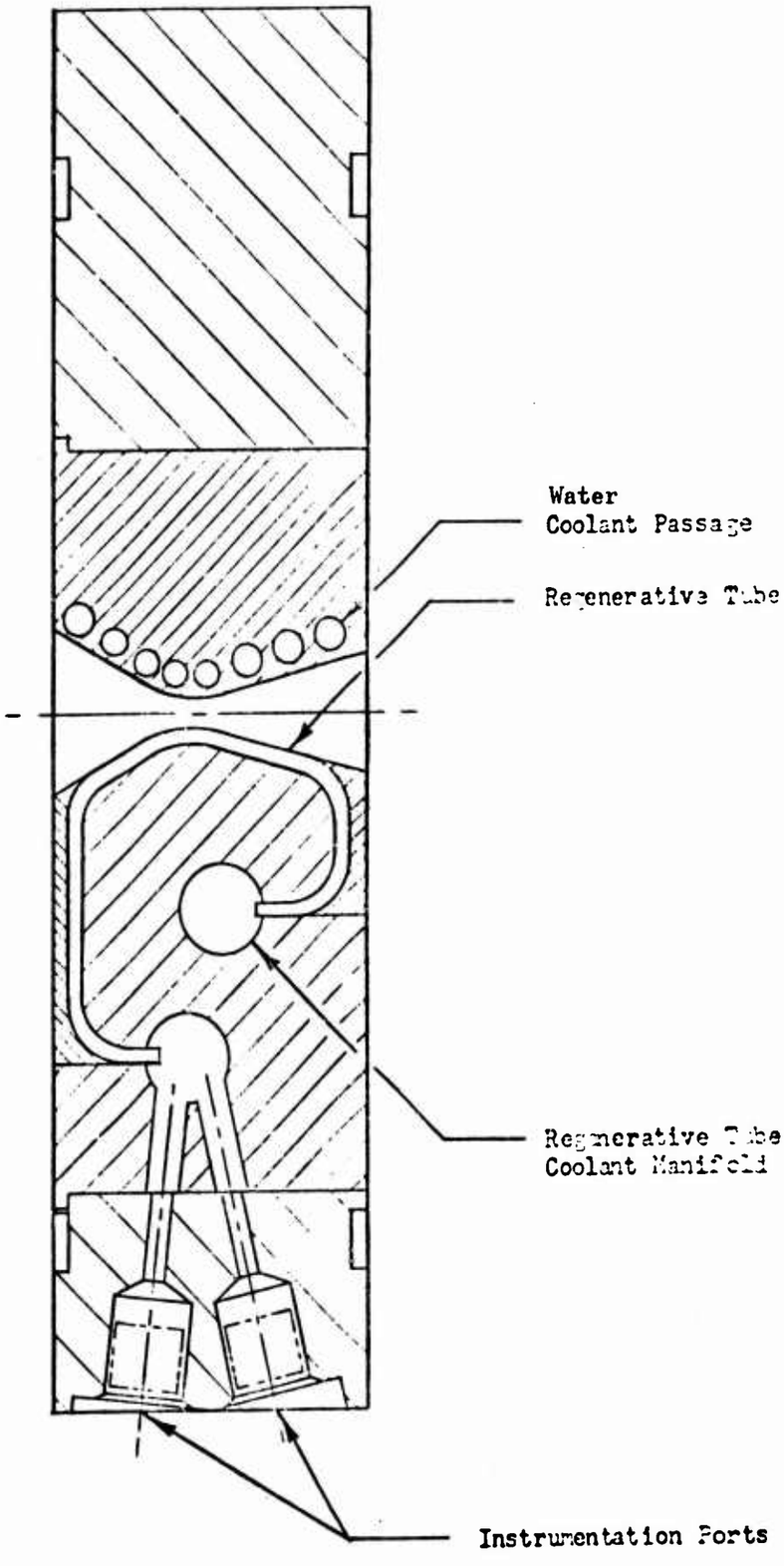

Figure 66. Regenerative Nozzle Wafer

greater than this limit, it was found that the outer-wall temperatures became excessive. Isotherm profiles for the thick-wall, nickel-tube design are shown in Fig. 67. It is seen that the peak wall temperatures is about 1600 F with a back-wall temperature of ~ 900 F.

(C) The use of either type of design appeared quite feasible from the heat transfer standpoint. The thick-wall tube concept allowed for a large reduction in the number of tubes and coolant passes required for adequate cooling. A sizeable saving in tube pressure drop (as much as half) was also achievable. A slight weight penalty for the thrust chamber, however, would result for thick tube design.

(U) These insert details, with the exception of the structural collar, are shown for the nickel-tube design in Fig. 68. In this figure, the tubes are shown after brazing to the backup member. The two tube covers are shown in the premachined configuration used for the brazing operation. The assembly, bolted together for brazing, is shown in Fig. 69. After this braze cycle, the assembly was machined to fit into the structural collar.

(U) The complete nickel tube-wall insert assembly is shown on Fig. 70. The large inlet tubes are the hydrogen coolant manifold inlets; the smaller tubes are the inlet and outlet tubes for the water cooling passages.

(U) The combustion chamber and nozzle insert assembled for testing is shown on Fig. 71.

b. Testing and Data Analysis

(C) For very low hydrogen temperatures, the effect of hydrogen temperature on heat transfer rates is quite significant. Therefore, to simulate the first-pass flow conditions, the liquid hydrogen was heated prior to entering the insert. The amount of preheating depended upon the degree of heating expected in the combustion zone of the chamber, since the tubes only include the converging-diverging portion of the nozzle near the throat. To simulate a range of preheating conditions, the test facility was provided with the features shown in Fig. 72. Both liquid and gaseous hydrogen were provided and combined in a mixing chamber when very low-temperature hydrogen was required. The use of a LN_2 heat exchanger in the gaseous hydrogen line was found to be a more satisfactory method of providing hydrogen at temperatures above 200 R. The hydrogen flowrate for this latter configuration was measured accurately by a sonic venturi prior to chilling in the heat exchanger. The same venturi was used to measure the flowrate of the GH_2 when it was mixed with LH_2 in the mixing chamber. This GH_2 flowrate measurement was added to the LH_2 flowrate measured by the turbine flowmeter to obtain the total hydrogen flow.

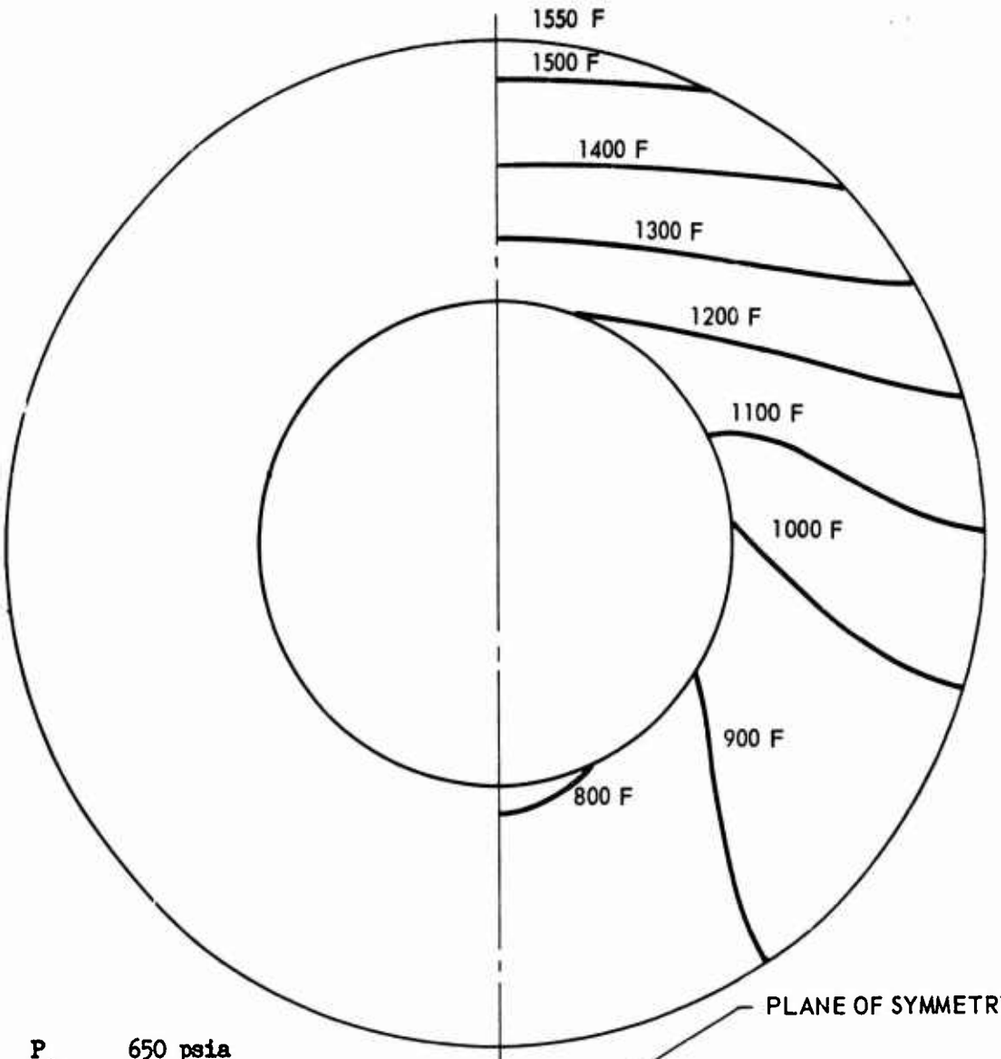

P_c	650 psia
T_{AW}	4140 F (FILM COOLING)
T_{H_2}	700 F (LAST PASS)
h_g	0.00408 $\frac{Btu}{IN.^2 - SEC - F}$
h_c	0.026 $\frac{Btu}{IN.^2 - SEC - F}$

TUBE DIMENSIONS

d_i	0.045 INCH
d_o	0.093 INCH
b_w	0.024 INCH

Figure 67. Cross-Sectional Temperature Distribution in Nickel Tube

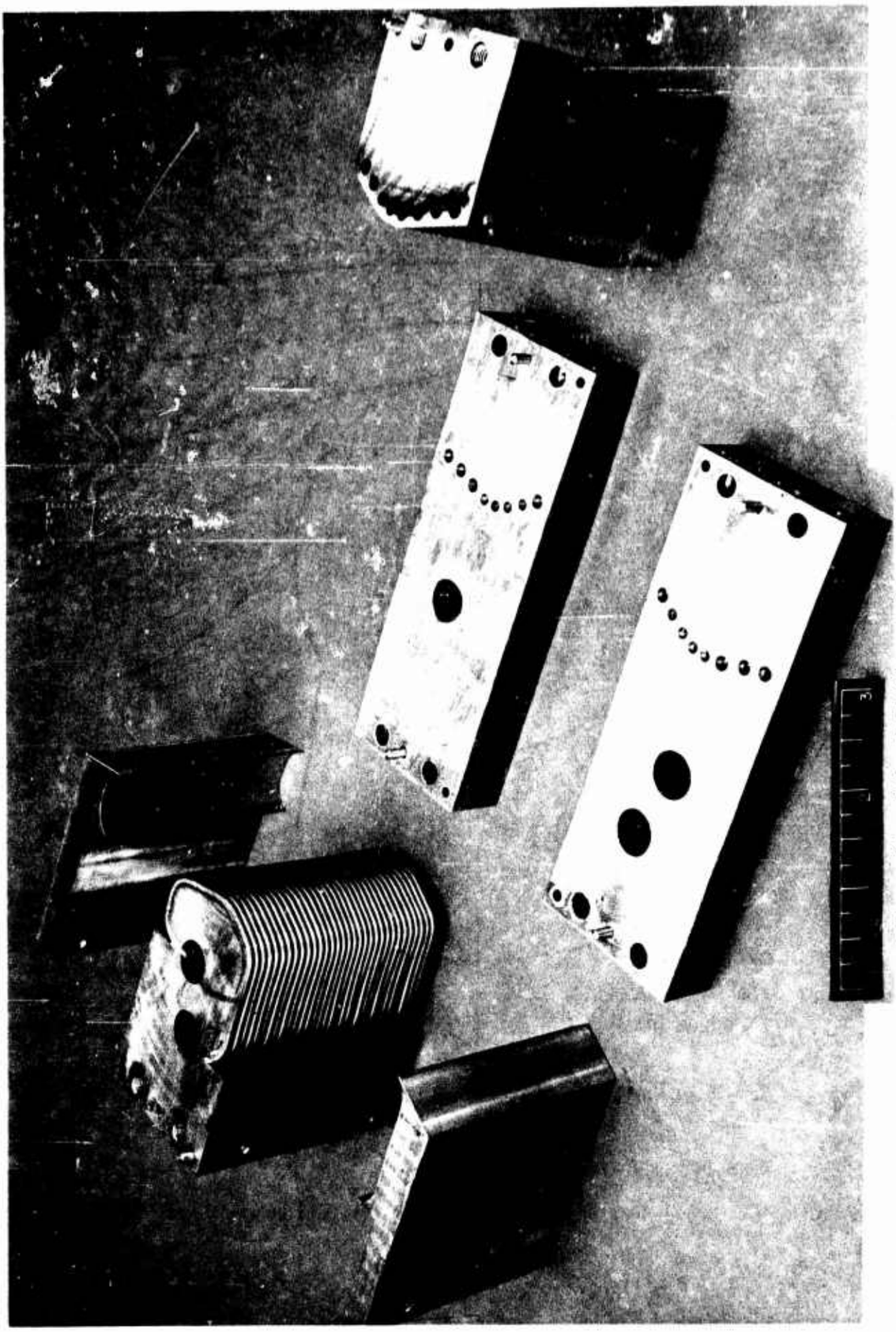

Figure 68. Tube Wall Throat Insert Components

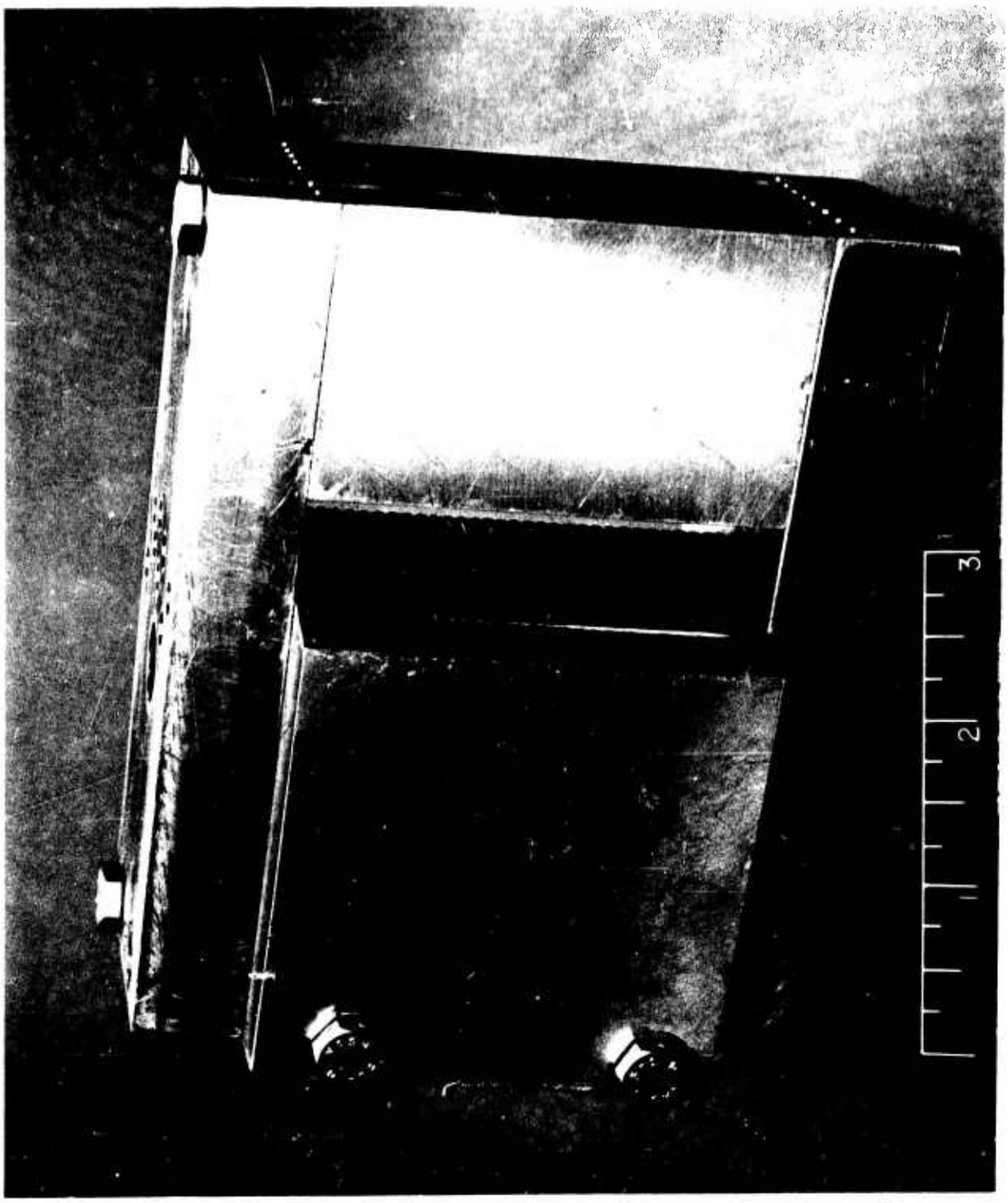

Figure 69 . Assembled Tube Wall Throat Core

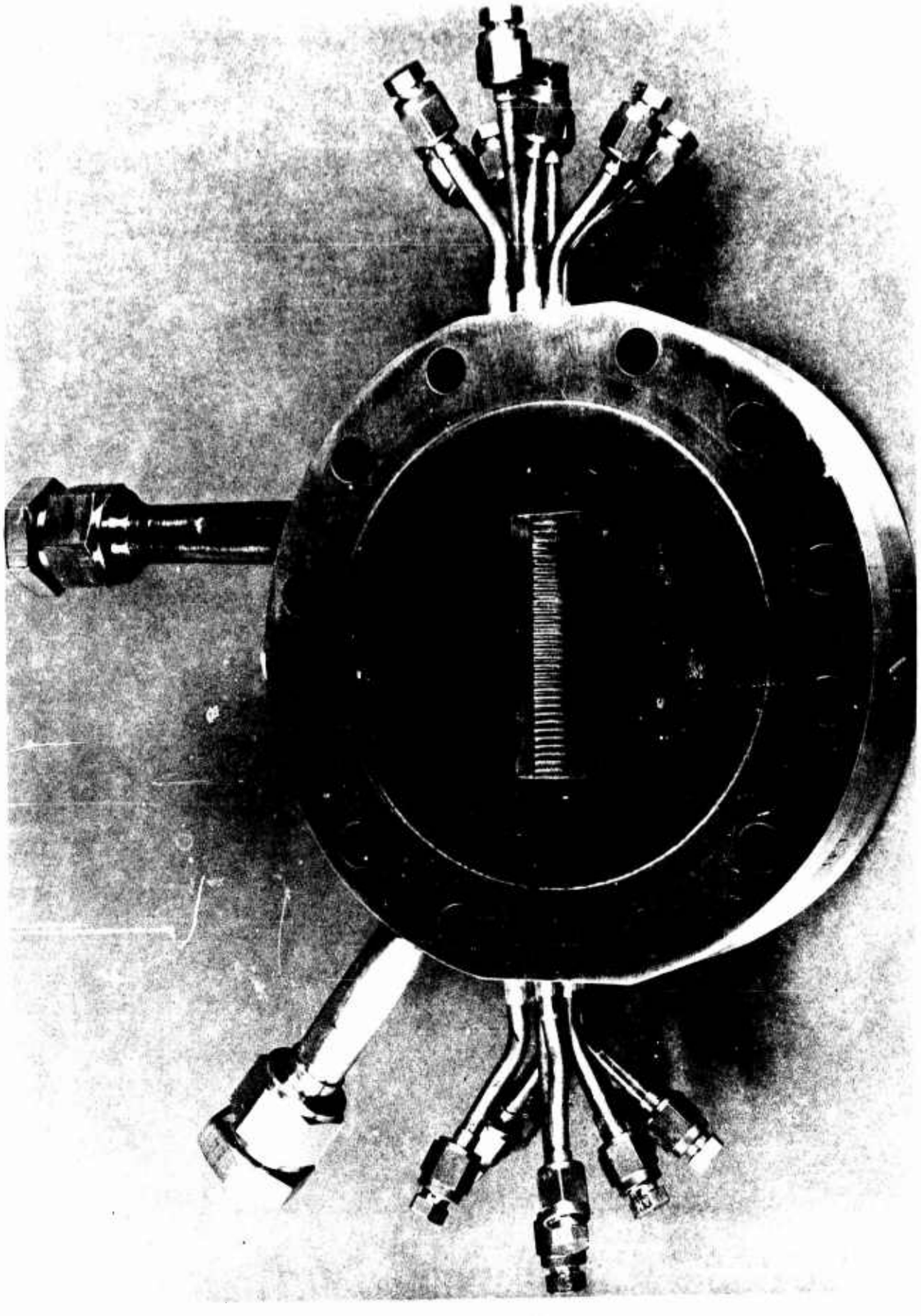

Figure 70. Nickel Tube-Wall Throat Insert

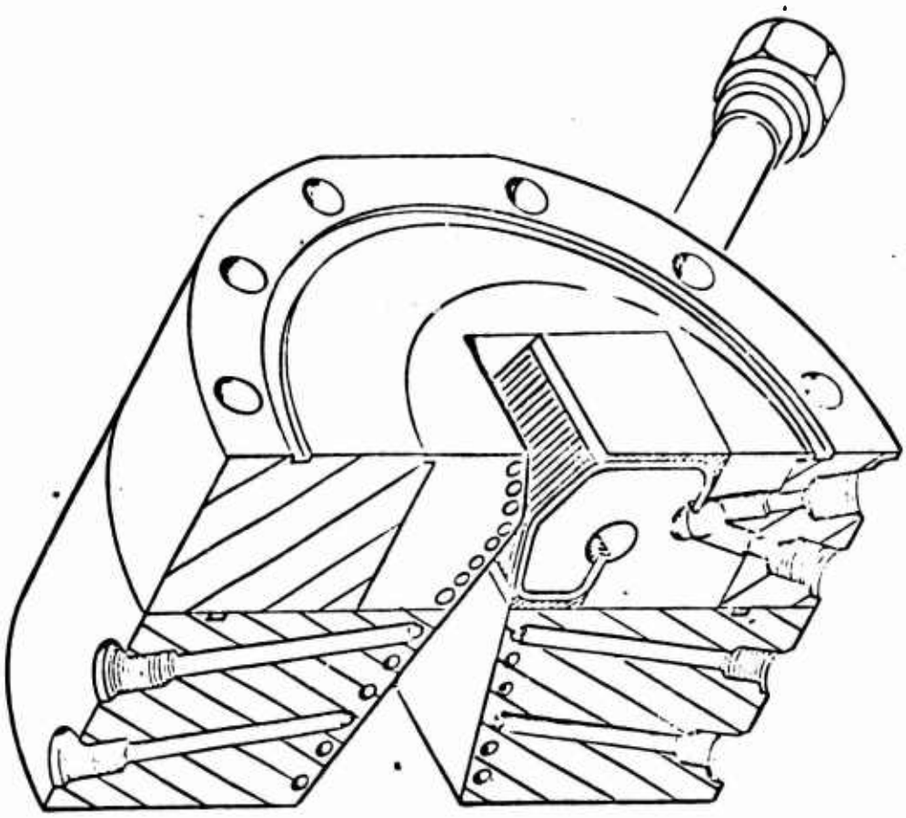

Figure71. Tube-Wall Insert and Water-Cooled Chamber

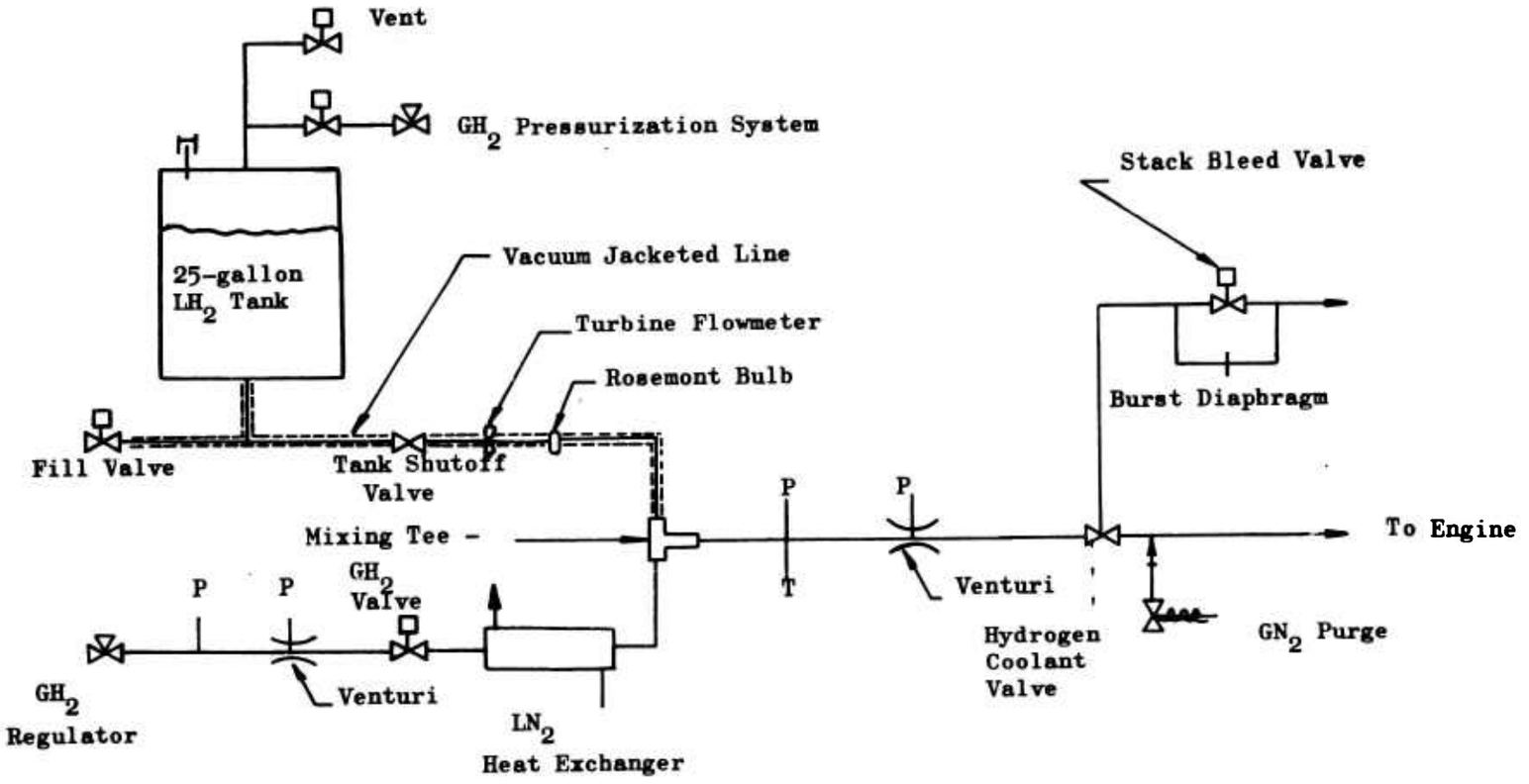

Figure 72 . Facility Schematic Showing Regenerative Cooling Lines

(C) CRES Tube-Wall Throat Insert Tests. The CRES tube-wall throat insert was completed and water-flow checks were performed. The pressure drop vs flow data agreed fairly well with the predicted values. As shown in Fig. 73, the measured pressure drops were lower than the estimated values.

(C) Testing of the stainless tube-wall insert was conducted with contour G chamber configuration and the 2-inch-wide impinging fan injector. This chamber configuration was chosen because of low heat transfer rates obtained during previous water-cooled segment testing . A total of five tests were conducted with the insert, and the results are summarized in Table 7. As noted, the measured heat input for the hydrogen-cooled tubes agreed relatively well with that of the water-cooled side of the nozzle thus verifying the previous solid-wall heat transfer measurement method.

(C) The fifth test of the CRES tube insert was conducted at a chamber pressure of 642 psia with chilled hydrogen as the coolant. Fourteen of the tubes were found to be eroded after the test. Analysis of the data indicated a chamber pressure overshoot was responsible for the tube damage. Motion pictures of the test and other test data indicated that the failure occurred early in the test. The chamber pressure rose to 835 psia, an excessive value for this design, during the start and maintained this pressure for a sufficient duration for the 0.012-inch thick CRES tube walls to reach thermal equilibrium.

(C) The ultimate and yield strength of 347 CRES from Ref. 4 are shown in Fig. 74. Although the stainless has very high strength at low temperatures, the strength falls to virtually zero above 2100 F, a temperature which is well below its melting point. The internal pressure stress of the stainless tubes was approximately 3000 psi. Referring to Fig. 74, the ultimate strength of the tube falls below this operating level at temperatures above 2040 F.

(C) During the chamber pressure overshoot on the failure test, the throat heat flux was estimated to be 41 Btu/in.^{2}sec. At this heat flux, the wall temperature was determined to be approximately 2200 F; sufficiently high to cause failure of the tubes. Under normal operating conditions, however, the CRES coolant tubes would be expected to operate satisfactorily.

(C) Nickel Tube-Wall Throat Insert. Water flow calibration of the nickel tube throat insert indicated an abnormally high pressure drop in the hydrogen tubes. Further examination to determine the cause of the tube blockage resulted in a sample of crystalline substance being collected from the tubes. The sample was subjected to analysis by X-ray diffraction techniques. The results of the analysis indicated that the material in the tubes was primarily Si 0_2. After further investigation, it was concluded that the Si 0_2 most likely entered the tubes during the water flow calibration tests. Attempts at removing the foreign material were unsuccessful, and the insert assembly was, therefore, not subjected to hot firing tests.

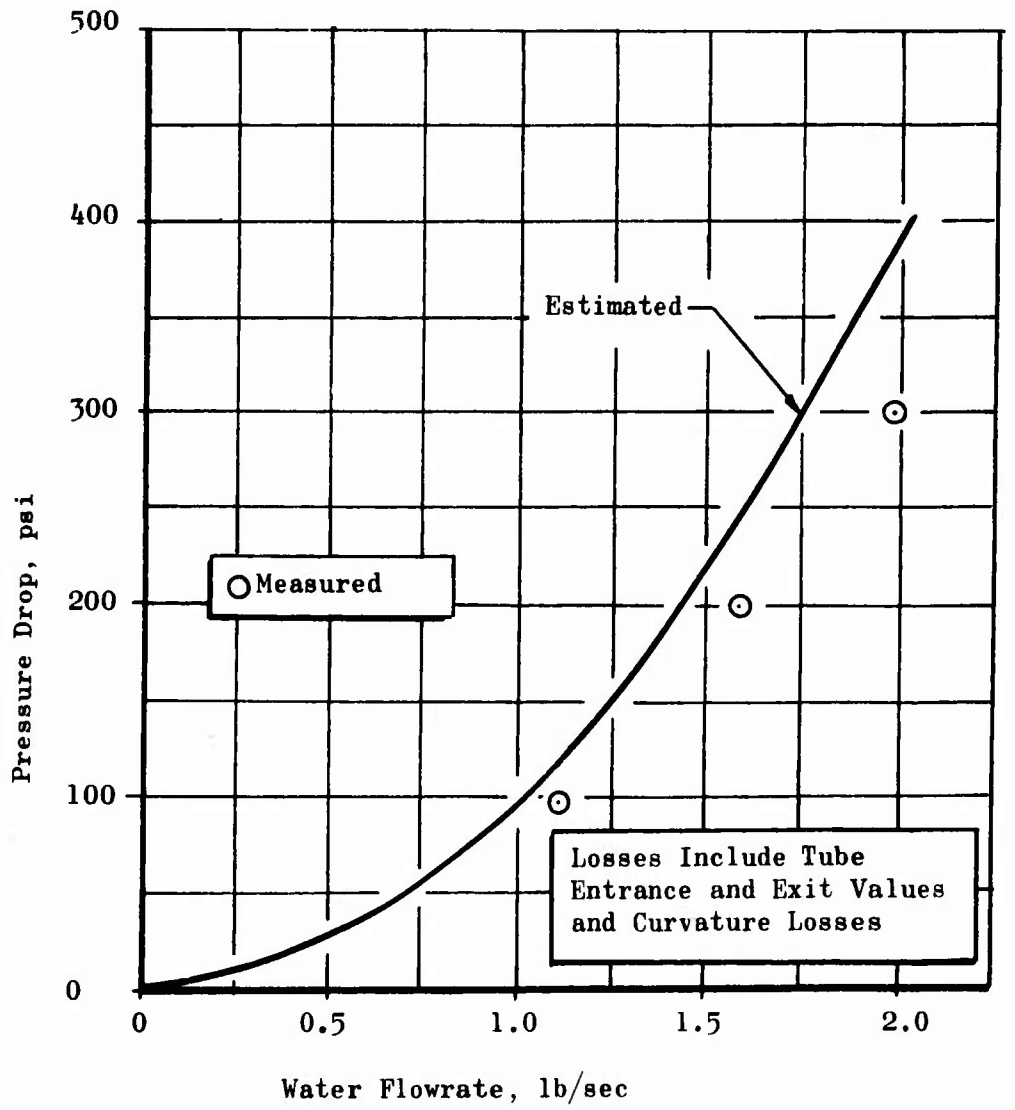

Figure 73 . Estimated and Measured Pressure Drops for Water-Flow Calibration of the CRES Tube Throat Insert

TABLE 7

CRES TUBE THROAT INSERT TEST SUMMARY

TEST NO.	DURATION (SEC)	P_c (PSIA)		H_2 COOLANT (LB / SEC)	HEAT INPUT (BTU/SEC)	
		MAXIMUM	NOMINAL		H_2 SIDE	WATER SIDE
1	.5	-	300	.230	-	-
2	3.5	398	291	.225	59	52
3	2.0	550	390	.229	65	64
4	2.0	691	504	.248	73	79
5	2.7	835	642	.547	-	83

CONFIDENTIAL

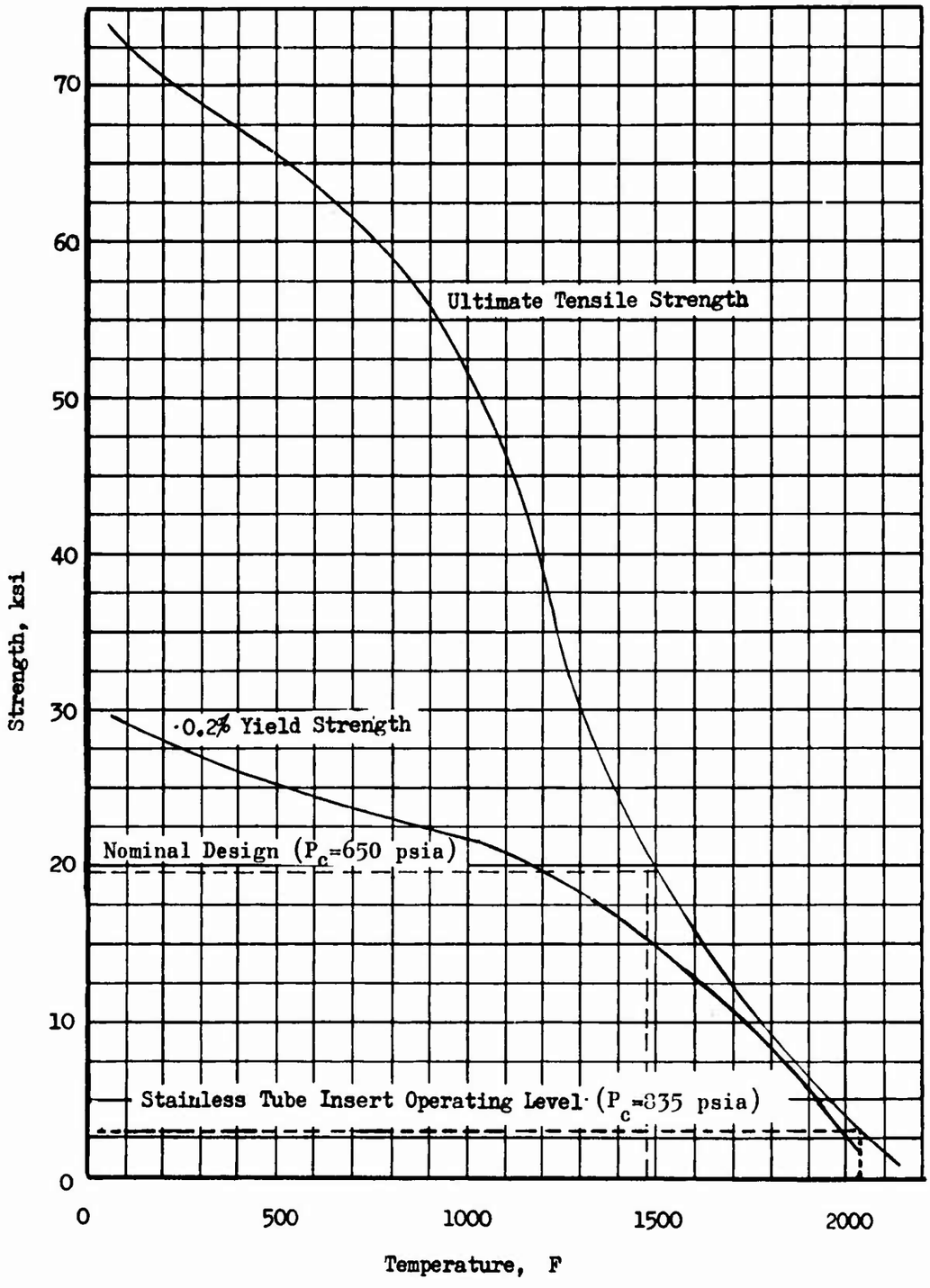

Figure 74. Tensile Strength of 347 CRES

3. TUBE WALL SEGMENTS

(U) The purpose of the tube-wall segment testing was to demonstrate complete regenerative cooling capability for the thrust chamber. Two identical units were fabricated and tested. A total of twenty hot firings were conducted.

a. Design Description

(C) An isometric view of the tube wall segment assembly is shown in Fig. 75. The segment is provided with two-pass cooling of each contour wall. After cooling one side of the segment the hydrogen may be externally ducted to the opposite contour wall. The combustion chamber geometry selected for the design was the contour G which showed the lowest heat transfer rates during the previous solid wall segment tests. The injector configuration was the two inch wide impinging fan design (Fig. 15) which showed good performance with the contour G chamber. The combustion chamber converges continuously to the throat at a 17-degree angle. The nozzle diverges at 15 degrees and has an expansion area ratio of 4:1.

(C) The side walls of the segment were water cooled. This did not strongly affect the comparison of results between the test segment and an actual baffled thrust chamber because less than 5 percent of the total heat load was transmitted to the baffles which the sidewalls simulate. Each side plate had individual inlet and outlet water manifolds which were connected by drilled passages. The length and diameter of these passages were varied to ensure proper distribution of flow along the length of the chamber.

(U) The question of freezing an ice layer in the side plate water passages during the hydrogen lead period of the start sequence was subjected to a detailed thermal analysis. The analysis showed that an ice layer thickness of only 0.0034 inch would result if the water coolant flowrate was maintained at 85 lb in./sec. The maximum time an ice layer 0.0034 inch could exist after ignition is 0.024 seconds, which is an order of magnitude faster than necessary to heat the wall to the melting point of copper. Therefore, no problem was expected during the hot firings. This was subsequently verified during testing.

(C) An exploded view of the tube-wall segment is shown in Fig. 76. This view is useful for illustrating the assembly sequence for the segment which was as follows. The tubes were electron-beam welded together and formed to the shape of the contour (Fig. 77). The tube bundle was then brazed to the structural member (strongback). The tubes and strongback were then brazed to the hydrogen manifold. Following this procedure, the side plates were electron-beam welded to the strongback and brazed to the hydrogen manifold. At the same time, the inserts were brazed to the tube bundles. The side-plate, water-manifold covers were then welded

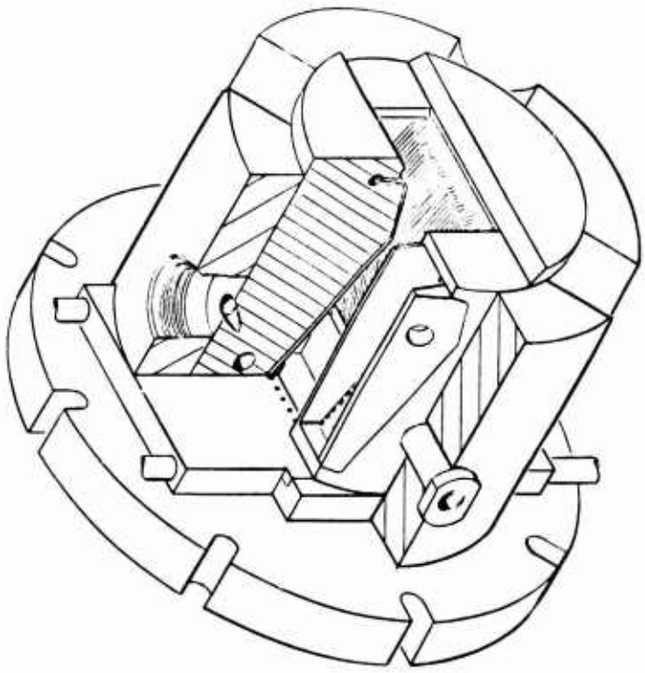

Figure 75. Tube-Wall Segment

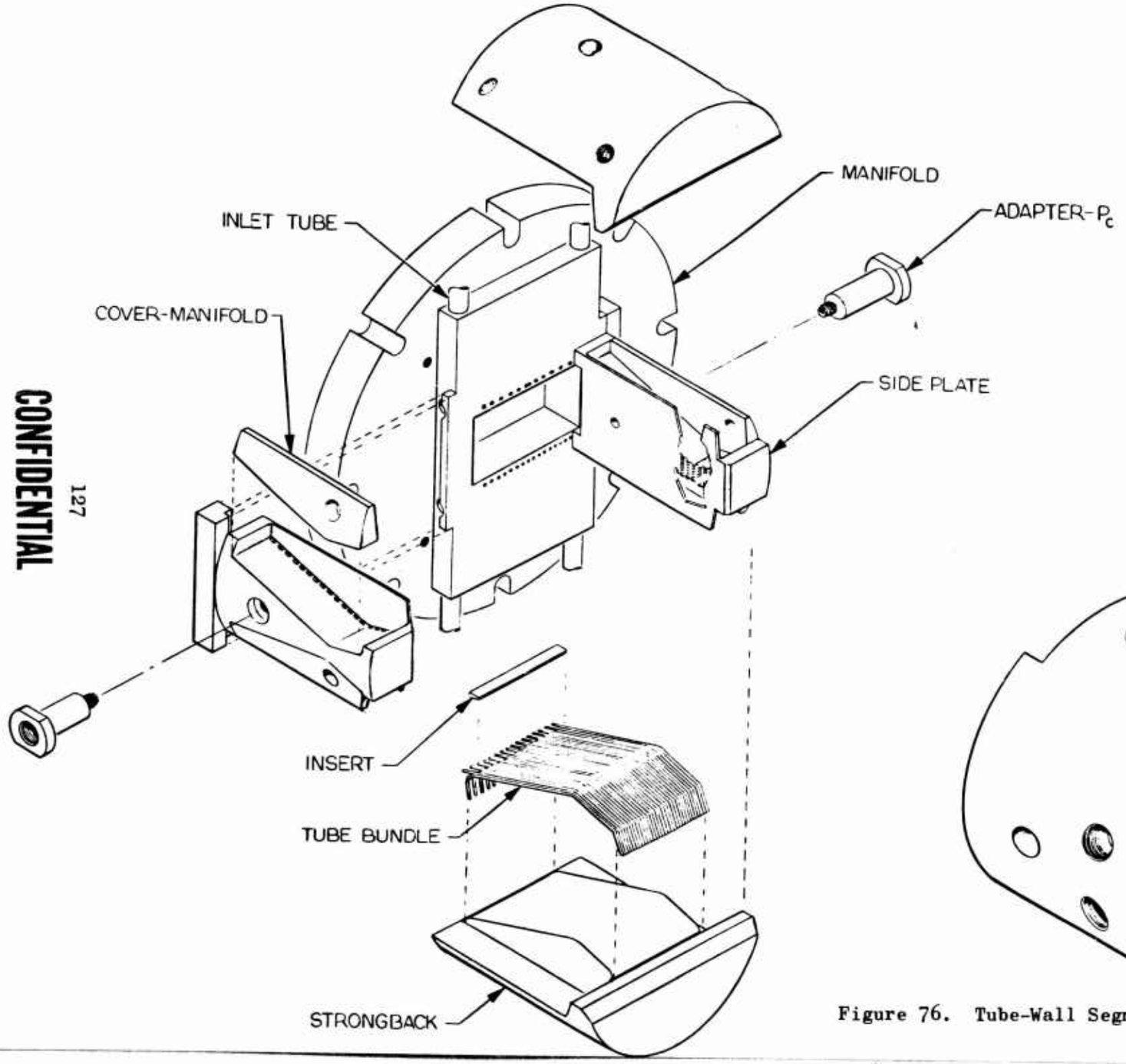

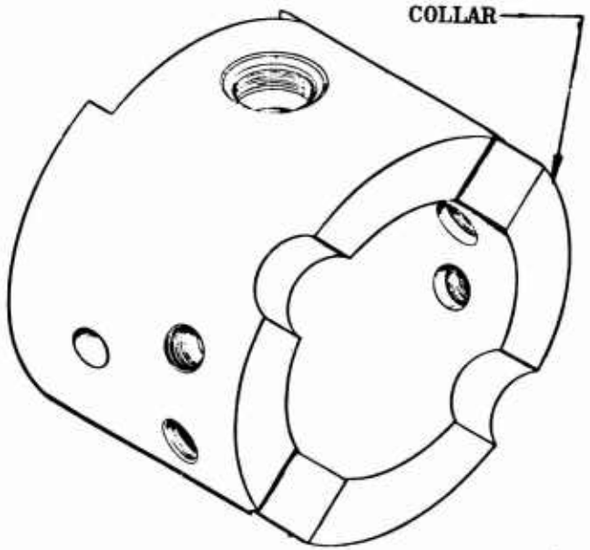

Figure 76. Tube-Wall Segment (Exploded View)

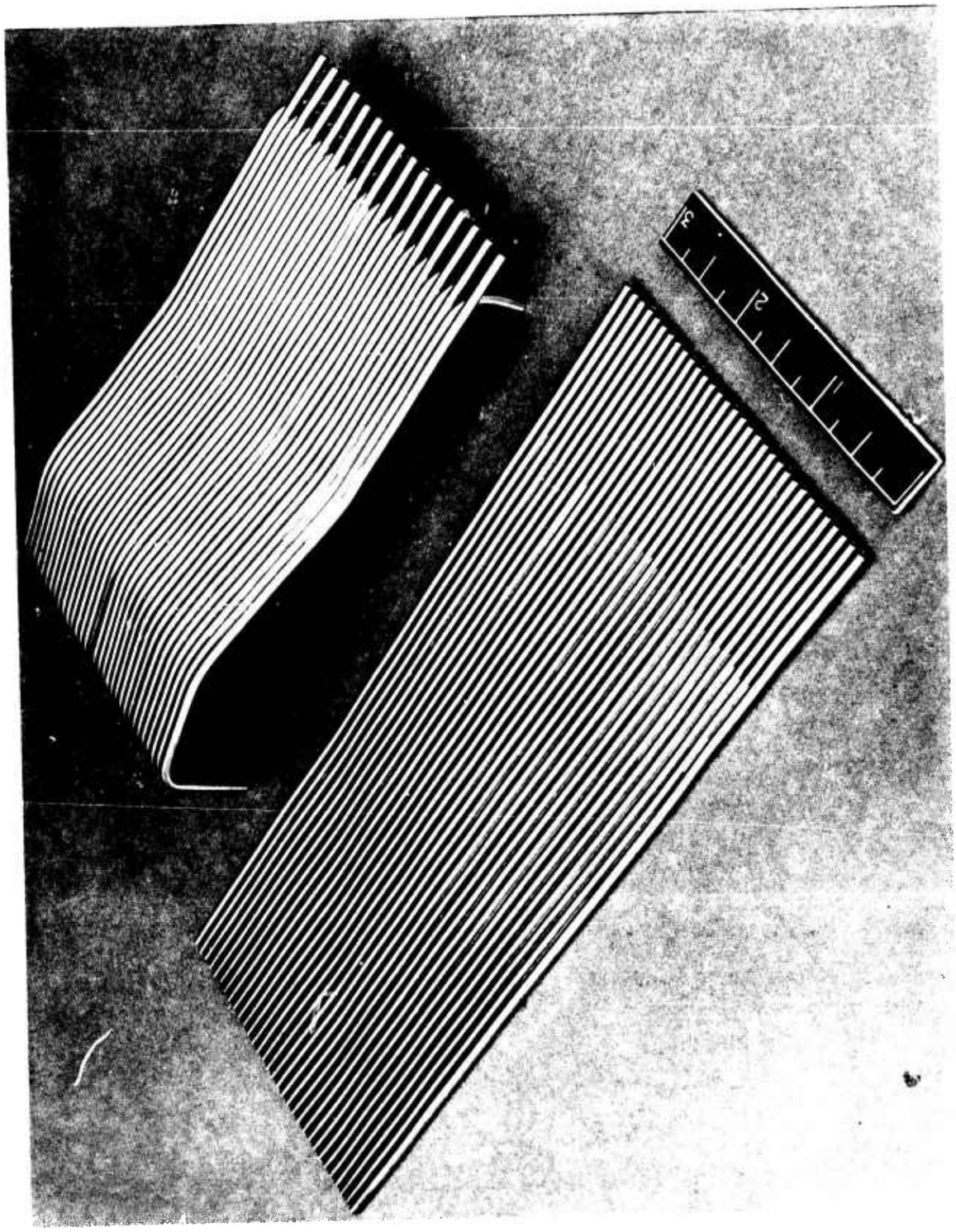

Figure 77. Sample EB-Welded Tube Blankets Before and After Forming

on and the assembly machined to provide a shrink fit into the round structural collar. This method of assembly provided opportunities for inspection of each critical braze joint before accessibility was lost. A completely assembled segment is shown on Figure 78.

(C) Nickel 200 was selected as the material for the hydrogen coolant tubes. This selection was made based on the favorable physical properties of this material as well as recent good tube test results with this material on other programs.

(C) The original tube design concept was that of having variable inside diameter with constant outside diameter. The tube was to be formed from a constant cross-section tube by tapering the tube to the desired internal contour, plating the tube, and grinding the plated tube to the required outside diameter (tube OD = 0.093 inch, tube ID at throat = 0.045 inch). Difficulties encountered in centerless grinding the tubes (holding concentricity tolerances), however, made this approach impractical.

(C) The final tube design selected was that of a constant outside diameter (0.093 inch) and constant inside diameter (0.045 inch). While this tube design had a higher pressure drop than a tube design with inside contouring, it did duplicate the minimum inside diameter of the critical throat region, the overall heat load to the coolant (bulk temperature rise), and the gas side tube wall temperature profile along the combustion chamber contour.

(C) Heat transfer analysis resulted in the specification of unequal numbers in tubes in the first and second passes. Seventeen first pass tubes were used compared to sixteen second pass tubes because the warmer hydrogen in the second pass of the number 2 side required a higher coolant mass velocity for a given tube wall temperature.

b. Tube Wall Segment Testing

(C) After completion of fabrication of the segments, they were hydrotested to 2000 psig and water flow calibrated. Pressure drop data agreed well with the analytical prediction as shown on Fig. 79.

(C) Twenty hot firings were conducted on the No.1 and No.2 segments, 8 tests on No.1, and 12 tests on No.2. A test summary is shown on Table 8. Initial tests were conducted with the hydrogen coolant flow ducted overboard after leaving the coolant jacket. A separate ambient hydrogen flow was provided to the injector manifold. After demonstration of satisfactory cooling in this manner, tests were conducted with the heated hydrogen from the coolant jacket routed to the injector manifold. The two sides of the segment were cooled in a parallel flow arrangement because of facility feed system pressure limitations. Tests on segment No. 1 were conducted with cold hydrogen (~ 100 R) entering the coolant jacket

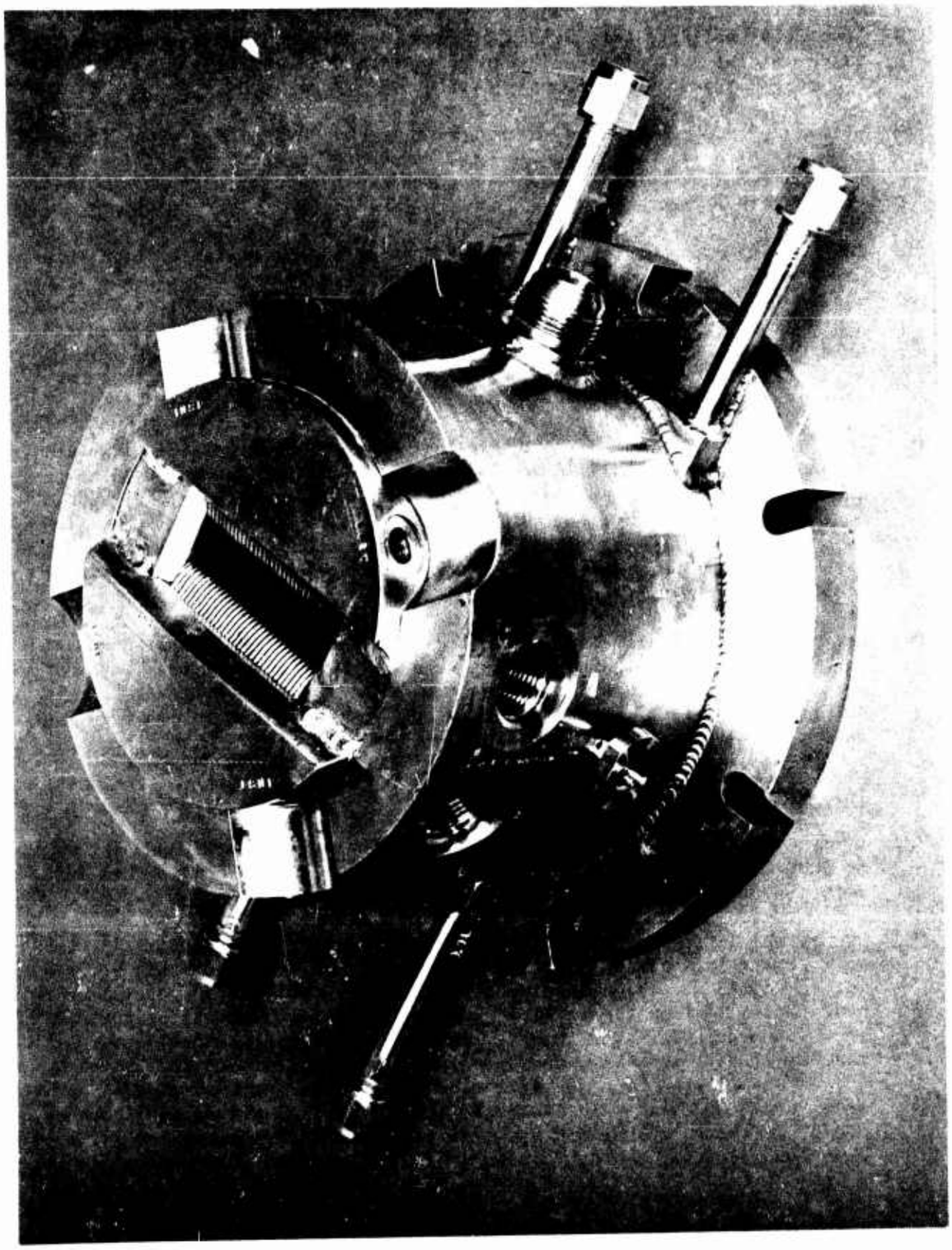

Figure 78. Completed Tube-Wall Segment

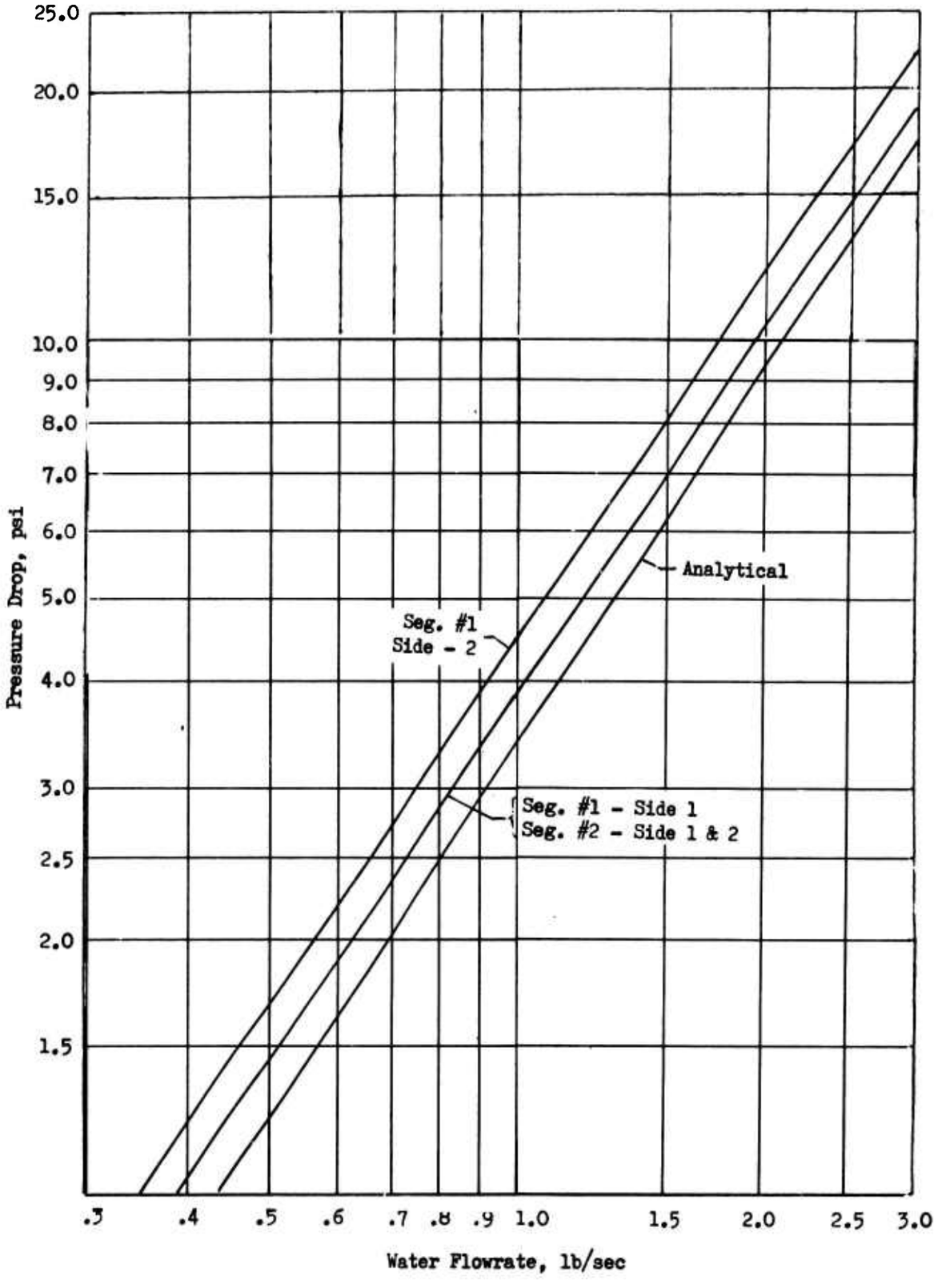

Figure 79. Pressure Drop vs Water Flowrate For Nickel Tube Wall Segments

TABLE 8

TUBE WALL SEGMENT TEST SUMMARY

(Mixture Ratio$_{(nominal)}$ = 13:1)

Segment Assembly	Run Number	Duration, seconds	Chamber Pressure, psia	Test Conditions
No. 1	87	0.2	250	Ambient H_2 to injector
	88	0.3	275	
	89	3.5	413	
	90	3.0	537	
	91	2.0	640	
	92	3.0	662	
	93	6.0	568	
	94	1.2	372	
No. 2	95	1.1	169	
	96	0.9	146	
	97	6.7	54	
	98	6.7	128	
	99	5.9	136	Coolant H_2 to injector
	100	9.1	75	
	101	7.6	79	
	102	26.4	269 to 141	Coolant H_2 to injector; dynamic throttling
	103	33.4	286 to 94	Coolant H_2 to injector; dynamic throttling
	104	7.2	662	Coolant H_2 to injector
	105	50.4	307 to 71	Coolant H_2 to injector; dynamic throttling
	106	1.5	249	Coolant H_2 to injector

thus simulating conditions for an actual engine on the first and second pass of the outer body of the chamber. Tests on the No. 2 chamber were conducted with ambient hydrogen entering the coolant jacket which simulated the condition of the down and up passes of the chamber inner body. A flow schematic of the hydrogen coolant flow circuit is shown on Fig. 80 with indicated pressure temperature and flow measurements.

(C) Dynamic throttling was conducted on three tests by programmed control of facility propellant supply pressures in a manner such that propellant flows were reduced while maintaining mixture ratio nearly constant at 13:1. Maximum throttling was accomplished on Test No. 105 where chamber pressure was continuously varied from 307 psia to 71 psia. This was the maximum dynamic throttling range possible without extensive facility modifications. The low end of the design throttle range was evaluated particularly because of concern over potential stability problems due to the F_2 two-phase flow condition which occurs in the injector at the low end of the throttle range. No instability was observed on these tests even though considerable F_2 vaporization in the injector was indicated to have occurred. These results are more fully discussed in the section on Performance Analysis which follows.

(C) A typical chamber pressure trace on one of the throttling tests (run 103) is shown on Fig. 81. The slow starting transient which is indicated resulted from no pre-chilling of the segment hardware prior to test start. Eliminating the pre-chill aided in reducing the time for the segment to reach thermal equilibrium.

c. Tube Wall Segment Performance Analysis

(C) A summary of the performance values obtained on the segment tests are shown in Table 9. All tests, except those which were of too short a duration for performance evaluation or where instrument malfunctions on critical parameters occurred, are included. Performance values at various chamber pressure levels during throttling tests No. 103 and No. 105 are shown on Tables 10 and 11.

(U) Analysis Method. The analysis procedures for the tube wall segment tests were basically the same as outlined previously for the solid wall segment tests (Section II). Theoretical c* was based on ambient hydrogen conditions since an energy balance takes into account the enthalphy added to the hydrogen from the cooling jacket.

(U) A change to the approach of determining the effective throat area was made, however, because of the inaccuracies in measuring the geometric throat with the contour formed by the tubes. The effective throat area ($A_{eff} = C_D A_{geom}$) was determined by calibration with GH_2 blowdowns using the following equation

$$\dot{W} = C_D A P_o \sqrt{\frac{\gamma Mg}{RT} \frac{2}{\gamma + 1} \frac{\gamma + 1}{\gamma - 1}}$$

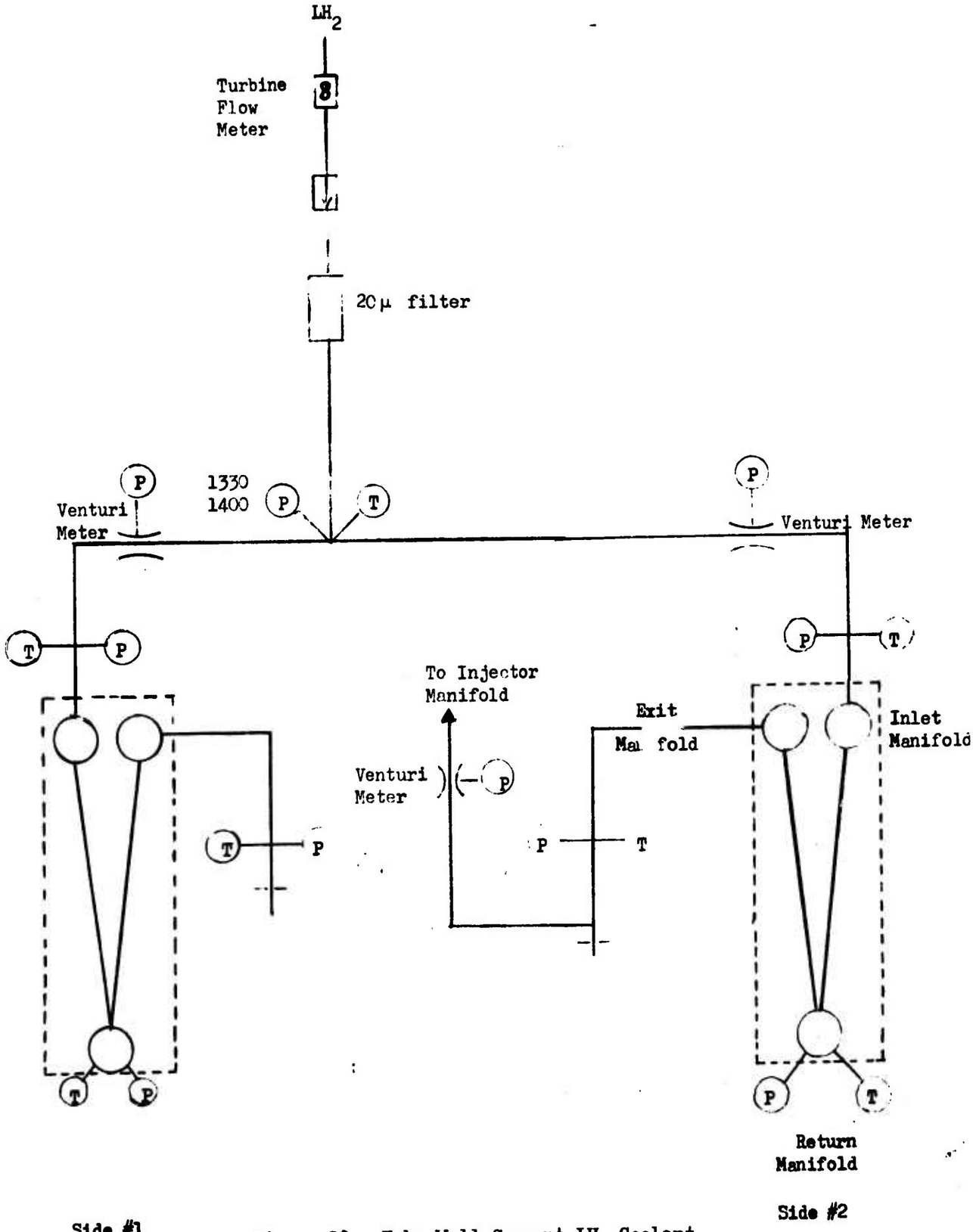

Figure 80. Tube Wall Segment LH_2 Coolant Circuit

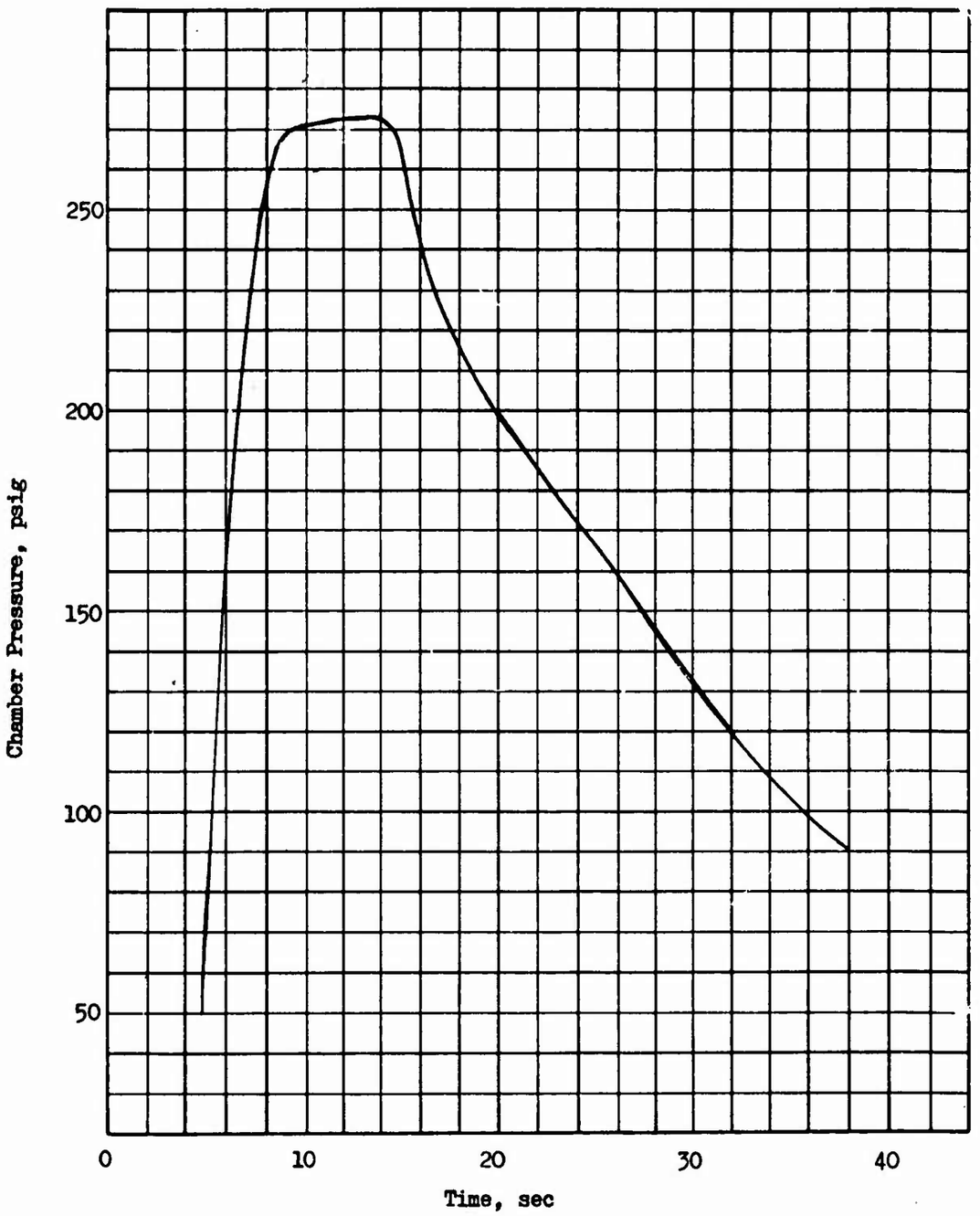

Figure 81. Chamber Pressure vs Time for Dynamic Throttling Test No. 103

TABLE 9 SUMMARY OF TUBE WALL SEGMENT PERFORMANCE

RUN No.	Duration (sec)	Chamber Pressure (psia)	Total Inj. Flow Rate (lbs/sec)	Mixture Ratio	Inj. Hydrogen Condition	C* Theoretical (ft/sec)	η_{C^*} (Percent)
89	3.5	413	0.777	12.1	Ambient	8185	96.9
90	3.0	537	1.016	13.4		8130	96.2
91	2.0	640	1.192	12.0		8220	96.3
92	3.0	662	1.184	10.8		8280	96.7
93	6.0	568	1.024	13.1		8170	96.3
99	5.7	136	0.220	12.4	Heated	8005	99.6
102	26.4	265-141*	.421 (max)	11.5		8175	99.4*
103	33.4	286- 94*	**	**		**	99.9-97.7*
104	7.2	662	1.039	14.1		8162	99.8
105	50.4	307-71*	**	**		**	99.6 -99.0*

* dynamic throttling tests

** Refer to Tables 10 and 11

CONFIDENTIAL

TABLE 10 SUMMARY OF THROTTLING TEST 103
(Heated H_2 to Injector)

P_c psia	W_t lb/sec	MR	C* Theo. ft/sec	η_{C^*} (P_c) %
276	0.441	13.9	8045	99.9
200	0.335	16.4	7850	98.4
147	0.234	18.0	7700	98.0
98	0.169	18.8	7790	97.7

TABLE 11 SUMMARY OF THROTTLING TEST 105
(Heated H_2 to Injector)

P_c psia	W_t lb/sec	MR	C* Theo. ft/sec	η_{C^*} (P_c) %
307	0.990	11.8	8645	99.0
296	0.390	11.3	8160	99.2
157	0.320	13.3	8030	99.2
196	0.239	13.0	8005	99.1
96	0.158	13.7	7930	99.6
71	0.119	13.9	7900	99.6

CONFIDENTIAL

where $\dot{W}$, the flow rate, was measured with a calibrated sonic venturi. Necessary pressure (Po) and temperature (T) measurements were also taken.

(U) The previous solid wall segments evaluation required a correction to the geometrical throat area due to thermal effects during the firing. This correction, however, was not required for the tube wall segments because analysis showed negligible thermal expansion of the tube backup structure would occur during a firing.

(C) C* Efficiencies. As noted from the results shown in Tables 9, 10 and 11, a significant performance improvement was realized when the heated hydrogen from the cooling jacket was used in the injector. The temperature of the hydrogen entering the injector was approximately 650 F on these tests. C* efficiencies in excess of 99 percent were obtained compared to approximately 96.5 percent for the ambient hydrogen injection tests. The heated hydrogen to the injector has a two-fold benefit in improving η_{C*}; increase of the hydrogen injection velocity and providing heat to the fluorine in the injector.

(C) Figure 82 shows η_{C*} plotted over the range of chamber pressures for the tube wall segment tests with heated hydrogen, for the tube wall tests with ambient hydrogen, and for the previous solid wall segment tests with ambient hydrogen. These tests were all conducted with the contour G chamber configuration and the same impinging fan injector. As shown, the ambient hydrogen performance values for the solid wall and tube wall segments agree very well at a η_{C*} of approximately 96.5 percent. The performance values for the tube wall segment with heated hydrogen, however, are substantially higher at approximately 99.5 percent. Several solid wall tests are also shown at the low end of the throttle range where the injection fluorine was purposely gasified by an external exchanger. These tests with the solid wall segment also showed improved performance over what was obtained with liquid fluorine injection.

(C) As discussed previously in the solid wall segment performance section (Section II, 5.c), a useful parameter for correlation of C* performance has been found to be the dynamic flow parameter $\dot{W}o\ Wf\ Vf$ where Wo and Wf are the oxidizer and fuel flow rates and Vf is the fuel injection velocity. This parameter is shown plotted for all contour G solid wall and tube wall tests in Fig. 83. The performance values achieved at the flow parameter value of approximately 2×10^{-3} are the tube wall segment tests with heated hydrogen. The effect of the hotter hydrogen on increasing the hydrogen injection velocity and improving performance is apparent. The variation in the flow parameter between approximately 3 to 5 on the other tests is attributed to the variation in mixture ratio within tests.

(C) An additional benefit from the heated hydrogen is the promotion of fluorine vaporization in the injector which further aids in achieving high performance as well as increasing injector pressure drop thus providing stable operation. For a 9:1 throttle range, an 81:1 change

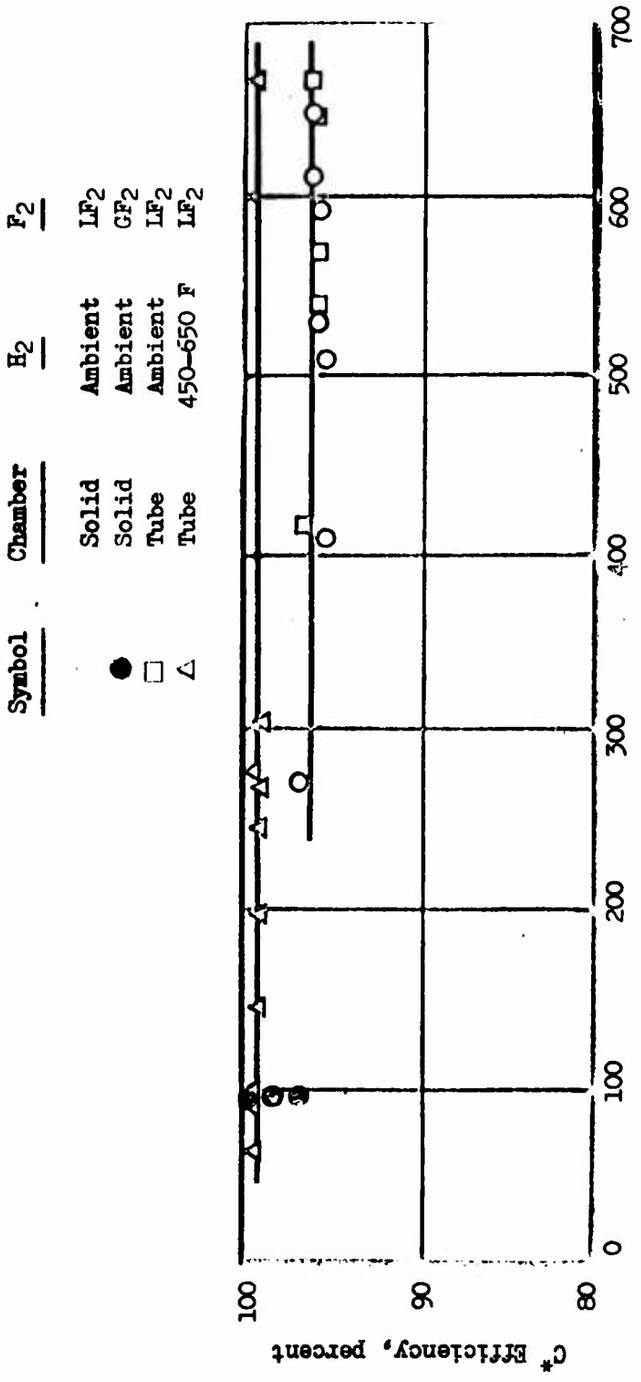

Figure 82. C^* Efficiencies in Contour G Chambers With Impinging Fan Injector

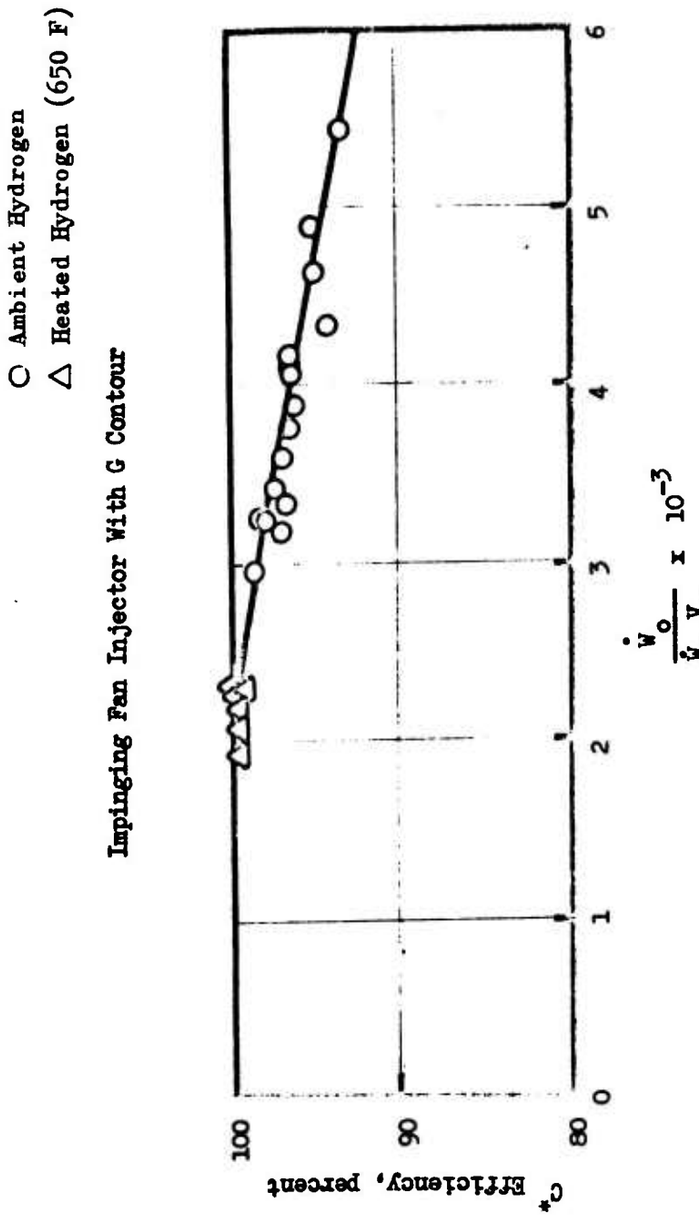

Figure 83. Effect of GH_2 Injection Velocity on Performance

in oxidizer pressure drop is required if vaporization did not occur. The results of throttling tests 103 and 105 shown on Fig. 84. indicate that two phase flow occurred below flow rates of approximately 0.4 lb/sec. The percent of fluorine vaporized increased as the flow decreased with approximately 50 percent being vaporized at the 70 psia chamber pressure flow rate point. No indications of stability problems occurred on these tests whereas on earlier solid wall segment tests with this chamber and injector configuration, instability resulted at the low end of the chamber pressure range when fluorine was introduced to the injector as a liquid (refer to Section II 6.g).

d. Tube Wall Segment Heat Transfer Analysis

(C) Twenty hydrogen cooled tube wall segments were conducted and are summarized in Table 12. The first 8 tests (87-94) with segment No. 1 utilized cryogenic hydrogen cooling. The remaining 12 tests with segment No. 2 utilized ambient hydrogen cooling. On the last test of the No. 1 segment, an internal leak within the segment is believed to have occurred which permitted water from the side plates to enter the hydrogen coolant tubes prior to the firing. Freezing of the water at test start restricted the hydrogen coolant flow with resultant burnout of a number of the tubes in the throat section. Testing of the No. 2 segment was concluded on Test 106 when an injector failure occurred at start and resulted in damage to the chamber tubes. Exact cause of the injector failure was not determined, however, it may have been caused by fatigue from the large number of previous tests with this injector (76 tests).

(U) The primary quantitative experimental data which were obtained from the tube wall test segments were total heat inputs. These were obtained from measurement of the coolant flowrate and coolant enthalpy rise. This latter quantity is calculated from the initial and final coolant temperatures and pressures for hydrogen. The resulting relation for the heat input is therefore simply

$$Q = \dot{W}_c \quad \Delta H \tag{1}$$

(U) In the case of ambient hydrogen cooling, the change in hydrogen specific heat was negligible over the range of temperature of interest and the heat input was calculated directly from measured quantities in accordance with equation (2)

$$Q = \dot{W}_c \quad \overline{C}_p \quad \Delta T_{BULK} \tag{2}$$

(U) The coolant flowrates were determined from flow venturis. The bulk temperature measurements were obtained from thermocouples placed upstream, downstream, and at the return manifold of the two-pass cooling circuit (Fig. 79). A relatively slow response of the exit bulk temperature to the heat input was experienced, however. This was apparently

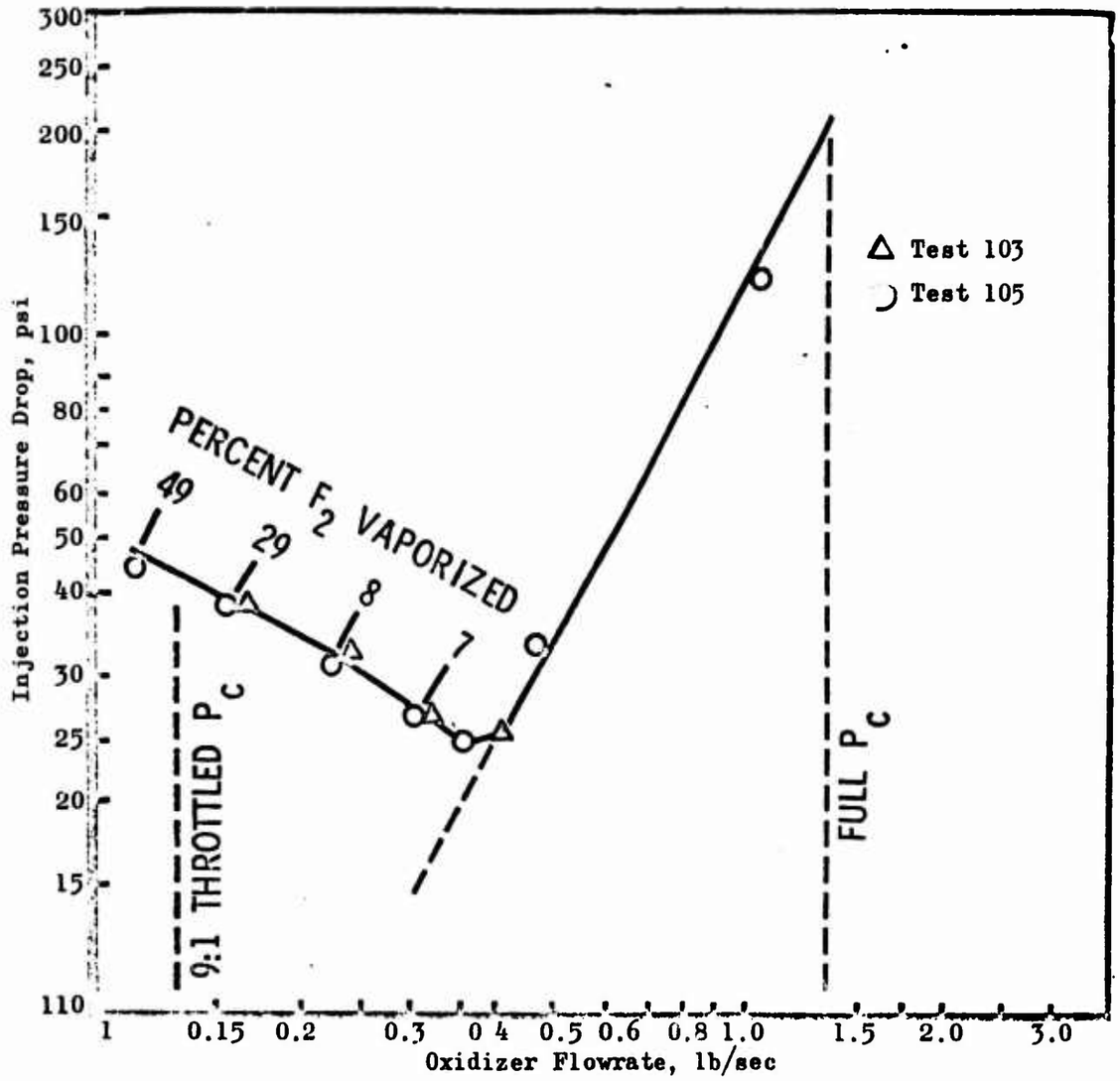

Figure 84. Injector Fluorine Pressure Drop vs Flowrate for Impinging Fan Injector

TABLE 12

TUBE WALL SEGMENT COOLANT TEST SUMMARY

Test No.	Duration (sec)	P_C (psia)	H_2 Coolant Flow (lb/sec)	Tube Wall Temp. (Throat Estimated) F	Segment No.
87	.20	250	.15	700	
88	.3	275	.165	730	
89	3.5	413	.148	1030	
90	3.0	537	.166	1310	
91	2.0	640	.163	1485	#1
92	3.0	662	.168	1510	
93	6.0	568	.148	1380	
94	1.2	372	.102 (#1 side)	1300	
95	1.3	169	.0456	1150	
96	.9	146	.046	1070	
97	6.7	54	.0457	704	
98	6.7	128	.0458	1010	
99	5.7	136	.0450	1035	
100	9.1	75	.0457	800	
101	7.6	79	.0452	800	#2
102	26.4	265-141*	.1095 - .0400	1070 - 1070	
103	33.4	286-94*	.0976 - .022	1200 - 1200	
104	7.2	662	.105	2040	
105	50.4	307-71*	.061 - .0096	1580 - 1519	
106	1.5	249	.102	1070	

* Dynamic Throttling Tests

CONFIDENTIAL

due to the influence of the water cooled end plates in conjunction with the high conductivity of the copper strong-back.

(C) A comparison of the temperature and chamber pressure traces indicated that the return manifold coolant temperature responded quickly to P_c variations. This temperature measurement was, therefore, used to estimate chamber heat inputs. Since there were 17 downpass tubes as compared to 16 uppass tubes the relation for the total temperature rise is

$$T_{BULK} = \frac{33}{17} \left(T_{FINAL} - T_{Initial}\right)_{\substack{\text{RETURN} \\ \text{MANIFOLD}}} \qquad (3)$$

(U) Note that the difference in initial and final temperatures at the return manifold were utilized. This was more accurate than subtracting the inlet temperature measurement from the return manifold measurement for cryogenic H_2 cooling due to incomplete chilldown of the segment before ignition.

(U) The measured coolant flowrates combined with the hot-gas convective film coefficients obtained from the solid wall segment tests were used to estimate the maximum tube wall temperatures (Table 12). The coolant convective coefficient for hydrogen was estimated from Rocketdyne previous data which included wall roughness effects.

(C) Heat Transfer Results. The heat inputs to the chamber for the tests with segment No. 1 are shown in Fig. 85. Although some data scatter is noted, the results indicated that the heat input did not decrease linearly with a chamber pressure but rather was about 2 to 3 times the value corresponding to a linear decrease from maximum chamber pressure (P_c = 650 psia). This agreed reasonably well with the data obtained from the water-cooled copper chamber tests (Fig. 65).

(C) The most severe test for segment No. 1 was test 92 at a chamber pressure of 662 psia because of the resulting wall temperature of 1510 F.

(C) Segment No. 2 utilized ambient hydrogen as the coolant and was subjected to more severe cooling requirements than segment No. 1. Tests 104 and 105 represented the most severe conditions and were evaluated in detail. Test No. 104 was at nominal chamber pressure (P_c = 662 psia) with only slight overcooling for a two-pass cooling design. Test 105 was a continuous throttling test from 307 psia to 71 psia using near and less than rated coolant flowrates. The actual and design coolant flowrates as a function of chamber pressure are presented in Fig. 86. The cooling margin associated with the tests is shown in Fig. 87 for the up and downpass circuits on both sides of the segment. (The downpass circuit has a lower flowrate per tube because there are more tubes). In Test 104 (P_c = 662 psia), the overcooling amounted to only 3 percent in the downpass circuit. In Test 105, the coolant flow actually dropped to 87 percent of rated flow at 71 psia on the side No. 1 downpass.

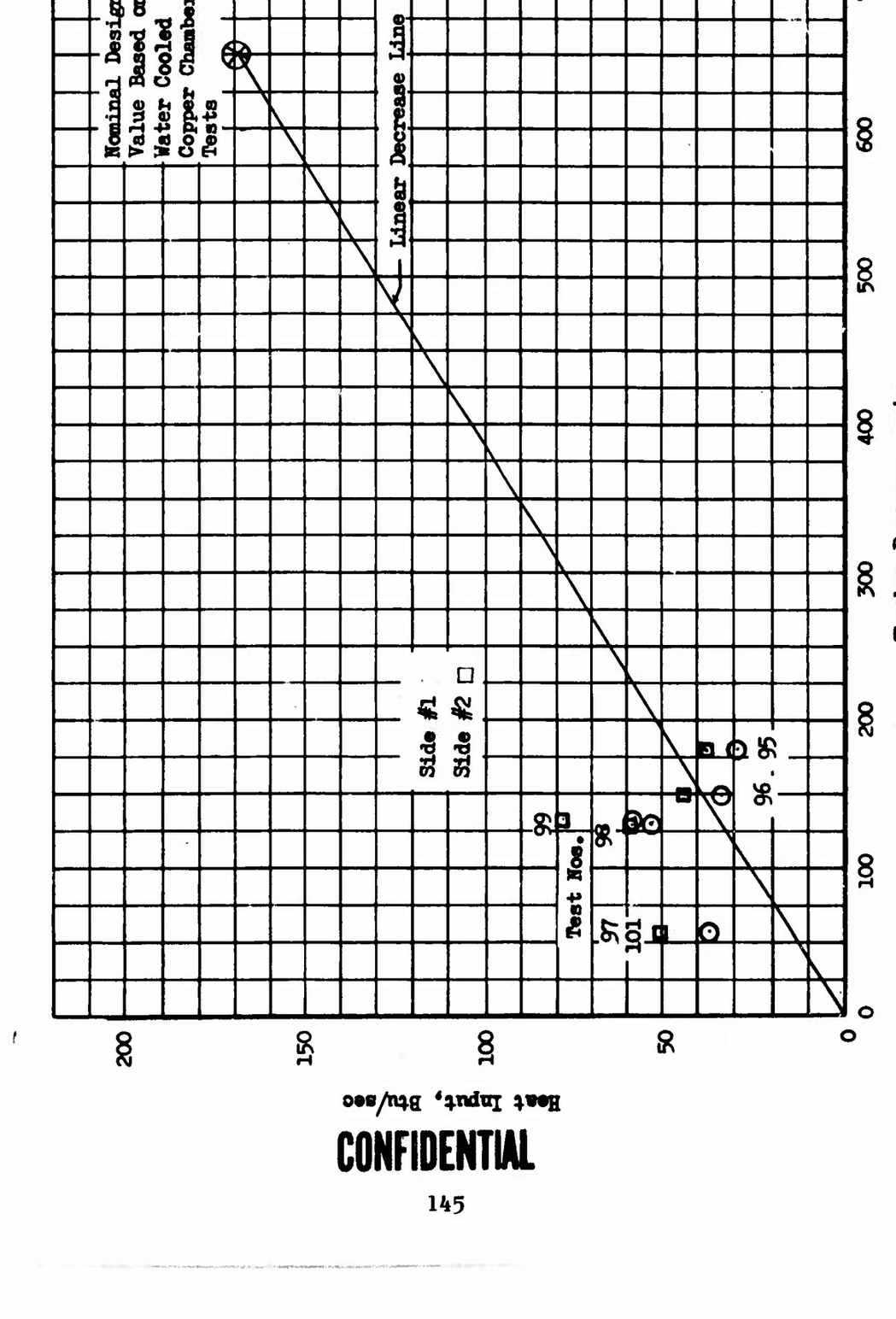

Figure 85. Measured Heat Input For Tube-Wall Segment No. 1

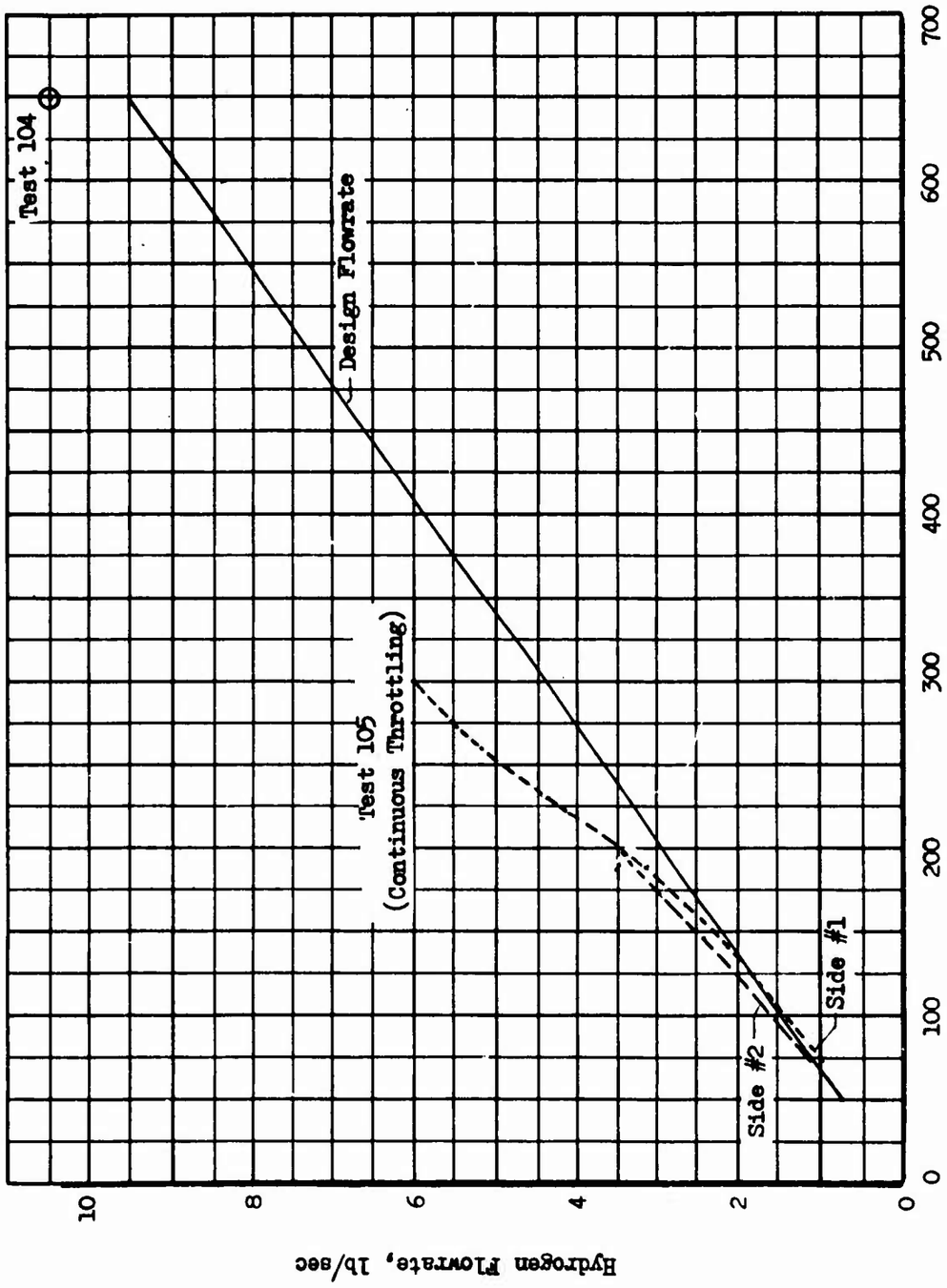

Figure 86. Comparison of Measured and Design Flowrates for Tube-Wall Segment No. 2

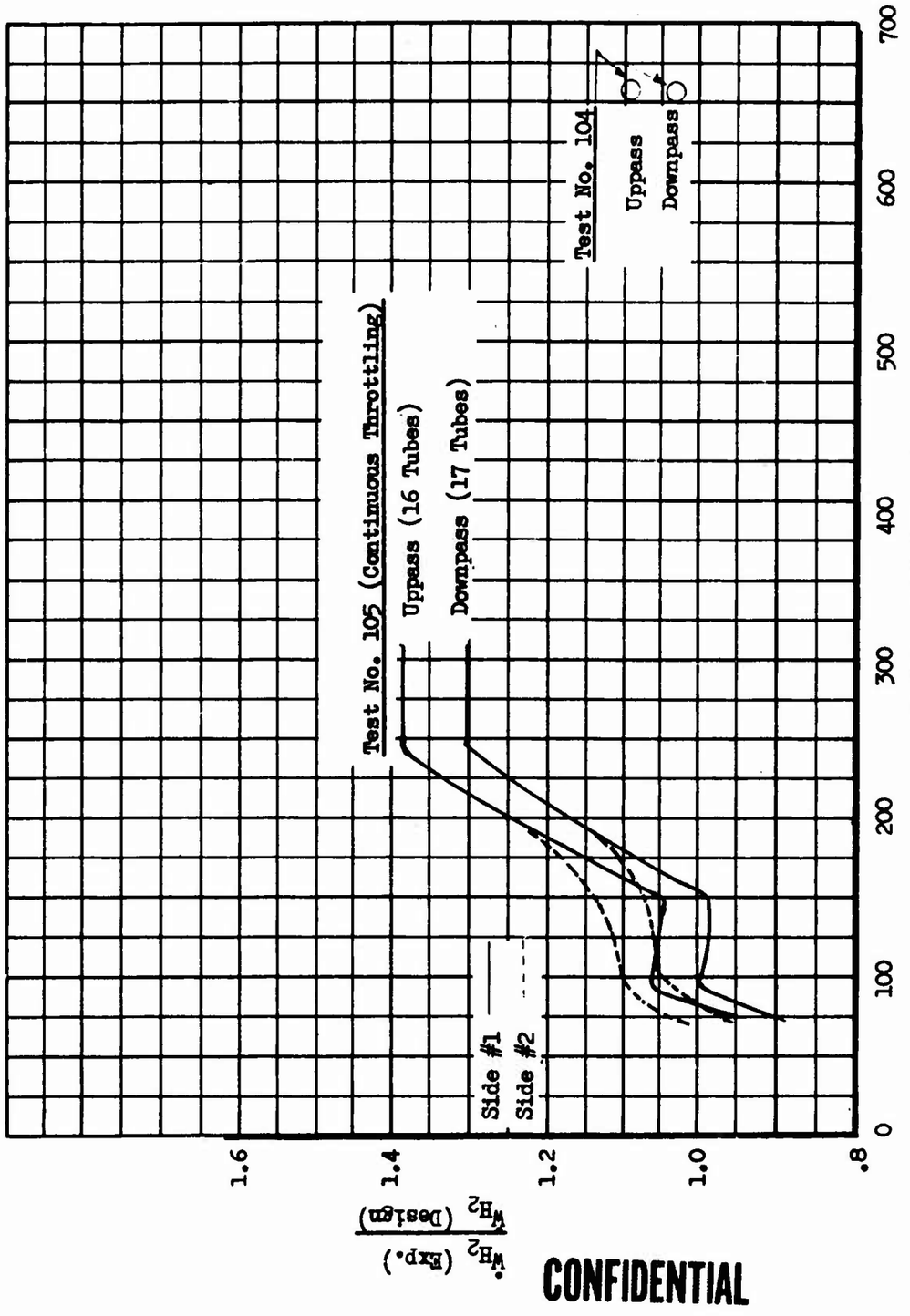

Figure 87. Cooling Margin For Tube-Wall Segment No. 2

(C) The resulting maximum tube-wall temperature were determined by two separate analytical methods. The one-dimensional method treats the tube wall as a plane slab and utilizes a simple heat balance across the wall. This method is quite satisfactory for thin-walled tubes and/or low conductivity materials such as CRES. Due to the thick-walled (0.024 inch) nickel tubes utilized in the segment design, however, it was believed more accurate to determine the wall temperature distribution by means of a thermal analyzer digital computer program.

(C) The results of these analyses for Tests 104 and 105 are compared in Fig. 88. The more exact thermal analysis predicted a maximum surface temperature of 2040 F for Test #104 (P_c = 662 psia) as compared to a 1900 F estimate using the simple one-dimensional approach. At throttled conditions the difference in the analytical results was much more pronounced. At a chamber pressure of 71 psia (Test 105), the thermal analysis program predicted a maximum wall temperature of 1519 F which was considerably lower than the 2110 F obtained with the simplified approach.

(U) The reason for the large difference in results at lower chamber pressures was that a larger percentage of tube circumferential heat conduction took place at lower heat flux levels. This allowed the heat input to be distributed over the entire inner tube circumference thereby decreasing the local heat flux to the coolant with a resultant decrease in the temperature differential across the coolant boundary layer. This condition is readily apparent from the tube isotherm profiles in Fig. 89 for a chamber operating at throttled conditions (a tube isotherm profile for the full thrust condition was shown in Fig. 67). At high flux levels (i.e., high P_c) the circumferential conduction is less influential and the local heat flux to the coolant is actually higher than at the heated surface due to the smaller surface area of transfer. The result is a temperature higher than would be estimated by a one-dimensional analysis.

(C) The most important result obtained from Tests 104 and 105 is related to the heat input to the segment as shown in Fig. 90. The heat input drops off nearly linear with chamber pressure. This is extremely important since it means that the coolant bulk temperature rise will remain relatively constant during throttling. Previous data with the copper segments and tube segment No. 1 indicated that the heat input at throttled conditions was two to three times the linear drop-off value. This would have resulted in very high coolant bulk temperature rises.

(C) The primary difference in the test conditions of Test 105 was that heated hydrogen (T ≈ 500 F) was injected into the chamber rather than ambient temperature (T ≈ 70 F) hydrogen. The water-cooled copper chamber results indicated that at throttled conditions a greater proportion of the heat input was near the injector end of the chamber. It is believed, therefore, that the increased combustion efficiency obtained from the heated hydrogen injection resulted in a reduction of the wall heat transfer rates in the vicinity of the injector. A check of tests 102 and 103

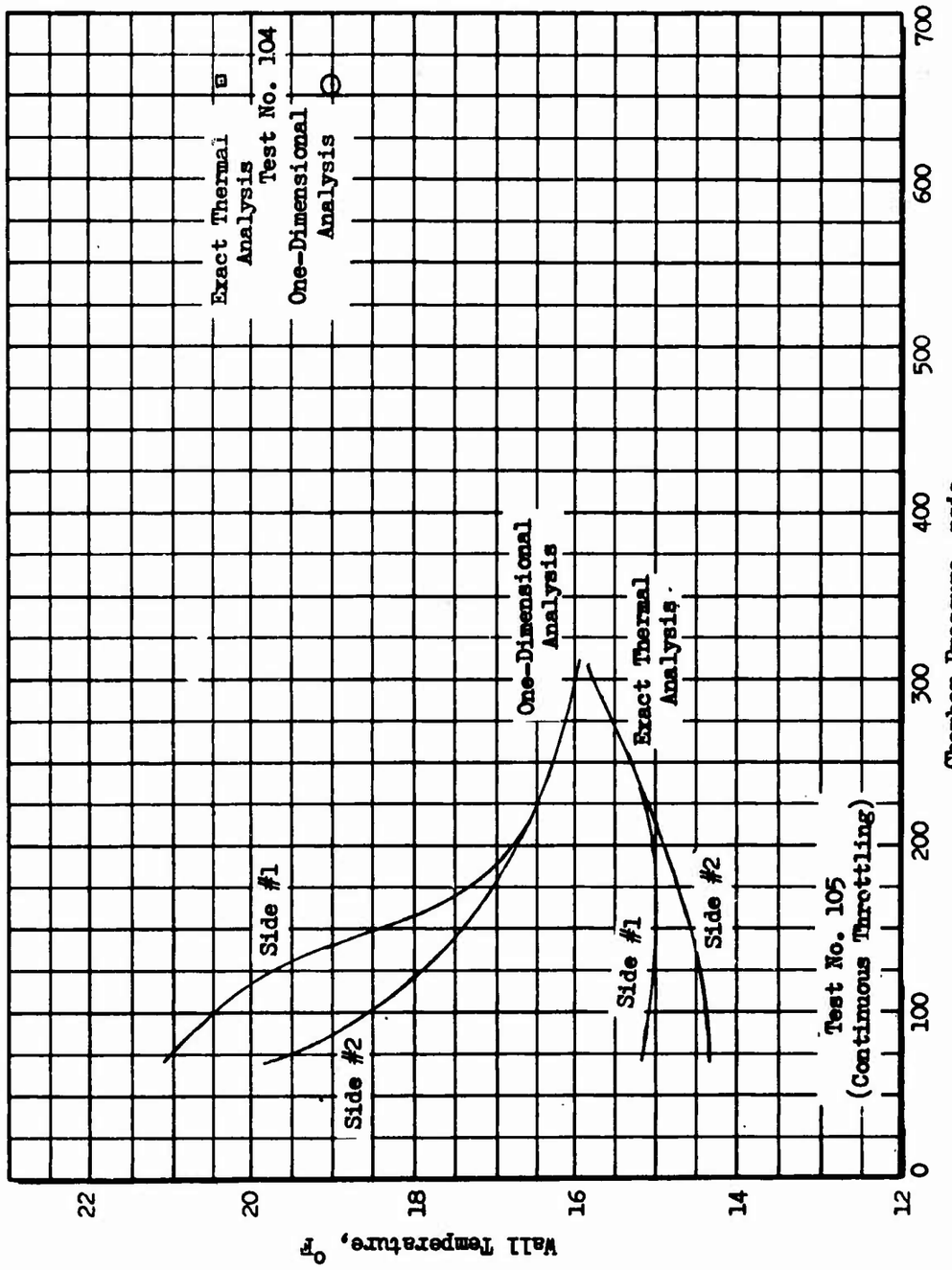

Figure 88. Estimated Peak Wall Temperatures For Tube-Wall Segment No. 2

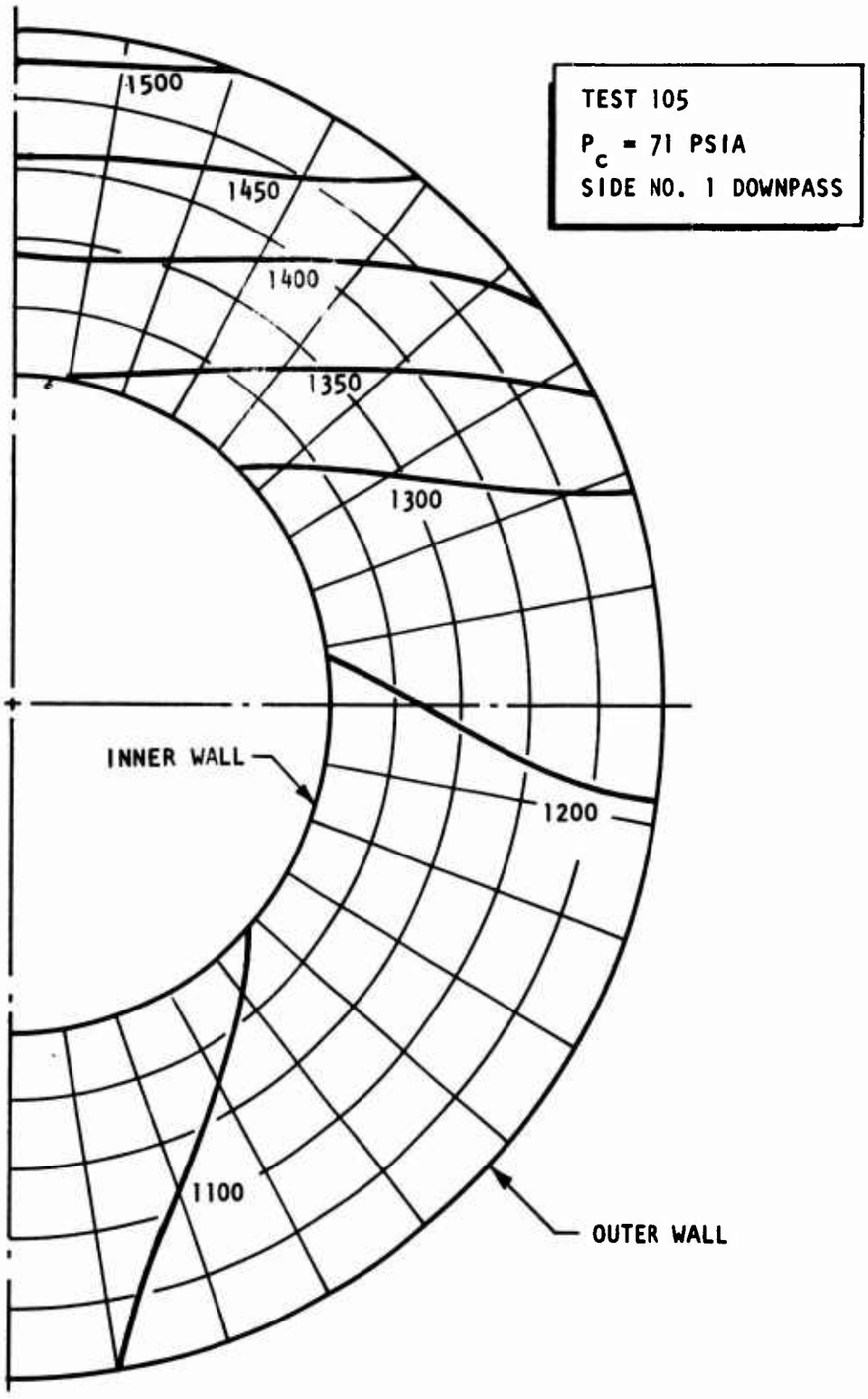

Figure 89. Coolant Tube Isotherm Profile

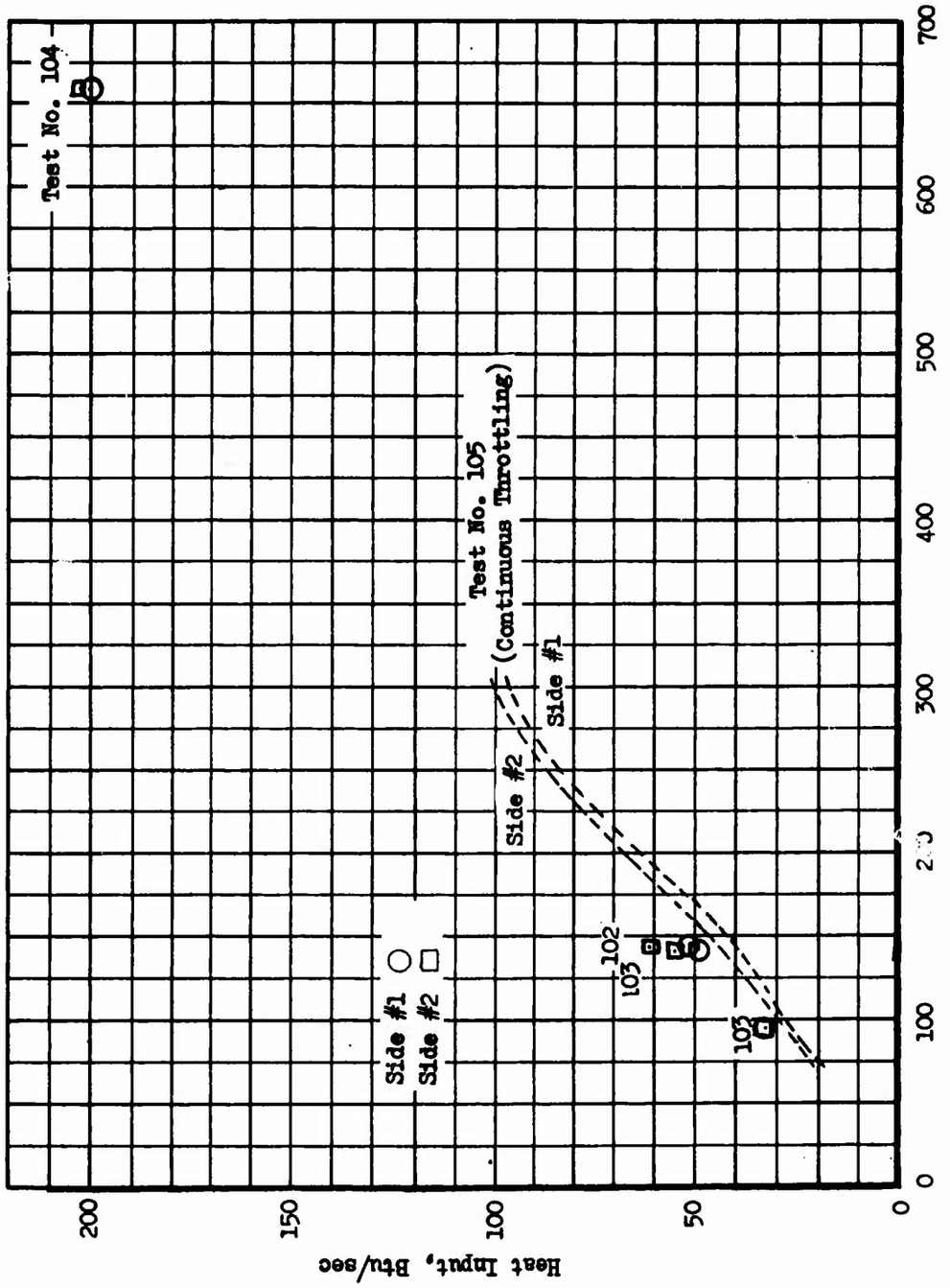

Figure 90. Measured Heat Input For Tube-Wall Segment No. 2

substantiates this theory as shown in Fig. 90. Test 102 and 103 utilized hydrogen injected at a somewhat lower temperature than 105 (≈ 100 F less) and had a heat input about 25 to 50 percent greater than Test 105 at a chamber pressure of 140 psia. Verification of this rational requires further testing of the solid wall segments using heated hydrogen injection.

(C) The total heat input at nominal chamber pressure (P_c = 650 psia) was about 17 percent higher than estimated from the copper segment tests. Part of this increase could be due to the increased surface area of tubes (scallop effect) as compared to the flat copper surface. The resulting hydrogen bulk temperature rise for the entire segment (rated coolant flow) is estimated at 1140 F. Assuming a 50 R inlet temperature, the hydrogen exit temperature would be 730 F. The use of ambient hydrogen during testing resulted in coolant bulk temperatures comparable (within 100 F) to those anticipated for the inner body contour of the full thrust chamber.

e. Summary of Significant Results

(C) The contour G chamber configuration with the impinging fan injector achieved C* efficiencies in excess of 99 percent with stable combustion over the entire design throttle range when operated in a regeneratively cooled configuration.

(C) Results of the cooling evaluation demonstrated the feasibility of regeneratively cooling the 30K toroidal combustion chamber with a two pass cooling circuit. Successful cooling was achieved at nominal chamber pressure (P_c = 650 psia) using essentially rated flow (3 percent overcooling) and at full throttled conditions (P_c = 71 psia) using less than rated flow. The heat input to the chamber drops off nearly linearly with chamber pressure when heated hydrogen is injected in place of ambient hydrogen at throttled conditions. This is due to reduced wall heat input near the injector end resulting from increased combustion efficiency.

4. LIGHTWEIGHT SUPPORT STRUCTURE SEGMENTS

(C) The purpose of the structural segments was to establish the structural integrity of rib and honeycomb support structures and to demonstrate, by means of mechanical loading tests, that the throat area can be maintained within 10 percent over the 9 to 1 throttling range. A comparative design analysis was conducted to select the optimum configuration. Using selected configurations, a more detailed design optimization was conducted to determine values of critical design parameters which would result in the lightest segment. The final step was the actual detailed design of combustion chambers using rib and honeycomb construction as the structural material. These design efforts as well as the fabrication and testing of segments of the chambers are described in this section.

a. Structural Support Concept Selection

(C) The annular thrust chamber design resulting from the Maneuvering Satellite Propulsion System study (Contract AF04(611)-10745) utilized a C-clamp support structure. With this support structure, the resistance to the chamber pressure is provided by bending of a beam surrounding the chamber. The bending imposed is symmetrical about a plane through the center of the injector, and the thickness of the skins used for the beams is determined by the throat deflection rather than the stress on the material. The design of the C-clamp structure required the determination of the maximum allowable throat gap variation as well as the optimum (lightest) structure to limit the variation to this value.

(U) During the present contract, detailed design analysis was conducted on the basic C-clamp structure concept as well as two alternate support structure concepts. The two alternate concepts have been designated the subsonic baffle and the subsonic bolt. The three design approaches are shown on Fig. 91 and are described in the following paragraphs.

(C) C-Clamp Design. Inner and outer combustor walls cantilevered from the injector form the C-clamp structure. The combustor walls were constant depth compound curved honeycomb panels; however, other types of structure such as webs and plates or "egg crate" could be used. A transition section joins the outer skin of the panels to the injector. The transition section is more rigid than the panels because of its influence on throat deflection. The injector forms the final link of the structure joining the inner and outer combustion chamber walls and transmitting the bending and shear reactions from one to the other. All of the structural components would be made of INCO 718 because of its high strength and low thermal expansion properties.

(C) The thrust chamber coolant path consists of a two-pass circuit on both the inner and outer combustor walls. The hydrogen coolant enters the inner combustor coolant circuit from the fuel inlet manifold. It then flows through the two-pass cooling circuit, and is manifolded across the injector to the outer combustor wall where it flows through a similar two-pass circuit. The hydrogen is then fed into the distribution manifold behind the injector face. The two propellant manifolds and the tapoff manifold are positioned outside the injector body and separate from each other to prevent heat transfer from the hot gas to the two cryogenic propellants. A Rigimesh face triplet injector was used for weight evaluation purposes.

(U) C-Clamp Structure Analysis Method. The C-clamp structure resists the pressure in bending. The structure is essentially symmetrical with respect to the center of the injector. Several different operating conditions were analyzed. The Rocketdyne modification of an existing structural computational program (which utilizes the IBM 7094 Computer) was used in the analysis of the various conditions. The program allows

(a) C-CLAMP STRUCTURE

(b) SUBSONIC BAFFLE STRUCTURE

(c) SUBSONIC BOLT STRUCTURE

Figure 91. Toroidal Chamber Structures

the structure to be broken up into up to 25 regions. Each region, in turn, can be broken into laminates and variation in temperatures, coefficients of thermal expansion, and Young's Modulus can be programmed through the composite shell thickness. In addition, the above parameters plus the pressure loading can be varied from station to station along each region.

(C) The study took into account a full range of engine operating conditions including chilldown, full thrust at start and steady state, and fully throttled at start and steady state. The initial reference temperature of the structure was 70 F.

(C) Subsonic Baffle Design. This design consists of inner and outer combustor walls joined through the injector and baffles. The baffles form the major structural ties between sides, alleviating the injector of this function. The structural panels act primarily as fixed-fixed beams supported on either end by the baffles. The construction techniques and materials are the same as used on the C-clamp design.

(C) The combustion chamber coolant circuit is two-pass like that of the C-clamp. The outer combustor wall is first cooled in parallel with the baffle. The baffles require approximately 7.6 percent of the total coolant to match temperature rise and pressure drop of the outer wall. The inner wall is then cooled with the total flow. This arrangement was found to minimize thermal stress and deflection of the baffle. It also allows the use of a practical baffle coolant-tube diameter. The baffle tubes are constant circumference and flattened slightly in the convergent section of the chamber.

(C) The same injector was used for all three concepts and incorporates a Rigimesh transpiration-cooled face welded to the body. The crossover passages in the back of the injector are spaced so that oxidizer and tapoff gas can pass between them. Fluorine flows from the supply manifold through posts which pass through the Rigimesh face. The posts are flush with the injector face on the combustion chamber side and have holes drilled in them to form the oxidizer part of the triplet injector. The fuel orifices are drilled through the Rigimesh face. Tapoff is through a series of hydrogen-cooled ports located on the injector face. The fluorine and tapoff manifolds are separated from the main injector body to minimize heat conduction between the cryogen fluorine, the hot tapoff gas, and the warm injector body.

(C) As in the C-clamp design, the outer combustor wall is made removable to facilitate inspection and servicing inside the combustor. Because the injector-to-outer combustor wall joint is not in a highly loaded area, the flange and bolts can be relatively light. Any seal leakage would be hydrogen, including the baffle bolts which have double seals under each head with fuel bleed in between. The baffle provides an excellent means of indexing one side of the combustor to the other.

The combustor rings are sufficiently flexible in the hoop direction so that the baffle bolts can easily pull the two halves together, thus taking up any diametrical tolerances.

(U) Subsonic Baffle Structure Analysis Method. The subsonic baffle backup structure acts basically as the interaction between two rings with radial ties and with a pressure between them (Fig. 92). The study has shown that if only a few baffles are used, a heavier combustion chamber is required to minimize throat area changes. For larger number of baffles (of the order of 20), the ring interaction solution reduces to essentially a fixed-fixed beam solution with the beam length equal to the developed length between the baffles (Fig. 93). The result is a reduction in overall chamber weight. An important structural conclusion can be shown by consideration of the fixed-fixed beam solution. The change in throat area is given by

$$\frac{\Delta A}{A} = \frac{4\pi^4}{45} \frac{P_c R^4}{gE} \frac{1}{td^2 N_B^4}$$

where:

ΔA = area under the deflection shape curve for two beams, in.^{2}

A = unpressurized area between two baffles, in.^{2}

E = $g\ 2\pi R/N_B$

P_c = chamber pressure, psia

R = chamber average radius, inches (The exact solution involves the use of the radii of the outer and inner rings; however, this difference is small.)

g = initial throat gap, inches

t = box section skin thickness, inches

d = depth of the box section, inches

N_B = number of baffles

(U) Because the fractional change in throat area is reduced in proportion to the inverse of the number of baffles to the fourth power, it is possible to reduce throat area change, due to the deflection of the backup "beams" to a small value. Throat area variation then becomes essentially the deflections of the baffles and the backup structure in the area of the baffles. The combination of a honeycomb or rib backup structure with a sufficient number of baffles will yield a system that is both rigid and light in weight.

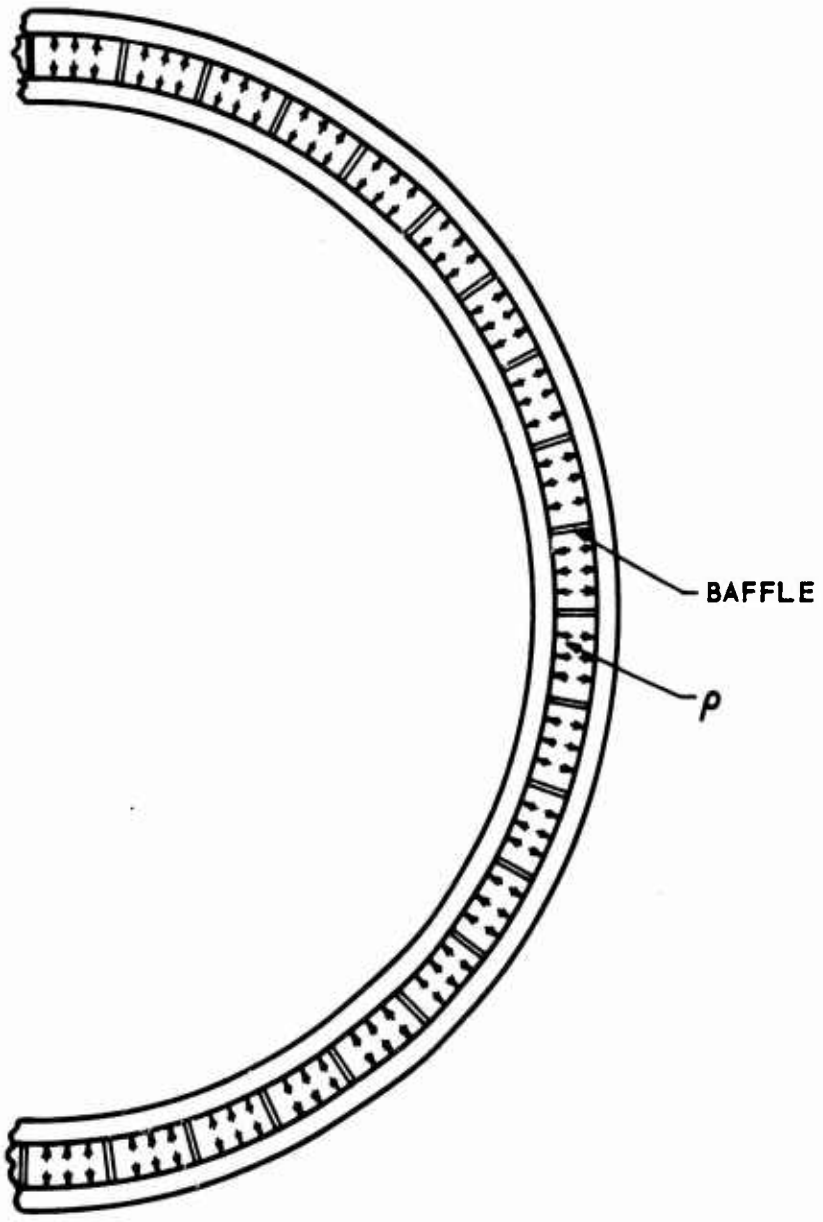

Figure 92. Two Rings With a Pressure Between Them - With Intermediate Baffle Ties

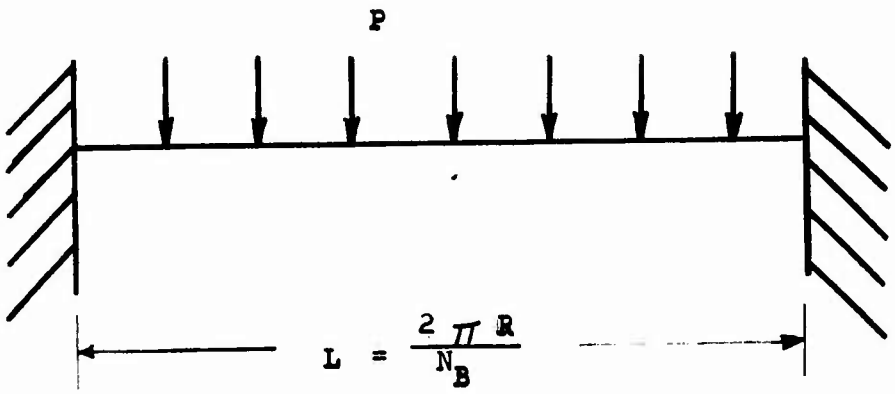

Figure 93. Fixed Fixed Beam

(U) The thermal deflection problem is controlled relatively easily by the baffle approach. The baffle spacing is sufficiently close (20 baffles were used for this preliminary study) that the differential thermal expansion between the inner and outer shrouds is essentially not allowed to occur. The inner shroud attempts to expand and the outer shroud (through the baffles) "reacts" this expansion. In the equilibrium position, both rings increase in diameter to an intermediate position between the "manufactured" diameter and the diameter the inner shroud would attempt to assume if it were not restrained. This was found to be an advantage in minimizing the loading on the baffle bolts. The pressure loading tends to put the bolts in tension and the thermal loading tends to compress the bolts. In the actual application, the bolts will be preloaded to prevent separation of the baffle to outer shroud surfaces.

(U) The thermal deflections and stresses were found using the "ring interaction" solution illustrated graphically in Fig. 94. First, the free thermal expansion, or contraction, of each skin of the shrouds was calculated. The hoop interaction between the inner and outer skins of each shroud was then found. In this part of the analysis, the stiffness of each skin and the stiffness of the honeycomb core were taken into account. The hoop interaction solution then gave a new "free position" for each shroud and the skin stresses from this effect. Deflections were then equalized between the inner and outer shrouds and the baffle. This portion of the solution entailed superimposing the bending and membrane deflections of each shroud (with 20 equally spaced radial loads) with the compressive deflection of the baffles. The bending stress and deflection profile between the baffles was then calculated and formed the "ring interaction" portion of the solution. The thermal deflection from the portion of the chamber downstream of the baffle was then added to this solution to give the total deflection.

(C) Subsonic Bolt Design. The subsonic bolt structure illustrated in Fig. 91 consists of inner and outer combustor walls joined by the injector and a series of bolts in the combustion chamber. The panels are of the same construction as the C-clamp and baffle chambers. The bolts are close enough together to form essentially a line load around the combustor. The main load path is similar to that of the C-clamp except that the length of the cantilever lip is considerably reduced. This results in greatly reduced throat deflection characteristics. The injector takes more separation and bending loads than the injector used with the subsonic baffle concept. It was found that thermal and pressure deflections of the combustor panels imposed large bending stresses on the subsonic bolt. To relieve this condition, a ball socket is provided to allow the structure to rotate around the bolt ends. The bolt is indexed on both ends to control throat gap and is not preloaded.

(C) The coolant circuit consists of the bolt coolant sleeve placed in series with the normal two-pass coolant system. The bolt is cooled before the chamber so that the cold hydrogen will cause the bolt to contract and minimize total throat deflection. The series coolant circuit also results

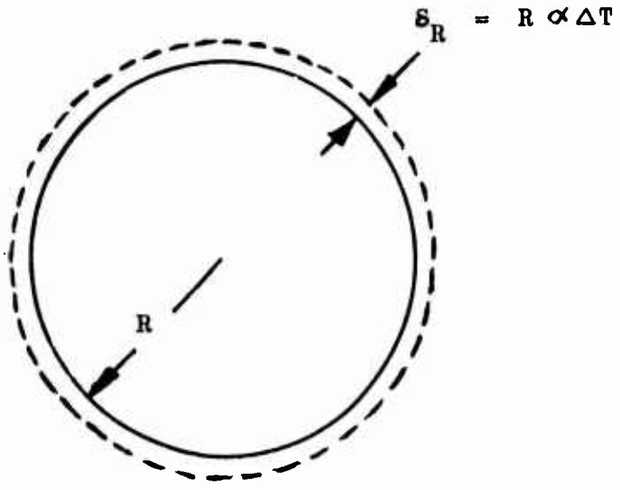

(a) Free Thermal Expansion of a Skin

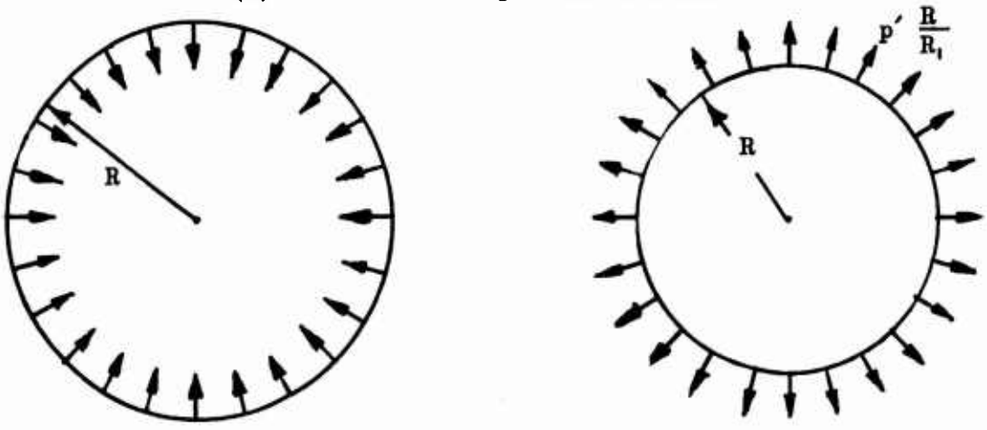

(b) Hoop Interaction Between Two Skins

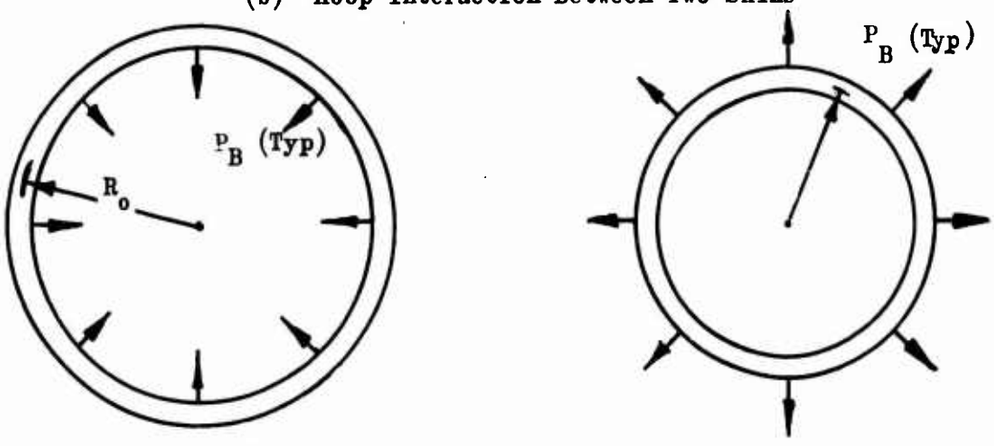

(c) Ring Interaction

Figure 94. Ring Interaction Analysis; Sub-Sonic Baffle

in a more reasonable bolt coolant passage size than a parallel arrangement which would use a small percentage of the total flow. At the intersection of the bolt and the thrust chamber wall, an annular transition cooling manifold collects the coolant from the thrust chamber tubes on one side of the bolt, manifolds it around the bolt and distributes it to the tubes on the other side of the bolt. The manifold is made of nickel for good heat transfer, and the flow area around the annulus is tapered to provide adequate cooling.

(C) The injector construction and manifolding is basically the same as used for the baffle and C-clamp designs. The hydrogen inlet manifold has been transferred to the inner combustor wall to provide for bolt cooling.

(C) Chamber accessibility is provided by the removable outer combustor and subsonic bolt-coolant sleeve assembly. All seals are hydrogen seals. Sealing of the ball joints at each end of the bolt is a problem area in that the joint must be easily removable yet allow a small amount of rotation.

(U) Manufacturing of the subsonic bolt chamber is comparable to the baffle design. There are more components to fabricate but they are broken down into less complex subassemblies.

(U) Subsonic Bolt Structure Analysis Method. For the subsonic bolt approach, the backup structure carries the pressure loading primarily as "in plane" bending. The bolt "ties" the inner and outer shrouds together in a manner similar to the baffle; however, the tie is not as efficient as the baffle tie. The subsonic bolt structure reduces to essentially a C-clamp with an intermediate tie. The local structure between the bolts acts circumferentially in a manner similar to the baffle. Because of the number of bolts required (52 were used in this study), the circumferential span between bolts is less than the span for the baffle.

(U) This structure was analyzed, using the same structural computation program as the C-clamp analysis. The analysis model is shown in Fig. 95. Temperatures and the corresponding values of Young's Modulus and coefficient of thermal expansion were varied in the same manner as they were in the C-clamp analysis. The solution required an iterative approach for each condition. The bolts were represented by a radially inward load at the junction of regions 3 and 4, and a radially outward load at the junction of regions 8 and 9. Repeated solutions were made until the differential radial deflection between the two junctions was equal to the bolt stretch due this loading minus the thermal contraction of the bolt.

(C) Results. The results of the comparative design analysis are presented in Table 13. The subsonic baffle concept stands out in its ability to restrict the variations in throat gap. The succession of concepts from C-clamp through bolt to baffle results in progressively reducing the cantilever action in the chamber.

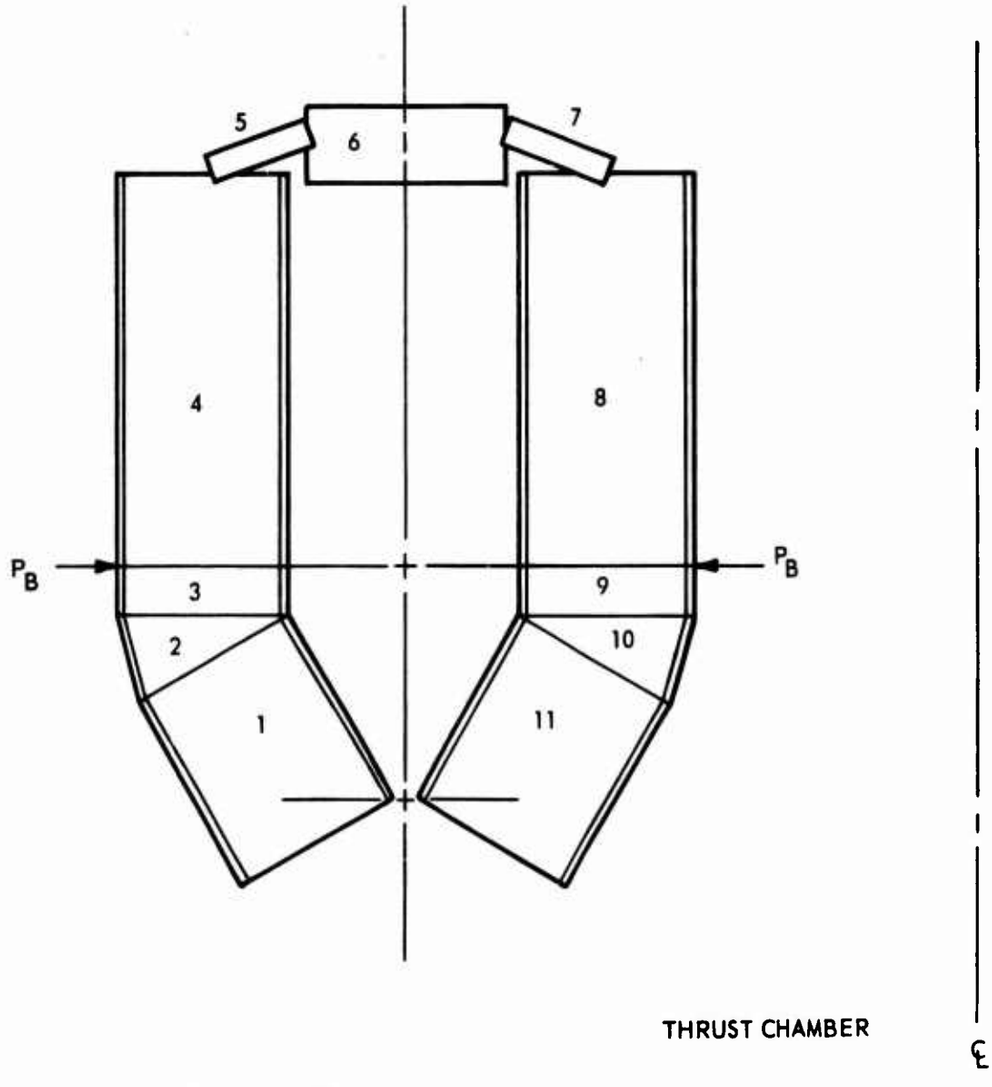

Figure 95. Subsonic Bolt Analysis Model

TABLE 13

STRUCTURAL SUPPORT CONCEPT COMPARISON

Concept	Throat Area Variation at Start, Percent		Weight, Percent	Coolant Δ P Increase, psi	Coolant Δ T Increase, F	Manufacturing Ease	Accessibility
	Full Thrust	Throttled					
C-Clamp	51	56	Reference	Reference	Reference	Reference	67 bolts
Subsonic Bolt	11	15	46	40	40	Slightly more complex	556 fasteners
Subsonic Baffle	4.6	3.5	41	0	40	Same as subsonic bolt	460 bolts

CONFIDENTIAL

(C) Baffle and bolt concepts weighed substantially less than the C-clamp segment. The weights of the two former concepts are sufficiently close together that additional design refinements could result in a negligible weight difference between these two concepts. It should be noted, however, that if baffles are required for combustion stability control, the weight of the subsonic bolt design would increase significantly.

(C) Because of the additional cooling required by the baffle and bolt concepts, a slight increase in coolant bulk temperature rise may be anticipated with respect to the C-clamp design. A small coolant pressure drop increase occurs in the bolt concept but not in the baffle concept because of the parallel cooling circuit in the latter.

(C) Some additional manufacturing complexity is incurred by the baffle and bolt concept. Relative fabrication simplicity is, in fact, the primary advantage of the C-clamp concept. The other advantages of the C-clamp is its relative accessibility.

(C) On the basis of the above results, the subsonic baffle concept was selected for further analysis. The light weight and rigidity of this concept were the most attractive features.

b. Optimization Analysis

(U) Subsequent to the selection of the subsonic baffle structural concept, analyses were conducted to determine the optimum baffle spacing, core configuration, and baffle bolt size. The analyses were based on the use of honeycomb core material, but the results will be near optimum for both core materials.

(U) The combustion chamber weight was optimized with respect to the back-up structure depth and number of baffles (fixed-fixed "beam" span). This was accomplished by first establishing a detailed base point design and then ratioing the weights of the skins, core material, baffles, closures, etc., in accordance with the following equation.

$$WT_{c.c.} = WT_{skins}\left(\frac{N_{B_1}}{N_{B_2}}\right)\left(\frac{d_1}{d_2}\right) + WT_{core}\left(\frac{N_{B_1}}{N_{B_2}}\right)^{0.75}\left(\frac{d_2}{d_1}\right)^{0.58} +$$

$$WT_{baffles}\left(\frac{N_{B_2}}{N_{B_1}}\right) + WT_{fwd\ closure}\left(\frac{(d_2 - a)}{(d_1 - a)}\right) +$$

$$WT_{aft\ closure}\left(\frac{d_2}{d_1}\right) + WT_{injector,\ manifolds,\ forward\ manifold\ body,\ and\ tubes}$$

Where:

N_B = Number of baffles

d = Back-up structure depth, inches

a = Forward manifold body depth, inches

1 = Subscript for the base point design

2 = Subscript for ratioed design point

(U) The equations for determining the variations of skin and core weight with the number of baffles and the backup structure depth are derived in Appendix C. The forward and aft closures are of constant thickness and, therefore, vary only with their respective depths. The remaining components of the combustion chamber are constant in weight.

(C) It should be noted that the weight per baffle was held constant. This assumption is not strictly correct, since there could be a small weight savings per baffle with increasing number of baffles. This did not prove to be significant in the actual study, since the number of baffles for optimum weight combustion chamber designs are very close to the number of baffles for the base point design. The weight per baffle is primarily determined by the size of bolts used; therefore, it does not change until the number of baffles has been increased sufficiently to allow the use of the next smaller bolt size. The base point design was a twenty-baffle combustion chamber with one-inch deep core structure.

(C) The above equation does not account for the cantilever loading at the bolt closest to the throat. Use of the equation would result in selection of 26 baffles with a core thickness of approximately 0.8 inch. When the cantilever bolt loading effect was also considered, the optimum configuration became 24 baffles with a core thickness of 1.25 inches.

(U) Baffle bolt sizing was based on pressure loading, installation loads and preloads. A thrust chamber pressure profile of full P_c from the injector to the throat plane was used to determine the applied bolt load. Since there is a complex load pattern involved in the bolt-baffle combination shown in Fig. 96, an analysis model was made to allow calculation of the bolt loads. The analog consists of a series of springs which represent the lumped flexibility of each component. The encircled numbers in Fig. 96 refer to the four-load (three bolts and the injector). The spring analogy for the first bolt and baffle combination is shown in Fig. 97.

(C) Each spring represents a component of the structure such as the bolt. The deflection continuity lines represent the points where the separate spring systems are joined into the backup structure. The overall deflection of each spring system is dependent on the other members of the system because they are all linked together through the inner and outer backup structures. The spring analogy for one baffle is shown in Fig. 98.

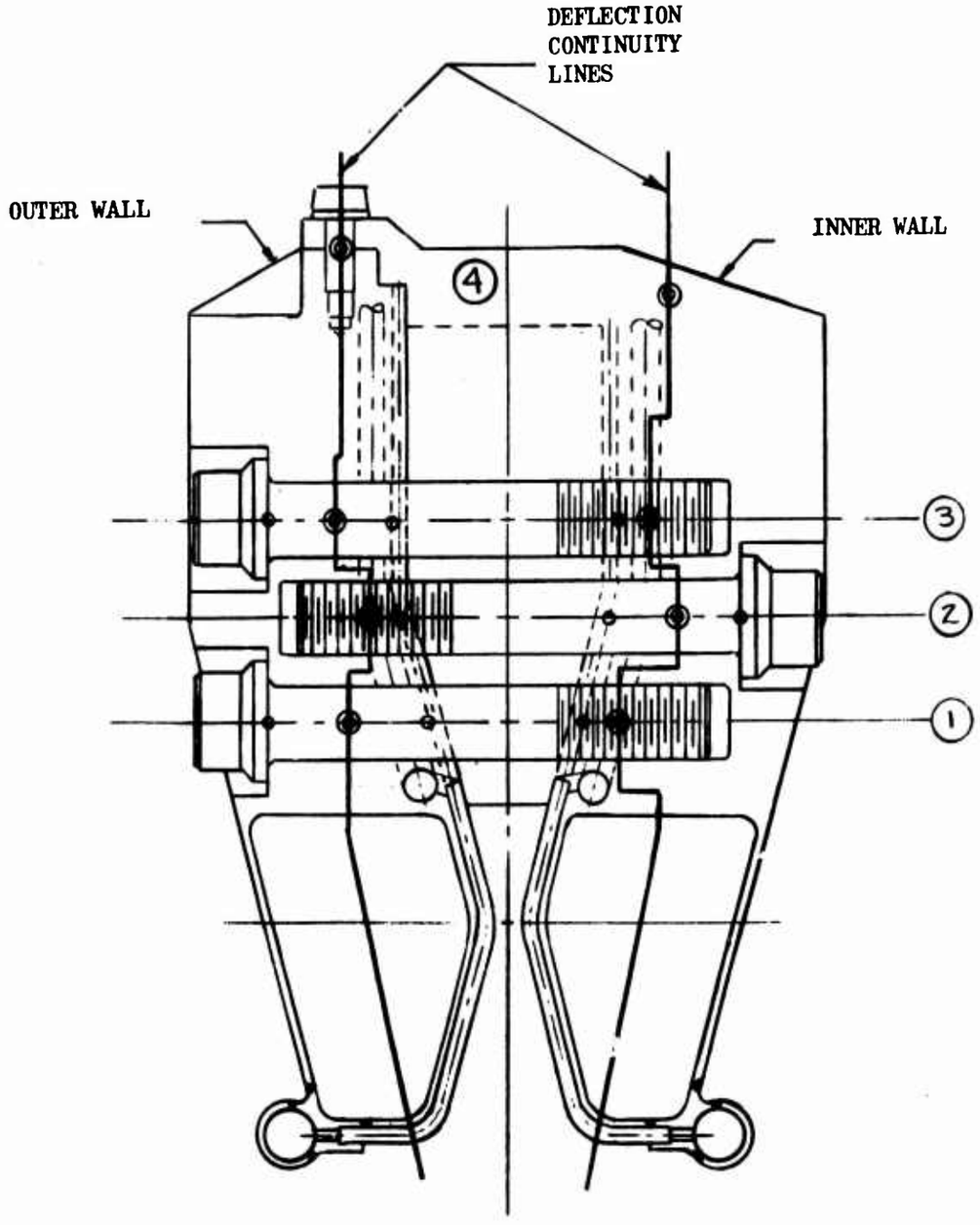

Figure 96 Thrust Chamber Cross Section Showing Deflection Continuity Lines

S_{NJ} = Member Flexibility (in./#)

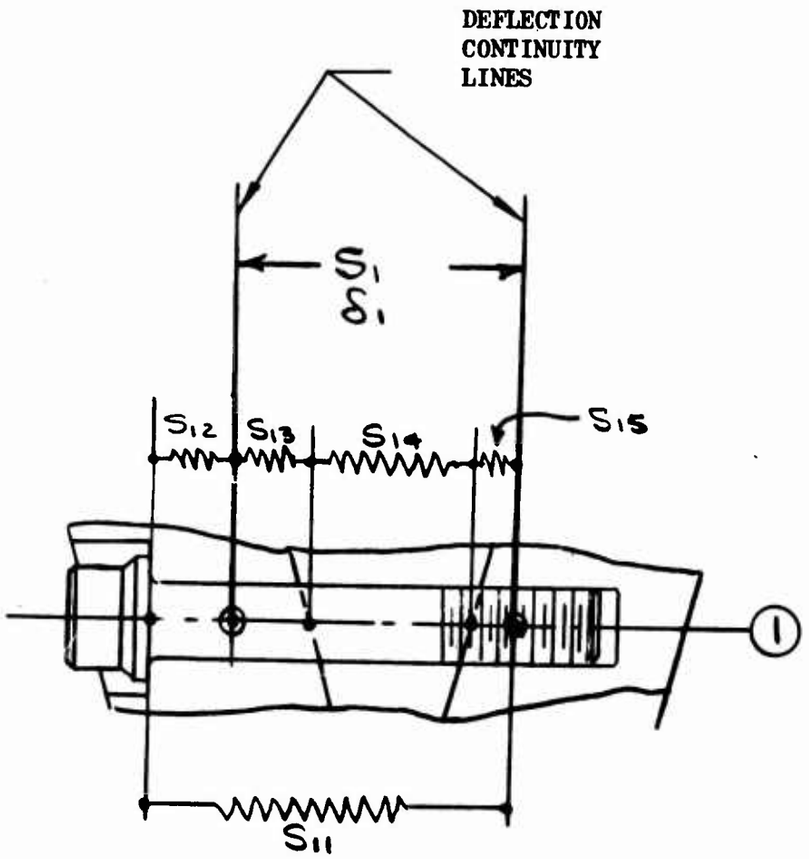

Figure 97. Spring Analog of Bolt Baffle Combination

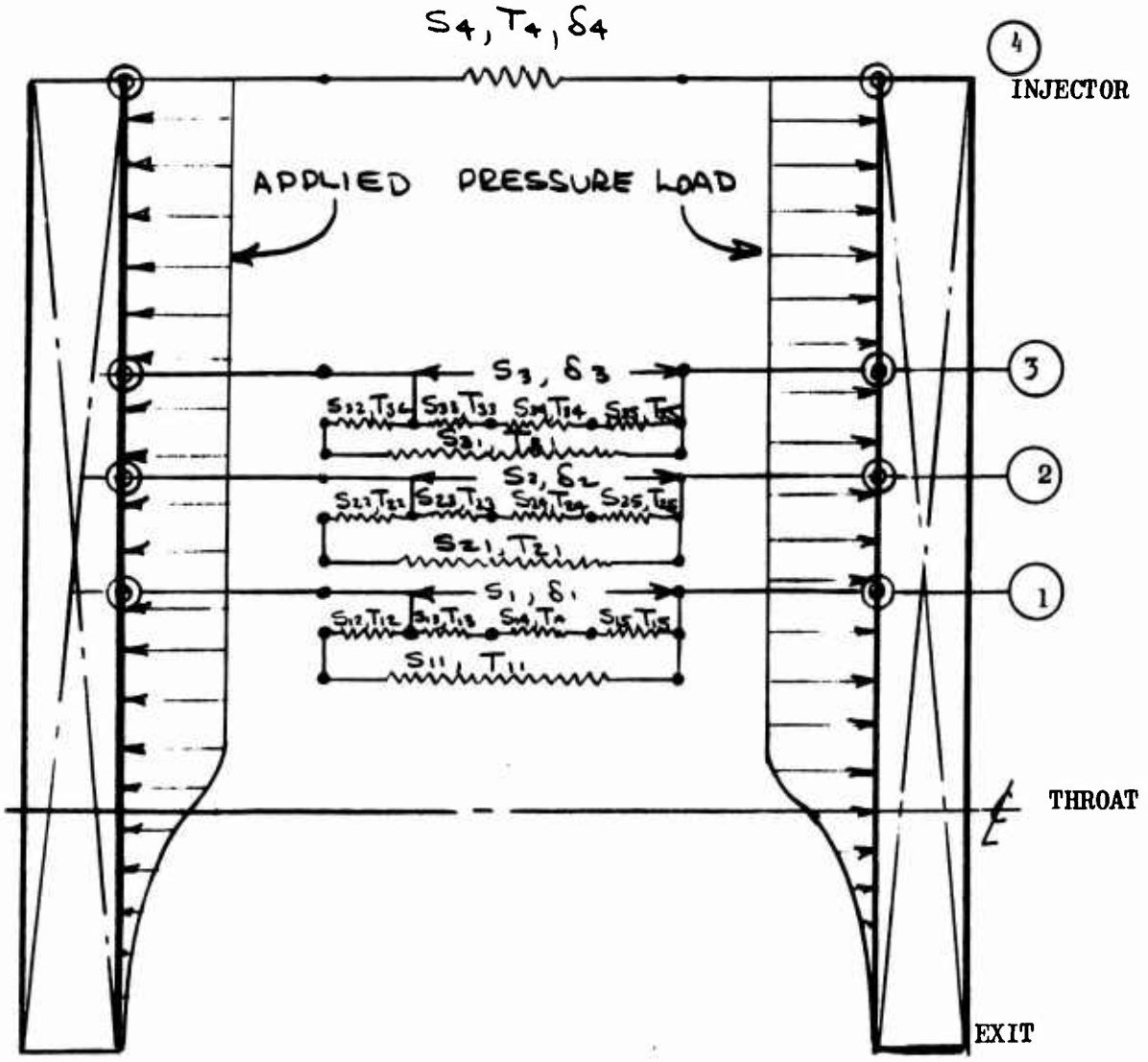

Figure 98. Spring Analog of Combustion Chamber-Baffle Combination

This method was used to calculate the bolt load due to chamber pressure. The installation load was also calculated. This load is due mainly to small misalignment caused by manufacturing tolerances. The chamber pressure and installation loads tend to separate the outer combustion chamber-baffle joint; therefore, the bolts must be preloaded to prevent separation. The maximum bolt load was then arrived at taking into account variation in friction factor during torqueing. The resulting bolt size was 0.4375 inch diameter.

c. Segment Design

(U) This effort consisted of the detailed design of two optimized thrust chamber segments using the subsonic baffle structural concept. The two segments differed only in the material used to provide rigidity and strength to the segments, i.e., honeycomb and rib structural material.

(C) Previous analysis had shown that a straight segment was a good approximation to the curved compartments of the flight engine. The inner and outer combustor walls are separable as in the flight engine. The two halves are bolted together by three bolts per baffle, eight injector bolts per compartment and ten end plate bolts. Since the segment is not a continuous ring as in the flight chamber, end plates were used to cap off the two end compartments. The end plates are rigid and do not deflect in the same manner as the baffles; therefore, a three-compartment segment was designed and deflection and stress data were taken primarily on the center compartment. Subsonic baffles of rigidity approximating that of a flight baffle were provided between the center and side compartments. A chamber pressure profile constant at 650 psia between injector and throat and zero downstream of throat was assumed for design purposes. As chamber contours were not finalized at the time, the segments were designed to a contour E (Section II) profile with a 15-degree convergent and 15-degree divergent half-angles. As nozzle contour, shroud contour, nozzle structure and thrust pick-up points were undefined at this time, the interactions between combustion chamber, nozzle, and thrust mount were not included in stress analysis.

(C) All structural components except end plates were sized for flight type operating conditions excluding thermal stresses since the latter were not simulated during the structural test program. Materials properties were taken at their projected operating temperatures in the flight engine. The material for all structural components except bolts is Inconel 718 which was chosen for its high strength, low thermal expansion, and relative ease of welding. The bolts were of A-286 high strength alloy because of its availability and suitability for this application. The structure was heat treated to 175 ksi strength after completion of the final weldment.

(C) Stress analysis of the engine chamber wall tubes indicated that, during hot firing, the heated tubes do not significantly stiffen the structure (less than one percent stiffness increase because of tubes). In a room temperature test, however, the tubes are effective and increase the

rigidity of the structure. Thus from a simulation standpoint, it was desirable to test the chamber structure without installing coolant tubes. For completeness and possible thermal testing at a future date, tube blankets were designed and fabricated for installation after the test program. Stainless steel tubing (300 series) of constant 0.0.0 inch wall x 0.093 inch O.D. was used.

(C) Two shapes of coolant tube panels were required to blanket the combustor walls. Sets of sixty-six tubes were necessary to cover the space between subsonic baffles on both the inner and outer walls of each of the three compartments. Additional sets of six shorter tubes were designed to cover the wall area downstream of the baffles. Each separate set of tubes was stacked side by side and electron beam welds were made between tubes to form panels. The tube panels were then bent to fit the chamber wall contour and formed at each end to fit into inlet and outlet manifold slots in the structure. The subsonic baffles were not covered with tubes, although they would require cooling in an actual engine.

(C) The injector consisted of an inner half representing the flight injector and an outer half representing the attach ring for the outer combustion chamber wall. The inner injector half was hollowed out and a thin Inconel -718 blank face sheet was electron beam welded on to simulate the passages and face of the flight injector. It also contained one port per compartment for pressurizing the segment. The bolted-together injector formed a backbone upon which the remainder of the structure was built. Baffles and end plates machined from plate stock were electron beam welded to the injector. The structural panel subassemblies were machined to fit and electron beam welded into the structure. This technique allowed the structural panels to be fabricated and inspected before they were installed in the structure. It also allowed the injector baffles and end plates to be released for fabrication before the structural panel design was finalized.

(U) Rib Segment Design. Several fabrication methods were considered for the rib structural panels. These included fully machined panels as well as methods of sheet metal fabrication.

(C) The latter design was selected, and the "U" channel construction technique was developed because of its inherent self-jigging properties. Each channel is rigid by itself and, therefore, minimizes distortion that would occur by welding nonrigid pieces together. Electron beam welding was chosen for its inherent controlability and minimum shrinkage effect. The structural panels were designed as subassemblies to facilitate manufacturing, allow for weld shrinkage, and permit scrapping of one panel if necessary without destroying the entire segment. (No rejections were required on either segment.)

(C) The structural panels were stressed essentially as fixed-fixed beams (Fig. 99) between baffles. The maximum stress occurs at the panel-to-baffle weld joint. Using a web spacing of 0.50 inch with 1.250-inch deep sections, the required web thickness was 0.025 for Class I welds and 0.040 for Class II welds. Web buckling was investigated and found

to be absent in this design. The skin thickness was 0.025 for Class I welds and 0.028 for Class II welds. The 0.025 Class I weld case was governed by face sheet crippling at the baffles. No attempt was made to optimize material thickness along the length of the beam.

(U) The baffle cantilever beam structure (Fig. 100) was designed to take loads in two directions. The shear loads developed by pressure loading between baffles (F_s) are distributed to the baffle bolts through two ribs (dimension b). Bending loads (F_m) and chamber pressure loads (P_c) are taken by the horizontal plates (dimension t).

(C) The cantilever portion of the baffle beam required a 0.100 face sheet thickness and a 0.060 shear web thickness on each side. The shear webs were formed by the panel closeouts. Three, 7/16-20, 200 ksi bolts were required for each baffle. The injector-to-outer combustor joint required eight, 1/4-28, 140 ksi bolts per compartment. The injector and attach flange thicknesses were the equivalent of .175-inch thick plates. Figures 101 and 102 are isometric and layout drawings respectively of the rib structural segment.

(C) Honeycomb Segment Design. To ensure that the strain and deflection measurements performed on both segments would be truly representative of the difference in structural panel construction, the honeycomb segment panel was designed to extend from the injector to the location of the seventh (throat) channel in the rib panel. Two channels, identical to the eighth and ninth channels in the rib segment, then completed the aft end of the honeycomb. The seven channels of the rib segment are directly comparable on the basis of loading, deflection, and weight with the honeycomb sandwich panel. Like the rib segment, the honeycomb design employed distinct structural panels fabricated as units, then welded into nearly identical baffles, injectors, and aft manifolds. In addition to the advantages mentioned for the rib segment, this design approach allowed development of brazing techniques on a small panel basis for the honeycomb segment.

(C) The honeycomb sandwich panel assembly included an outer and inner face sheet, forward and aft honeycomb sections, and a core splice sheet. Sheets and core sections were fabricated from Inconel 718 alloy. Structurally, the face sheets form the two flanges of a beam to transmit bending moments through the panel. The honeycomb core brazed between these sheets held them apart, thus multiplying their effective moment of inertia and stabilizing them against buckling failure.

(C) A face sheet thickness of 0.040 inch was required at the panel to baffle attachment plane assuming a Class II weld. Class I weld quality would have reduced maximum face sheet thickness to 0.024 inch, but radiographic inspection requirements for this class would not be met. Sheet thickness could have been tapered from 0.040 at the edges to 0.020 at the compartment centerline in a minimum weight design.

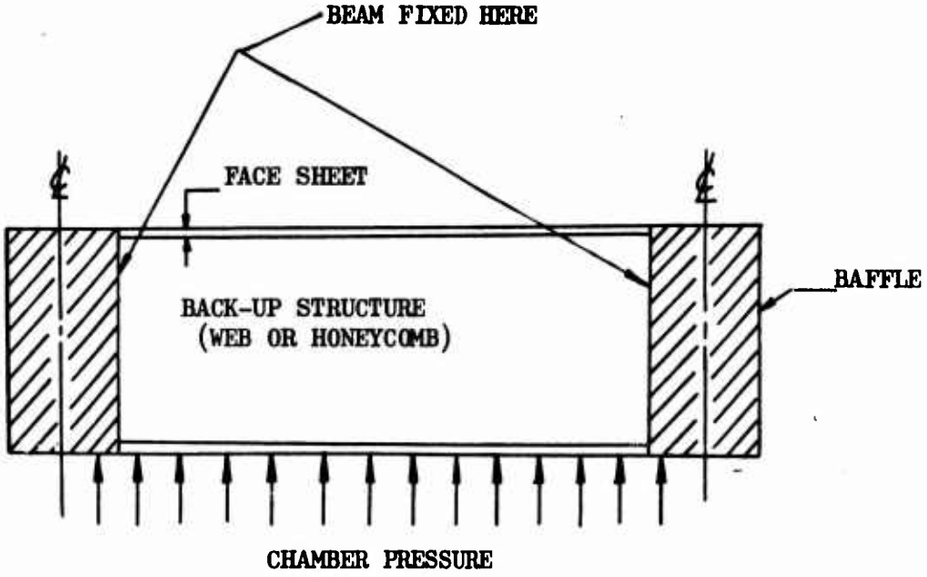

Figure 99. Schematic of Core Loading

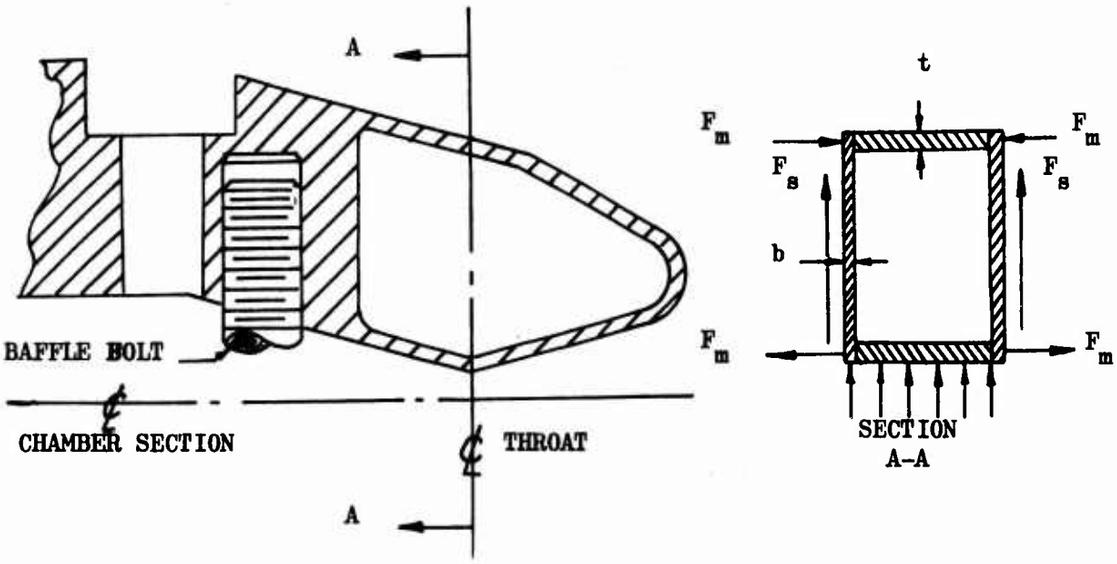

Figure 100. Cantilever Loading of Baffle Bolts

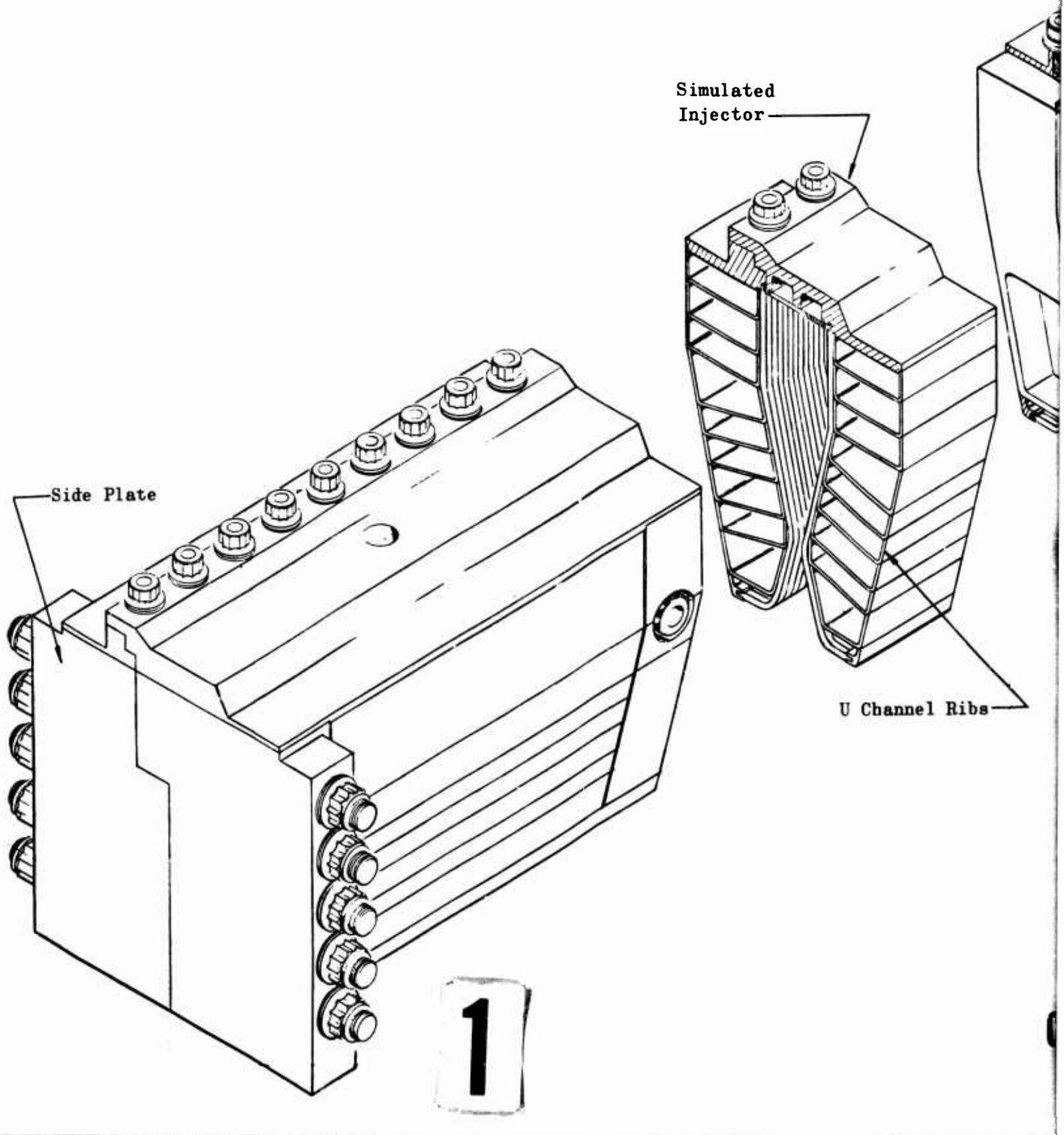

1

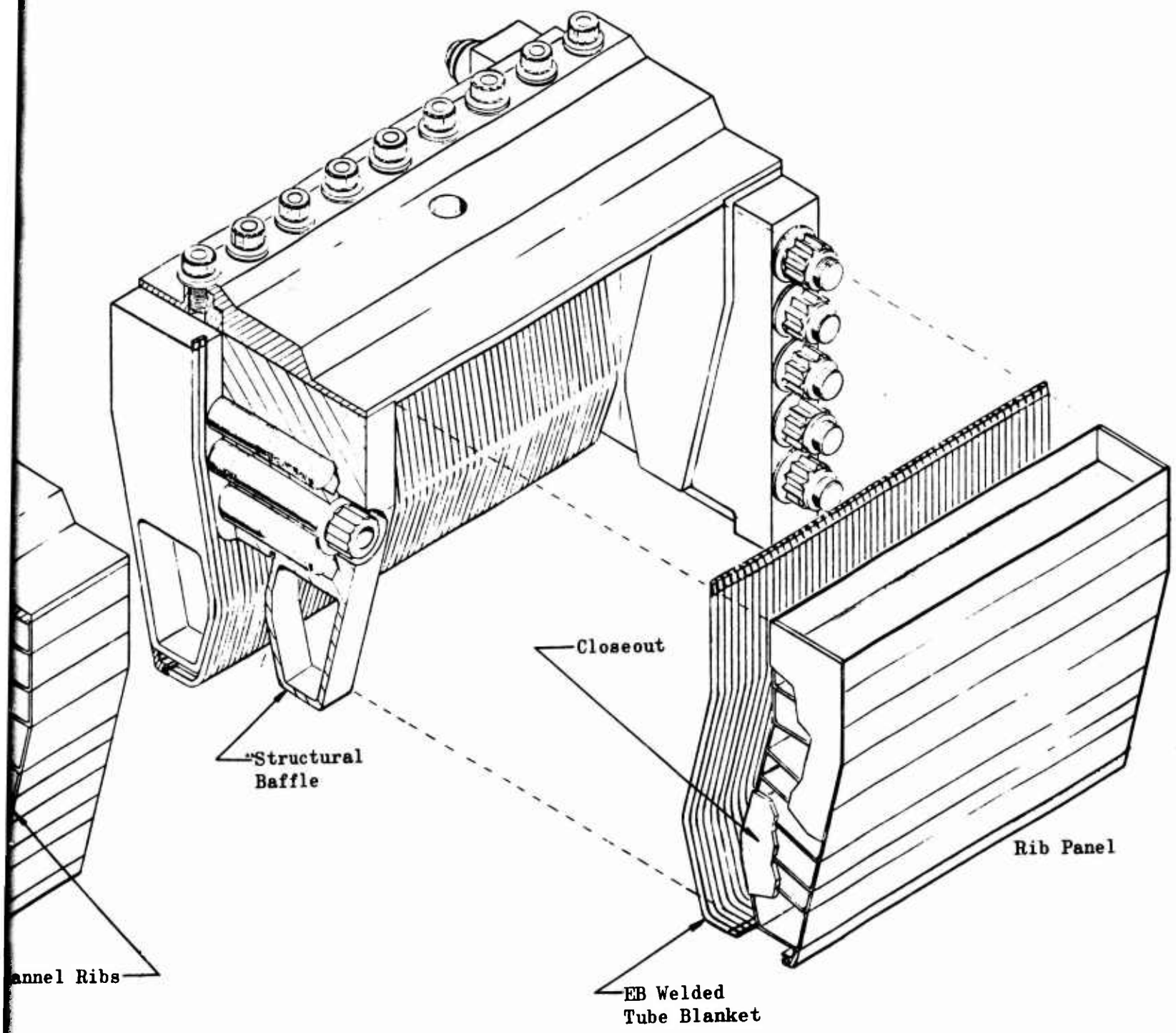

2

Figure101 Rib Structure Segment

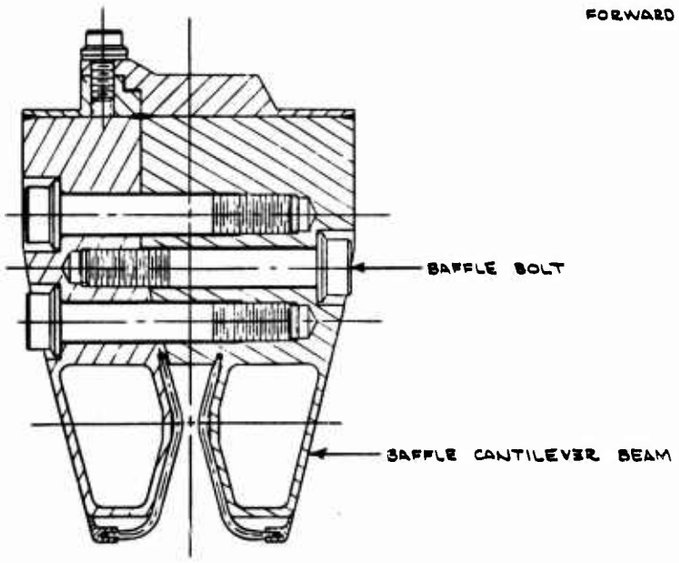

SECTION B-B

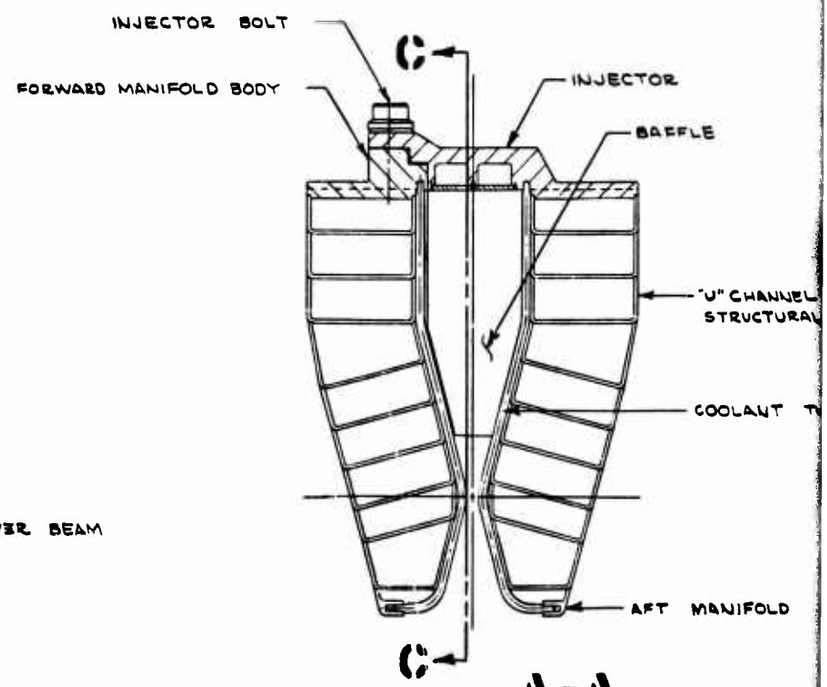

SECTION A-A

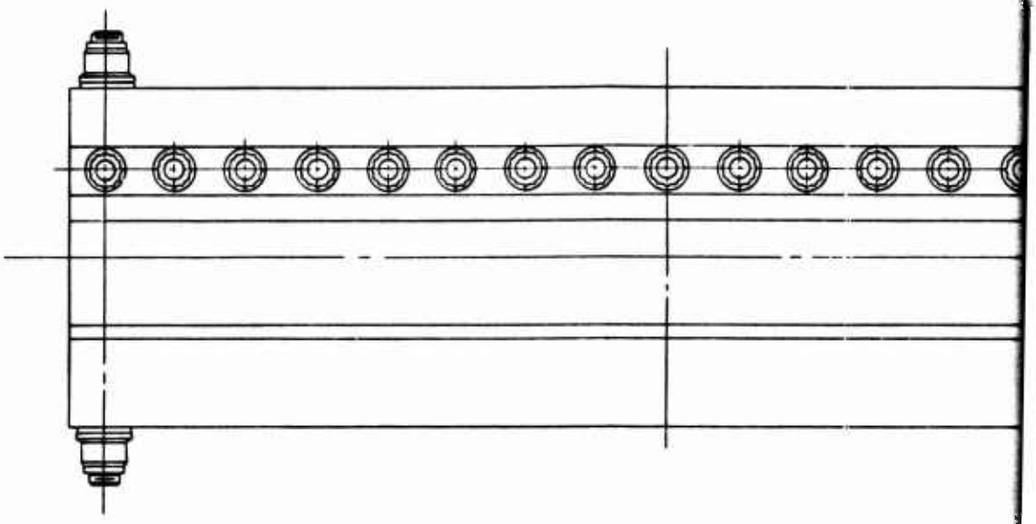

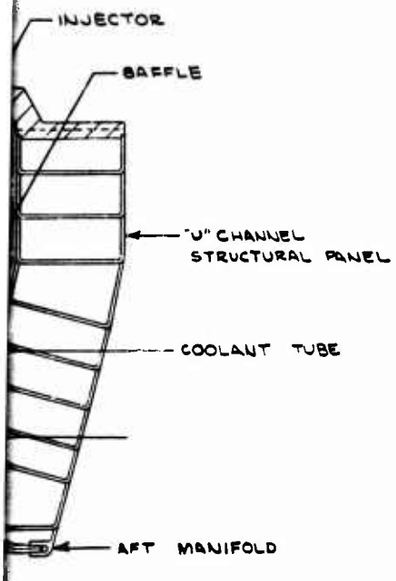

A-A

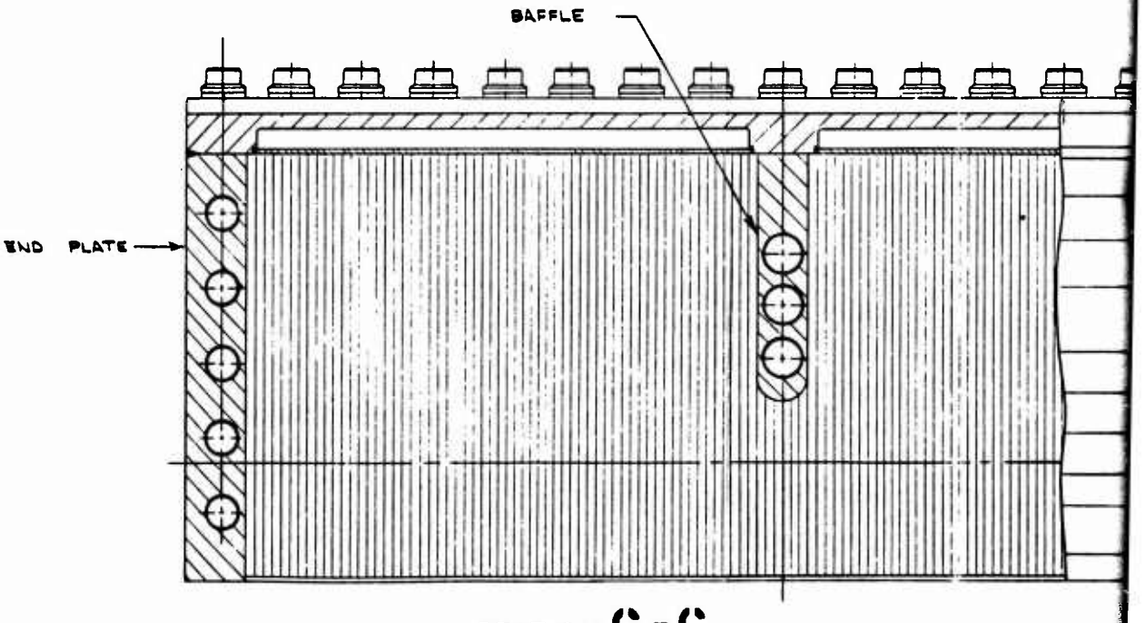

SECTION C-C

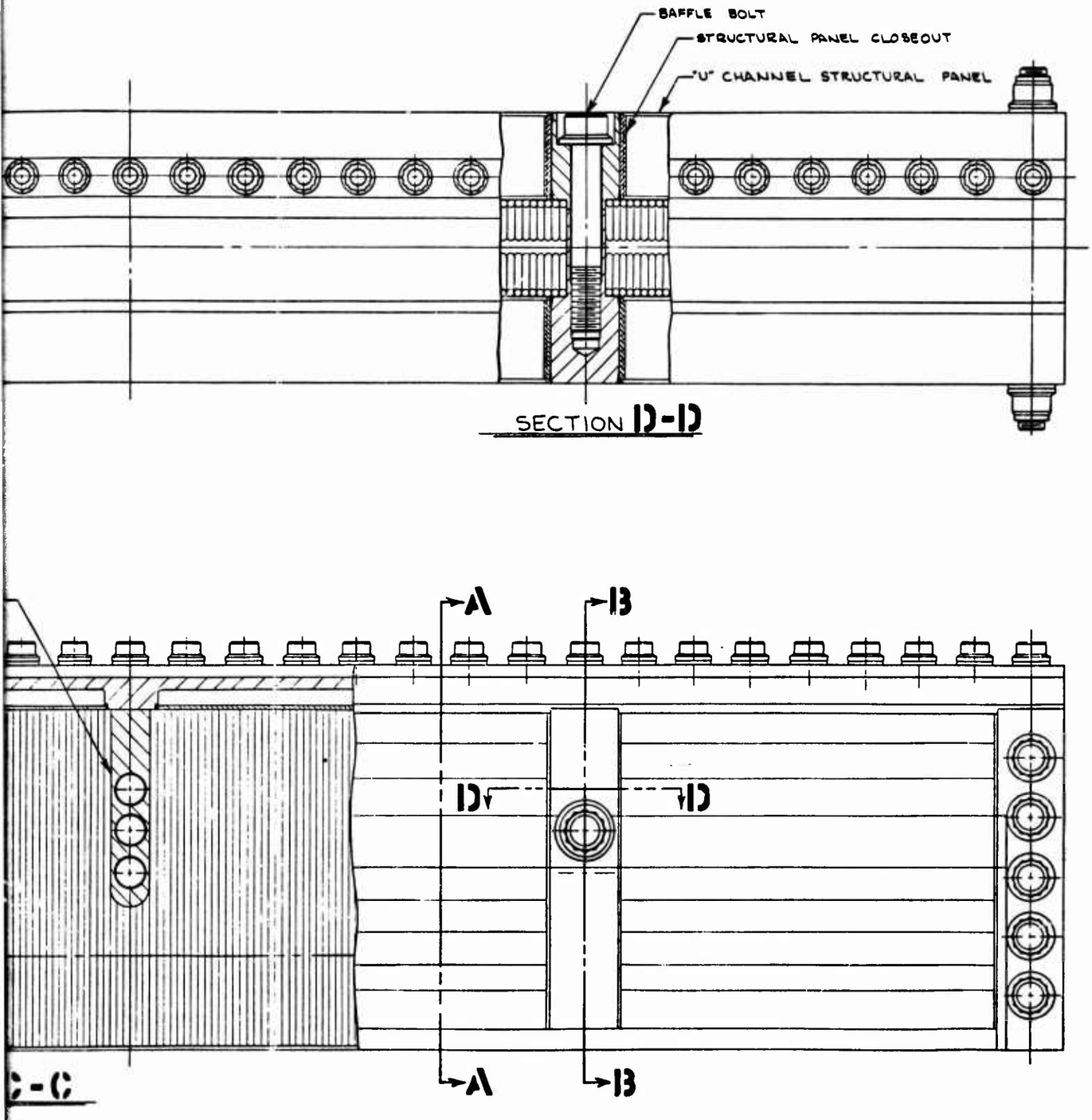

Figure 102. Structural Test Segment Rib Supports

(U) Two, 1/8-inch vent holes were drilled through each face sheet to permit replacement of air with an inert argon atmosphere during furnace braze. The holes were placed at low stress points in the sheets.

(U) Honeycomb core sections resist the shear loads in the panel. The sandwich was assembled by furnace-brazing the core sections to the face sheets.

(C) The honeycomb core designed for this simulator had a hexagonal cell size (distance across flats of hexagon) of 0.125 inch. Cell walls were .004-inch thick. It was fabricated by first passing a .004-inch thick foil ribbon through a perforating machine which formed lines of tiny holes about 0.10 inch apart. These holes allow venting of each cell during furnace brazing. The ribbon was then passed between corrugating wheels which form three sides of the hexagonal cell. By resistance welding many such corrugated foil strips together, a honeycomb core section was built up. As the core shear strength perpendicular to the ribbon direction is only some 70 percent of that parallel to the ribbon, the foil strips were oriented parallel to the injector.

(C) Honeycomb core density was determined by the maximum shear loads occurring at the panel to baffle junction. No attempt was made to vary core density below that necessary at the panel edges, but in an engine panel, the core foil thickness could be linearly tapered by chemical milling to near zero at the panel center. Calculations indicated a required maximum core density of 35 pounds per cubic foot. The density of the delivered core sections was 40.1 pounds per cubic foot. While many combinations of hex cell size and foil ribbon thickness would produce the necessary core density, a cell size greater than .125 inch would not provide enough braze fillet area in contact with the face sheets to prevent delamination.

(C) A critical area in the sandwich panel design is that of the braze bonds between the core sections and the face sheets. These bonds must transmit shear loads equal to those taken by the core. Once a particular cell size and consequent bond length per unit face sheet area is chosen, bond strength is a function of braze alloy shear strength and size of the fillets formed by the alloy. As the silver based alloys usually used for brazed honeycomb bonding (aircraft applications) have insufficient strength at the relatively high required operating temperatures, a higher melting point alloy, Palniro 7 (70 Au-8 Pd-22 Ni) was investigated for the segment panels.

(U) This alloy has an ultimate shear strength of 26,000 pounds per square inch at 1200 F, the maximum structure temperature expected. Figure 103 presents fillet size requirements versus braze alloy shear strength.

(C) The 15-degree converging combustion chamber contour was accommodated by making a miter joint in the core. The core sections were cut on an angle and brazed to either side of a splice sheet in the panel assembly braze cycle as shown in Fig. 104.

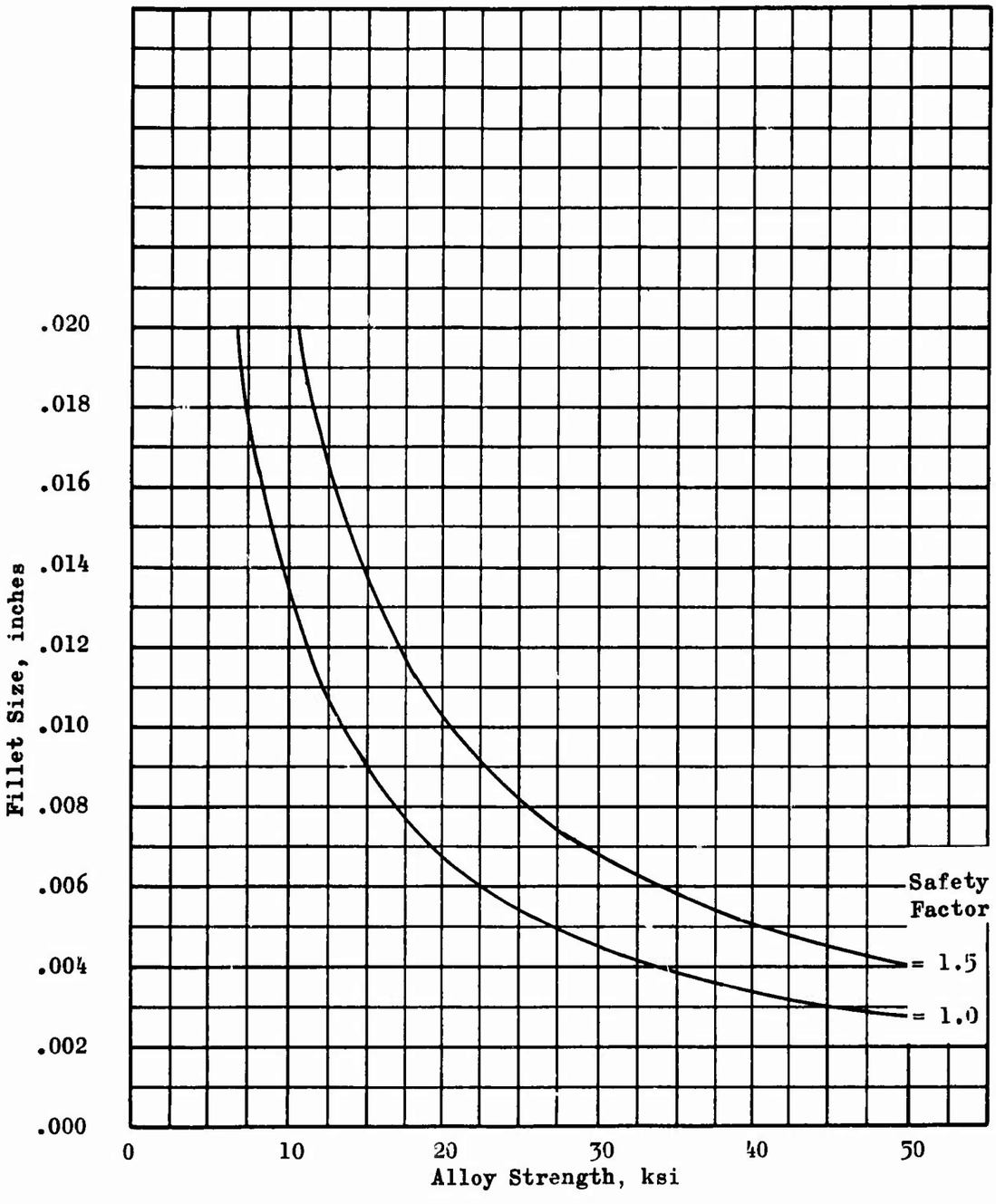

Figure 103. Required Fillet Size vs Alloy Strength

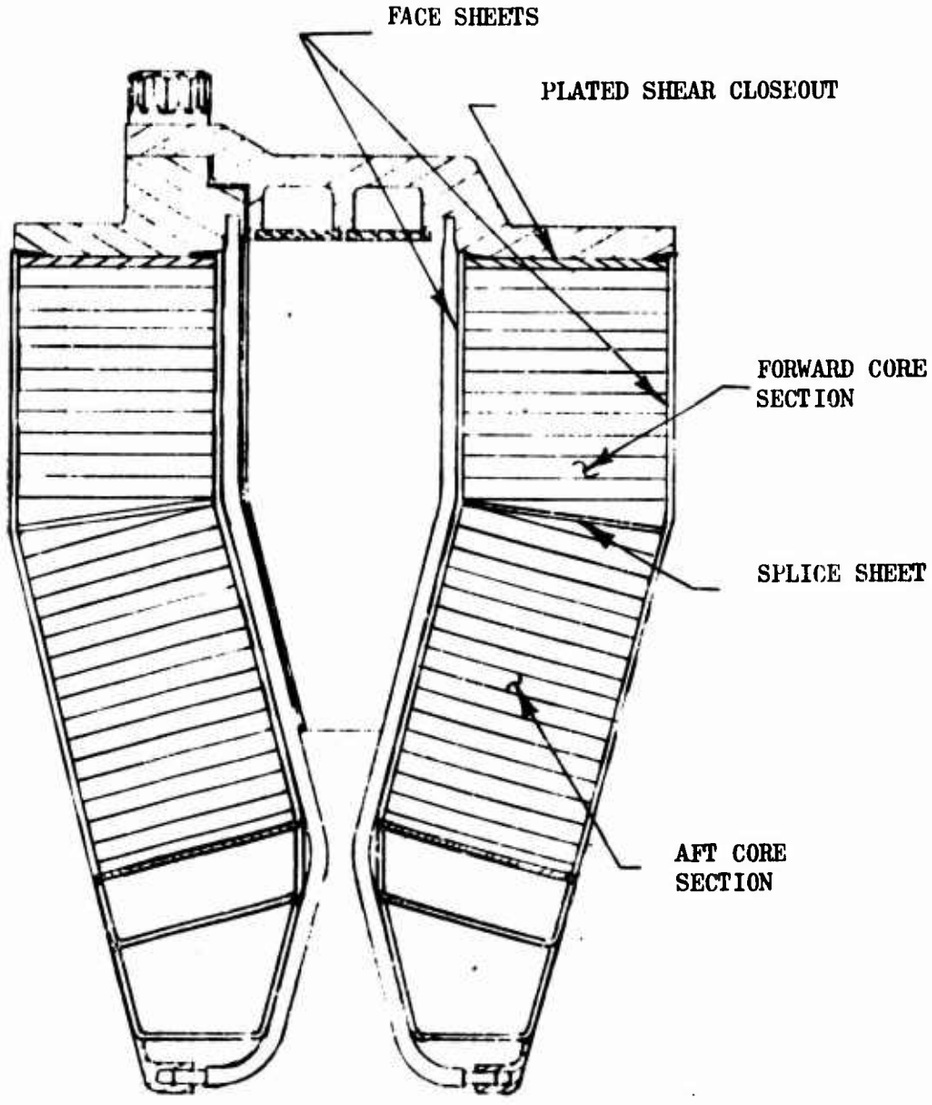

Figure 104 Cross-Section of Honeycomb Segment

(U) Two alternate methods of producing this angle contour were considered: (1) bending a flat honeycomb panel; and (2) machining the angle in an initially thicker section. Bending the core in one direction causes the panel to assume an undesirable saddle shape. Furthermore, the structural integrity of the resistance welds under the forces necessary to produce a 15-degree bend was in question. Corrugation wheels were not immediately available to fabricate a core of the requisite depth for a machined 15-degree angle.

(C) In order to transmit shear loads from the honeycomb to the baffles and injector, a shear joint must be formed between these members directly, as the face sheet thicknesses are only sufficient to transmit the panel edge moment. In more lightly loaded structure, this joint is usually brazed, some percentage of the braze joint being cracked by distortion as the panel is welded into surrounding structures. As this joint is very difficult to X-ray or repair after assembly in the honeycomb segment, it was considered safer to substitute a relatively deep electron beam weld between baffle or injector and honeycomb. As the thin gauge honeycomb cannot be welded to these thick sections directly, the design incorporated a thick layer of nickel plating on the edges of the core sections. This approach was verified by sampling before assembly of the segment.

(C) To prevent diffusion of electroformed nickel into the face sheet to baffle welds, which were stressed to full Inconel-718 allowable levels, the design included a .060-inch thick Inconel-718 closeout between the electroformed nickel and the baffle. The nickel layer was first electron beam welded to the honeycomb panel closeout to transmit shear, then the face sheets were brazed over this joint. Finally, an electron beam weld was made joining closeout and face sheet to baffle. An intermediate closeout was not necessary at the more lightly loaded honeycomb panel-to-injector weld.

(U) Alternate methods of shear connection between honeycomb panels and surrounding structure offer weight advantages over electroformed nickel edges, but fairly extensive development sampling would be necessary to ensure comparable reliability. Brazed connections might be developed that would not be cracked by nearby welding. Oversize honeycomb core sections might be compacted at the edges to form a nearly solid edge which could be welded directly to baffle and injector.

(U) Although a complete honeycomb structural segment was designed, analytical results as outlined below resulted in the conclusion that accurate throat gap variations for a complete honeycomb segment could be obtained by doubling the deflections measured on the honeycomb wall side of a composite segment consisting of one honeycomb side and one rib side. To reduce fabrication time and effort, therefore, only one honeycomb side (the outer wall) was fabricated in addition to the complete rib structural segment.

(U) Two factors were determined by the analysis: (1) the equality of deflection of the inner and outer walls was established to verify the procedure of obtaining the throat gap variations by doubling the honeycomb wall deflections; (2) the effect of the moment of inertia of the inner wall on the deflections of the honeycomb outer wall.

(U) The inner and outer bodies were mirror images of each other and differed only in that the inner body was welded to the baffles whereas the outer body was bolted to the baffles. The three outer wall-to-baffle bolts were pre-torqued to values which prevented separation of the outer wall from the baffle. Under this condition, the bolted and welded joints were identical with respect to the effect of throat gap deflections. Therefore, the inner and outer walls of a complete honeycomb segment would be expected to deflect equally.

(U) The effects of the inner wall rigidity on outer wall deflections were analyzed by isolation of the outer wall as a free body and consideration of the forces acting on it. Forces and moments result at the following locations:

a) Chamber walls

b) baffle bolts

c) injector bolts

d) baffle bearing area

e) injector bearing area

(U) The direct effects of chamber pressure on each of the walls is independent of the outer wall since the system is in static equilibrium. Injector bolt loads are independent of the inner structural panel design. Differences in moment of inertia between the rib and honeycomb structural panels could cause approximately a 3 percent difference in baffle bolt preload. The effect of this load differential is localized to the baffle-bolt preload area.

(U) The forces and moments transmitted to the honeycomb wall by the injector and baffles depend upon the amount that these members delect under the loads that are transmitted to them by either direct pressure or by the inner wall. If honeycomb and rib structural panels are considered as fixed end beams between baffles, the shear, S, and moment, M, transmitted to the fixed ends of such a beam of area, A, and length, L, is dependent only on the pressure loading, P, as indicated by the equations

$$S = PA/2$$

$$M = PAL^2/12$$

(U) The construction of the inner wall would, therefore, not affect the loads transmitted by the baffles to the honeycomb outer wall.

(U) Changing the inner wall from a honeycomb structure to a rib structure would affect the moment transmitted through the injector to the outer honeycomb wall by an amount estimated to be less than 10 percent. This would, in turn, influence the throat deflection of the honeycomb wall by less than 1.5 percent. Thus, if a deflection of 5 percent of the initial throat gap would have occurred on each wall of a complete honeycomb segment, the deflection of the honeycomb wall in the composite structure would be less than 5.08 percent. This difference, 0.08 percent or 0.0001 inch, approaches the accuracy limitations of the dial gauge instrumentation. Based on the above analytical results, it was concluded that by measuring the deflections of the honeycomb side of a composite structural segment, the data could be used to predict the deflection and throat area changes of a complete honeycomb segment. An isometric drawing of the composite structural segment is shown in Fig. 105.

d. Fabrication

(U) The fabrication activity was divided into two distinct efforts, sample fabrication and complete fabrication. In order to assure that the actual segment fabrication effort would proceed efficiently, the designs were carefully analyzed to determine the materials, processes, and techniques with which the amount of experience or data necessary to assure success was lacking. An economical sample fabrication program was then conducted in these areas to acquire the necessary techniques or obtain required design data. This approach proved quite successful in the segment fabrication task.

(U) Sample Fabrication Program. T program was primarily devoted to the development of welding and bra g techniques applicable to the specific se t designs.

(C) For th ib segment, "U" chann samples were welded together using lectr beam and Tungsten Ine Gas (TIG) welding methods to determine od most suitable for th s application*. TIG welding has the advantage of requiring less exact fitting tolerances prior to welding since the weld rod metal can bridge small surface discontinuties. However, if proper fitting tolerances can be held, the EB welding technique results in a cleaner and lighter weld since the parent welding supplies the molten weld material. The width and penetration depth of the weld are dtermined by control settings on the equipment. Once these proper settings have been determined by s sample weld, all channel welds are made at the same settings so that a uniform weld is rapidly made. Test samples of channels were EB welded to provide the optimum equipment settings and to determine if fit-up problems did exist. The fit-up designs and techniques proved to be quite compatible with the EB welding process and very good samples were obtained. A photograph of an EB weld sample and an enlargment of one of the channel to channel EB welds are shown in Fig. 106 and 107.

*Under previous company sponsored effort a TIB welded structural segment was fabricated and showed the weld method to be applicable but with resulting relatively heavy welds.

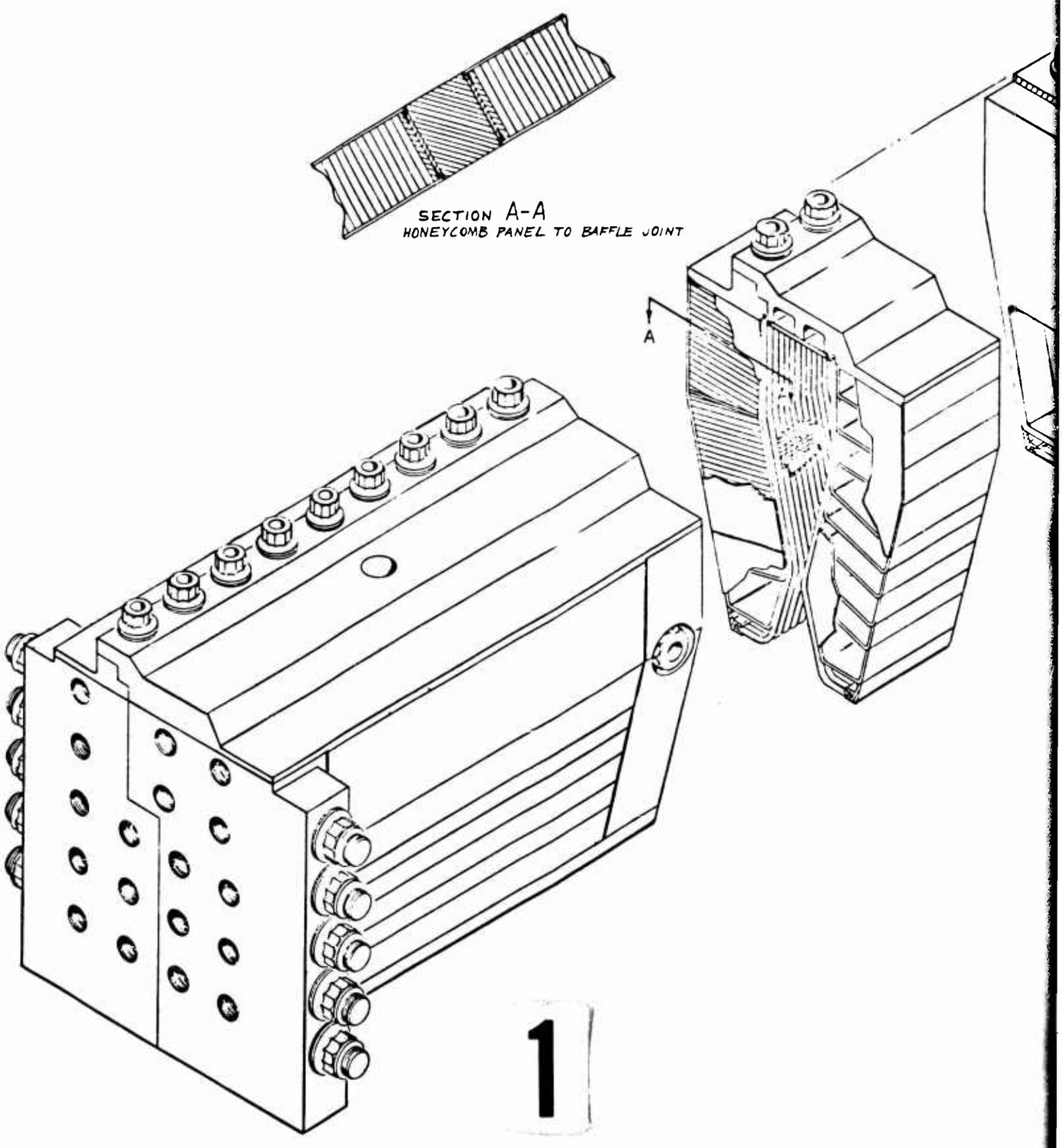
SECTION A-A
HONEYCOMB PANEL TO BAFFLE JOINT
A

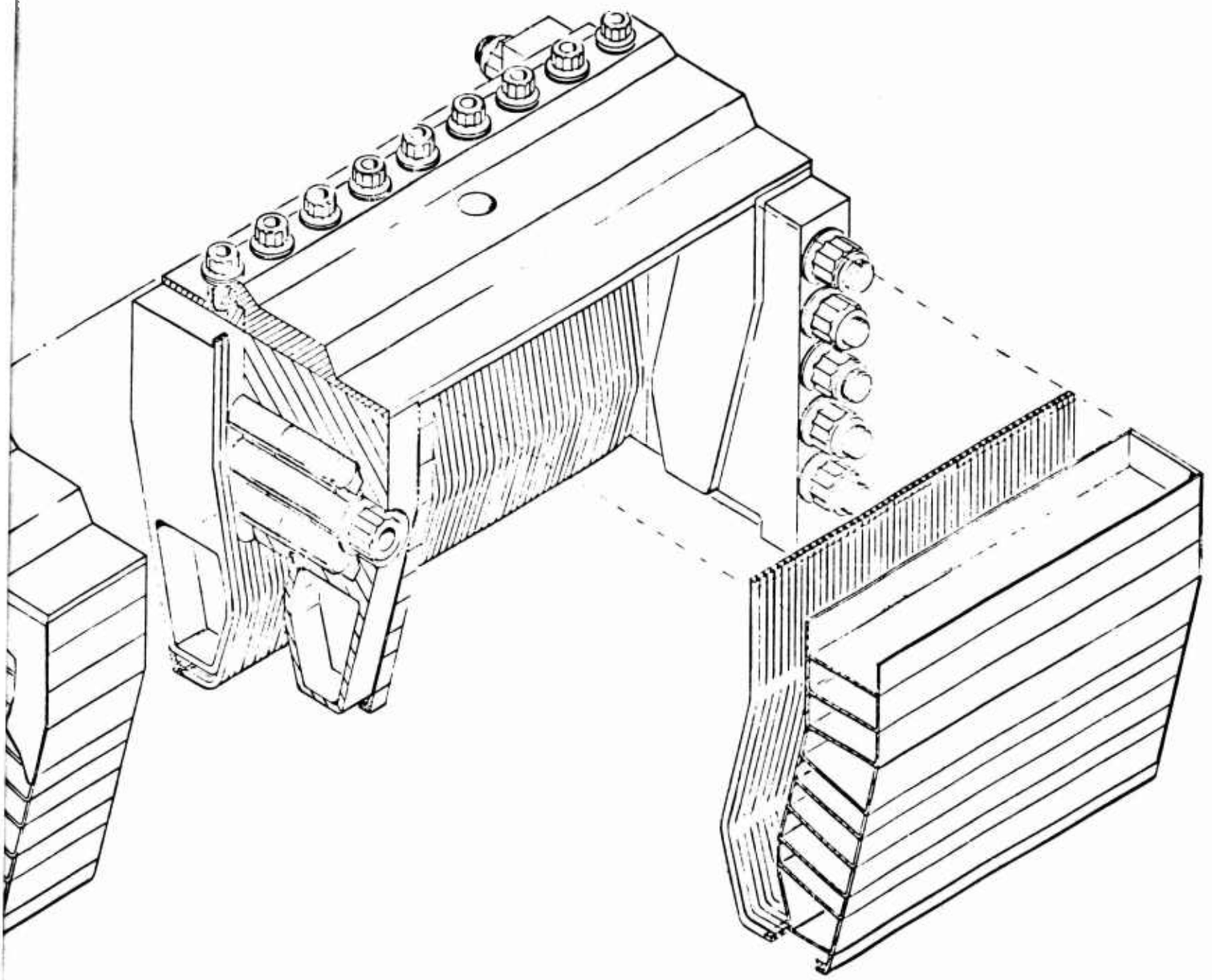

Figure 105. Composite Rib/Honeycomb Structural Segment

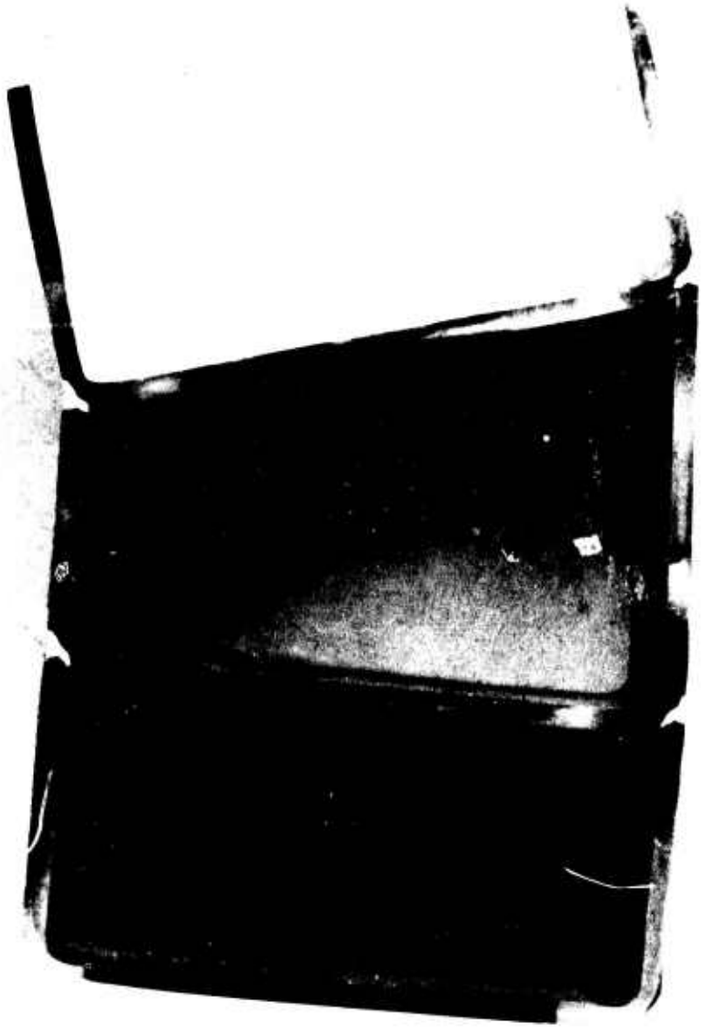

Figure 106. Sample of Electron Beam welded Kic Channels

Figure 107. Closeup of Electron Beam Weld in Single Rib Channels

(C) Samples of Inconel-718 were subjected to the same thermal history as experienced by the complete segment. For the honeycomb segment, this included the braze cycle for the panel assembly. The results indicated that a heat treat to 175,000 psi (ultimate) could be achieved for the parent material and 131,000 psi for the electron beam weld. Complete results of the tests are shown in Table 14. The heat treatment consisted of 25 minutes at 1775 F, 8 hours at 1325 F, and 8 hours at 1150 F. Prior to the heat treatment, the ultimate tensile strength of the welded sample was 33,300 psi.

(U) Several samples simulating various facets of the honeycomb structural panel design were prepared before fabrication of the segment panels was initiated. The samples inlcuded a mechanical test specimen, a sample of nickel plating into honeycomb edge-like notches, several subscale braze samples, and a full scale structural panel similar to those used in the honeycomb segment.

(C) The honeycomb structural panel design requires electroplating and machining operations to provide a flat surface of electroformed nickel on the irregular surfaces of three edges of a honeycomb core section while masking the two faces and the fourth edge. The honeycomb core is brazed to the face sheets to form a beam structure. A braze material had to be selected which had high strength at the elevated temperatures of the thrust chamber tubes carrying the regeneratively heated hydrogen to the injector. The nickel-plated layer at the edge of the core must be electron-beam welded to Inconel-718 baffles and injector. This weld must be of sufficient strength to transmit shear loads between the core sections and the baffles.

(C) Accordingly, the first fabrication sample involved nickel plating an Inconel-718 block with notches machined along one edge to simulate the edge of honeycomb core. It was found that the nickel deposited more rapidly on the raised points of the edges and would tend, eventually, to form inclusions of plating solution. This tendency was eliminated by an initial plating operation, a machine cut across the edge to gain a flatter surface, and a final plating and machining of the surface (Fig. 108).

(U) The plated block was incorporated into a mechanical test specimen designed to establish the shear strength of the electron-beam weld between Inconel-718 and the plated nickel layer. The nickel-plated Inconel-718 inner block was welded between the arms of a U-shaped outer block, also of Inconel-718 as shown in Fig. 109.

(U) Four welds were made between the plating layer and the U-shaped block, along top and bottom of the two opposite unnotched sides of the rectangular block. The notched plating specimen edge (simulating the exterior cells of the honeycomb panel) was oriented perpendicular to the welded edges so that failure of the welds would not distort the

TABLE 14

PROPERTIES OF INCONEL-718

As Received Material	Ultimate Tensile Strength, psi	Yield Strength, psi	Elongation percent
Longitudinal	114,700	51,700	70
Transverse	115,600	50,200	66
Material After Weld and Heat Treat			
Longitudinal	179,300	118,300	16
Transverse	174,700	113,800	16.5
Weld Joint After Heat Treat	130,900	112,000	6

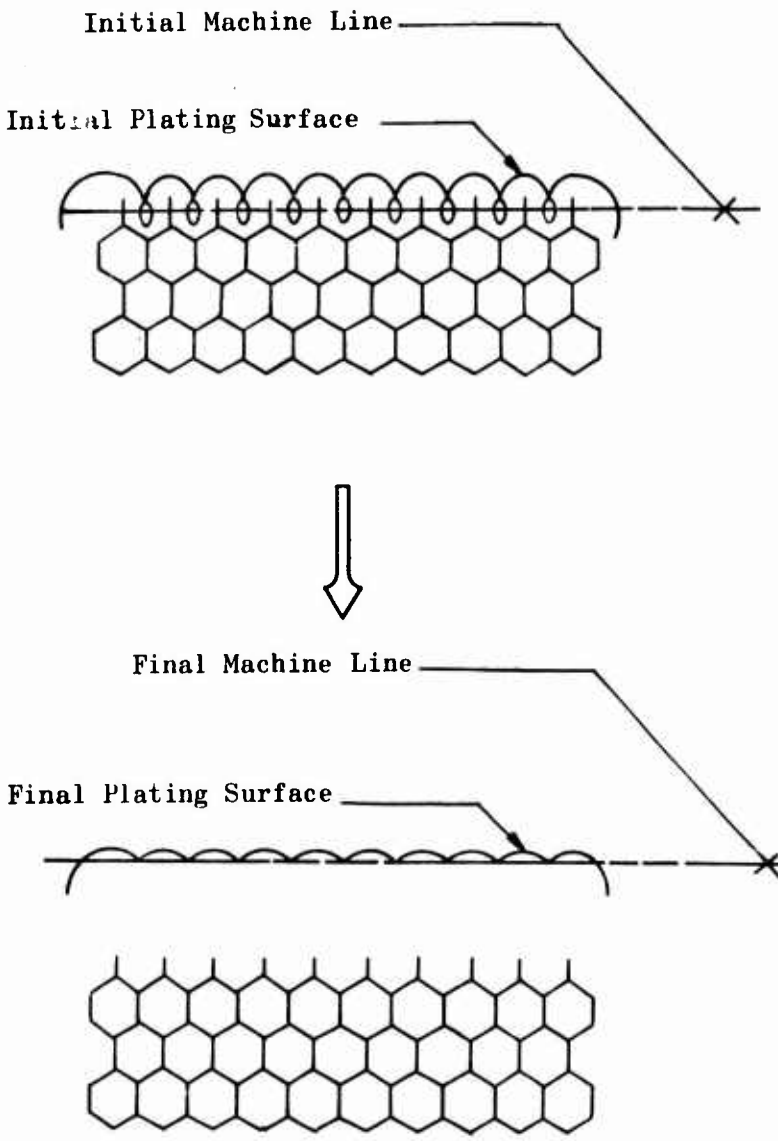

Figure 108 . Honeycomb Edge Plating Sample

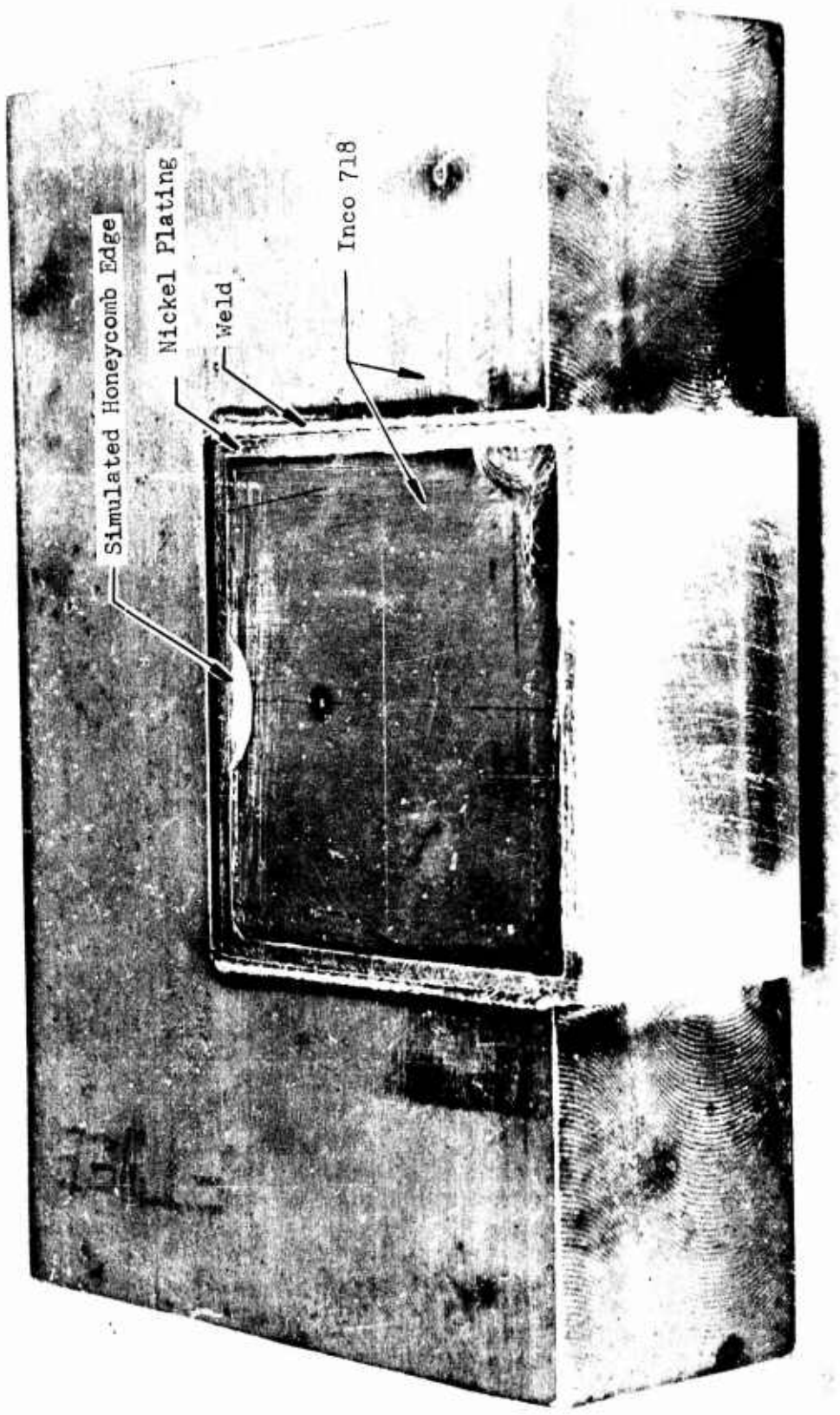

Figure 109. Nickel Plating and Weld Samples

(U) plating over the notches. Weld penetration was sized so that the specimen would fail in shear across the welds. As the weld beads were essentially castings of molten Inconel-718 plus pure nickel, it was expected that the weld shear strength would be intermediate between that of pure annealed nickel and that of Inconel-718, a nickel base alloy.

(U) The specimen was heat treated after weld in a cycle that produced both the high annealing temperature which will be encountered during the actual honeycomb panel braze cycle at a temperature of 1930 F and the age hardening (8 hours at a temperature of 1325 F) to be used during the panel attachment weld heat treat. Thus, any metallurgical reactions which would occur in the segment would have been duplicated in the weld sample. Before mechanical test, a thin slice through the weld cross-sections of the specimen was removed for etching and microphotography. Microscopic and fluorescent dye penetrant inspection of this section indicated that the electron beam did not completely contact the plating and the block on one of the four welds, producing incomplete fusion and penetration. As a result, a slightly wider beam was used on the actual segment welds.

(U) The specimen was tested to failure between the platens of a testing machine. The imposed shear load simulates the load imposed on the weld by chamber pressure as shown in Fig. 110. Inspection of the parted sample indicated that diffusion bonding had occurred over part of the area between unwelded portions of the two blocks during the heat treat cycle. Corrections for this bonded area and the incomplete penetration of the fourth weld were made in the calculation of weld failure stress. The resulting ultimate weld shear strength was 40,000 psi; i.e., double the strength of nickel plating or one-fourth the strength of Inconel-718. The plating layer exhibited excellent ductility and adhesion to the inner block. Thus, the weld specimen test showed that the structural panel-to-baffle shear joint design was entirely adequate under the calculated load.

(U) Two subscale braze samples were prepared to check aspects of the planned honeycomb panel assembly braze cycle (Fig. 111). In particular, the stack pressure and alloy characteristics (fillet size, wetting properties, and corrosiveness) were of interest. Both full and subscale panel samples were brazed in an inner retort box having a thin sheet of metal foil welded over its top. By partially evacuating the retort, any pressure up to a full atmosphere could be applied through the foil to the honeycomb-sandwich assembly. Adequate pressure must be applied to ensure contact between the core and the braze alloy foil which was tack-welded to the face sheets. Excessive pressure must be avoided to prevent crushing the core. The pressure applied was scaled form that used during lower temperature honeycomb brazing at Los Angeles Division of North American Aviation. To ensure that air would not leak into the inert argon atmosphere in the in the inner retort, an outer retort was placed around the inner and filled with additional argon at atmospheric pressure.

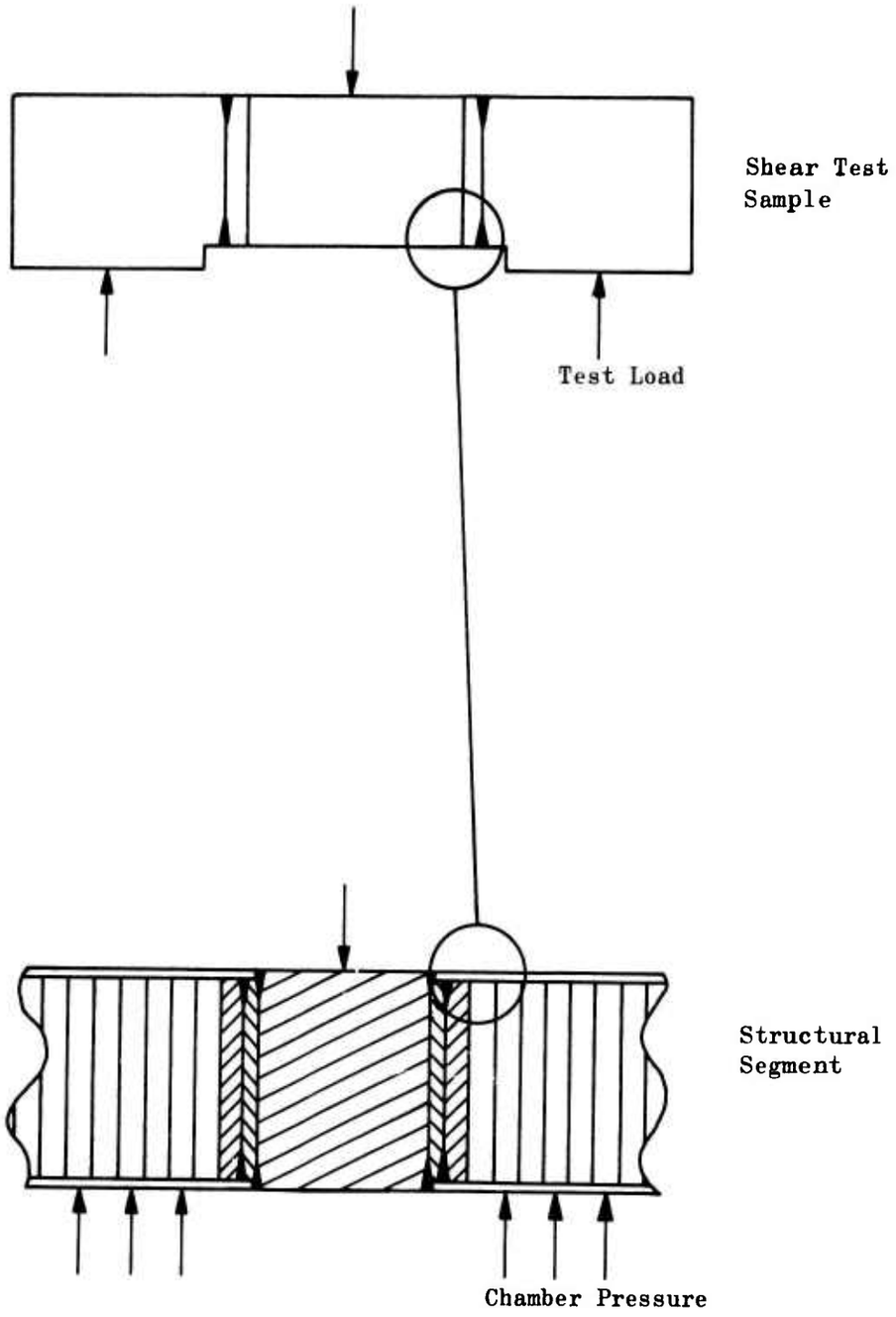

Figure 110. Plated Edge Joint Weld Sample

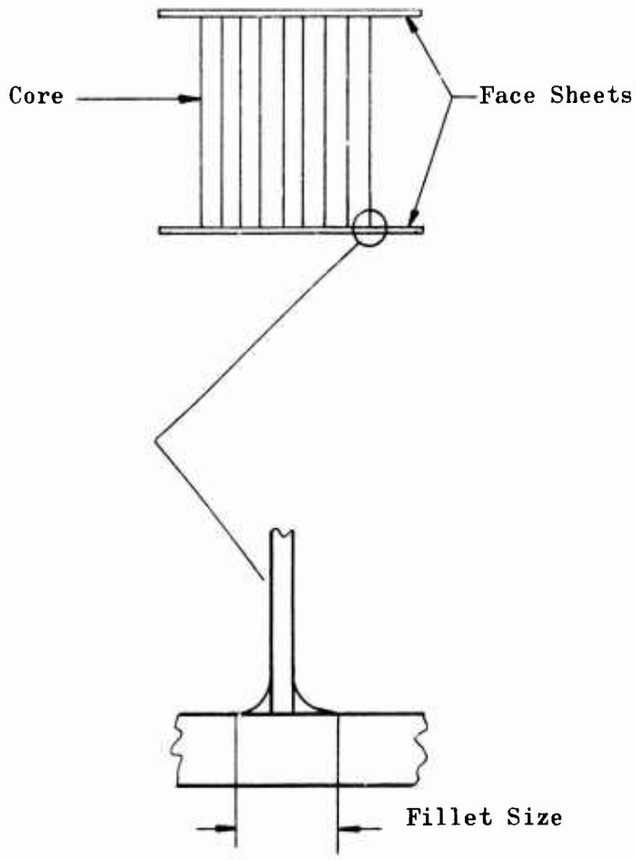

Figure 111 . Subscale Honeycomb Braze Samples

(U) Shear strength data on the preferred braze alloy, Palniro No. 7 and two alternate alloys are shown in Fig. 112. One of the subscale braze samples employed Palniro No. 7 alloy with a thin plating of nickel on the brazed surfaces, the other used the same alloy without plating. These two samples resulted in good wetting characteristics and fillet size with no erosion of the thin-gage core foil in both subscale samples. Therefore, no specimens were brazed with alternate alloys. The thin nickel plating over the brazed surfaces did produce slightly better wetting of the surface, and was used on the full-scale panel sample. Microsections prepared from both subscale samples indicated fillet sizes between 0.006 and 0.008 inch, which were adequate for the test segment shear loads. A microsection of the nickel-plated sample braze joint is shown in Fig. 113.

(U) A full-size honeycomb panel was then brazed. This sample was intended to verify design factors that could not be checked at subscale; e.g., whether the fixtures to be used for the segment panels were adequate to ensure braze bonds at all necessary points in the assembly. Chamfered plexiglas masks were fabricated to exclude nickel from unplated surfaces on the honeycomb core sections. Honeycomb panels with masks prior to plating are shown in Fig. 114. Core edges were plated, machined off, and replated as was done with the plating sample. The replating cycle was terminated early on the sample core sections because of time limitations. The panel assembly, consisting of inner and outer face sheets, forward and aft core sections, and a splice sheet, was sandwiched between relatively thick upper and a lower form blocks of Inconel-718 cut to the desired shape of the final panel.

(U) Diffusion bonding between form blocks and face sheets was prevented by placing stopoff- coated parting sheets of 0.010 thick CRES foil between them. Temperature and thermal gradients were monitored by three thermocouples. The first thermocouple was placed at the periphery of the assembly, the other two were inserted through machined ports to the centers of the upper and lower form blocks. Pressure was applied to the sandwich by partially evacuating the inner retort as with the subscale samples. The plated and brazed sample panel is shown in Fig. 115. A system of holes and grooves were machined into the form blocks to permit replacement of air with inert argon throughout the perforated core cells.

(U) Sectioning and ultrasonic inspection of the brazed panel revealed bonds at all necessary points except a small area between the outer face sheet and core near the splice sheet. A reduction of outer face-sheet bend radius together with provision for a chamfer on the core sections was made on the actual segment and resulted in complete bonding.

(C) Segment Fabrication. The results of the sample fabrication program resulted in accomplishment of the actual segment fabrication effort with no major problems. Because of the fewer samples required for the rib segment, the actual fabrication effort on this segment was

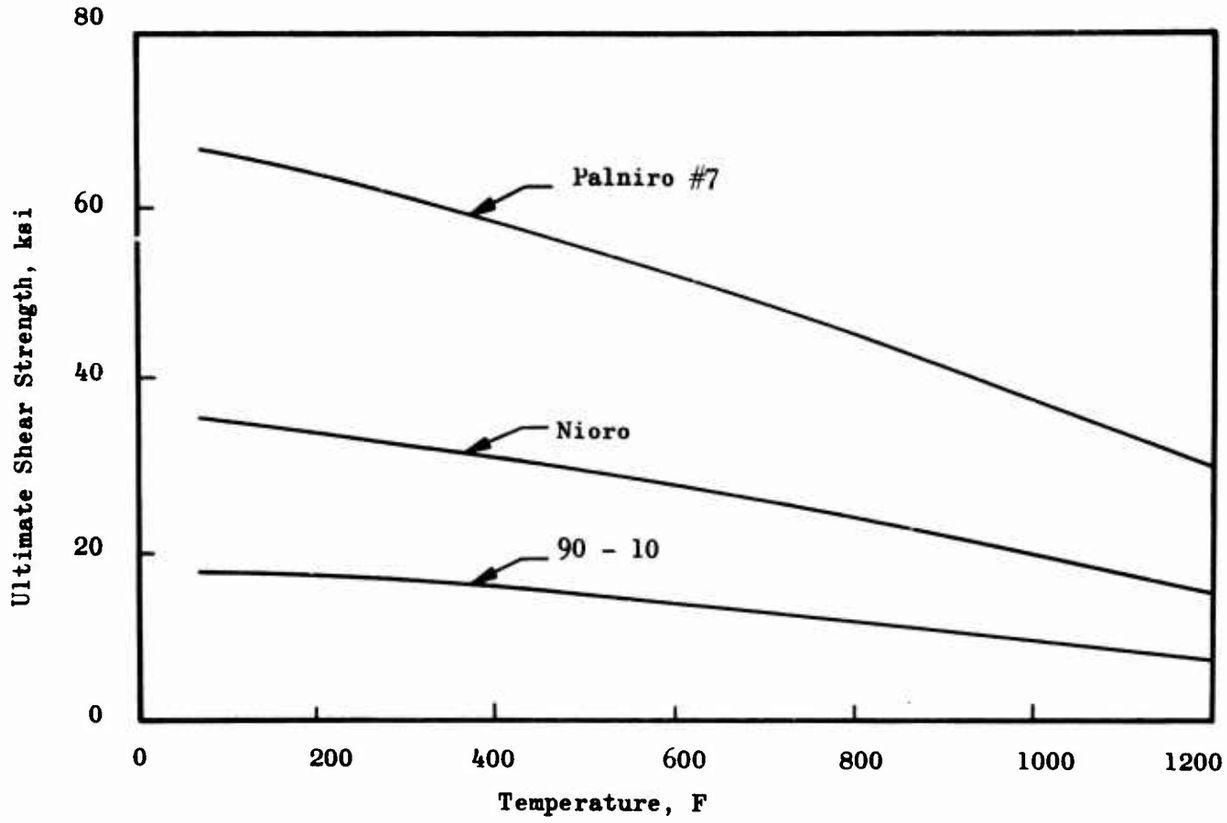

Figure 112. Shear Strength of Candidate Braze Alloys

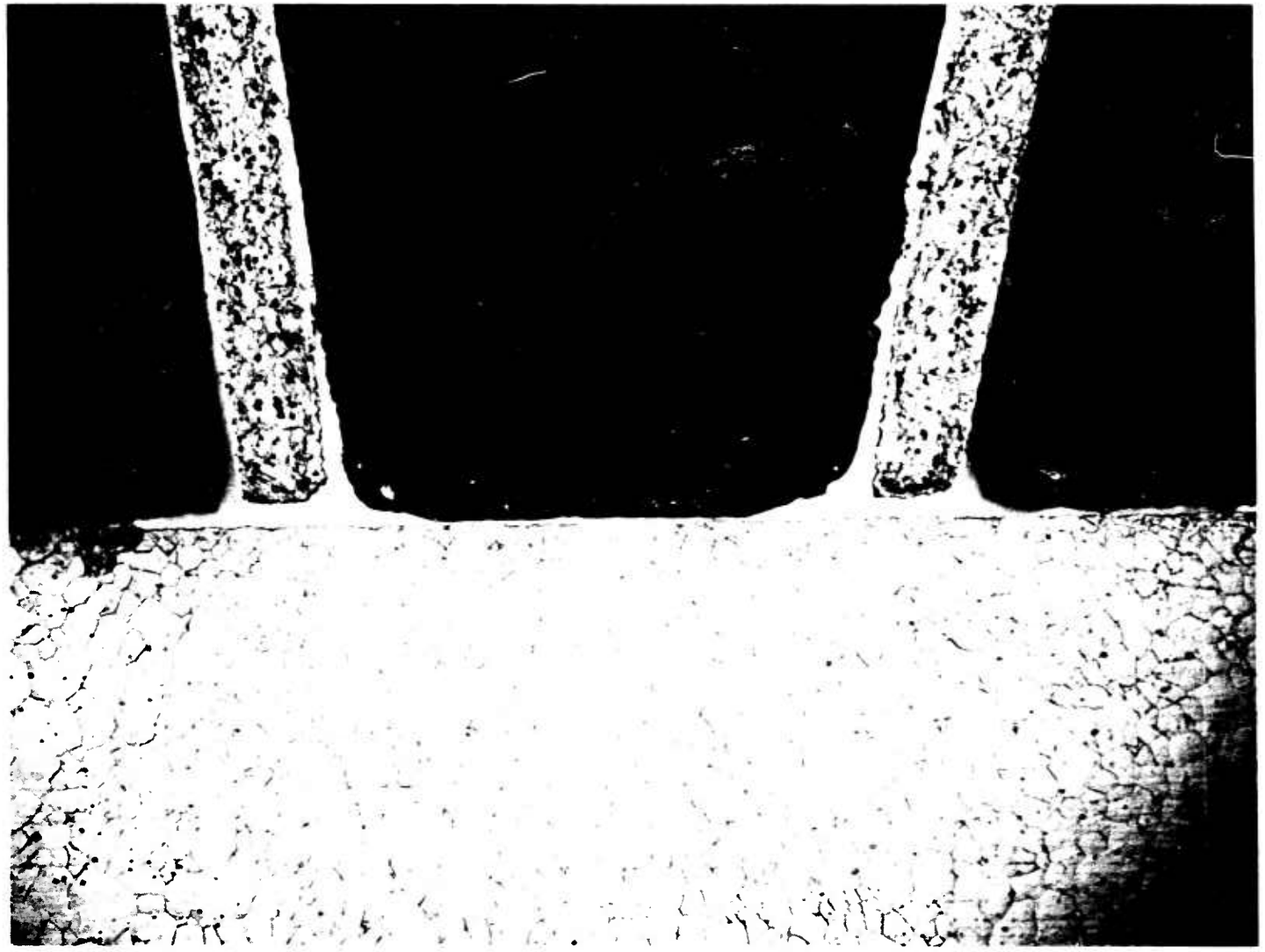

Figure 113. Face Sheet to Honeycomb Braze

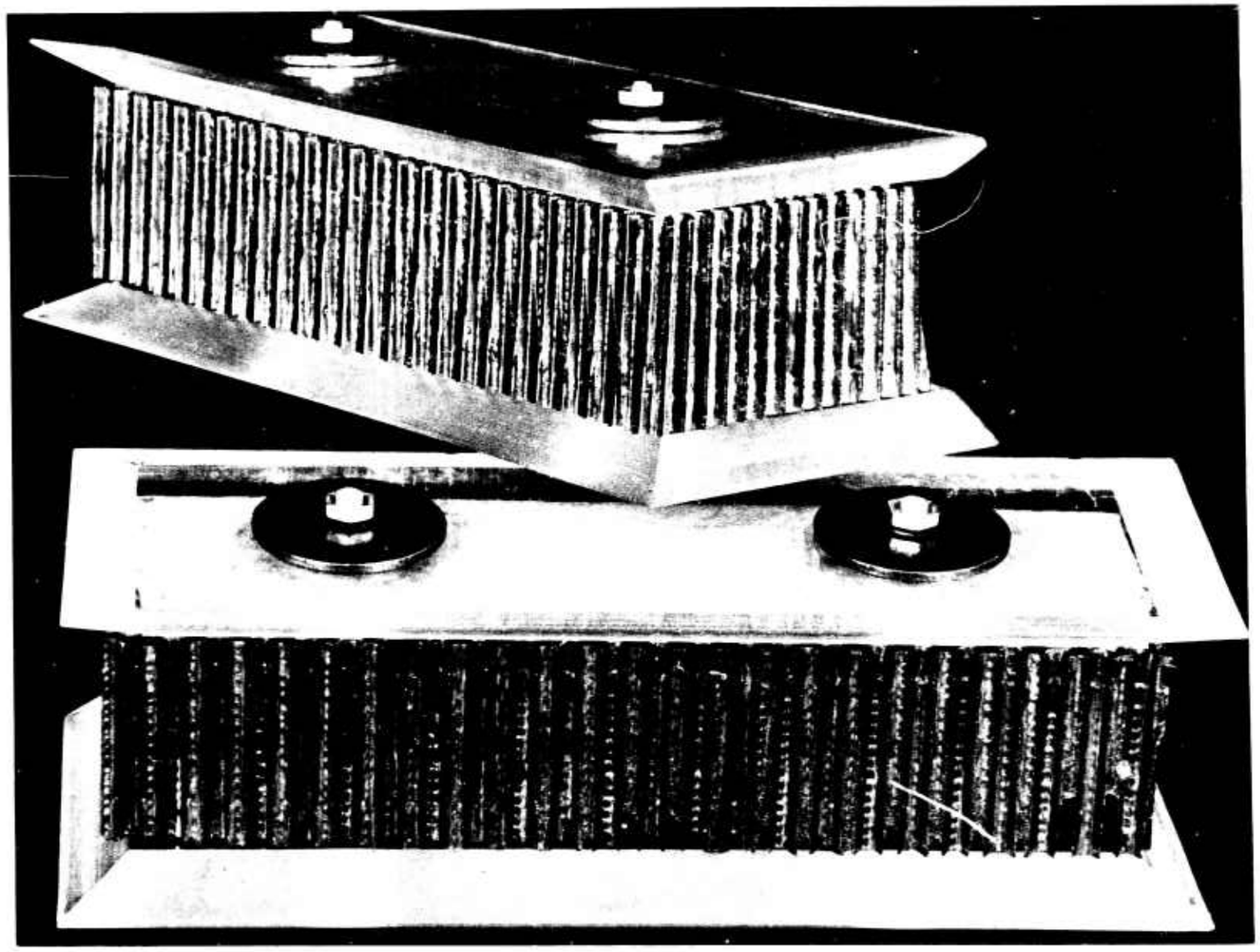

Figure 114. Honeycomb Panels and Masks Prior to Nickel Plating

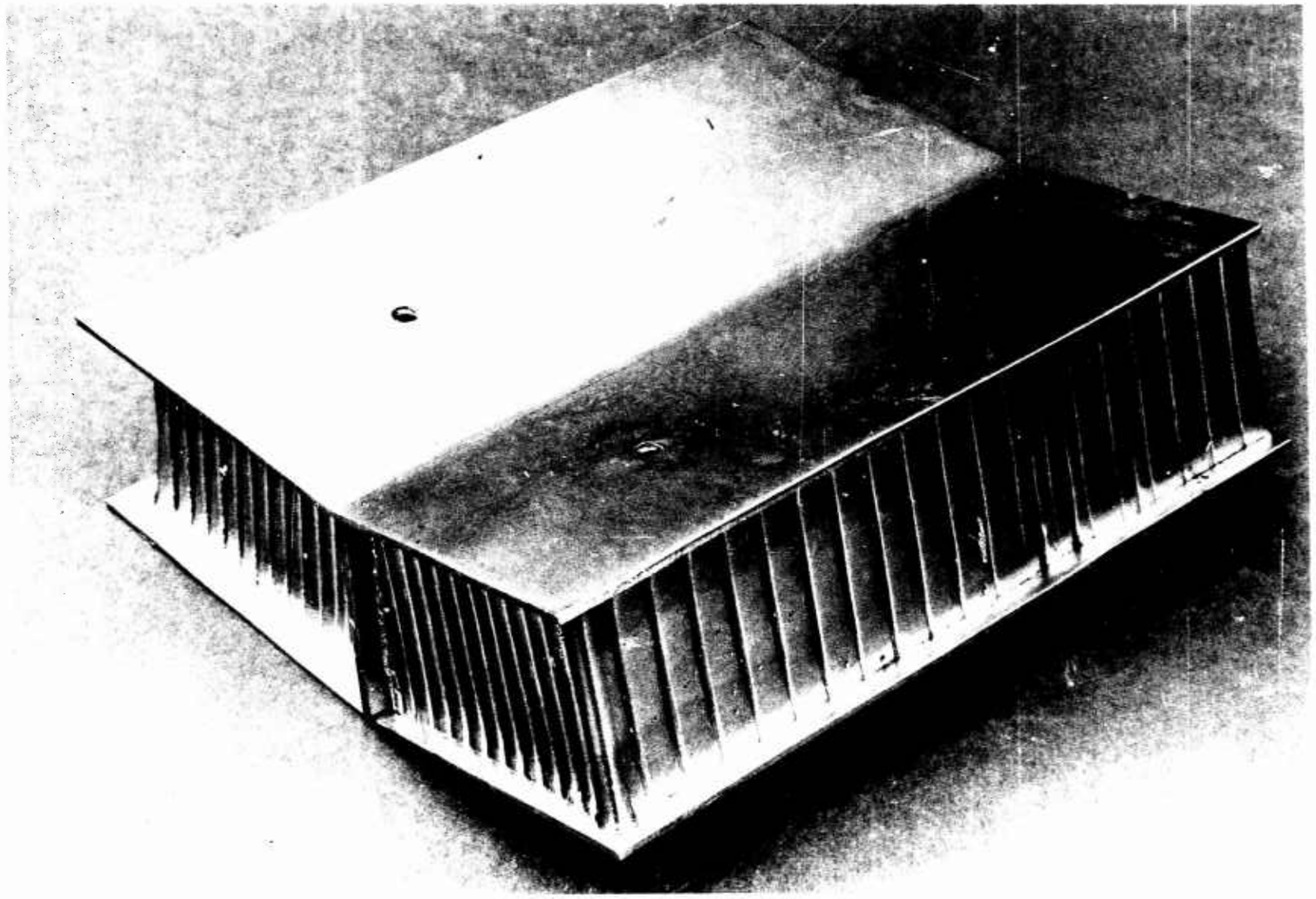

Figure 113. Plated and Brazed Honeycomb Panel

(C) initiated and completed first. The segments are nearly identical except for the panels. The fabrication procedure for both segments was to electron beam weld the baffles and end plates to the injector in a weld fixture. This fixture also served as the restraining device for the segments during the heat treat process after the assembly had been completed. The structural panels were electron-beam welded to the baffles and injector, and an aft manifold was electron-beam welded to each side of the segments.

(C) The chamber tubes were 0.093 O.D. x 0.010 wall CRES tubing. Five tubular panels were used to cover each structural wall: three panels, consisting of 66 tubes each, to cover the area between baffles, and two panels, consisting of 6 tubes each, to cover the wall from the downstream end of the baffle to the exit manifold. The tubes were electron beam welded together to form a flat panel. To keep the stack flat while welding, the tubes were held in a fixture which clamps the tube ends against a flat plate. The panels were then bent much like a piece of sheet metal to match the chamber contour. The ends of the tubes were flattened to provide a rectangular cross section for insertion into the manifold grooves.

(U) The rib panels consisted of U-shaped channels that were stacked in closeout plates. The plates were rigidly held in a fixture during welding to keep the panel straight and hold the distance between ends. The chamber contour was built into the closeouts and is therefore maintained in the channels.

(C) The beginning of the rib panel assembly is shown in Fig. 116. The U channels were preformed from 0.044 inch standard sheet stock by a punch and die, cut to length, and pierced with a venting hole. They were then assembled onto the milled closeouts which serve as jigs during assembly. The complete panel, fitted into the closeouts, is shown in Fig. 117. The tapped holes in the closeouts were used in bolting the assembly into the weld fixture which prevents distortion of the panel during the welding operation. The completely welded panel is shown in Fig. 118. The milled slots in the closeouts provided locations for butt welding the panels to the closeout. The closeouts were subsequently milled down, removing most of the material visible in the photographs and leaving only sufficient material for welding to the structural baffles. A closeup view of the EB welded channels and closeout is shown in Fig. 119. The uniformity of the weld is evident in this photograph. The lines between the channel welds are scribe marks used for location purposes. Dye penetrant, X-ray, and ultrasonic inspection techniques were employed on the final panel assembly.

(C) The remainder of the parts, baffles, end plates and injector except for the exit manifolds were machined from one-inch plate stock. The exit manifolds were made from formed and welded 0.040 inch sheet. All critical mating surfaces between components were match-machined to enable close fits without extremely tight tolerances. Figure 120 shows the injector, baffles and end plates placed in the weld-heat

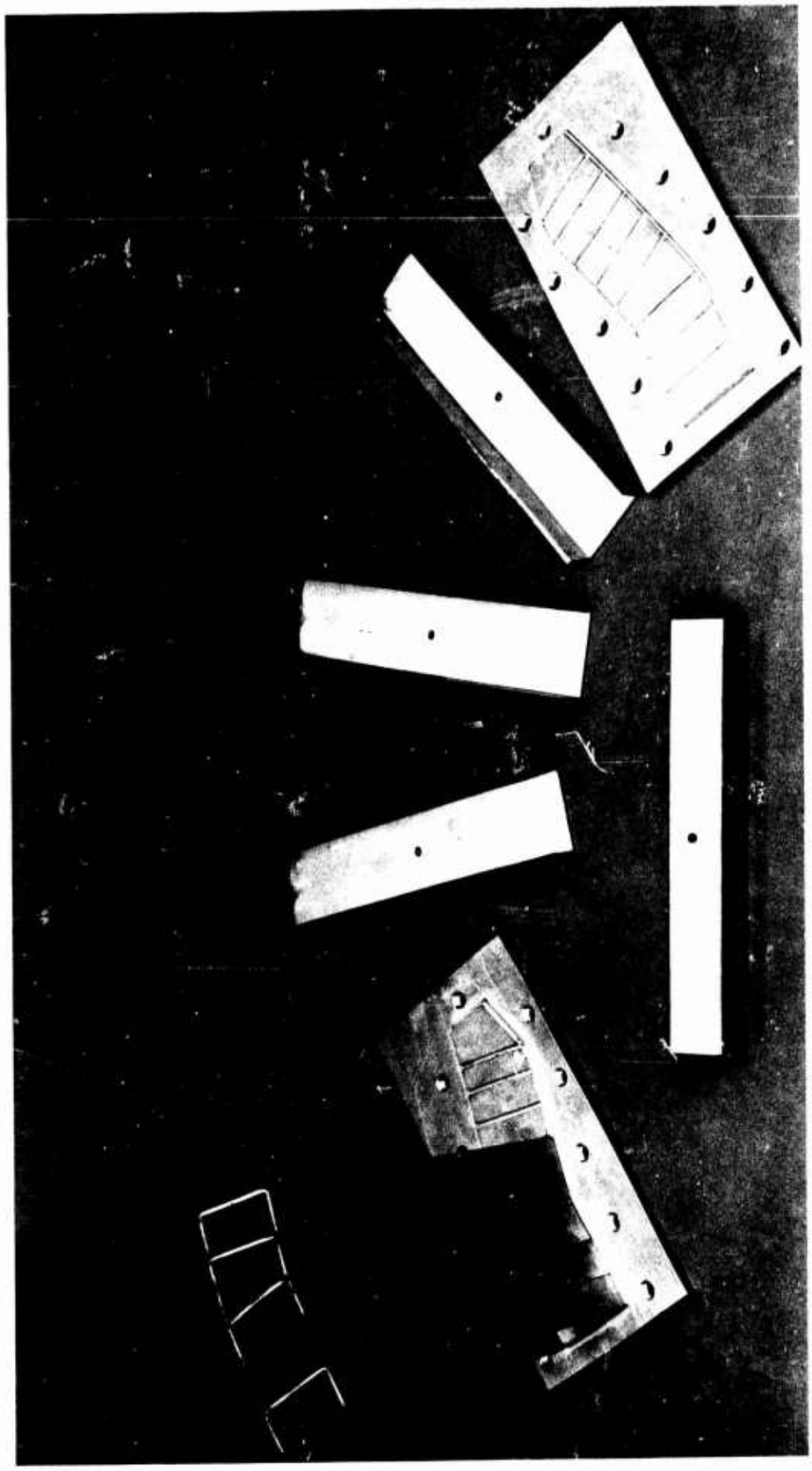

Figure 116. Partial Assembly of Rib Panel

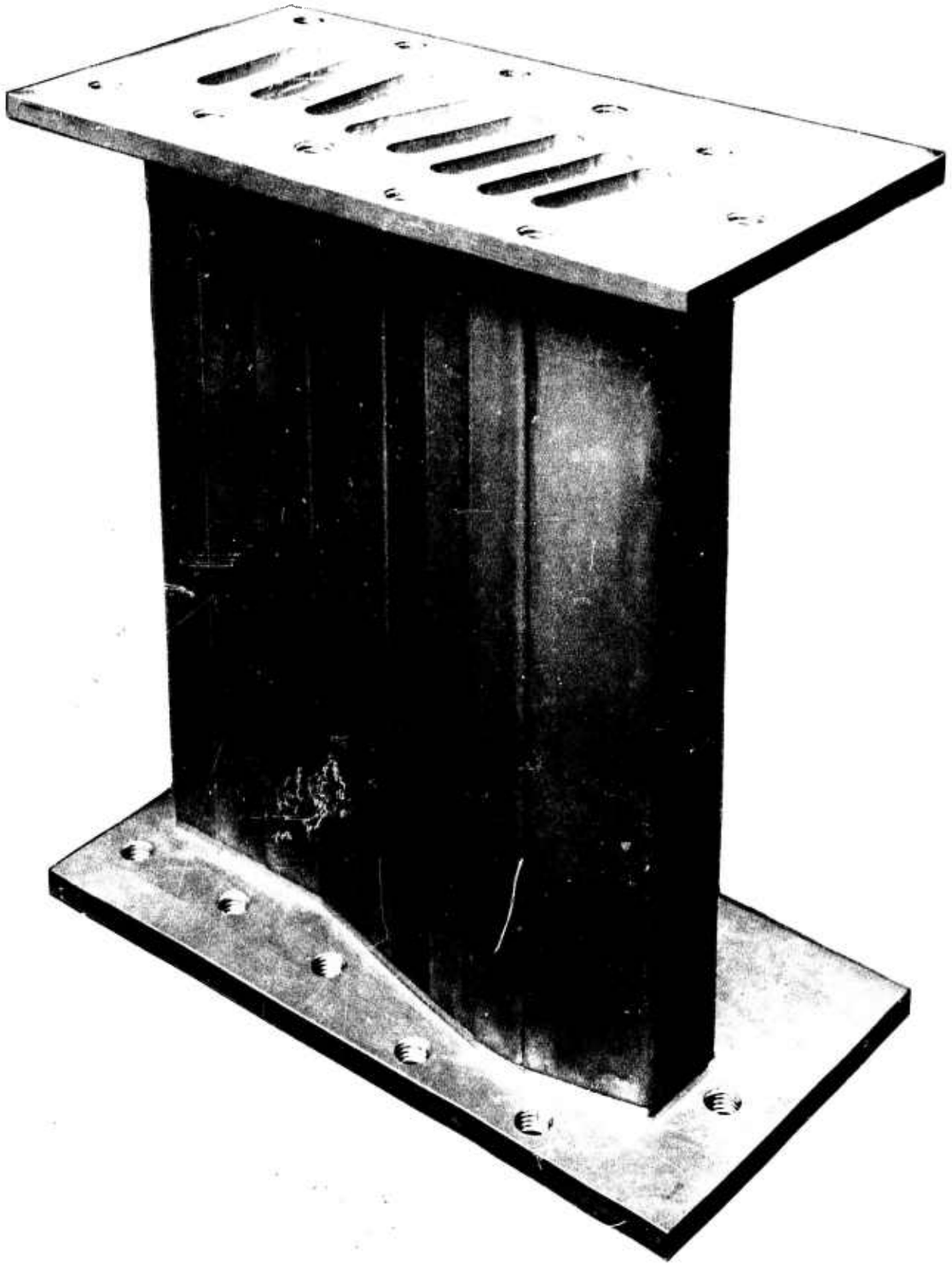

Figure 117. Rib Panel Before Welding

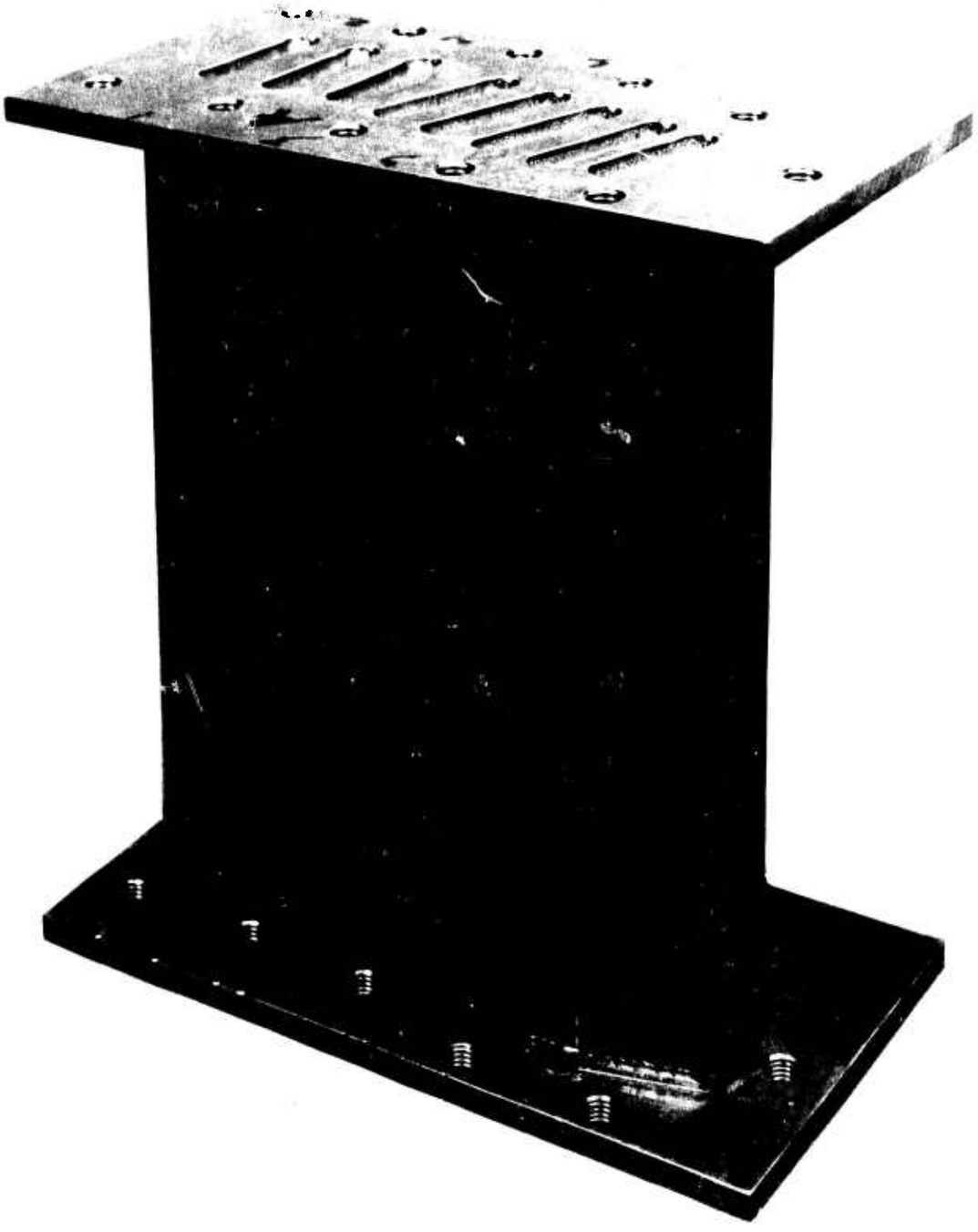

Figure 118. Rib Panel After EB Welding

Figure 119. Rib Panel EB Welds

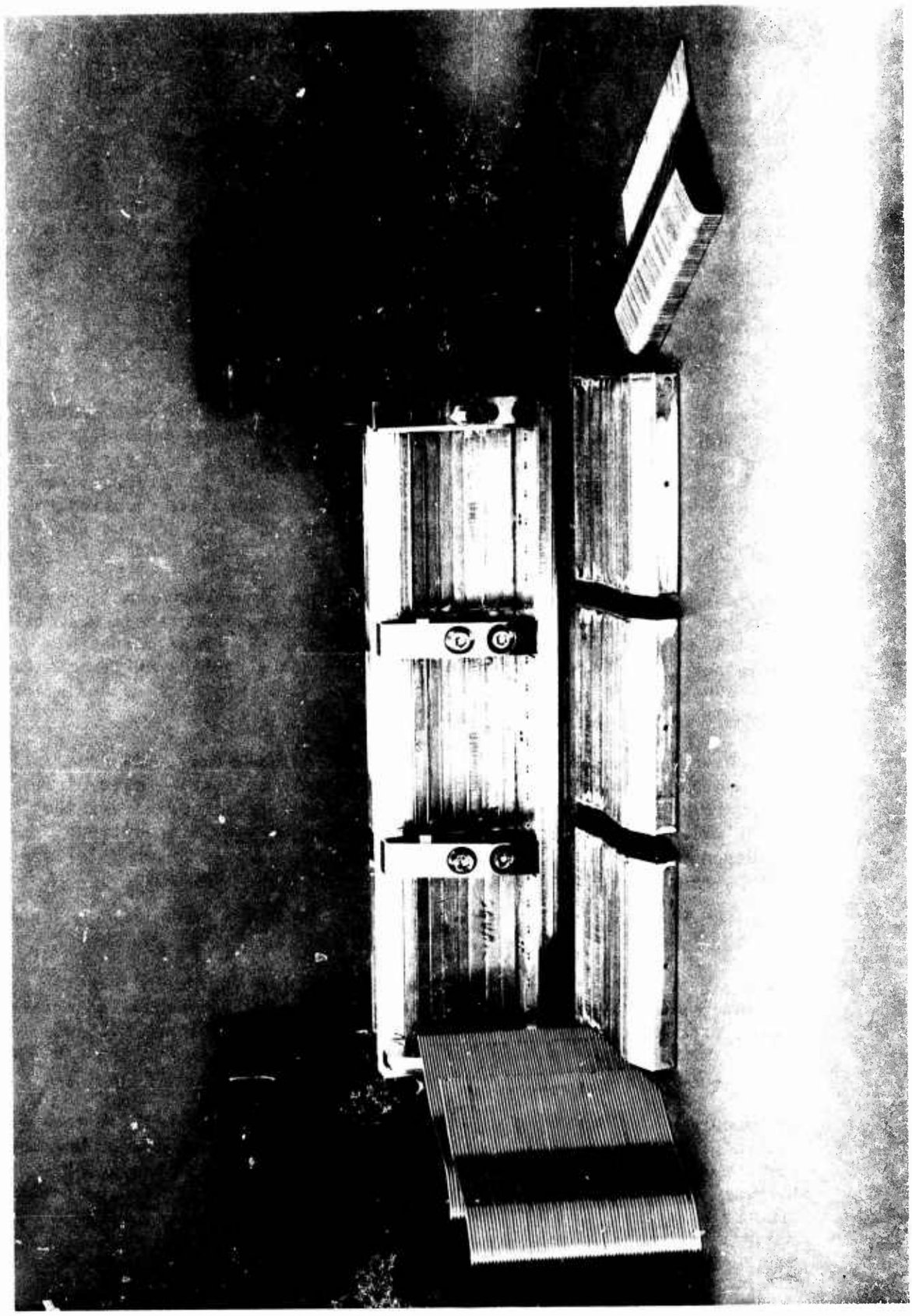

Figure 120. Partially Assembled Rib Structural Segment

(C) treat fixture. Three finish machined structural panels are shown in place and the other three are laying in front of the assembly. Three of the welded and formed panel tube panels are also shown. The heat-treated structure and formed tube stack are shown in Fig. 121.

(U) Honeycomb panel construction was initiated with the high speed abrasive sawing of the honeycomb cores. The core faces were cut to final dimension using electrical discharge machining to provide burr-free surfaces for brazing. The machined honeycomb cores were then masked with plexiglas sheets. Each panel consisted of two pieces of honeycomb. The masked face and aft honeycomb sections were then electroplated using the alternately plating-machining sequence determine during the sample fabrication program.

(C) After the final machining operation the two plated honeycomb sections were placed on top of the outer face sheet (which had been overlayed with braze foil) in the lower form block which served as a jig during the braze operation. Figure 122 shows the form block, core sections, and closeout plates. A 0.040 inch Inconel-718 sheet was inserted between the core sections before adding the inner face sheet and upper form block.

(U) Figure 123 shows a complete brazed and trimmed honeycomb panel, together with its aft channel subassembly. The three honeycomb panels were bolted into the weld-heat treat fixture together with the other components and welds were made between the honeycomb and channel subassemblies at the face sheets. Figures 124 and 125 show the weld setup before and after assembly in the fixture.

(U) The chamber pressure loads were simulated hydraulically. To contain the hydraulic pressure, a throat plug was made by pouring a low temperature molten alloy (Cerrobend) into the throat region, removing the outer wall and plug, coating the plug and segment with a silicone rubber compound (RTV-11) and reassembling the unit. The injector and end plate joints were also sealed with the rubber compound.

e. Segment Weights

(U) During the segment fabrication, accurate weights of the individual components were recorded. These data, together with the design criteria used, provide information for comparing the weights of the rib and honeycomb segments on an as-fabricated basis. Comparisons can also be made on the basis of weight reductions resulting from many factors.

(C) A summary of the as-fabricated weights is given in Table 15 on the basis of one compartment, i.e., segment weights between two compartment center-lines, including the fabble. On this basis, the honeycomb structural panel is 42 percent heavier than the rib panel which results in the honeycomb compartment weight being approximately 15 percent

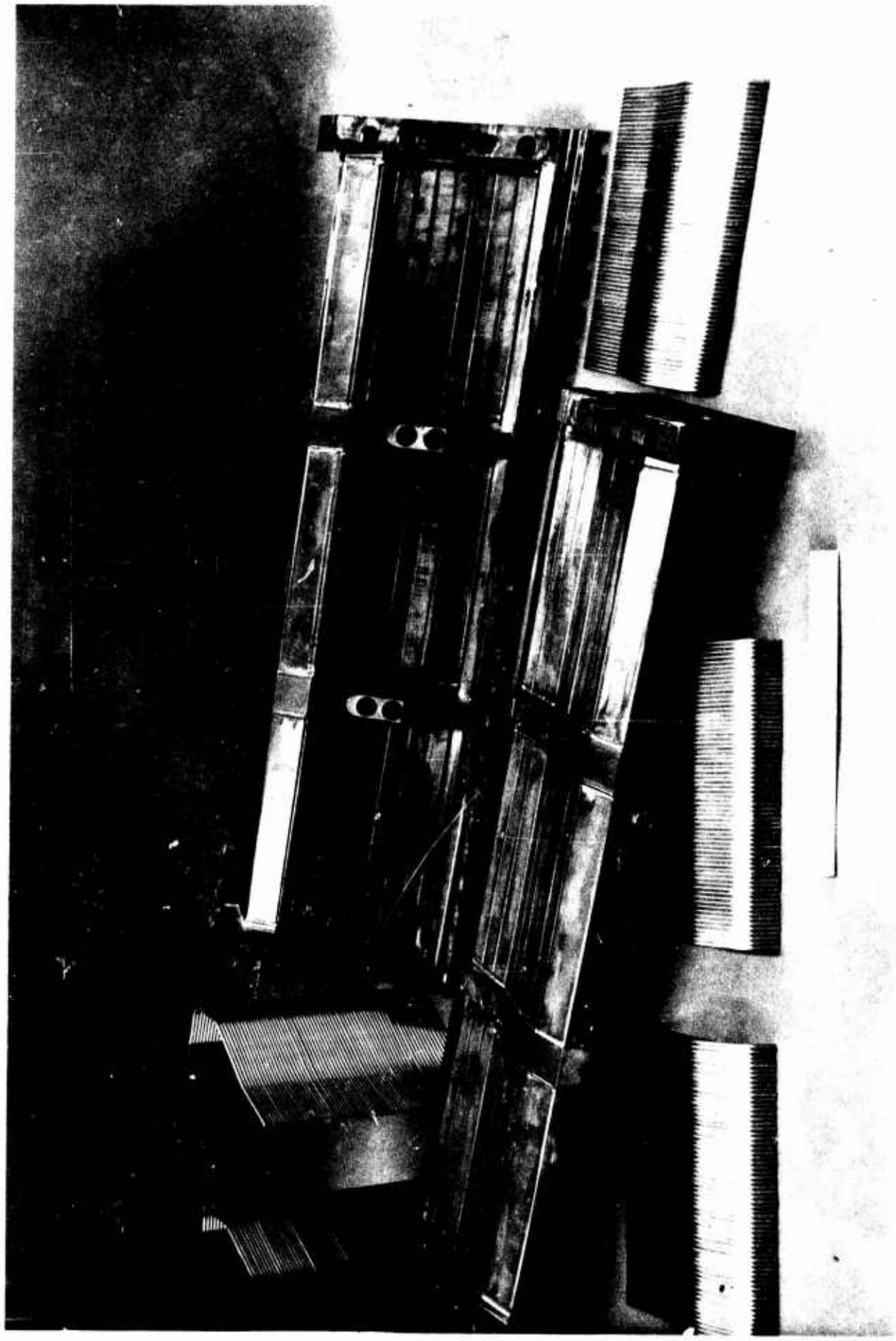

Figure 121. Rib Structural Segment After Heat Treat

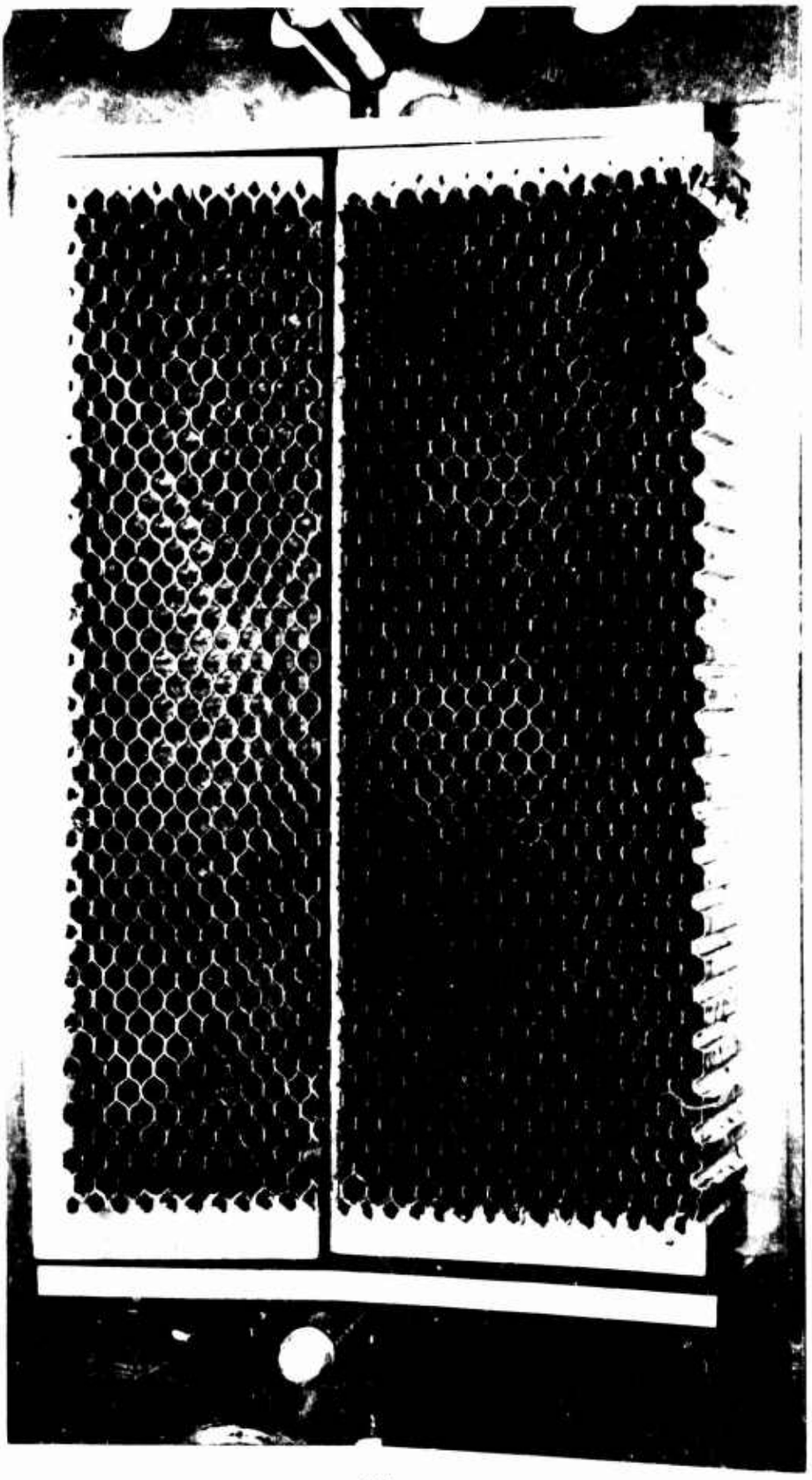

Figure 122. Plated Honeycomb Cores & Closeouts in Formblock

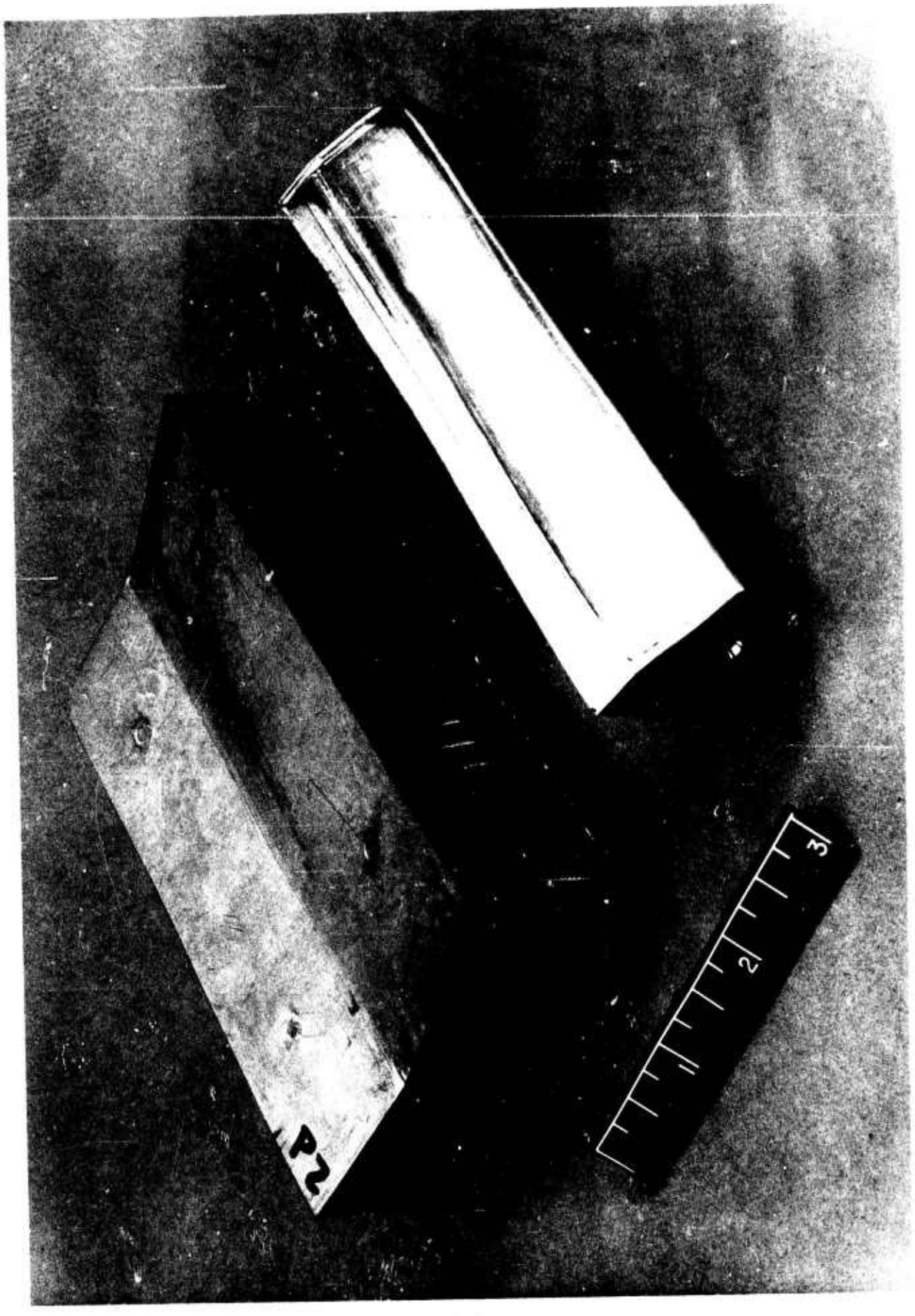

Figure 123. Honeycomb Panel With Rib Aft Structure.

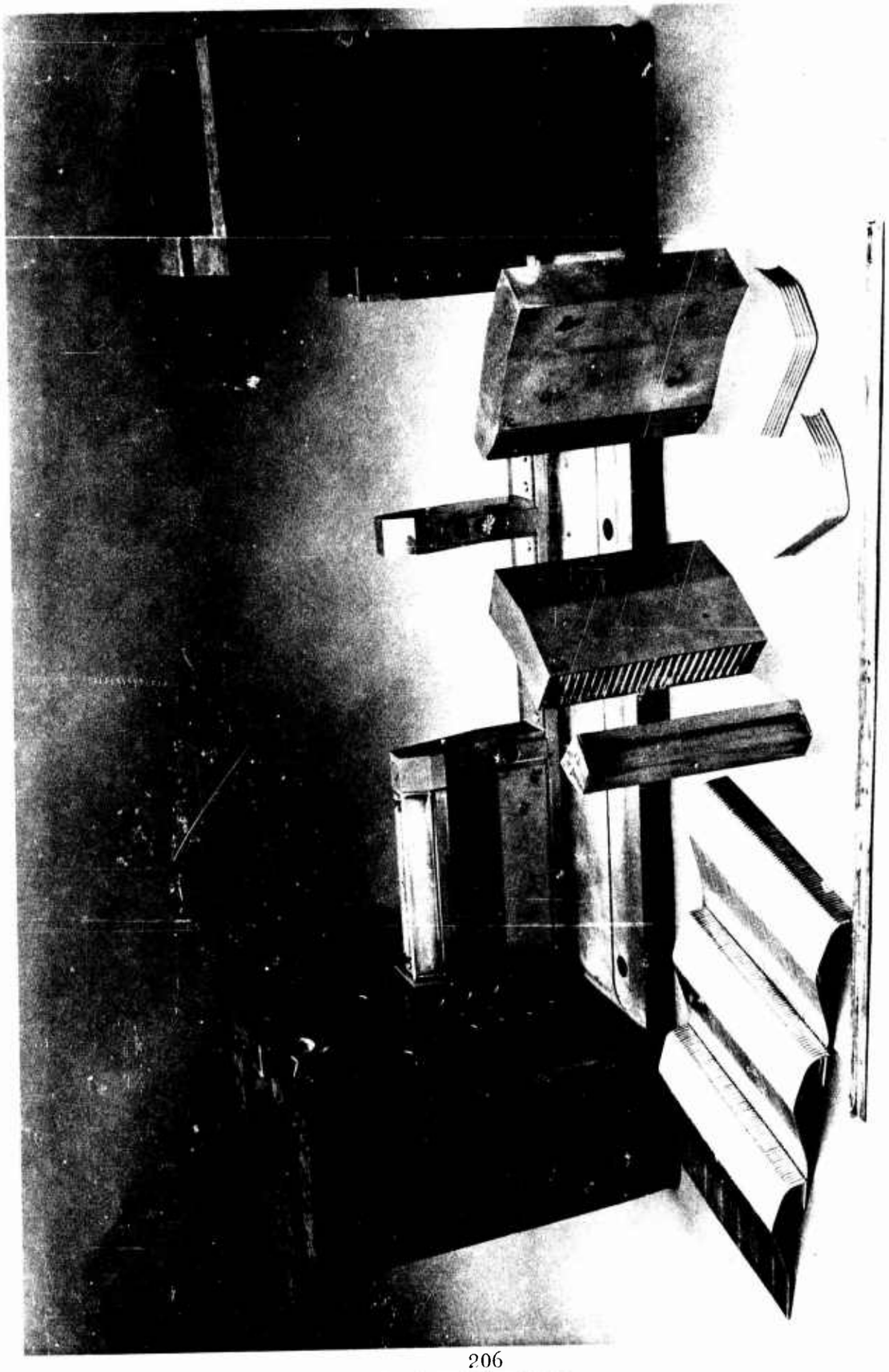

Figure 124. Partially Assembled Honeycomb Structural Segment.

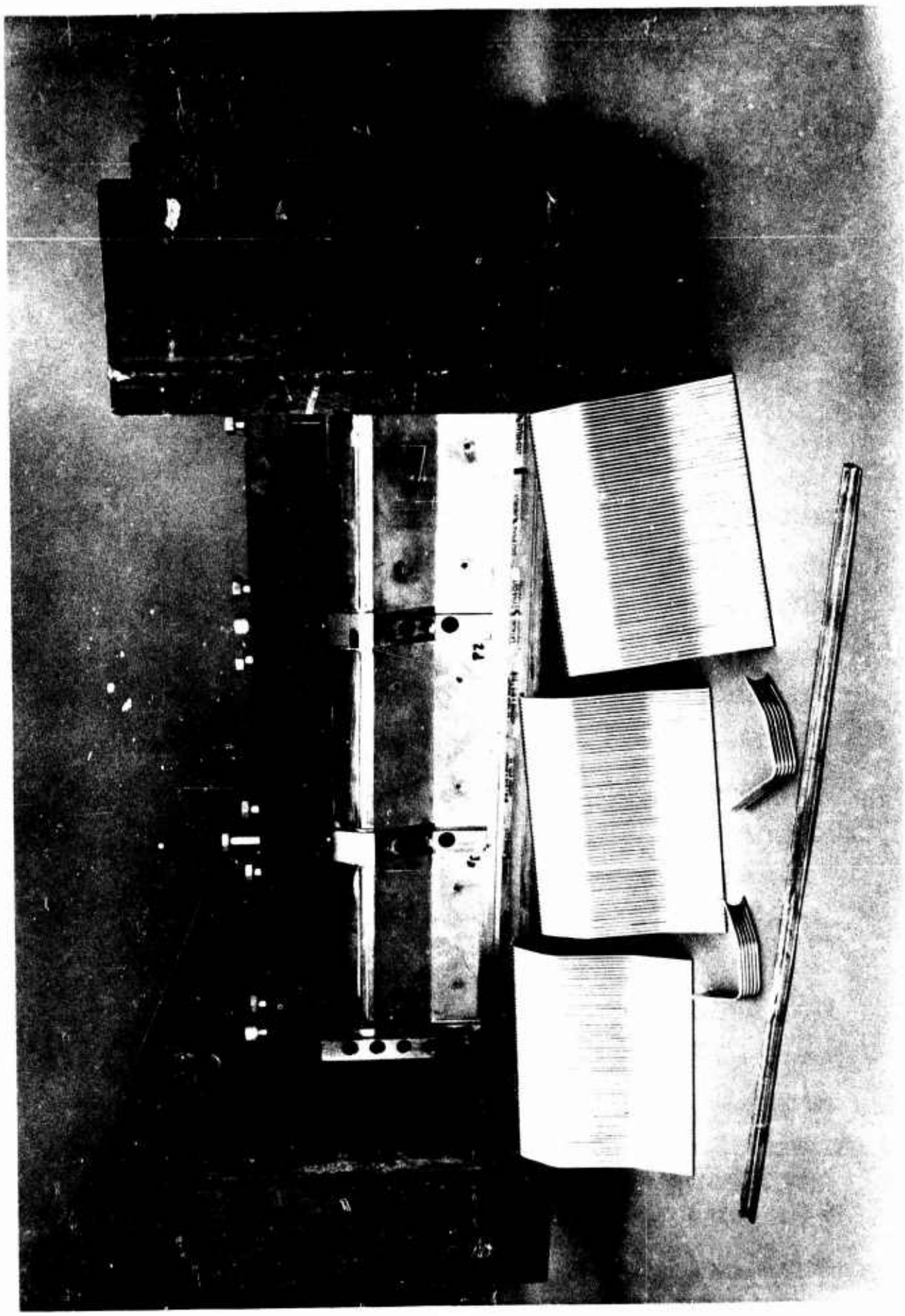

Figure 125. Honeycomb Panel and Baffles Assembled in Weld Fixture.

TABLE 15

STRUCTURAL SEGMENT WEIGHT COMPARISON

	Weight Per Compartment, lbs.			
	Rib		Honeycomb	
	(lbs)		(lbs)	
Outer Combustor		3.796		4.513
Structural Panel	1.703		2.420	
Baffle	0.978		0.978	
Inj. Attach Ring	0.773		0.773	
Exit Manifold	0.062		0.062	
Panel Tubes	0.259		0.259	
Baffle Tubes	0.021		0.021	
Inner Combustor		4.770		5.487
Structural Panel	1.703		2.420	
Baffle	1.375		1.375	
Injector	1.350		1.350	
Exit Manifold	0.062		0.062	
Panel Tubes	0.259		0.259	
Baffle Tubes	0.021		0.021	
Fasteners		0.621		0.621
3 Baffle Bolts & Washers	0.492		0.492	
8 Inj. Bolts & Washers	0.129		0.129	
TOTAL:		9.187		10.621

(C) greater than the rib compartment weight. The total weight of a 24-compartment thrust chamber using rib and honeycomb structures would be 220 and 255 pounds, respectively. However, several weight reductions could be accomplished as indicated in the following paragraphs.

(C) As previously noted, some of the materials used were heavier than required by design simply because of availability of these items. In the rib structural panel, the U channels were made from 0.044-inch sheet stock although the design required only 0.040 inch for the web portion and 0.028 inch for the face sheet portion. A weight reduction of 0.600 pounds per compartment would result from use of the design values. Reduction of the Inconel sheet thickness in the honeycomb panel from 0.044 inch to the design values and reduction of the honeycomb core density from the available 40.5 lbs/ft^3 to the design 35 lbs/ft^3 would reduce the compartment weight by 0.862 pounds.

(C) On the basis of the experience gained during the fabricated of the panels, additional weight savings can be effected. By eliminating the closeouts in all unnecessary area, a weight reduction of 0.40 pounds could be achieved for the rib segment. By a similar elimination, where applicable, to the honeycomb segment and also removing the nickel plating in unnecessary areas the weight of each compartment would be reduced by 1.10 pounds. The segments, therefore, could have been built with present knowlege such that the compartment weights would be 8.18 and 8.66 pounds, respectively, for the rib and honeycomb structures. The honeycomb compartment would be only 6 percent heavier than the rib compartment and the complete chamber weights would be approximately 200 pounds.

(C) Further weight reductions could be effected with the expenditure of additional effort to develop the necessary techniques. These reductions involve improved methods of joining the panels to the baffles and injectors. By eliminating the closeout construction and obtaining Class I welds to the baffle (or by utilizing an integral construction method), an additional weight savings of 1.02 pounds per compartment would be effected which would result in a thrust chamber weight of approximately 175 pounds. These results are summarized in Table 16. It may thus be concluded that the weights of the rib and honeycomb structures are fairly similar for the combustion chamber.

f. Structural Tests

(C) Both the rib segment and the composite segment consisting of the rib inner body and the honeycomb outer body were subjected to a number of cycles of hydraulic pressure from 0 to 650 psig to verify their structural integrity and to obtain data indicating the effect of chamber pressure on throat area. Analytical models of both segments were formulated and used to predict the deflections under test conditions as well as under actual chamber pressure loading. The two conditions were not exactly equivalent because of the effects of the device used to contain the hydraulic pressure; in this case, the throat plug.

TABLE 16

SUMMARY OF POTENTIAL WEIGHT REDUCTIONS

Condition	Weight Per Compartment (lbs)		Honeycomb Weight / Rib Weight
	Rib	Honeycomb	
As-fabricated	9.19	10.62	1.15
Using As-designed Materials	8.59	9.76	1.14
Using State-of-art Lightening Methods	8.19	8.66	1.06
Class I Welds or Integral Construction	7.17	7.72	1.08

(U) Details of the analytical method are presented in Appendix D. The outer body half of the chamber was modeled as a space gridwork of beam-like members. This equivalent model was analyzed by computer using the stiffness method. The same basic analytical model was used for both structures. The member section properties were varied to reflect the differences in the construction of ribbed and honeycomb core segments. The space gridwork used in the analysis is shown in Fig. 126. Pressure loads were applied to the structural model as equivalent nodal point forces and moments.

(C) Throat area changes were determined from calculated deflections. A throat area change of 2.6 percent was calculated for the case of no throat plug for the rib structure. The corresponding change for the honeycomb construction was 2.9 percent. Both deflections were evaluated at 650 psia.

(C) The calculated deflections at the midspan of the center compartment for both the rib and honeycomb type segments are shown in Fig. 127. The usefulness of honeycomb panels in stiffening the structure is evident in the area of the injector but results in similar deflections at the throat. For a complete thrust chamber, the actual operating throat deflections will be slightly greater than those calculated, since additional loads are introduced by the shroud pressures aft of the throat.

(U) The use of a metal throat plug seal in the test imposed chamber loads not normally present when pressure alone is considered. The forces acting on the structure due to internal chamber pressure with and without the throat plug are shown in Fig. 128. Consideration of the free body diagram of the plug shows that the magnitude of the normal load on the converging chamber section is dependent on the frictional shear traction developed between the plug and the chamber wall. The analyses were performed for both segments using a friction factor of 0.2. Comparison of the measured mid-compartment deflections with the throat deflections calculated considering the throat plug loads is shown in Table 17.

TABLE 17

MAXIMUM THROAT DEFLECTION AT 650 PSI (C)

	Measured Deflection	Calculated Deflection
Rib Structure	0.0077"	0.0079"
Honeycomb/Rib Structure	0.0071"	0.0080"

(C) From these data, it can be concluded that the differences in rigidity between the rib and honeycomb structural segments are small.

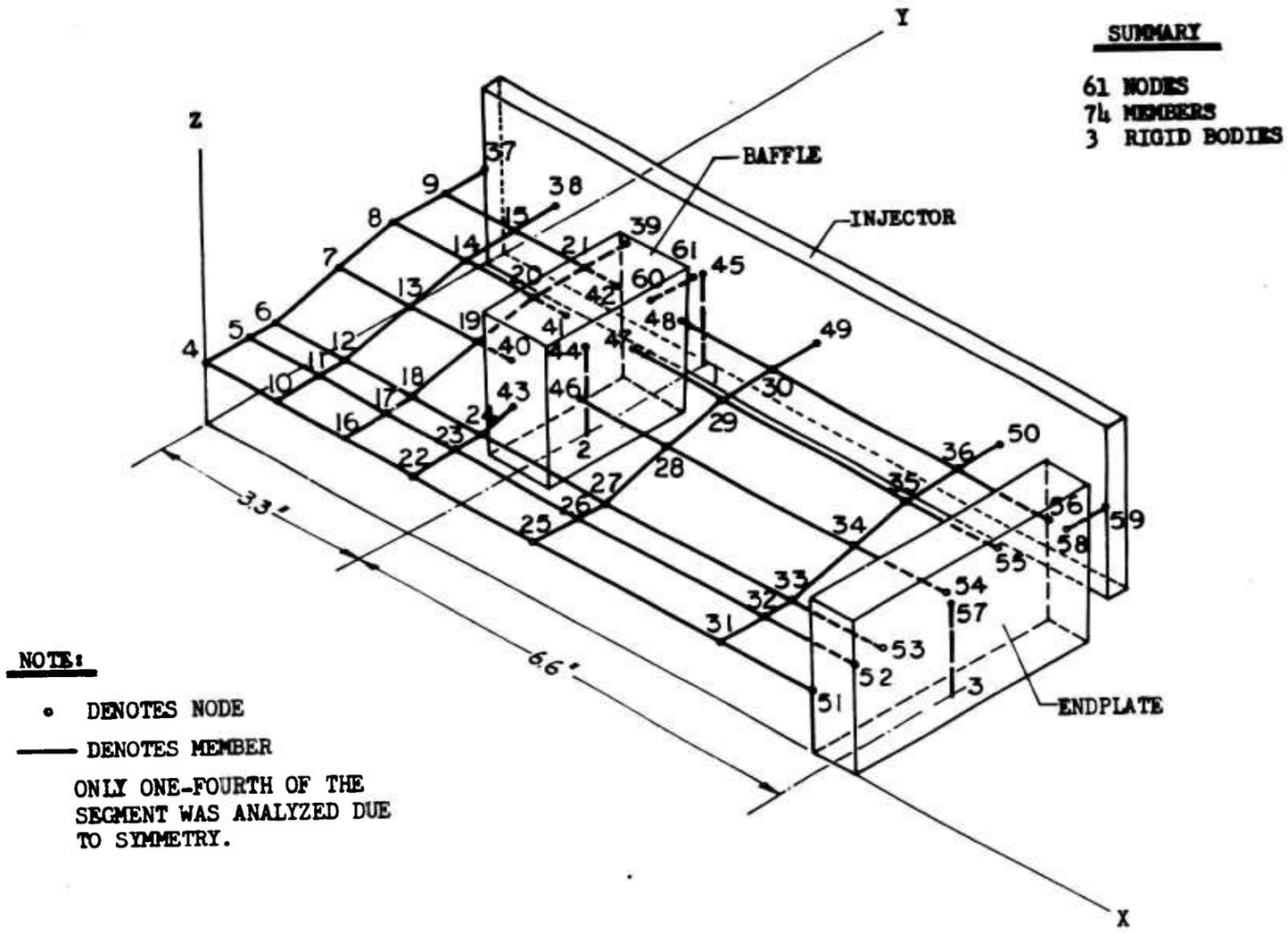

Figure 126. Analytical Model of Segment Outerbody.

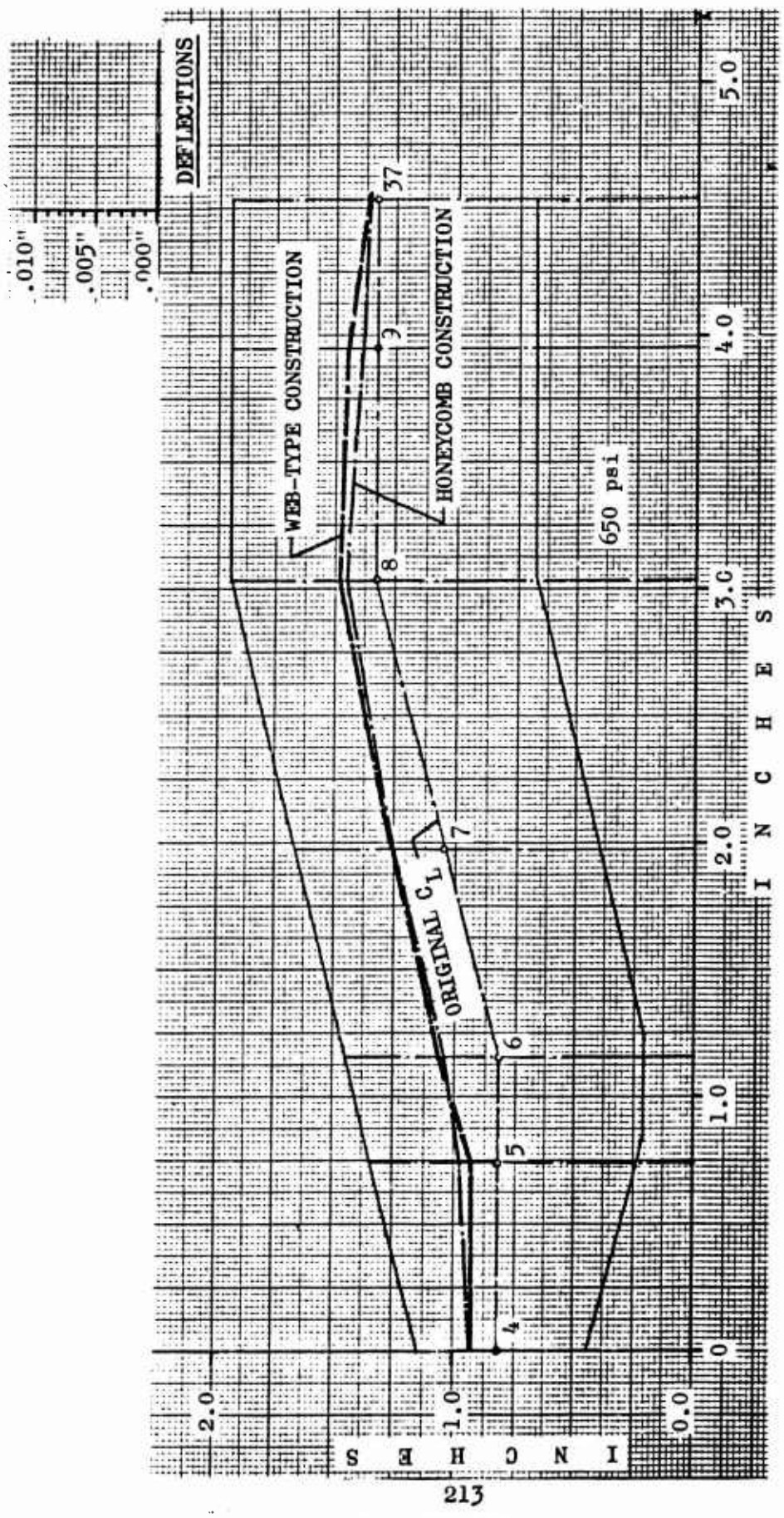

Figure 127. Calculated Deflections at Midspan of Segments

CASE I: LOADS WITH THROAT PLUG

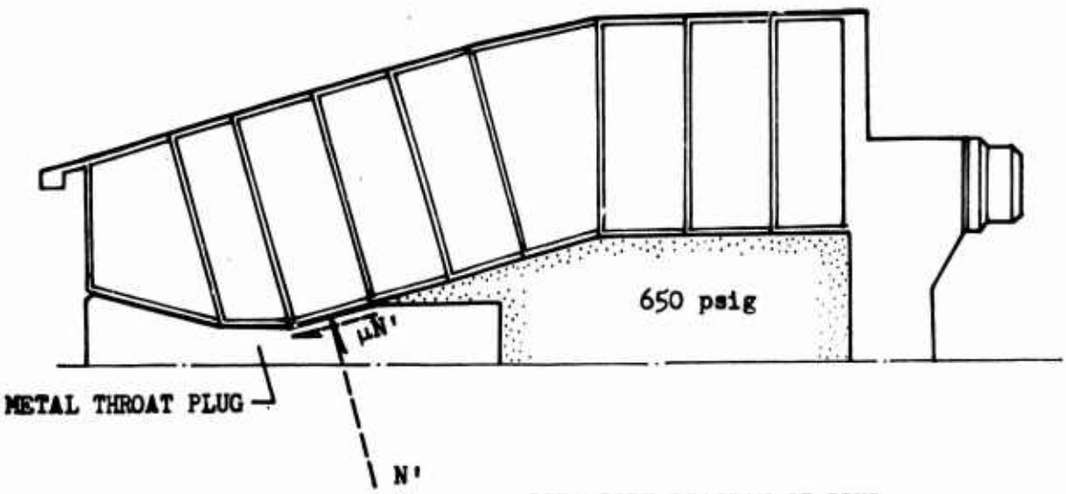

FREE BODY DIAGRAM OF PLUG

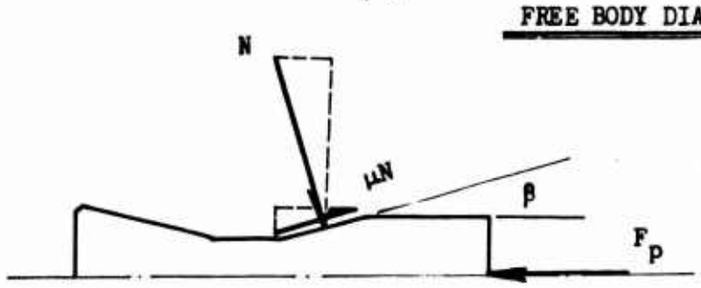

$$\Sigma F = 0$$

$$F_p = N\sin\beta + \mu N\cos\beta$$

CASE II: LOADS WITHOUT THROAT PLUG

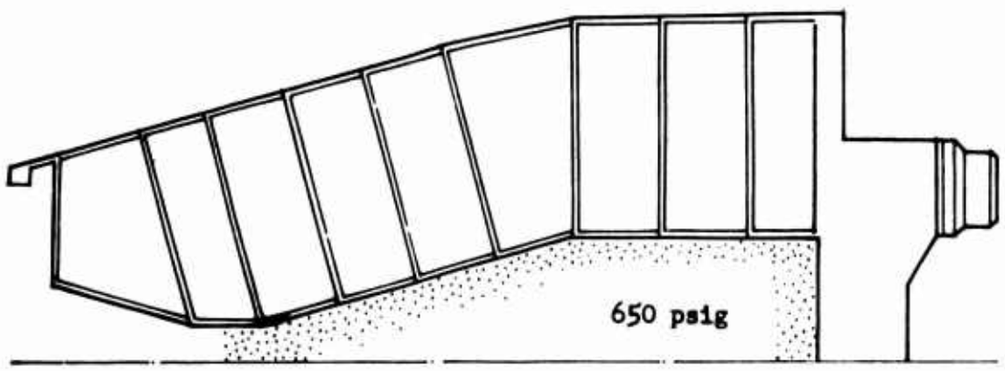

Figure 128. Structural Loads With and Without Throat Plugs

(U) For the rib structure, strain gages were placed on the outer body of the center compartment. In addition, four of the six baffle bolts were strain gaged in order to determine the bolt load variation along the baffle. The strain gage and instrumented bolt locations are shown in Fig. 129.

(C) Throat deflections were measured by dial gages mounted on each side of the throat at three locations. The instrument accuracy of these gages was 0.0001 inch. The positions of the dial gages are also shown in Fig. 129. The test arrangement is shown in Fig. 130. The rib segment was hydrostatically cycled from 0 to 650 psig a total of 22 times with no damage to the segment. The measured bolt loads and strains are plotted versus pressure in Fig. 131 and 132. The measured total throat deflections at 650 psig were 0.0077 inch at the midspan of the center compartment and 0.0040 inch at the baffle as shown in Fig. 133. The maximum measured change in bolt load due to pressure was 2160 pounds. The maximum strain at 650 psig was 420 μ in/in at location 1. (Fig. 129).

(C) The honeycomb composite structural segment was cycled to 650 psig a total of 15 times without any damaging effects. Less extensive data were taken on this segment but the midspan total deflection was 0.0071 inch. The difference between the total measured midspan deflection for the honeycomb/rib composite segment and the complete rib segment was 0.0006 inch. The difference between the deflections of a complete honeycomb segment and a complete rib segment would be twice this value, or 0.0012 inch.

g. Conclusions From Structural Segments

(C) On the basis of the data obtained during this program, it may be concluded that lightweight thrust chamber structures can be fabricated using rib or honeycomb material that will result in limiting throat area variations resulting from chamber pressure to much less than the target goal of 10 percent of the nominal throat area. The weight and rigidity data obtained for the rib and honeycomb segments indicated that these criteria would not form a strong basis for selection of either concept. Ease of fabrication for the two types of structure was also fairly similar for the segment construction but could change significantly when applied to fabrication of a complete thrust chamber.

BOLT 005
BOLT 003
S.G. 3
S.G. 1
S.G. 4
S.G. 2
S.G. 5
S.G. 7
S.G. 5
S.G. 8
A
12
10
8
6
4
2
5
3
1
11
9
7
A

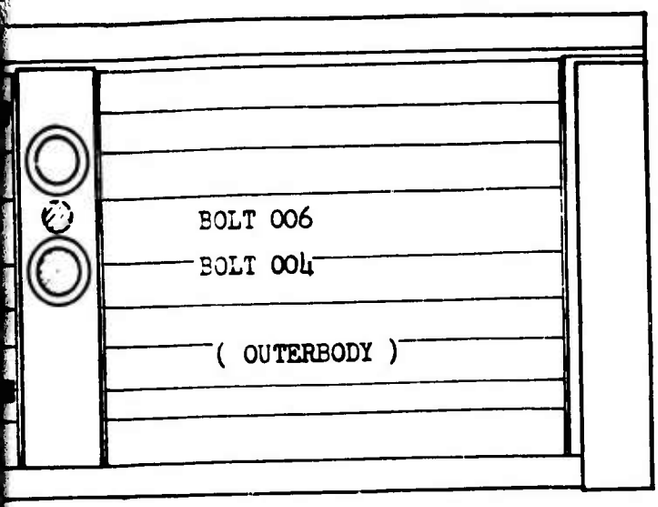

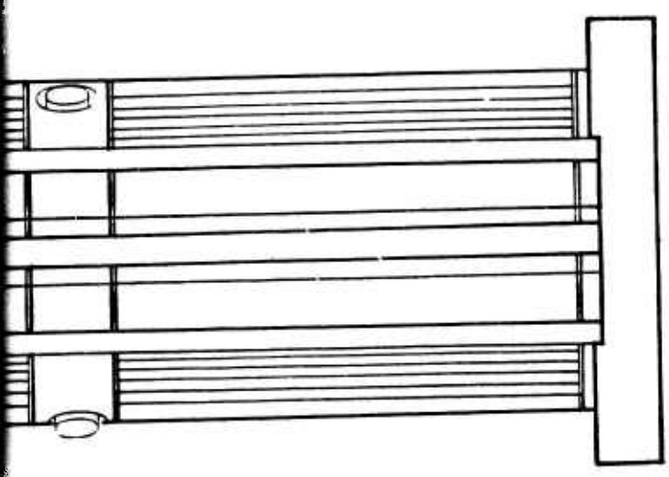

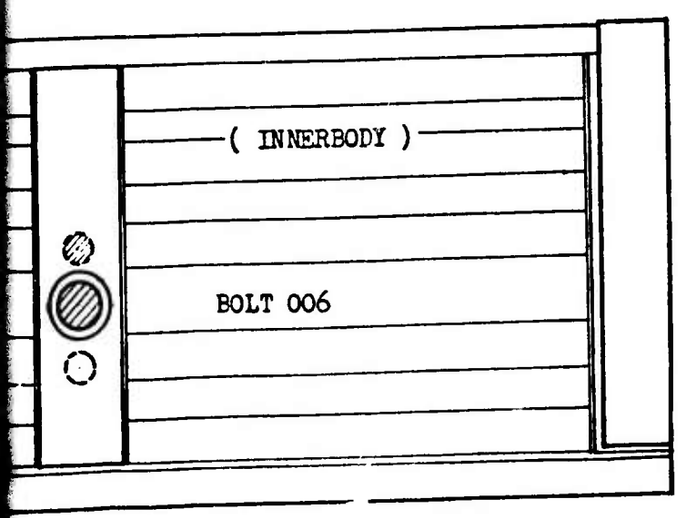

NOTE:

- DENOTES INSTRUMENTED BOLT
- DENOTES STRAIN GAGE
- DENOTES DIAL GAGE

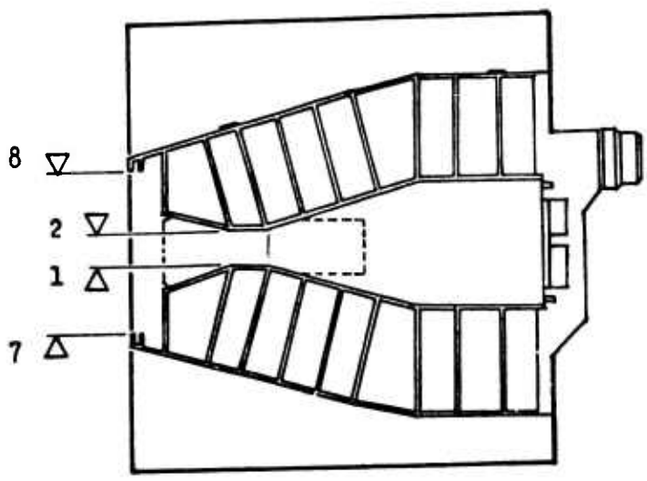

SECTION A - A

(TYPICAL 3 PLACES)

Figure 129. Instrumentation for Rib Structure Segment

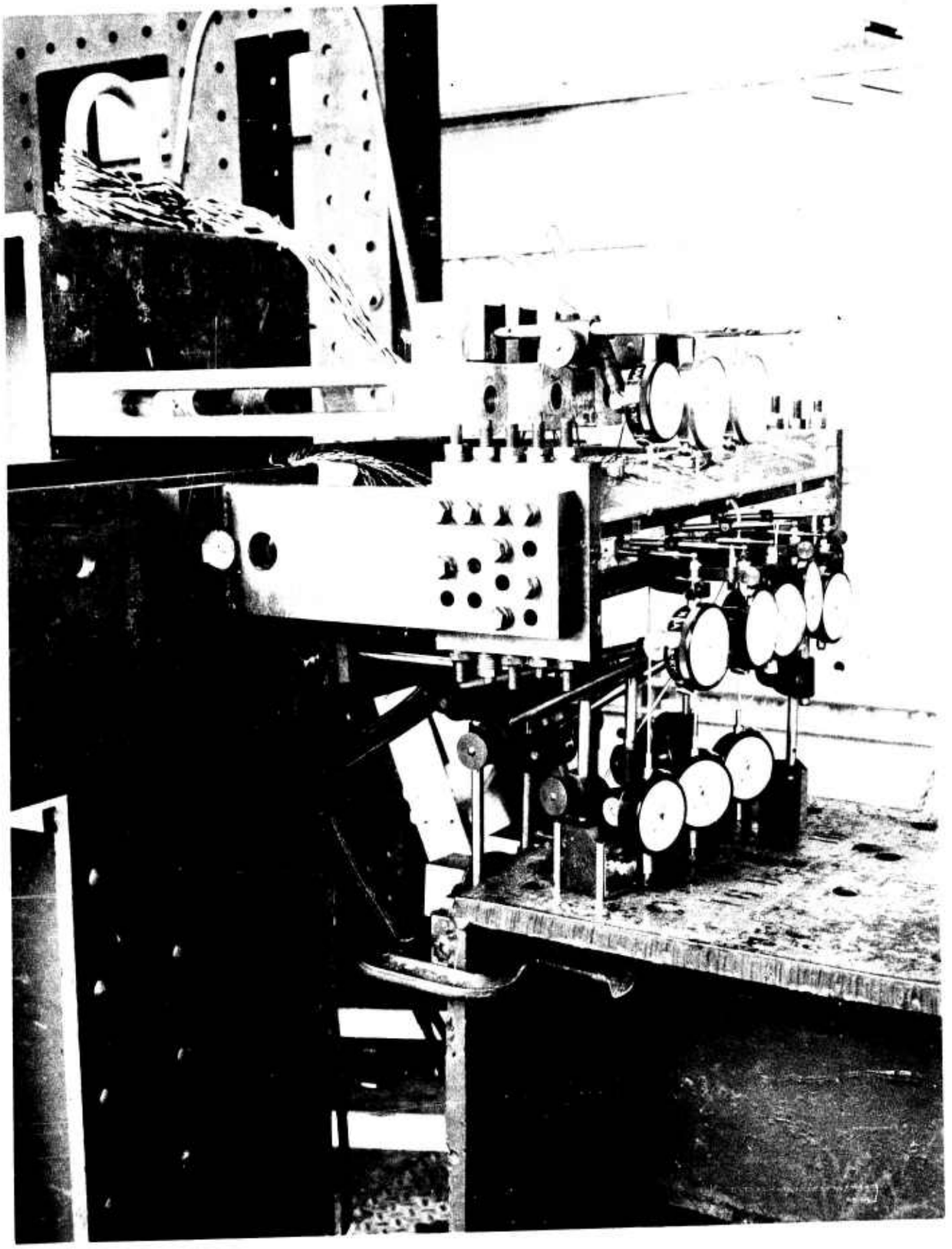

Figure 130. Test Setup for Structural Segments

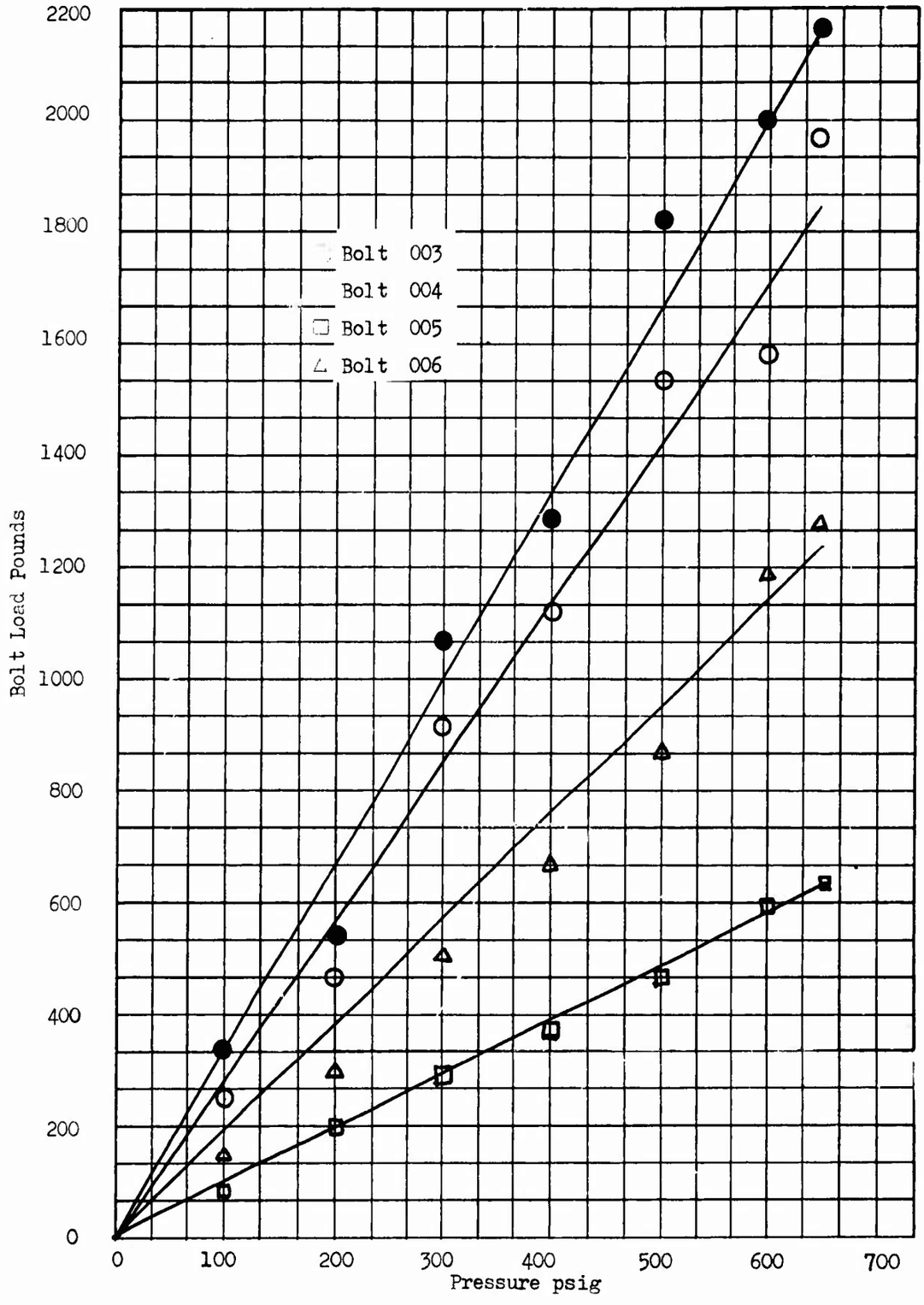

Figure 131. Measured Bolt Load vs Pressure For Rib Segment

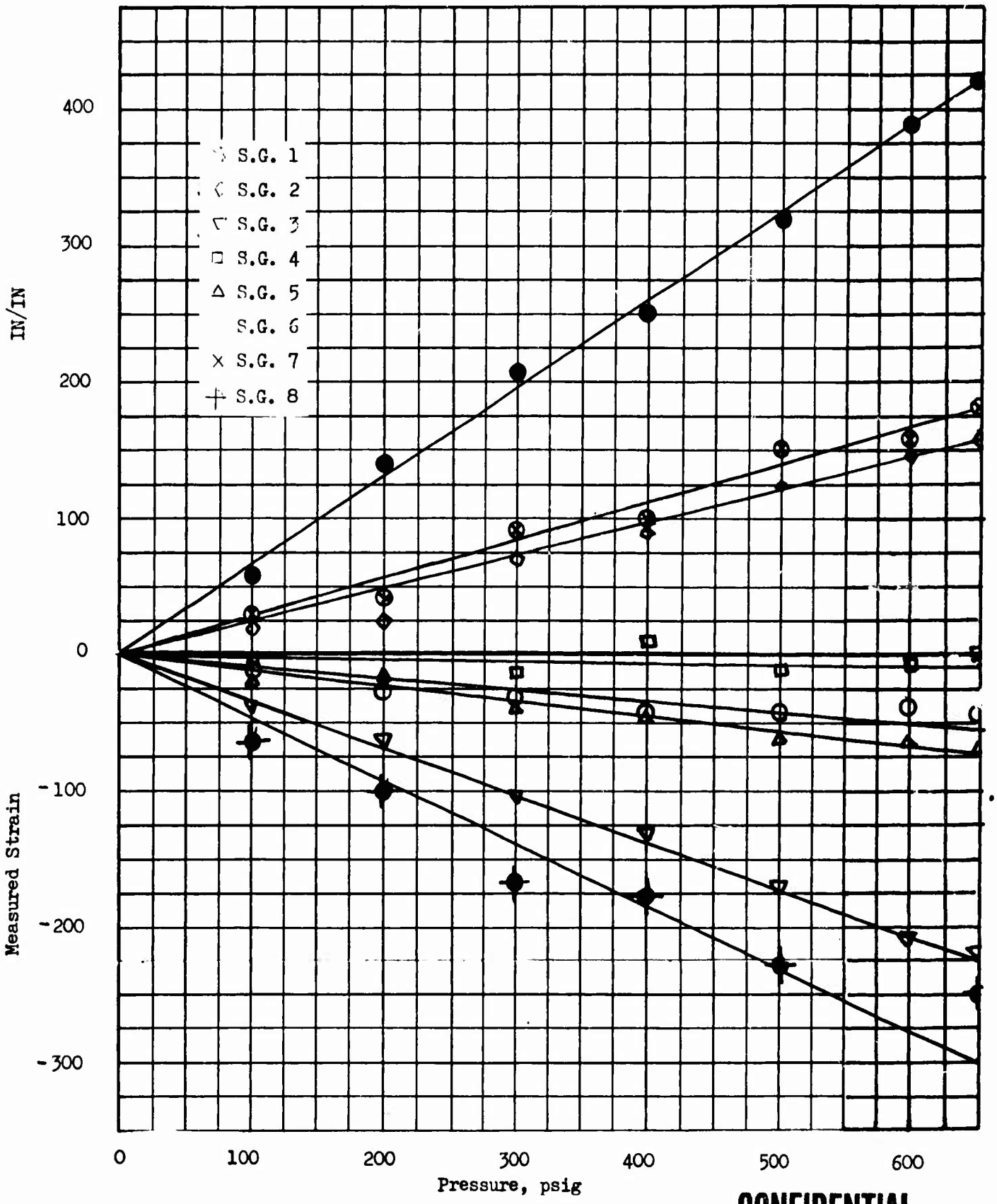

Figure 132. Measured Strain vs Pressure for Rib Segment

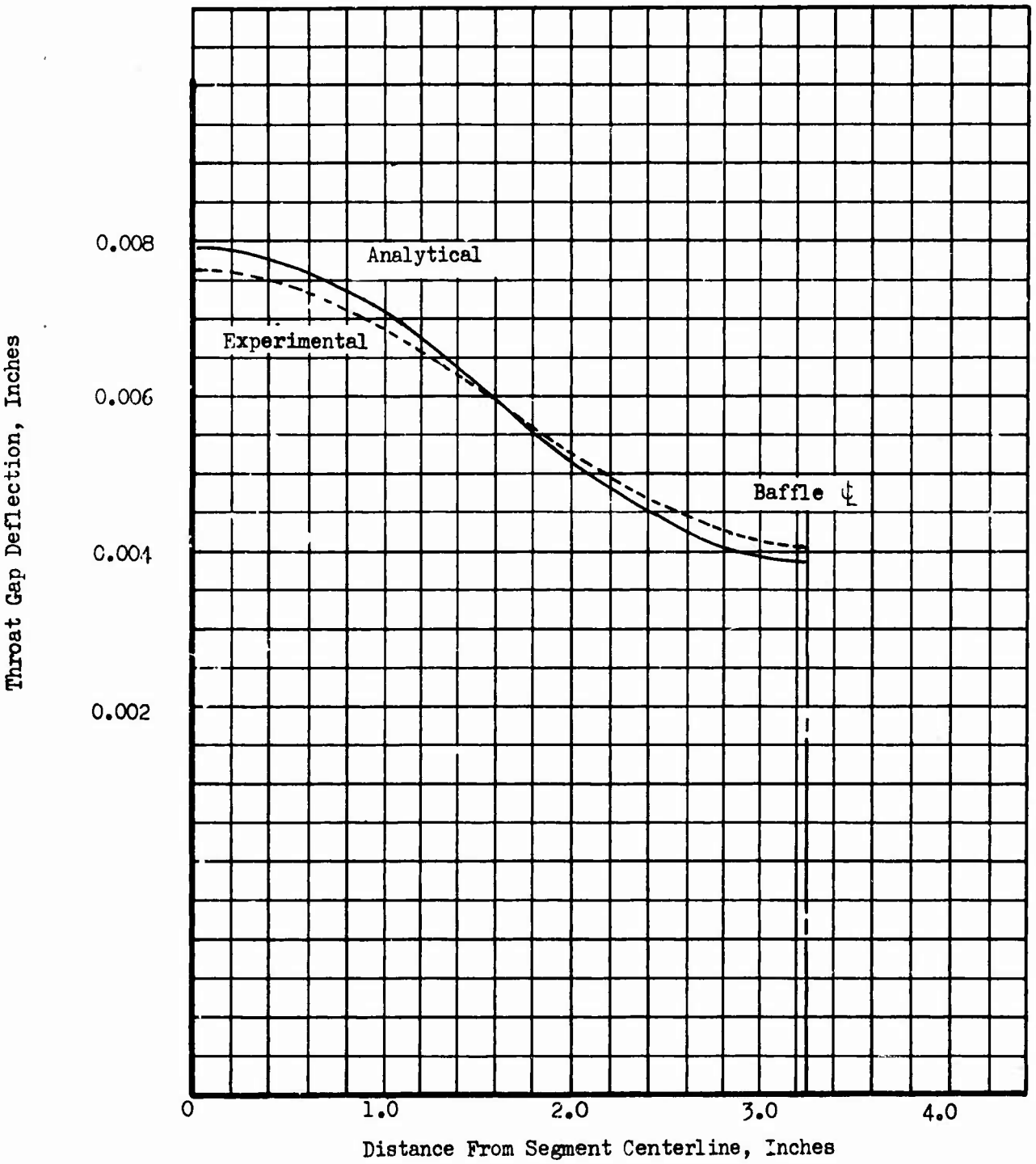

Figure 133. Rib Structural Segment Throat Deflection at 650 psig

SECTION IV

CONCLUSIONS AND RECOMMENDATIONS

(C) On the basis of the analytical and experimental results obtained during this program, the following may be concluded:

1. Chamber performance (η_c*) in excess of 99 percent can be achieved over the design 9:1 throttling range.

2. This performance can be maintained while limiting heat transfer rates to values compatible with a two-pass regenerative cooling configuration.

3. The heat transfer and performance characteristics of the thrust chamber depend strongly upon the geometric configuration (contour) of the chamber, the injector configuration, and the interaction between the two.

4. Hot gas for use as a turbine drive fluid can be obtained by tapping combustion chamber gases through the injector without significantly degrading combustion chamber performance.

5. The properties of these tapoff gases are relatively insensitive to throttling over the range of chamber pressures tested (290 to 483 psia).

6. Use of injector mixture ratio bias as a heat transfer control mechanism results in substantial performance losses if compensating injector redesign is not accomplished.

7. Injector stability throughout the throttle range can be achieved when the oxidizer is injected as a two-phase fluid.

8. Thrust chamber performance, heat transfer characteristics, and system stability can be investigated relatively inexpensively and with considerable flexibility using water-cooled segments.

9. Evaluation of particular regenerative cooling configurations (e.g., tube materials and dimensions) can be accomplished in tube-wall segments.

10. Throat area deflections resulting from thermal and chamber pressure loads can be reduced to small values by the structural-baffle configuration.

11. The throat area variations resulting from chamber pressure changes are analytically predictable for the subsonic baffle configuration and amount to less than 3 percent over the 0 to 100 percent chamber pressure range.

12. Chambers using rib or honeycomb as the structural material weigh approximately the same and exhibit similar throat area pressure sensitivities.

(C) Based on the favorable results obtained to date, further work for demonstration of the complete thrust chamber is recommended. Additional tests should be conducted using full-compartment-width segments (~ 6 inches baffle-to-baffle distance) to further refine the contour G geometry for maximum cooling margin and to evaluate the aspects of the baffle cooling. This testing should also include bomb or pulse gun tests to evaluate the degree of inherent combustion stability of the design. Additional segment injector comparative evaluation tests should also be conducted prior to making a final selection between the triplet and impinging fan patterns. Heated hydrogen at engine injector design inlet conditions should be used on all future segment tests because of its strong influence on performance and stability.

(C) Following the above additional segment tests, design and fabrication of a full 360 degree thrust chamber should be undertaken to demonstrate the performance, stability, and regenerative cooling of the complete prototype design. This can be accomplished with a high degree of confidence as a result of the data obtained from the segment testing.

REFERENCES

1. R-3999, Investigation of Cooling Problems at High Chamber Pressure, Final Report for Period 9 April 1962 to 8 January 1963, Rocketdyne, a Division of North American Aviation, Inc., Canoga Park, California, May 1963.

2. "Liquid Propellant Handbook", Batelle Memorial Institute, October 1955, page 10-7.

3. CR-54978, Fluorine-Hydrogen Performance Evaluation, Phase J: Part I: Analysis, Design and Demonstration of High Performance Injectors for the Liquid Fluorine-Gaseous Hydrogen Propellant Combination, Rocketdyne, a Division of North American Aviation, Inc., Canoga Park, California, July 1966.

4. Goldman, A.: "Material Properties Notebook", AMM 6109-3002, Rocketdyne, 31 May 1966.

5. Liguori, R. R. and Stephenson, J. W.: The Heating Program, Report No. 417-5.0, Astra, Inc., Raleigh, North Carolina, 1 January 1961.

6. Rubinstein, M. F.: "Matrix Computer Analysis of Structures", Prentice-Hall, Inc., 1966.

7. Martin, H. C.: "Introduction to Matrix Methods of Structural Analysis", McGraw-Hill Book Co., 1966.

8. K. Eisemann, Woo, L. et al., "Space Frame Analysis by Matrices and Computer", Journal of the Structural Div. ASCE, December 1962.

9. Faddeev, D. K. and Faddeeva, V. N., W. H. Freeman and Company, "Computational Methods of Linear Algebra", 1963.

10. "Plane Framework Methods for Plates in Extension", Yehram and Husain, Journal of the Engr. Mechanics Div. ASCE, February 1966.

11. "Grid Framework Method for Plates in Flexure", Yehram and Husain, Journal of the Engr. Mechanics Div. ASCE, June 1965.

12. Shanley, F. R., "Strength of Materials", McGraw-Hill (1957), pp. 190-193.

APPENDIX A

TEMPERATURE DISTRIBUTION AND RESULTING STRAINS IN THROAT REGION OF WATER COOLED COPPER SEGMENT

(U) The heating program (Ref. 5) was used to compute the temperature distribution in the throat region of the copper water-cooled test segment. The throat section and region analyzed are shown in Fig. A-1. The geometry was approximated by rectangular regions as shown in Fig. A-2.

(U) Portions of the coolant-side wall assumed to be in a nucleate boiling regime were fixed at a temperature of 700 F. For coolant-side boundaries where the wall temperature was too low for nucleate boiling, a convective film coefficient computed from the equation:

$$h_c = 0.023 \frac{k}{D} \left(\frac{\rho VD}{\mu} \right)^{0.8} \left(\frac{C_p}{k} \right)^{0.4}$$

was used. The thermal conductivity of the copper wall was assumed to be 0.00462 Btu/in-sec-deg F.

(U) The temperature distribution computed for a gas-side film coefficient of 0.003 Btu/in^2-sec-deg F is presented in Fig. A-2.

On the basis of these thermal calculation results variations in the geometric throat plane resulting from the following causes were analyzed.

1. Thermo-elastic-plastic deformation which occurs as a result of the steep temperature gradients near the nozzle surface.

2. Thermal growth of the entire nozzle block arising from its average temperature increase (considered separately from the steep temperature gradient zone).

3. Deflections resulting from the variable combustion gas static pressure loading acting normal to the nozzle surfaces.

(U) The deflections arising from the above three causes were calculated separately. The total throat area change was obtained by superimposing the results of the three analyses.

Thermo-Elastic-Plastic Deformation

(U) From the general equation for total strain we have:

$$\epsilon_T = \epsilon_E + \epsilon_p + \epsilon_{Th} \qquad (1)$$

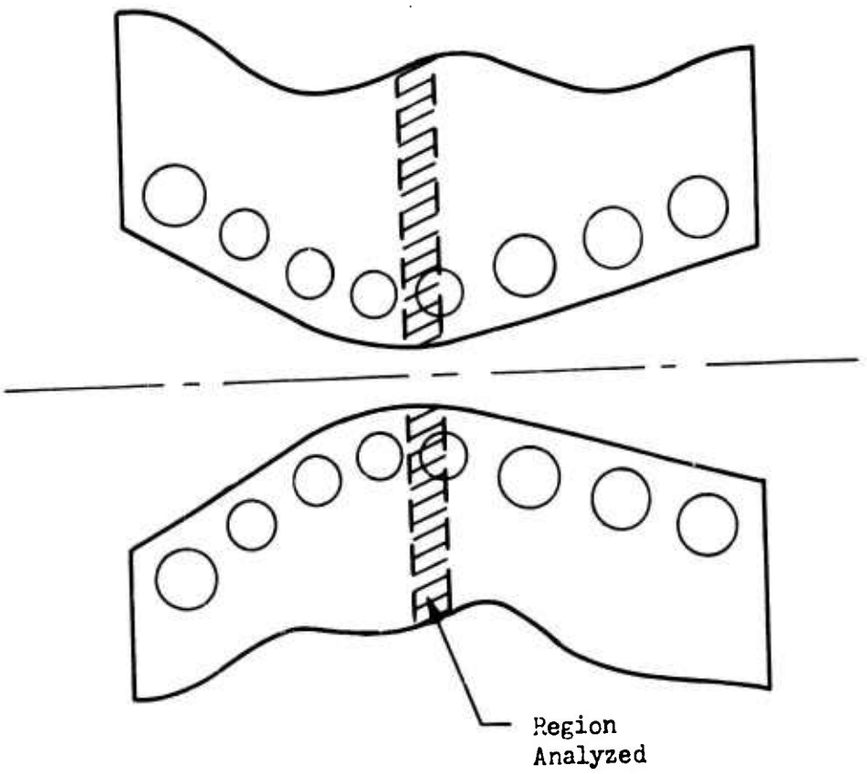

Figure A-1. Throat Region Geometry for Water-Cooled Copper Segment

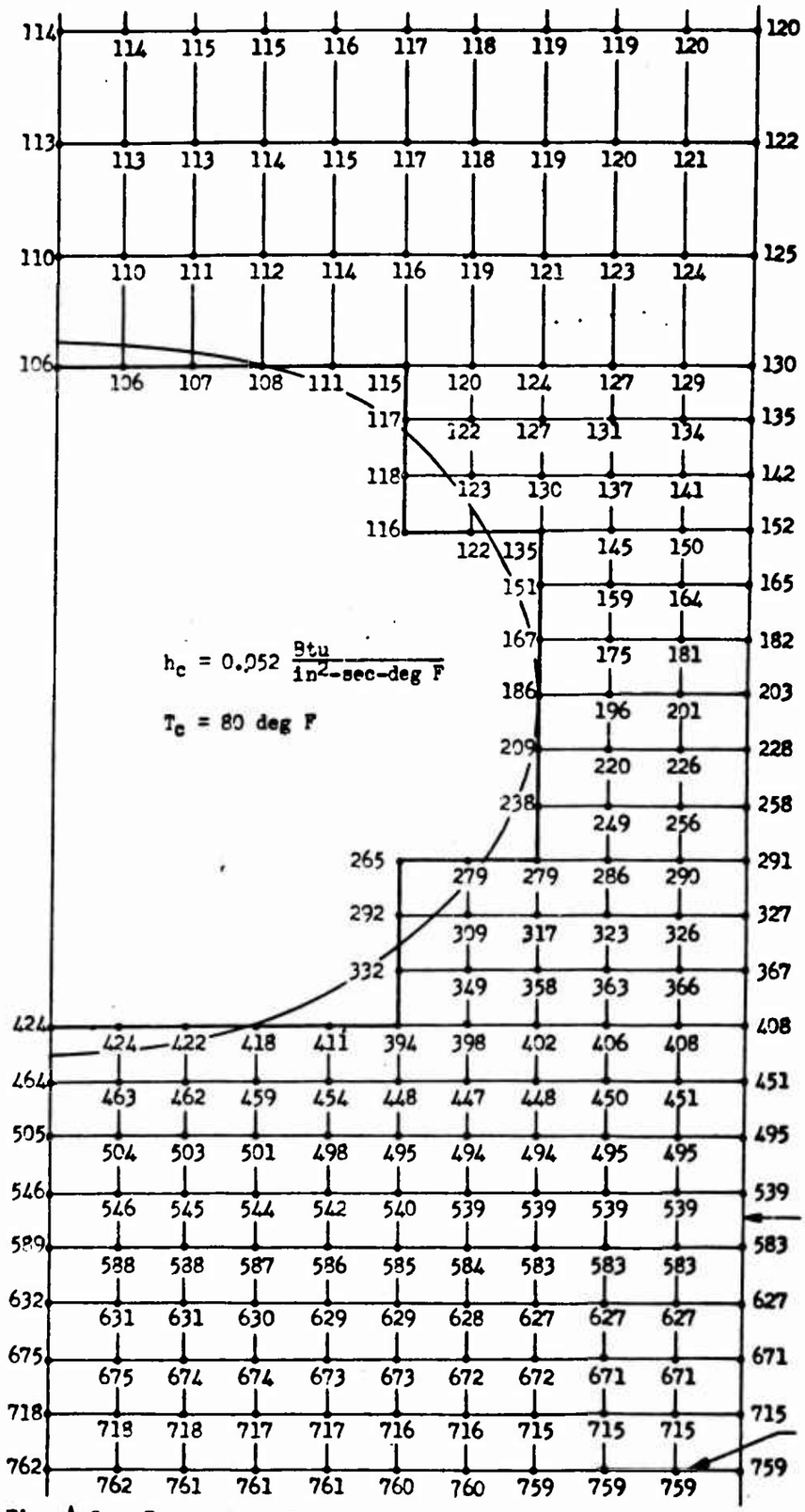

Fig. A-2. Temperature Distribution in Throat Region of Water-Cooled Copper Segment - hg = 0.003 $\frac{Btu}{in^2\text{-sec-deg F}}$

Which simply states that the total strain is the sum of the elastic, plastic and thermal strain components. The first and last terms of Eq (1) may be treated as reversible. The second term is ordinarily considered as irreversible; however, for this case, it will be found that reverse plastic flow occurs as a result of temperature decay at cutoff, although not in a completely reversible manner.

(U) Considering the first term of Eq (1), the elastic strain component, we have from the general equations of elastic strain

$$\epsilon_x = (\sigma_x - \mu \sigma_y - \mu \sigma) / E \qquad (2)$$

$$\epsilon_y = (\sigma_y - \mu \sigma_x - \mu \sigma_z) / E \qquad (3)$$

$$\epsilon_z = (\sigma_z - \mu \sigma_y - \mu \sigma_x) / E \qquad (4)$$

where the relationship between stress and strain is linear. Since we shall find that the thermal gradients induce stresses far in excess of the elastic limit, a similar set of equations for plastic strain would be desirable. However, the non-linearity of the relationship between tensile plastic strain and stress make this difficult.

(U) One analytical technique which has been devised to overcome this problem is based on the assumption of a linear relationship between the octahedral shear stress and plastic strain. While the derivation of the desired linear plastic strain equations will not be given here, Ref. 12 shows how the equations which are developed by the above assumption are given by

$$\epsilon_{xp} = (\sigma_x - \mu_p \sigma_y - \mu_p \sigma_z) / E_{sec} \qquad (5)$$

$$\epsilon_{yp} = (\sigma_y - \mu_p \sigma_x - \mu_p \sigma_z) / E_{sec} \qquad (6)$$

$$\epsilon_{zp} = (\sigma_z - \mu_p \sigma_y - \mu_p \sigma_x) / E_{sec} \qquad (7)$$

(U) where E_{sec} is the secant modulus of elasticity taken from the tensile-stress-strain diagram for plastic strain only. This diagram must be entered at an effective stress $\bar{\sigma}$ which represents the stress resulting from combined multiaxial load.

(U) To determine $\bar{\sigma}$ in terms of the principal stresses, the following assumption is made: The degree of plastic action was governed by the plastic strain energy involved.
The resulting equation for the effective stress $\bar{\sigma}$, as derived in Ref. 12, is

$$\bar{\sigma} = \sqrt{(\sigma_x - \sigma_y)^2 + (\sigma_x - \sigma_z)^2 + (\sigma_y - \sigma_z)^2}/\sqrt{2} \qquad (8)$$

(U) When the three principal stresses are known, it is then possible to calculate the plastic strains by the following steps:

1. Calculate the effective stress $\bar{\sigma}$ from Eq (8).
2. Enter the plastic stress-strain diagram for simple tension at this value of $\bar{\sigma}$ and determine E_{sec}.
3. Use this value of E_{sec} in Eq's 5, 6, and 7 together with a value of $\mu_p = 1/2$ (Poisson's ratio for ideal plastic flow).

(U) The above method is based on the deformation theory of plasticity, and is frequently used in problems of this nature because of the simplification arising from the linearized assumptions.

(U) The solution to the present problem is complicated by the steep temperature gradients which result in variable thermal strains and material properties, and a complex cross-sectional shape. In order to accomplish a practical solution, an analytical model was established which divided the steep temperature gradient zone into a series of flat plate elements of assumed constant elevated temperature and material properties. The thermo-elastic-plastic deformation of each plate element was then calculated, based on the principal stresses. While this technique does not account for shear stresses and resulting strains which may develop in the x y plane between adjacent elements, these strains induce relatively small strains in the z direction.

(U) The principal stresses in this case were seen to be the result of restraints against thermal growth imposed by the material surrounding the plate elements. Because of the complex geometric shape, the technique used was to estimate the maximum and minimum restraints in three dimensions for each element. The deformations normal to the nozzle surface arising from these maximum and minimum restraint conditions were then calculated for each element and added for the total deformation at the surface, resulting in a maximum and minimum total deformation.

(U) All of the restraint conditions may be described as either uniaxial restraint

$$\sigma_y = \sigma_z = 0, \qquad \sigma_x = f(\epsilon_x) \tag{9}$$

or biaxial restraint

$$\sigma_z = 0, \ \sigma_x = f(\epsilon_x) = \sigma_y = f(\epsilon_y) \tag{10}$$

(U) Substituting either of the stress states (9 and 10) into Eq (8), we find that in both cases,

$$\bar{\sigma} = \sigma_x \text{ or } \bar{\sigma} = \sigma_x = \sigma_y \tag{11}$$

or that the effective stress $\bar{\sigma}$ for either of the assumed restraint conditions is equal to the principal stress (this is unique to these two conditions). Circumstance (11) then affords a further simplification of the analysis. Starting with the basic relationship (1) the total strain in the z direction, (normal to the nozzle surface)

$$\epsilon_{z_T} = \epsilon_{z_E} + \epsilon_{z_p} + \epsilon_{z_{Th}} \tag{12}$$

(U) Substituting values of ϵ_{z_E} and ϵ_{z_p} from Eq's (4) and (7)

$$\epsilon = (\sigma_z - \mu\sigma_x - \mu\sigma_y)/E + (\sigma_z - \mu_p\sigma_x - \mu_p\sigma_y)/E_{sec} + \epsilon_{z_{T_h}} \tag{13}$$

(U) Considering the stress state for uniaxial restraint, (10), and substituting in (13)

$$\epsilon_{z_T} = (-\mu\sigma_x)/E - (\mu_p\sigma_x)/E_{sec} + \epsilon_{z_{Th}} \tag{14}$$

(U) Similarly, for biaxial restraint conditions (11)

$$\epsilon_{z_T} = -2\mu\sigma_x/E - 4\mu_p\sigma_x/E_{sec} + \epsilon_{z_{Th}} \tag{15}$$

(U) A relationship between E_{sec} and σ was obtained from the tensile stress-strain diagram. By previous identity,

$$E_{sec} = \bar{\sigma} / \epsilon_p = \bar{\sigma} / (\epsilon_T - \frac{\sigma}{E}) \tag{16}$$

(U) Since $\bar{\sigma} = \sigma$ for the two assumed conditions of restraint,

$$E_{sec} = \sigma/(\epsilon_T - \frac{\sigma}{E}) = \sigma/(\epsilon E - \sigma) \tag{17}$$

(U) Substituting this value for E_{sec} in Eq (14) and adding the appropriate subscripts,

$$\epsilon_z = -\mu\sigma/E - \mu_p\sigma(\epsilon_x E - \sigma_x)/E\epsilon + \epsilon_{z_{Th}} \tag{18}$$

simplifying

$$\epsilon_z = -[\mu\sigma_x + \mu_p(\epsilon_x E - \sigma_x)]/E + \epsilon_{z_{Th}} \tag{19}$$

(U) Similarly, for biaxial restraint conditions

$$\epsilon_z = -\left[2\mu\sigma_x + 4\mu_p\left(\epsilon_x E - \sigma_x\right)\right]/E + \epsilon_{z_{Th}} \qquad (20)$$

(U) Equations 19 and 20 express the total strain normal to the surface of each element in terms of known quantities, and include the effects of continuing elastic volume dilatation during non-ideal plastic flow.

(U) For computation purposes, the following values were used in Eq's (19) and (20):

$\mu = 1/3$

$\mu_p = 1/2$

$\sigma_x = f(\epsilon, T)$ taken from the tensile stress-strain curve at the average temperature of the element, at the appropriate value of ϵ_{x_T}

$\epsilon_{x_T} = -\alpha\Delta T$, taken from absolute expansion data

$\epsilon_{z_{Th}} = \alpha\Delta T$, taken from absolute expansion data

ΔT= the average temperature rise of each plate element above the steady state temperature of the nozzle block. This was obtained by numerically averaging the temperature over the cross section of each element.

(U) The resulting thermo-elastic-plastic deformation was calculated for both throat sides and the throat area variations plotted in Fig. 28.

Thermal Growth of the Entire Nozzle Block and Pressure Effects

(C) The thermal analysis results indicated that the copper temperature at the cold side of the water passages was in the order of 120 F for hg = 0.003 Btu/in^2-sec-F. Because of the very high thermal conductivity of the copper this temperature is fairly constant over the entire nozzle block (behind the water passages to the ambient surface). A gross temperature rise of this magnitude (approximately 50F) would affect the throat area by approximately 0.1 percent.
The effect of 650 psia chamber pressure on the throat area was found to be even less significant than the effect of copper block temperature rise.

APPENDIX B

SOLID WALL SEGMENT BASE PRESSURE MEASUREMENTS

(U) The determination of performance based on thrust measurement requires consideration of base pressure effects on the segment. This effect can lead to errors in the measured thrust values.

(C) A diagram of the base of the engine showing the aft closure ring and the angular position nomenclature is presented in Fig. B-1. Extensive data were accumulated on the pressure difference with respect to ambient pressure at various locations on the base for different thrust levels. The data are presented in Table B-1 and indicated that the base pressure was quite small, especially with the 15-degree exit angle nozzle where the lower values approached the accuracy of the measurements. The pressure on the base of the ring was found to be approximately-0.03 psi. The data for the 30 degree exit nozzle indicated trends of increasing negative base pressure with increasing chamber pressure and proximity to the nozzle flow field. However, when the data are presented on the basis of a percentage contribution to the thrust, the base pressure effect varied from 0.5 to 1.0 percent with most of the data indicating a thrust reduction of 0.7 ± 0.1 percent resulting from aspiration of the base. Accordingly, the appropriate corrections were applied to the values of measured thrust.

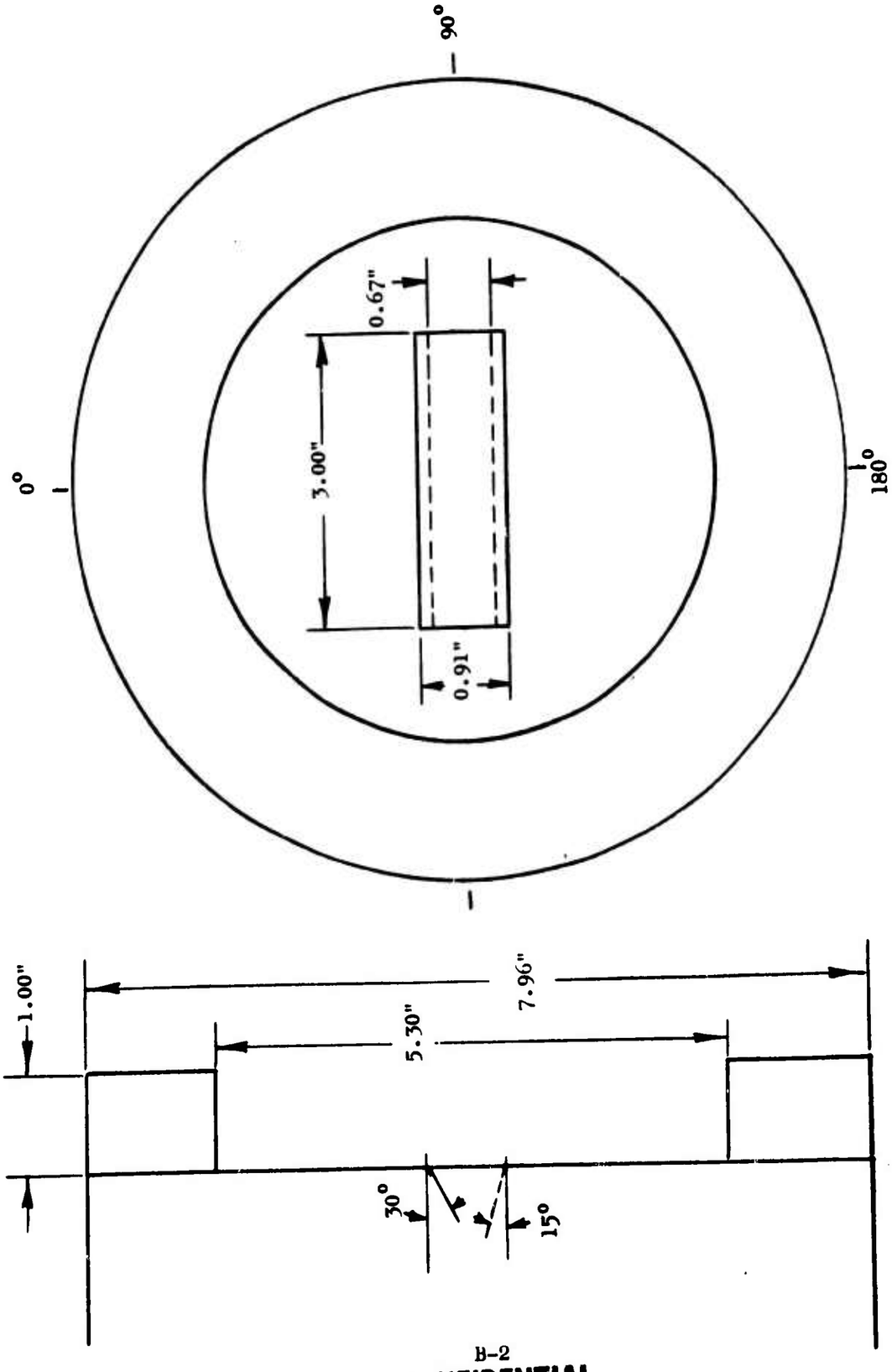

Figure B-1. Solid-Wall Segment Base

TABLE B-1

ENGINE BASE-PRESSURE DATA

Exit Angle deg.	Position Angle Deg.	Position Dist. From ℄, in.	P_c psia	P_{Base} psi (neg.)
15	0	0.75	300	0.05
			410	0.05
			360	0.05
			440	0.05
			420	0.04
15	0	1.5	430	0.02
			300	0.02
			380	0.02
			430	0.03
			480	0.03
			470	0.03
15	0	3.0	450	0.03
30	0	1.5	440	0.08
			460	0.08
30	0	3.0	510	0.05
			300	0.04
			440	0.05
			560	0.05
30	90	3.0	410	0.06
			500	0.07
			600	0.08
			320	0.06
			600	0.08

APPENDIX C

STRUCTURAL WEIGHT EQUATIONS

(U) The variations of skin and core weight with the number of baffles and the backup structure depth are illustrated by reference to the bending and shear stres formulas. The backup structure between baffles acts as a fixed-fixed beam with uniform loading. The maximum bending moments and shear loads occur at the baffles and are given in Eq. (1) and (2) for a unit-width beam. (See nomenclature list at end of Appendix.)

$$M = \frac{pL^2}{12} \tag{1}$$

$$V = \frac{pL}{2} \tag{2}$$

(U) The length of the beam is then inversely proportional to the number of baffles.

$$L = \frac{2\pi R}{N_B} \tag{3}$$

$$M = \frac{\pi^2}{3} R^2 p \frac{1}{N_B^2} \tag{4}$$

$$V = \pi R p \frac{1}{N_B} \tag{5}$$

(U) The variations in bending moments and shear loading are, therefore:

$$\frac{M_2}{M_1} = \left[\frac{N_{B_1}}{N_{B_2}}\right]^2 \tag{6}$$

$$\frac{V_2}{V_1} = \frac{N_{B_1}}{N_{B_2}} \tag{7}$$

(U) For the honeycomb backup structure, the section modulus and bending stress are as given in Eq. (8) and (9) respectively.

$$Z = dt \tag{8}$$

$$\sigma_B = \frac{M}{dt} \tag{9}$$

(U) For a constant bending stress

$$\frac{\sigma_{B_2}}{\sigma_{B_1}} = \frac{M_2}{Z_2} \quad \frac{Z_1}{M_1} = \left[\frac{N_{B_1}}{N_{B_2}}\right]^2 \frac{d_1 t_1}{d_2 t_2} \tag{10}$$

so that the skin thicknesses and resulting weights are given by

$$\frac{W_{T_2}}{W_{T_1}} = \frac{t_2}{t_1} = \left[\frac{N_{B_1}}{N_{B_2}}\right]^2 \frac{d_1}{d_2} \tag{11}$$

(U) The honeycomb design is based upon the critical shear stress

$$F_S^{\,1} = 1.307 \left[\frac{\rho_C^{\,1}}{\rho_C}\right]^{1.34} \frac{F_{SU}}{d^{0.44}} \tag{12}$$

For a given material, the ratio of the critical shear stresses is:

$$\frac{F_{S_2}^{\,1}}{F_{S_1}^{\,1}} = \left[\frac{\rho_{C_2}^{\,1}}{\rho_{C_1}^{\,1}}\right]^{1.34} \left[\frac{d_1}{d_2}\right]^{0.44} \tag{13}$$

The actual shear stress is

$$\frac{F_{S_2}^{1}}{F_{S_1}^{1}} = \frac{V_2}{d_2} \quad \frac{d_1}{V_1} = \frac{N_{B_1}}{N_{B_2}} \quad \frac{d_1}{d_2} \tag{14}$$

Solving Eq. (13) and (14) simultaneously

$$\frac{\rho_{C_2}^{1}}{\rho_{C_1}^{1}} = \left[\frac{N_{B_1}}{N_{B_2}}\right]^{0.75} \left[\frac{d_1}{d_2}\right]^{0.42} \tag{15}$$

(U) The resulting weight variation is then:

$$\frac{W_{T_2}}{W_{T_1}} = \frac{\rho_{C_2}^{1}}{\rho_{C_1}^{1}} \quad \frac{d_2}{d_1} = \left[\frac{N_{B_1}}{N_{B_2}}\right]^{0.75} \left[\frac{d_2}{d_1}\right]^{0.58} \tag{16}$$

APPENDIX D

STRUCTURAL ANALYSIS METHOD

1. SPACE FRAME ANALYSIS

(U) The thrust chamber outer body was idealized as a 3-dimensional gridwork of (beam-like) members and rigid bodies. Chamber pressure loads were simulated by applying equivalent forces and moments at the intersection of the members (node points). The individual members and rigid bodies were assembled into the equivalent structure utilizing the stiffness method, i.e., nodal equilibrium equations were written. The resulting stiffness matrix was inverted and the nodal displacements determined. The nodal displacements were then utilized to determine the individual member reactions. Many books and papers have been published on this method of analysis (Ref. 6 through 8).

(U) The following is a brief outline of the method and a description of the analysis computer program as used at Rocketdyne:

(U) All six degrees of freedom are allowed for each nodal point. Three-dimensional structures can be analyzed. The members must be of doubly symmetric cross section, but the principal axes of the section may be arbitrarily oriented. The influence of shear deformation and rigid bodies can be included in the analysis. The entire analysis has been programmed for the IBM system/360 Model 40-65 computers.

The forces and displacements of each member are referred to the member and the common axis systems:

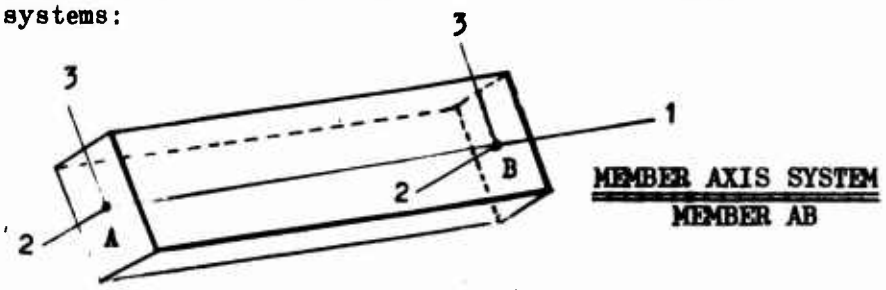

MEMBER AXIS SYSTEM
MEMBER AB

(U) The member 1-axis is the elastic line of the member, the 2 and 3-axes are along the principal axes of the cross section of the member. Each member and member axis system is referred to a common orthogonal axis system.

(U) The forces and displacements at each end (Nodes A and B) of member AB are expressed as the (12 × 1) column vectors $\{F\}_M$ and $\{U\}_M$

$$\{F\}_M = \begin{Bmatrix} F_1^A \\ F_2^A \\ F_3^A \\ M_1^A \\ M_2^A \\ M_3^A \\ F_1^B \\ F_2^B \\ F_3^B \\ M_1^B \\ M_2^B \\ M_3^B \end{Bmatrix}_M \quad \text{and} \quad \{U\}_M = \begin{Bmatrix} U_1^A \\ U_2^A \\ U_3^A \\ \Theta_1^A \\ \Theta_2^A \\ \Theta_3^A \\ U_1^B \\ U_2^B \\ U_3^B \\ \Theta_1^B \\ \Theta_2^B \\ \Theta_3^B \end{Bmatrix}_M$$

where

F_1^A, F_1^B = Component of node force at A and B along the member i axis.

M_1^A, M_1^B = Component of node moment at A and B along the member i axis.

U_1^A, U_1^B = Component of node displacement at A and B along the member i axis.

Θ_1^A, Θ_1^B = Component of node rotation at A and B along the member i axis.

(U) The member forces and displacements are related by the (12 x 12) member stiffness matrix k_M, i.e.

$$\left\{ F \right\}_M = \left[k \right]_M \left\{ U \right\}_M$$

where

$$\begin{bmatrix} k_{11} & k_{12} \cdots & k_{112} \\ \vdots & & \vdots \\ k_{121} \cdots & & k_{1212} \end{bmatrix}_M$$

= (12 x 12) symmetric member stiffness matrix which relates forces and moments referred to member axis system.

(U) These member stiffness matrices are derived for all the members joining node points or joining rigid bodies.

$$\left\{ F \right\}_{M_1} = \left[k \right]_{M_1} \left\{ U \right\}_{M_1}$$

$$\left\{ F \right\}_{M_2} = \left[k \right]_{M_2} \left\{ U \right\}_{M_2}$$

N = No. of members

$$F_{M_N} = \left[k \right]_{M_N} \left\{ U \right\}_{M_N}$$

(U) The vector rotation transformation matrix which relates the member axis system to the common axis system is used to express the member forces and displacements as components along the common axis system.

Let

$$\{X\}_C = [\lambda]\{X\}_M$$

$\{X\}_C$ = (3 x 1) any vector referred to common axis system

$\{X\}_M$ = (3 x 1) same vector referred to member axis system

$[\lambda]$ = (3 x 3) rotation transformation matrix of direction cosines between the common and member axes.

(U) Then the force and displacement vectors for the Nth member can be referred to the common co-ordinate system by

$$\{F\}_C = [T]\{F\}_M \quad \text{or} \quad \{F\}_M = [T]^{-1}\{F\}_C$$

and $$\{U\}_C = [T]\{U\}_M \quad \text{or} \quad \{U\}_M = [T]^{-1}\{U\}_C$$

where $$[T] = \begin{bmatrix} [\lambda] & & 0 \\ & [\lambda] & \\ 0 & & [\lambda] \end{bmatrix}$$ = (12 x 12) member transformation matrix

(U) Then the member force-displacement relationship can be written

$$\{F\}_M = [k]_M \{U\}_M$$

or

$$[T]^{-1} \{F\}_c = [k]_M [T]^{-1} \{U\}_c$$

or

$$\{F\}_c = [T] [k] [T]^{-1} \{U\}_c$$

but $[T]$ is orthogonal, therefore

$$[T]^{-1} = [T]^T$$

and the member force-displacement relationship, referred to the common axis system, becomes

$$\{F\}_c = [T] [k] [T]^T \{U\}_c$$

which is rewritten as

$$\{F\}_c = [k]_a \{U\}_c$$

where

$$[k]_c = [T]\,[K]_M\,[T]^T$$

= Member stiffness matrix referred to common axis system.

(U) The member stiffness matrices referred to the common axis system are computed for members 1 through N:

$$[k]_{c_1} = [T]_1\,[k]_{M_1}\,[T]_1^T$$

$$[k]_{c_2} = [T]_2\,[k]_{M_2}\,[T]_2^T$$

$$\vdots \qquad\qquad \vdots$$

$$[k]_{c_N} = [T]_N\,[k]_{M_N}\,[T]_N^T$$

(U) The total structure stiffness matrix for the system is constructed from those (12 x 12) member stiffnesses by summing components at the nodes and is defined as

$$[K_T]_{(N \times N)}$$

(U) The force-displacement relation for the entire structure is now expressible as

$$\underset{N \times 1}{\{F_T\}} \qquad \underset{N \times N}{[K_T]} \qquad \underset{N \times 1}{\{U_T\}}$$

As the matrix K_T is now formed, it is singular (i.e., DET K_T = 0) and the matrix equation has only trivial solutions. When the boundary conditions are applied (and the corresponding rows and columns of K_T removed) the unknown displacements can be found by inversion of the reduced K_T matrix

$$\{U\} = [K_T]^{-1} \{F\}$$

Reduced non-singular system of equations...

(U) The inversion of the reduced $[K_T]$ matrix is performed by using the square-root (Choleski's) method, where the given system

$$\{F\} = [K_T]\{U\}$$

is replaced by the system

$$\left.\begin{aligned} [S]^T \{A\} &= \{F\} \\ [S]\{U\} &= \{A\} \end{aligned}\right\}$$ equivalent system

i.e.

$$[K] = [S]^T [S]$$

Where

[S] = Triangular matrix

(U) When the displacements are known, the forces and stress resultants with respect to the member axis system are calculated.

2. APPLICATION TO STRUCTURAL SEGMENTS

(U) The thrust chamber outer body segment was idealized as a space gridwork of beam-like members. The injector, baffles, and end plates were assumed to displace as rigid bodies. The rigid bodies were supported by members whose stiffness match the geometric dimensions of the injector, baffle and end plate.

(U) The member section properties were calculated from drawing dimensions of the rib and honeycomb segments. In the analysis of the rib-type structure, the longitudinal members were assumed to have "I" beam-type sections. The transverse members were assumed to have only the combined skin section properties. In the analysis of the honeycomb segment, the members were assumed to be of rectangular cross section with the outer skins carrying the direct and bending axial loads. The properties of these members are given in Tables D-1 and D-2. The numbers refer to points shown in Fig. 126. A more rigorous method for determining equivalent section properties for plane and plate structures is given in Ref. 10 and 11.

(U) Shear deformation was considered for the members, where shear deformation factors of 1.00 and 1.20 were assumed for the "I"-type members and the rectangular members, respectively. Shear deformation is the deflection (besides the bending moment induced deflection) which is imposed by shear forces:

$$U_s = a \int \frac{1}{AG} \frac{\partial U}{\partial V} \quad V \, dx$$

where

$\frac{U}{V}$ = Deflection due to unit shear load, V = 1 lb., and U = strain energy of the member.

A = Cross sectional area

G = Shear modulus (Lamé's parameter)

V = Applied shear force

a = Shear deformation factor

(U) Because the bolts used to tie the baffle sections together were preloaded the stiffness of the baffle support member used in the analysis was modified. This was done by calculating an equivalent modulus for the member.

TABLE D-1

RIB STRUCTURE MEMBER SECTION PROPERTIES

MEMBER END A	MEMBER END B	AREA	INPUT AND CALCULATED STRAIGHT MEMBER PROPERTIES YOUNGS MODULUS	SHEAR MODULUS	2 MOMENT OF INERTIA	3 MOMENT OF INERTIA	TORSIONAL CONSTANT	2 SHEAR FACTOR	3 SHEAR FACTOR
4	5	9.5999956E-02	29.00E 06	11.15E 06	1.2799999E-05	1.1519998E-02	1.1519998E-02	1.20000	1.20000
5	6	9.5999956E-02	29.00E 06	11.15E 06	1.2799999E-05	1.1519998E-02	1.1519998E-02	1.20000	1.20000
6	7	9.5999956E-02	29.00E 06	11.15E 06	1.2799999E-05	1.1519998E-02	1.1519998E-02	1.20000	1.20000
7	8	9.5999956E-02	29.00E 06	11.15E 06	1.2799999E-05	1.1519998E-02	1.1519998E-02	1.20000	1.20000
8	9	9.5999956E-02	29.00E 06	11.15E 06	1.2799999E-05	1.1519998E-02	1.1519998E-02	1.20000	1.20000
9	-37	9.5999956E-02	29.00E 06	11.15E 06	1.279[illegible]9E-05	1.1519998E-02	1.1519998E-02	1.20000	1.20000
10	11	8.8000000E-02	29.00E 06	11.15E 06	1.1700[illegible]E-05	8.9499988E-03	8.9499988E-03	1.20000	1.20000
11	12	8.8000000E-02	29.00E 06	11.15E 06	1.170000 -05	8.9499988E-03	8.9499988E-03	1.20000	1.20000
12	13	8.8000000E-02	29.00E 06	11.15E 06	1.170000[illegible] 05	8.9499988E-03	8.9499988E-03	1.20000	1.20000
13	14	8.8000000E-02	29.00E 06	11.15E 06	1.1700[illegible] 5	8.9499988E-03	8.9499988E-03	1.20000	1.20000
14	15	8.8000000E-02	29.00E 06	11.15E 06	1.170000[illegible]	8.9499988E-03	8.9499988E-03	1.20000	1.20000
15	-38	8.8000000E-02	29.00E 06	11.15E 06	1.1700000E-05	8.9499988E-03	8.9499988E-03	1.20000	1.20000
16	17	8.8000000E-02	29.00E 06	11.15E 06	1.1700000E-05	8.9499988E-03	8.9499988E-03	1.20000	1.20000
17	18	8.8000000E-02	29.00E 06	11.15E 06	1.1700000E-05	8.9499988E-03	8.9499988E-03	1.20000	1.20000
18	19	8.8000000E-02	29.00E 06	11.15E 06	1.1700000E-05	8.9499988E-03	8.9499988E-03	1.20000	1.20000
19	20	8.8000000E-02	29.00E 06	11.15E 06	1.1700000E-05	8.9499988E-03	8.9499988E-03	1.20000	1.20000
20	21	8.8000000E-02	29.00E 06	11.15E 06	1.1700000E-05	8.9499988E-03	8.9499988E-03	1.20000	1.20000
21	-39	8.8000000E-02	29.00E 06	11.15E 06	1.1700000E-05	8.9499988E-03	8.9499988E-03	1.20000	1.20000
22	23	3.8399994E-01	29.00E 06	11.15E 06	5.1999997E-02	5.9199996E-02	6.3399971E-02	1.00000	1.00000
23	24	4.3049997E-01	29.00E 06	11.15E 06	8.7759972E-02	5.9199996E-02	1.1639994E-01	1.00000	1.00000
24	-43	4.4999999E-01	29.00E 06	11.15E 06	1.0535997E-01	7.4439943E-02	1.3849998E-01	1.00000	1.00000
25	26	2.3299998E-01	29.00E 06	11.15E 06	3.0999989E-05	1.6499996E-01	1.6499996E-01	1.20000	1.20000
26	27	2.3299998E-01	29.00E 06	11.15E 06	3.0999989E-05	1.6499996E-01	1.6499996E-01	1.20000	1.20000
27	28	2.3299998E-01	29.00E 06	11.15E 06	3.0999989E-05	1.6499996E-01	1.6499996E-01	1.20000	1.20000
28	29	2.3299998E-01	29.00E 06	11.15E 06	3.0999989E-05	1.6499996E-01	1.6499996E-01	1.20000	1.20000
29	30	2.3299998E-01	29.00E 06	11.15E 06	3.0999989E-05	1.6499996E-01	1.6499996E-01	1.20000	1.20000
30	-49	2.3299998E-01	29.00E 06	11.15E 06	3.0999989E-05	1.6499996E-01	1.6499996E-01	1.20000	1.20000
31	32	2.3299998E-01	29.00E 06	11.15E 06	3.0999989E-05	1.6499996E-01	1.6499996E-01	1.20000	1.20000
32	33	2.3299998E-01	29.00E 06	11.15E 06	3.0999989E-05	1.6499996E-01	1.6499996E-01	1.20000	1.20000
33	34	2.3299998E-01	29.00E 06	11.15E 06	3.0999989E-05	1.6499996E-01	1.6499996E-01	1.20000	1.20000
34	35	2.3299998E-01	29.00E 06	11.15E 06	3.0999989E-05	1.6499996E-01	1.6499996E-01	1.20000	1.20000
35	36	2.3299998E-01	29.00E 06	11.15E 06	3.0999989E-05	1.6499996E-01	1.6499996E-01	1.20000	1.20000
36	-50	2.3299998E-01	29.00E 06	11.15E 06	3.0999989E-05	1.6499996E-01	1.6499996E-01	1.20000	1.20000
4	10	8.1999958E-02	29.00E 06	11.15E 06	8.0799982E-03	2.1299999E-03	4.4699991E-05	1.00000	1.00000
10	16	8.1999958E-02	29.00E 06	11.15E 06	8.0799982E-03	2.1299999E-03	4.4699991E-05	1.00000	1.00000
16	22	8.1999958E-02	29.00E 06	11.15E 06	8.0799982E-03	2.1299999E-03	4.4699991E-05	1.00000	1.00000
22	25	8.1999958E-02	29.00E 06	11.15E 06	8.0799982E-03	2.1299999E-03	4.4699991E-05	1.00000	1.00000
25	31	8.1999958E-02	29.00E 06	11.15E 06	8.0799982E-03	2.1299999E-03	4.4699991E-05	1.00000	1.00000
31	-51	8.1999958E-02	29.00E 06	11.15E 06	8.0799982E-03	2.1299999E-03	4.4699991E-05	1.00000	1.00000
5	11	8.3999991E-02	29.00E 06	11.15E 06	1.6025998E-02	8.3999988E-04	4.7999987E-05	1.00000	1.00000

TABLE D-1 (CONT'D)

RIB STRUCTURE MEMBER SECTION PROPERTIES

11	17	8.3999991E-02	29.00E 06	11.15E 06	1.6025998E-02	8.3999988E-04	4.7999987E-05	1.00000	1.00000
17	23	8.3999991E-02	29.00E 06	11.15E 06	1.6025998E-02	8.3999988E-04	4.7999987E-05	1.00000	1.00000
23	26	8.3999991E-02	29.00E 06	11.15E 06	1.6025998E-02	8.3999988E-04	4.7999987E-05	1.00000	1.00000
26	32	8.3999991E-02	29.00E 06	11.15E 06	1.6025998E-02	8.3999988E-04	4.7999987E-05	1.00000	1.00000
32	-52	8.3999991E-02	29.00E 06	11.15E 06	1.6025998E-02	8.3999988E-04	4.7999987E-05	1.00000	1.00000
6	12	8.8499963E-02	29.00E 06	11.15E 06	2.1175999E-02	8.3999988E-04	4.9499999E-05	1.00000	1.00000
12	18	8.8499963E-02	29.00E 06	11.15E 06	2.1175999E-02	8.3999988E-04	4.7999987E-05	1.00000	1.00000
18	24	8.8499963E-02	29.00E 06	11.15E 06	2.1175999E-02	8.3999988E-04	4.9499999E-05	1.00000	1.00000
24	27	8.8499963E-02	29.00E 06	11.15E 06	2.1175999E-02	8.3999988E-04	4.9499999E-05	1.00000	1.00000
27	33	8.8499963E-02	29.00E 06	11.15E 06	2.1175999E-02	8.3999988E-04	4.9499999E-05	1.00000	1.00000
33	-53	8.8499963E-02	29.00E 06	11.15E 06	2.1175999E-02	8.3999988E-04	4.9499999E-05	1.00000	1.00000
7	13	2.5559998E-01	29.00E 06	11.15E 06	6.0099997E-02	3.9069999E-02	8.7199995E-05	1.00000	1.00000
13	19	2.5559998E-01	29.00E 06	11.15E 06	6.0099997E-02	3.9069999E-02	8.7199995E-05	1.00000	1.00000
19	-40	2.5559998E-01	29.00E 06	11.15E 06	6.0099997E-02	3.9069999E-02	8.7199995E-05	1.00000	1.00000
-46	28	2.5559998E-01	29.00E 06	11.15E 06	6.0099997E-02	3.9069999E-02	8.7199995E-05	1.00000	1.00000
28	34	2.5559998E-01	29.00E 06	11.15E 06	6.0099997E-02	3.9069999E-02	8.7199995E-05	1.00000	1.00000
34	-54	2.5559998E-01	29.00E 06	11.15E 06	6.0099997E-02	3.9069999E-02	8.7199995E-05	1.00000	1.00000
8	14	9.8499954E-02	29.00E 06	11.15E 06	2.4766997E-02	1.8300000E-03	5.4799995E-05	1.00000	1.00000
14	20	9.8499954E-02	29.00E 06	11.15E 06	2.4766997E-02	1.8300000E-03	5.4799995E-05	1.00000	1.00000
20	-41	9.8499954E-02	29.00E 06	11.15E 06	2.4766997E-02	1.8300000E-03	5.4799995E-05	1.00000	1.00000
-47	29	9.8499954E-02	29.00E 06	11.15E 06	2.4766997E-02	1.8300000E-03	5.4799995E-05	1.00000	1.00000
29	35	9.8499954E-02	29.00E 06	11.15E 06	2.4766997E-02	1.8300000E-03	5.4799995E-05	1.00000	1.00000
35	-55	9.8499954E-02	29.00E 06	11.15E 06	2.4766997E-02	1.8300000E-03	5.4799995E-05	1.00000	1.00000
9	15	1.9679999E-01	29.00E 06	11.15E 06	4.9619999E-02	2.0869996E-02	8.1499995E-05	1.00000	1.00000
15	21	1.9679999E-01	29.00E 06	11.15E 06	4.9619999E-02	2.0869996E-02	8.1499995E-05	1.00000	1.00000
21	-42	1.9679999E-01	29.00E 06	11.15E 06	4.9619999E-02	2.0869996E-02	8.1499995E-05	1.00000	1.00000
-48	30	1.9679999E-01	29.00E 06	11.15E 06	4.9619999E-02	2.0869996E-02	8.1499995E-05	1.00000	1.00000
30	36	1.9679999E-01	29.00E 06	11.15E 06	4.9619999E-02	2.0869996E-02	8.1499995E-05	1.00000	1.00000
36	-56	1.9679999E-01	29.00E 06	11.15E 06	4.9619999E-02	2.0869996E-02	8.1499995E-05	1.00000	1.00000
-60	-61	1.9499998E 00	29.00E 06	11.15E 06	8.5699999E-01	1.6249996E-01	1.0194998E 00	1.20000	1.20000
-58	-59	1.4599991E 00	29.00E 06	11.15E 06	6.4199996E-01	8.3099961E-02	7.2509998E-01	1.20000	1.20000
3	-57	2.9299994E 00	29.00E 06	11.15E 06	4.0259991E 00	1.6679996E-01	4.1693993E 00	1.20000	1.20000
2	-44	1.5400000E 00	83.80E 05	32.20E 05	9.8999995E-01	3.9399996E-02	1.0293999E 00	1.20000	1.20000
1	-45	1.9799995E 00	29.00E 06	11.15E 06	6.6299997E-03	2.1589996E 01	2.1589996E 01	1.20000	1.20000

NOTE....IF ZERO INERTIAS ARE ASSIGNED, PRINTED SOLUTIONS FOR CORRESPONDING ROTATIONS ARE WITHOUT VALUE.

TABLE D-2

HONEYCOMB STRUCTURE MEMBER SECTION PROPERTIES

INPUT AND CALCULATED STRAIGHT MEMBER PROPERTIES

MEMBER END A	MEMBER END B	AREA	YOUNG'S MODULUS	SHEAR MODULUS	2 MOMENT OF INERTIA	3 MOMENT OF INERTIA	TORSIONAL CONSTANT	2 SHEAR FACTOR	3 SHEAR FACTOR
4	5	9.5999956E-02	29.00E 06	11.15E 06	1.2799999E-05	1.1519998E-02	1.1519998E-02	1.20000	1.20000
5	6	9.5999956E-02	29.00E 06	11.15E 06	1.2799999E-05	1.1519998E-02	1.1519998E-02	1.20000	1.20000
6	7	9.5999956E-02	29.00E 06	11.15E 06	3.5299998E-02	1.1519998E-02	4.6820000E-02	1.20000	1.20000
7	8	9.5999956E-02	29.00E 06	11.15E 06	3.5299998E-02	1.1519998E-02	4.6820000E-02	1.20000	1.20000
8	9	9.5999956E-02	29.00E 06	11.15E 06	3.5299998E-02	1.1519998E-02	4.6820000E-02	1.20000	1.20000
9	-37	9.5999956E-02	29.00E 06	11.15E 06	3.5299998E-02	1.1519998E-02	4.6820000E-02	1.20000	1.20000
10	11	8.8000000E-02	29.00E 06	11.15E 06	1.1700000E-05	8.9499988E-03	8.9499988E-03	1.20000	1.20000
11	12	8.8000000E-02	29.00E 06	11.15E 06	1.1700000E-05	8.9499988E-03	8.9499988E-03	1.20000	1.20000
12	13	8.8000000E-02	29.00E 06	11.15E 06	3.6699999E-02	8.9499988E-03	4.5649998E-02	1.20000	1.20000
13	14	8.8000000E-02	29.00E 06	11.15E 06	3.6699999E-02	8.9499988E-03	4.5649998E-02	1.20000	1.20000
14	15	8.8000000E-02	29.00E 06	11.15E 06	3.6699999E-02	8.9499988E-03	4.5649998E-02	1.20000	1.20000
15	-38	8.8000000E-02	29.00E 06	11.15E 06	3.6699999E-02	8.9499988E-03	4.5649998E-02	1.20000	1.20000
16	17	8.8000000E-02	29.00E 06	11.15E 06	1.1700000E-05	8.9499988E-03	8.9499988E-03	1.20000	1.20000
17	18	8.8000000E-02	29.00E 06	11.15E 06	1.1700000E-05	8.9499988E-03	8.9499988E-03	1.20000	1.20000
18	19	8.8000000E-02	29.00E 06	11.15E 06	3.6699999E-02	8.9499988E-03	4.5649998E-02	1.20000	1.20000
19	20	8.8000000E-02	29.00E 06	11.15E 06	3.6699999E-02	8.9499988E-03	4.5649998E-02	1.20000	1.20000
20	21	8.8000000E-02	29.00E 06	11.15E 06	3.6699999E-02	8.9499988E-03	4.5649998E-02	1.20000	1.20000
21	-39	8.8000000E-02	29.00E 06	11.15E 06	3.6699999E-02	8.9499988E-03	4.5649998E-02	1.20000	1.20000
22	23	3.8399994E-01	29.00E 06	11.15E 06	5.1999997E-02	5.9199996E-02	6.3399971E-02	1.00000	1.00000
23	24	4.3049997E-01	29.00E 06	11.15E 06	8.7759972E-02	5.9199996E-02	1.1639994E-01	1.00000	1.00000
24	-43	4.4999999E-01	29.00E 06	11.15E 06	1.0535997E-01	7.4439943E-02	1.3849998E-01	1.00000	1.00000
25	26	2.3299998E-01	29.00E 06	11.15E 06	3.0999989E-05	1.6499996E-01	1.6499996E-01	1.20000	1.20000
26	27	2.3299998E-01	29.00E 06	11.15E 06	3.0999989E-05	1.6499996E-01	1.6499996E-01	1.20000	1.20000
27	28	2.3299998E-01	29.00E 06	11.15E 06	8.3299994E-02	1.6499996E-01	2.4799997E-01	1.20000	1.20000
28	29	2.3299998E-01	29.00E 06	11.15E 06	8.3299994E-02	1.6499996E-01	2.4799997E-01	1.20000	1.20000
29	30	2.3299998E-01	29.00E 06	11.15E 06	8.3299994E-02	1.6499996E-01	2.4799997E-01	1.20000	1.20000
30	-49	2.3299998E-01	29.00E 06	11.15E 06	8.3299994E-02	1.6499996E-01	2.4799997E-01	1.20000	1.20000
31	32	2.3299998E-01	29.00E 06	11.15E 06	3.0999989E-05	1.6499996E-01	1.6499996E-01	1.20000	1.20000
32	33	2.3299998E-01	29.00E 06	11.15E 06	3.0999989E-05	1.6499996E-01	1.6499996E-01	1.20000	1.20000
33	34	2.3299998E-01	29.00E 06	11.15E 06	8.3299994E-02	1.6499996E-01	2.4799997E-01	1.20000	1.20000
34	35	2.3299998E-01	29.00E 06	11.15E 06	8.3299994E-02	1.6499996E-01	2.4799997E-01	1.20000	1.20000
35	36	2.3299998E-01	29.00E 06	11.15E 06	8.3299994E-02	1.6499996E-01	2.4799997E-01	1.20000	1.20000
36	-50	2.3299998E-01	29.00E 06	11.15E 06	8.3299994E-02	1.6499996E-01	2.4799997E-01	1.20000	1.20000
4	10	8.1999958E-02	29.00E 06	11.15E 06	8.0799982E-03	2.1299999E-03	4.4699991E-05	1.00000	1.00000
10	16	8.1999958E-02	29.00E 06	11.15E 06	8.0799982E-03	2.1299999E-03	4.4699991E-05	1.00000	1.00000
16	22	8.1999958E-02	29.00E 06	11.15E 06	8.0799982E-03	2.1299999E-03	4.4699991E-05	1.00000	1.00000
22	25	8.1999958E-02	29.00E 06	11.15E 06	8.0799982E-03	2.1299999E-03	4.4699991E-05	1.00000	1.00000
25	31	8.1999958E-02	29.00E 06	11.15E 06	8.0799982E-03	2.1299999E-03	4.4699991E-05	1.00000	1.00000
31	-51	8.1999958E-02	29.00E 06	11.15E 06	8.0799982E-03	2.1299999E-03	4.4699991E-05	1.00000	1.00000
5	11	8.3999981E-02	29.00E 06	11.15E 06	1.6025998E-02	8.3999988E-04	4.7999987E-05	1.00000	1.00000

TABLE -2(CONT'D)

HONEYCOMB STRUCTURE MEMBER SECTION PROPERTIES

11	17	8.3999991E-02	29.00E 06	11.15E 06	1.6025998E-02	8.3999988E-04	4.7999987E-05	1.00000 1.00000
17	23	8.3999991E-02	29.00E 06	11.15E 06	1.6025998E-02	8.3999988E-04	4.7999987E-05	1.00000 1.00000
23	26	8.3999991E-02	29.00E 06	11.15E 06	1.6025998E-02	8.3999988E-04	4.7999987E-05	1.00000 1.00000
26	32	8.3999991E-02	29.00E 06	11.15E 06	1.6025998E-02	8.3999988E-04	4.7999987E-05	1.00000 1.00000
32	-52	8.3999991E-02	29.00E 06	11.15E 06	1.6025998E-02	8.3999988E-04	4.7999987E-05	1.00000 1.00000
6	12	8.8499963E-02	29.00E 06	11.15E 06	2.1175999E-02	8.3999988E-04	4.9499999E-05	1.00000 1.00000
12	18	8.8499963E-02	29.00E 06	11.15E 06	2.1175999E-02	8.3999988E-04	4.7999987E-05	1.00000 1.00000
18	24	8.8499963E-02	29.00E 06	11.15E 06	2.1175999E-02	8.3999988E-04	4.9499999E-05	1.00000 1.00000
24	27	8.8499963E-02	29.00E 06	11.15E 06	2.1175999E-02	8.3999988E-04	4.9499999E-05	1.00000 1.00000
27	33	8.8499963E-02	29.00E 06	11.15E 06	2.1175999E-02	8.3999988E-04	4.9499999E-05	1.00000 1.00000
33	-53	8.8499963E-02	29.00E 06	11.15E 06	2.1175999E-02	8.3999988E-04	4.9499999E-05	1.00000 1.00000
7	13	1.0549998E-01	29.00E 06	11.15E 06	4.0599998E-02	1.7600000E-02	5.8199998E-02	1.20000 1.20000
13	19	1.0549998E-01	29.00E 06	11.15E 06	4.0599998E-02	1.7600000E-02	5.8199998E-02	1.20000 1.20000
19	-40	1.0549998E-01	29.00E 06	11.15E 06	4.0599998E-02	1.7600000E-02	5.8199998E-02	1.20000 1.20000
-46	28	1.0549998E-01	29.00E 06	11.15E 06	4.0599998E-02	1.7600000E-02	5.8199998E-02	1.20000 1.20000
28	34	1.0549998E-01	29.00E 06	11.15E 06	4.0599998E-02	1.7600000E-02	5.8199998E-02	1.20000 1.20000
34	-54	1.0549998E-01	29.00E 06	11.15E 06	4.0599998E-02	1.7600000E-02	5.8199998E-02	1.20000 1.20000
8	14	9.8499954E-02	29.00E 06	11.15E 06	2.4766997E-02	1.8300000E-03	5.4799995E-05	1.00000 1.00000
14	20	9.8499954E-02	29.00E 06	11.15E 06	2.4766997E-02	1.8300000E-03	5.4799995E-05	1.00000 1.00000
20	-41	9.8499954E-02	29.00E 06	11.15E 06	2.4766997E-02	1.8300000E-03	5.4799995E-05	1.00000 1.00000
-47	29	9.8499954E-02	29.00E 06	11.15E 06	2.4766997E-02	1.8300000E-03	5.4799995E-05	1.00000 1.00000
29	35	9.8499954E-02	29.00E 06	11.15E 06	2.4766997E-02	1.8300000E-03	5.4799995E-05	1.00000 1.00000
35	-55	9.8499954E-02	29.00E 06	11.15E 06	2.4766997E-02	1.8300000E-03	5.4799995E-05	1.00000 1.00000
9	15	9.9999964E-02	29.00E 06	11.15E 06	3.6579996E-02	1.3039999E-02	4.9619999E-02	1.20000 1.20000
15	21	9.9999964E-02	29.00E 06	11.15E 06	3.6579996E-02	1.3039999E-02	4.9619999E-02	1.20000 1.20000
21	-42	9.9999964E-02	29.00E 06	11.15E 06	3.6579996E-02	1.3039999E-02	4.9619999E-02	1.20000 1.20000
-48	30	9.9999964E-02	29.00E 06	11.15E 06	3.6579996E-02	1.3039999E-02	4.9619999E-02	1.20000 1.20000
30	36	9.9999964E-02	29.00E 06	11.15E 06	3.6579996E-02	1.3039999E-02	4.9619999E-02	1.20000 1.20000
36	-56	9.9999964E-02	29.00E 06	11.15E 06	3.6579996E-02	1.3039999E-02	4.9619999E-02	1.20000 1.20000
-60	-61	1.9499999E 00	29.00E 06	11.15E 06	8.5699999E-01	1.6249996E-01	1.0194998E 00	1.20000 1.20000
-58	-59	1.4599991E 00	29.00E 06	11.15E 06	6.4199996E-01	8.3099961E-02	7.2509998E-01	1.20000 1.20000
3	-57	2.9299994E 00	29.00E 06	11.15E 06	4.0259991E 00	1.6679996E-01	4.1693993E 00	1.20000 1.20000
2	-44	1.5400000E 00	83.80E 05	32.20E 05	9.8999995E-01	3.9399996E-02	1.0293999E 00	1.20000 1.20000
1	-45	1.9799995E 00	29.00E 06	11.15E 06	6.6299997E-03	2.1589996E 01	2.1589996E 01	1.20000 1.20000

NOTE....IF ZERO INERTIAS ARE ASSIGNED, PRINTED SOLUTIONS FOR CORRESPONDING ROTATIONS ARE WITHOUT VALUE.

CONFIDENTIAL
Security Classification

DOCUMENT CONTROL DATA - R&D
(Security classification of title, body of abstract and indexing annotation must be entered when the overall report is classified)

1 ORIGINATING ACTIVITY (Corporate author)
Rocketdyne, a Division of North American Aviation, Inc., 6633 Canoga Avenue, Canoga Park, California

2a REPORT SECURITY CLASSIFICATION
CONFIDENTIAL

2b GROUP
4

3 REPORT TITLE
ADVANCED THRUST CHAMBER FOR SPACE MANEUVERING PROPULSION
(Unclassified Title)

4 DESCRIPTIVE NOTES (Type of report and inclusive dates)
Final Report on Tasks II and III

5 AUTHOR(S) (Last name, first name, initial)
Diem, H. G. and Pauckert, R. P.

6 REPORT DATE	7a TOTAL NO OF PAGES	7b NO OF REFS
July 1967	270	12

8a CONTRACT OR GRANT NO.	9a ORIGINATOR'S REPORT NUMBER(S)
AF04(611)-11617	R-6730-1
b. PROJECT NO	
c	9b. OTHER REPORT NO(S) (Any other numbers that may be assigned this report)
d	AFRPL-TR-67-214

10 AVAILABILITY/LIMITATION NOTICES
In addition to security requirements which must be met, this document is subject to special export controls and each transmittal to foreign governments or foreign nationals may be made only with prior approval of AFRPL, Edwards, California 93523

11 SUPPLEMENTARY NOTES	12 SPONSORING MILITARY ACTIVITY
	Air Force Rocket Propulsion Laboratory Research and Technology Division Edwards, California

13 ABSTRACT
An analytical and experimental study was conducted to evaluate the critical design aspects of a toroidal thrust chamber for an aerospike engine using LF_2/LH_2 propellants. Combustion chamber performance, heat transfer characteristics, regenerative cooling capability, and structural integrity were investigated and demonstrated by testing segments of the complete chamber.

The experimental efforts were first conducted with water-cooled segments and resulted in the selection of a near-optimum injector/combustion chamber configuration which was found to give high C* efficiency while maintaining heat transfer rates within the capability of a two-pass regenerative cooling system design. Withdrawal of combustion chamber gases through the injector for turbine drive was also demonstrated. Tube wall segments, designed on the basis of the solid-wall segment test results, demonstrated two-pass regenerative cooling and feed system stability over the 9:1 throttling range. Chamber performance in excess of 99 percent C* efficiency over the throttle range was achieved.

Structural segments, fabricated using lightweight rib and honeycomb support structures, were cycled from 0 to 650 psig using hydraulic pressure to simulate chamber pressure. Analytical and experimental data agreed closely and indicated that throat area variations over the throttling range would be less than 3 percent for chambers using either the rib or honeycomb designs.

DD FORM 1473

CONFIDENTIAL
Security Classification

CONFIDENTIAL
Security Classification

KEY WORDS	LINK A		LINK B		LINK C	
	ROLE	WT	ROLE	WT	ROLE	WT
Fluorine/Hydrogen Propellants						
Advanced Thrust Chamber						
Throttling						
Testing						
Segments						
Heat Transfer						
Performance						

INSTRUCTIONS

1. **ORIGINATING ACTIVITY:** Enter the name and address of the contractor, subcontractor, grantee, Department of Defense activity or other organization *(corporate author)* issuing the report.

2a. **REPORT SECURITY CLASSIFICATION:** Enter the overall security classification of the report. Indicate whether "Restricted Data" is included. Marking is to be in accordance with appropriate security regulations.

2b. **GROUP:** Automatic downgrading is specified in DoD Directive 5200.10 and Armed Forces Industrial Manual. Enter the group number. Also, when applicable, show that optional markings have been used for Group 3 and Group 4 as authorized.

3. **REPORT TITLE:** Enter the complete report title in all capital letters. Titles in all cases should be unclassified. If a meaningful title cannot be selected without classification, show title classification in all capitals in parenthesis immediately following the title.

4. **DESCRIPTIVE NOTES:** If appropriate, enter the type of report, e.g., interim, progress, summary, annual, or final. Give the inclusive dates when a specific reporting period is covered.

5. **AUTHOR(S):** Enter the name(s) of author(s) as shown on or in the report. Enter last name, first name, middle initial. If military, show rank and branch of service. The name of the principal author is an absolute minimum requirement.

6. **REPORT DATE:** Enter the date of the report as day, month, year; or month, year. If more than one date appears on the report, use date of publication.

7a. **TOTAL NUMBER OF PAGES:** The total page count should follow normal pagination procedures, i.e., enter the number of pages containing information.

7b. **NUMBER OF REFERENCES:** Enter the total number of references cited in the report.

8a. **CONTRACT OR GRANT NUMBER:** If appropriate, enter the applicable number of the contract or grant under which the report was written.

8b, 8c, & 8d. **PROJECT NUMBER:** Enter the appropriate military department identification, such as project number, subproject number, system numbers, task number, etc.

9a. **ORIGINATOR'S REPORT NUMBER(S):** Enter the official report number by which the document will be identified and controlled by the originating activity. This number must be unique to this report.

9b. **OTHER REPORT NUMBER(S):** If the report has been assigned any other report numbers *(either by the originator or by the sponsor)*, also enter this number(s).

10. **AVAILABILITY/LIMITATION NOTICES:** Enter any limitations on further dissemination of the report, other than those imposed by security classification, using standard statements such as:

(1) "Qualified requesters may obtain copies of this report from DDC."

(2) "Foreign announcement and dissemination of this report by DDC is not authorized."

(3) "U. S. Government agencies may obtain copies of this report directly from DDC. Other qualified DDC users shall request through _____."

(4) "U. S. military agencies may obtain copies of this report directly from DDC. Other qualified users shall request through _____."

(5) "All distribution of this report is controlled. Qualified DDC users shall request through _____."

If the report has been furnished to the Office of Technical Services, Department of Commerce, for sale to the public, indicate this fact and enter the price, if known.

11. **SUPPLEMENTARY NOTES:** Use for additional explanatory notes.

12. **SPONSORING MILITARY ACTIVITY:** Enter the name of the departmental project office or laboratory sponsoring *(paying for)* the research and development. Include address.

13 **ABSTRACT:** Enter an abstract giving a brief and factual summary of the document indicative of the report, even though it may also appear elsewhere in the body of the technical report. If additional space is required, a continuation sheet shall be attached.

It is highly desirable that the abstract of classified reports be unclassified. Each paragraph of the abstract shall end with an indication of the military security classification of the information in the paragraph, represented as *(TS), (S), (C), or (U)*

There is no limitation on the length of the abstract. However, the suggested length is from 150 to 225 words.

14. **KEY WORDS:** Key words are technically meaningful terms or short phrases that characterize a report and may be used as index entries for cataloging the report. Key words must be selected so that no security classification is required. Identifiers, such as equipment model designation, trade name, military project code name, geographic location, may be used as key words but will be followed by an indication of technical context. The assignment of links, rules, and weights is optional.

CONFIDENTIAL
Security Classification